DISSERTATION

DEVELOPING PAPER-BASED DEVICES FOR MAPPING AGRICULTURAL PESTICIDES

AND ENVIRONMENTAL CONTAMINANTS

Submitted by

Ruth F. Menger

Department of Chemistry

In partial fulfillment of the requirements

For the Degree of Doctor of Philosophy

Colorado State University

Fort Collins, Colorado

Summer 2021

Doctoral Committee:

        Advisor: Charles S. Henry
        Co-Advisor: Thomas Borch

        A.R. Ravishankara
        James R. Neilson
        Pankaj Trivedi

ABSTRACT

DEVELOPING PAPER-BASED DEVICES FOR MAPPING AGRICULTURAL PESTICIDES

AND ENVIRONMENTAL CONTAMINANTS

The detection of environmental contaminants is important to ensure the health of both humans and the environment. Currently, detection is done by instrumentation like liquid or gas chromatography coupled with mass spectrometry. While sensitive and selective for multiple analytes, these instruments suffer from disadvantages like large size, high sample cost, and the need for a trained analyst to run the samples. As an alternative, microfluidic paper-based analytical devices (μPADs) are becoming more common as inexpensive, fast, easy to use devices to detect and quantify a variety of analytes. My research has been focused on developing μPADs for three different analytes: pesticides, PFAS, and heavy metals.

In order to ensure proper crop protection and pest management, it is important to manage and optimize pesticide application. Currently, this is done by water-sensitive papers, which often inaccurately portray the presence of pesticide due to humidity and extraneous water droplets that are not pesticide. In Chapter 2, I have developed a method that uses filter paper to capture a fluorescent tracer dye that has been mixed with the pesticide and then sprayed over the crop. The filter papers are imaged with a lightbox and Raspberry Pi camera system and then analyzed to determine percent coverage. After optimization and validation of the method to WSP, the filter paper method was used to evaluate pesticide distribution in a citrus grove in Florida (Chapter 3). The data from these field studies was used to make recommendations for which application method is best for the different types of pesticides.

Paper-based devices are inherently limited by the inability to control fluid properties like mixing. In order to incorporate mixing but also retain a small device that does not require external power to initial flow, a microfluidic device was fabricated out of two glass slides. A staggered herringbone pattern is laser ablated into the slides, and a channel is formed by double-sided adhesive (Chapter 4). Mixing was quantified using blue and yellow dyes. A reaction between horseradish peroxidase and hydrogen peroxide was used as a representative enzymatic reaction and also to determine enzyme kinetics. Since the microfluidic device is made of glass, it is also compatible with non-aqueous solvents. Paper-based devices do not work well with organic solvents because the hydrophobic wax on the paper is dissolved by the solvent.

In Chapter 5, the dissertation returns to traditional μPADs for environmental contaminants. Per- and polyfluoroalkyl substances (PFAS) are class of compounds that are highly persistent, toxic, bioaccumulative, and ubiquitous. While multiple instrument-based methods exist for sensitive and selective detection in a variety of matrices, there is a huge need for a fast, inexpensive, and easy-to-use sensor for PFAS detection. This would enable widespread testing of drinking water supplies, ensuring human health. A μPAD was developed for the detection of perfluorooctane sulfonate (PFOS) where the ion-pairing of PFOS and methylene green forms a purple circle. The diameter of the purple circle can be measured by the naked eye with a ruler or with the help of a smartphone to correlate the diameter back to PFOS concentration. At a cost of cents per sample, this μPAD enables fast and inexpensive detection of PFOS to ensure safe drinking water.

A common issue with environmental μPADs is the relatively high limits of detection compared to what is needed for regulatory purposes. It can be challenging to lower the limits of detection without incorporating an external pretreatment and/or preconcentration step. As μPADs

are small and handle only a small volume of sample (<120 µL), there is the possibility of increasing the sample capacity of the device but without significantly increasing the device size or analysis time. By adding multiple layers of absorbent filter paper underneath radial device for heavy metal detection, the sample volume increased to 1 mL, decreasing the limit of detection for a radial copper detection card from 100 ppb to 5 ppb (Chapter 6).

The research presented here achieves the goal of developing µPADs for environmental contaminants. They can be used in different ways to visualize the presence of the contaminant for monitoring and management purposes, ultimately ensuring human and environmental health.

ACKNOWLEDGMENTS

The last four years would not have happened without so much support from so many people. First, my advisors Chuck and Thomas have been champions for me from the very beginning when I was having a hard time choosing which lab to join. Since then, they have encouraged me to follow my research ideas as they have come up, as long as they were "fun and fundable." Both Chuck and Thomas model management, mentorship, and advising styles that I hope to have in the future: kind and respectful while also pushing me and my labmates to become better researchers, critical thinkers, and communicators of science. I also appreciate both of their encouragement to step away from work and get outside for some fresh air as they do in their own lives. We are all better researchers and people for taking time away from work.

I am so lucky that Chuck and Thomas have each cultivated lab groups that are accepting, supportive, and most of all fun to be around. My graduate school experience was made so much better by the Henry and Borch lab groups. Although the coronavirus pandemic put a hold on group gatherings for a time, I have appreciated all the group parties, BBQs, boat days, ski trips, as well as the research support through many practice talks and paper edits. Kate McMahon and Chloe Beardsley have been especially helpful over the past year, providing advice regarding experiments, figures, and manuscripts through our little environmental subgroup.

I would like to thank all the friends and family who have supported me along the way. I am so grateful for all the life talks over coffee, wine, and beer, as well as all the ski days, mountain trips, camping trips, and float trips. They are all truly highlights of my time here. A special thanks goes to Andrea Westlie, who has weathered all the highs and lows by my side since day 1. Finally,

I would like to thank my parents and family for encouraging curiosity and a love of science early on and also a love of the outdoors.

TABLE OF CONTENTS

CHAPTER 1: INTRODUCTION

1.1 Environmental Contaminants

The presence of humans on Earth has significantly contributed to environmental pollution.[1] Various industries like mining, agriculture, burning of fossil fuels, urban development, improper disposal of chemical solvents, and material production release harmful chemicals into the environment.[2] These environmental contaminants include but are not limited to heavy metals, pesticides, pharmaceuticals, personal care products, persistent organic pollutants, bacteria, explosives, and perfluorinated species.[3, 4] As these chemicals travel through the environment, they can pose a threat to the health of the ecosystem, as well as to humans through drinking water pollution.

Environmental contaminants can put environmental and human health at risk, causing mutagenic, carcinogenic, and teratogenic effects. Pollution (including air, water, occupational, and soil sources) is considered one of the world's biggest health risks, a leading cause of disease and death worldwide according to a recent Global Burden of Disease study (Figure 1.1).[5-8] Another recent report by the World Health Organization (WHO) reported that 3 in 10 people worldwide lack access to clean drinking water, with the majority of those people (~92%) living in poor or middle-income countries.[5, 9] While the best way to reduce water pollution would be to reduce the input of contamination in the first place, it is important to monitor the presence and spread of contamination, especially in resource-limited settings, to ensure safe drinking water.
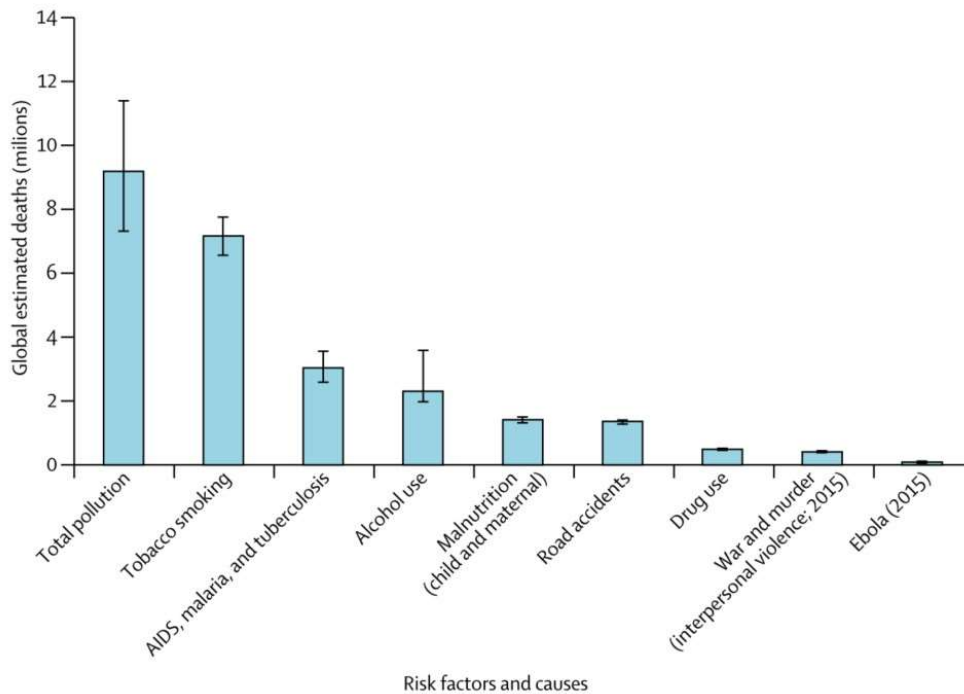
Figure 1.1 Global estimated deaths by major risk factor and cause. Total pollution includes air, water, occupational, and soil sources. Figure obtained with permission from Landrigan *et al.*, 2018.

1.2 Traditional Detection Methods

There are many detection methods available to monitor environmental contaminants and trends in their distribution. Many of these methods are laboratory-based, like liquid chromatography (LC), gas chromatography (GC), or inductively coupled plasma (ICP) coupled with mass spectrometry (MS), depending on the analyte. The EPA has developed and validated a set of standard protocols that are used to demonstrate compliance with government regulations.[10] For example, heavy metals are often analyzed by ICP-MS,[11] and pesticides can be quantified by LC-MS/MS.[12] While these instrumental methods are sensitive and selective, they are also non-portable, expensive, time-consuming, and require trained lab personnel to run. Environmental analysis often occurs in remote locations where sample transport back to the lab is not ideal, like carrying many liters of water back to a lab from a Superfund site or collecting drinking water

samples from various homes. The instruments mentioned before (LC-MS, GC-MS, ICP-MS) are usually not easily portable due to solvent, power, and pressure requirements. In addition, many areas of contamination are in resource-limited settings like developing countries.[9] To monitor environmental contaminants at the site of interest and potential contamination, methods that are fast, inexpensive, and portable are more desirable. These types of methods also empower citizens to evaluate their own drinking water.

1.3 Microfluidic Paper-Based Analytical Devices (μPADs)

When contaminant levels above the regulatory limits are found in the environment, immediate action should be taken to evaluate the status of the site and decide how to proceed to reduce the contamination. In some cases, a treatment like a sorbent or ion exchange can be applied,[13] while monitored natural attenuation (a more passive approach) is also recommended by the EPA.[14] A sensor-like device as an alternative and complementary detection method would provide real-time information about the presence of contaminants at a much lower cost than traditional instrumentation. The data can then be used to make immediate decisions regarding remediation, ensuring human and environmental health.[15]

An emerging platform for point-of-need (PON) detection of environmental contamination is microfluidic paper-based analytical devices (μPADs). Paper has been used as a substrate for chemical testing for centuries – like the use of litmus paper in pH strips starting in 1784.[16] In 2007, the Whitesides group at Harvard University demonstrated patterning small (i.e., microfluidic) channels on paper with a SU-8 epoxy-based photoresist. This hydrophobic barrier served to direct fluid flow, resulting in a device to detect glucose and protein in urine.[17] A new branch of paper-based PON devices followed, with thousands of papers being published and increasing numbers

each year (Figure 1.2). Using paper as a substrate is beneficial for PON purposes as it is disposable, inexpensive, flexible, biocompatible, easy to manipulate, and safe to handle.[18-23] The hydrophilic nature of the paper fibers induces capillary flow to draw the sample through the paper, eliminating the need for external instrumentation to drive fluid flow and contributing to making the devices portable and disposable.[23] Recent reviews highlight common themes and future directions of µPADs.[20, 22, 24-31]
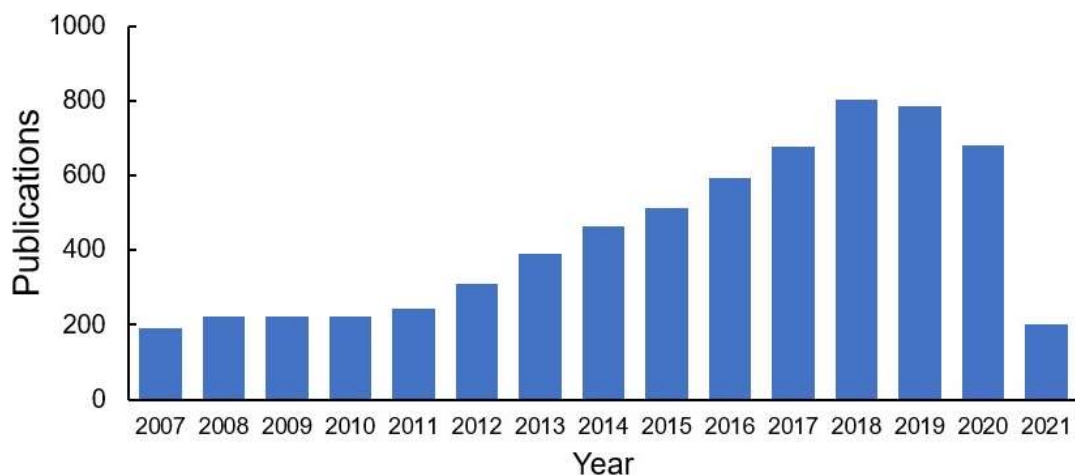
Figure 1.2 Publications per year for the search term "paper based analytical device" in Web of Science. Accessed 05.06.2021.

There are various methods for fabricating µPADs and forming the hydrophobic channels to direct fluid flow, including wax printing, photolithography, screen-printing, inkjet printing, and laser treatment.[23, 25] Wax printing is the most common as the procedure is rather simple and enables researchers all over the world to quickly prototype and manufacture devices with limited equipment. To wax print a device, a design is printed on a piece of filter paper with a printer that uses solid ink wax instead of liquid ink (like in an inkjet or laser printer).[32] Then, when the device is heated in an oven or on a hot plate, the wax melts into the paper, forming a 3-dimensional hydrophobic barrier (Figure 1.3).[33] This barrier directs fluid flow through the paper, with the capillary action of the paper acting as a passive pump.
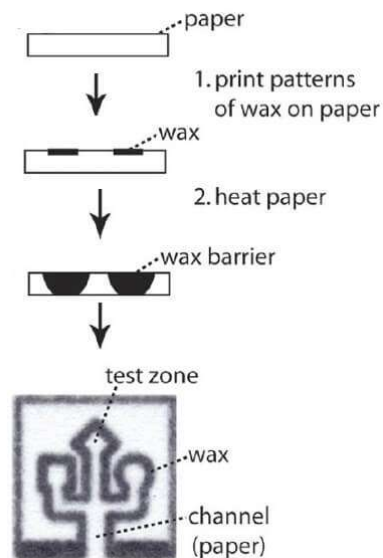
Figure 1.3 Fabrication of wax-printed paper-based analytical device (μPAD). Figure obtained with permission from Martinez *et al.*, 2010.

Paper is also ideal for storing and immobilizing reagents, eliminating the need for multiple external user steps of adding reagents. The reagents are also used to design a μPAD for a particular analyte.[28] For example, a complexing agent might be used to form a colored complex with certain heavy metals.[34] For biological assays, an enzyme can convert a chromophore in the presence of the analyte, generating a measurable response.[24] Enzyme-linked sandwich immunoassays (ELISA) have been performed on paper.[35] For redox-active molecules, electrochemical methods like chronoamperometry or voltammetry can be applied by incorporating electrodes into the μPADs.[36] The aggregation or separation of nanoparticles (gold and silver nanoparticles, quantum dots, carbon dots) can be measured with different methods: surface plasmon resonance, colorimetry, electrochemistry.[22] They can also be synthesized to be specific for an analyte or analyte class by tuning the nanoparticle composition, size, and morphology.[37]

μPADs use a variety of detection techniques, like colorimetry, fluorimetry, or electrochemistry.[30] For colorimetry, the analyte of interest reacts with a reagent that has been

preloaded in the detection region, producing a color change. This simple readout can be measured by naked eye and provide a yes/no answer as to whether an analyte is present or not. For more quantitative analysis, the degree of color change or distance of color formed can also be measured.[38-42] Smartphone apps have been developed to analyze the color change and compare the result to a calibration curve.[43] Fluorimetry and electrochemistry usually outperform colorimetry in terms of quantification like sensitivity and detection limits, but more instrumentation is required.[36] Recent efforts have been promising in terms of miniaturizing the instrumentation and making it more portable.[44]

1.4 Challenges of Colorimetric μPADs for Environmental Monitoring (This section is based on a review article on which I wrote the section on Environmental Monitoring, with modifications and edits for this document)[45]

The properties of μPADs described above, especially for colorimetric ones, make μPADs ideal for environmental monitoring; however, they also come with challenges. The devices ideally need to detect and quantify analytes at levels at or below those set by regulatory agencies such as the U.S. EPA and WHO.[46] Depending on the analyte, these limits can be in the ppt – ppb range; however, the LODs of colorimetric μPADs are often in the ppb – ppm range.[23, 47] An external preconcentration step can help detect low concentrations but that adds extra time and steps to the analysis. Since the regulatory limits are based on toxicology studies for different organisms, it is important to keep these in mind when developing a colorimetric μPAD – to maximize the applicability in the real world.

The devices must be selective for the intended analyte or class of analytes. Depending on the mechanism for color formation, there can be interferences from other similar analytes.[48, 49] For example, heavy metal detection on μPADs often relies on complexation with a colorimetric

6

indicator. Since heavy metals can have similar chemical properties, the resulting color of the complex is the same. Masking agents can be used to reduce the interference from competing metals.[49] In addition, environmental samples often contain interferences from the sample matrix, like organic and inorganic ions, organic matter, and surfactants, any of which could affect detection, depending on the analyte of interest.[48, 50-56] Sometimes pretreatment steps like purification and/or preconcentration are required which increases cost and time and decreases ease of use of a μPAD.[57, 58] Reagent stability is also critical, since the devices may need to be transported and used under a wide range of temperature, humidity, and sunlight conditions.[58-60] Proper storage conditions, like a sealed container, can protect devices from humidity and light.[61] Finally, there has been significant progress in data processing by moving from large, expensive, lab-based instruments to smartphones and image analysis software to provide fast, quantitative data. However, there are still many variables that need to be controlled to ensure reproducible data processing – like variable lighting at field sites. The use of lightboxes, algorithm correcting, and machine learning can all help to improve data processing in variable conditions, [28, 58, 62, 63]

In this thesis, I will be discussing how I have developed μPADs for PON environmental analysis. These devices have been designed to detect different analytes in the environment: pesticides, heavy metals, and perfluoroalkyl substances (PFAS). The work in the following chapters describes how μPADs can address the shortcomings of traditional analytical methods and provide alternative or complementary detection methods. The challenges in developing colorimetric μPADs that were mentioned will be kept in mind, as well as the overall goal of maintaining simplicity to provide fast and easy to use devices.

1.5 Measuring Spatial Distribution of Pesticides

Crop protection relies on the application of pesticides to control insects and other pests that negatively impact crops. For adequate protection and also to reduce extraneous pesticide in the environment, it is important to ensure efficient and adequate pesticide application and distribution within the crop. Excessive pesticide use can cause pest resistance and have unintended toxicity on other organisms.[64, 65] In humans, pesticides can irritate the skin or eyes, cause cancer, or negatively impact the nervous, hormone, or endocrine systems.[66] An optimized pest management program will reduce costs and time spent applying pesticides, increasing profits for the farmer. Thus, it is important to measure the distribution of pesticide application to ensure application efficiency.

Currently, water-sensitive papers (WSP) are used to measure the spatial distribution of pesticides.[67-69] The paper cards are attached to a crop and turn from yellow to blue in the presence of water during pesticide application.[67, 68] WSP are very general as they react to any sources of water, not just pesticide, so they often produce false positive results, especially in humid environments. Therefore, in Chapter 2, I developed a new method to evaluate the spatial distribution of pesticides in crops. The method uses paper as a substrate and a fluorescent dye as a surrogate for the pesticide (Figure 1.4). The method is less expensive, faster, and more accurate than the current industry standard of water-sensitive paper.[70]
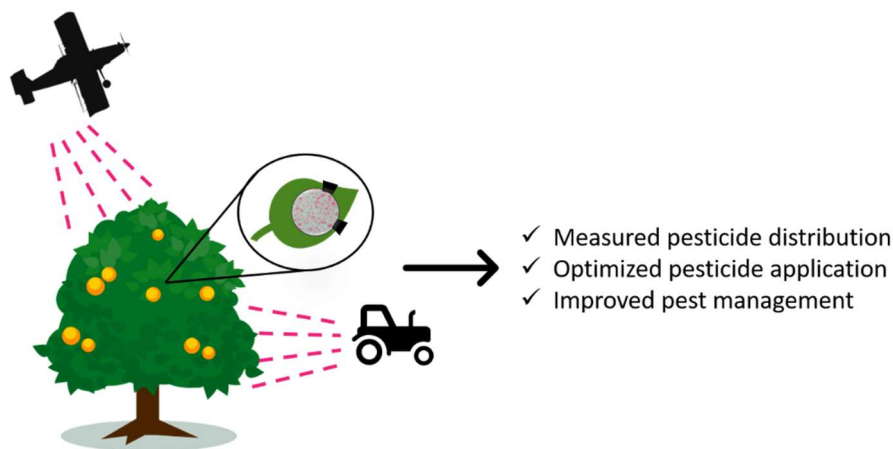
Figure 1.4 Schematic of newly developed method for evaluating pesticide distribution (Chapter 2).

The spatial distribution of pesticides is not well measured in many crops, especially in dense orchard trees like citrus trees.[71] This lack of data is critical when attempting to design a pest management plan for certain diseases. For example, citrus greening disease is a crop disease that is widespread in amongst citrus groves in Florida, China, and Brazil – all major citrus producers.[72] The disease has decreased production in Florida by 74% since 2005.[73] The main management plan is to apply pesticides to the citrus trees to reduce the population of psyllids, the vector of the disease.[72, 74] The psyllids prefer to reside on the underside of leaves, so pesticide application throughout the tree and especially the bottom of the leaf is important.[75] In Chapter 3, we applied the newly developed paper-based method in a citrus grove in Florida. The field studies demonstrated how the new method is used to determine pesticide coverage under a variety of spraying settings (Figure 1.5).[71] This data was used to advise on an improved pest management plan for treating citrus greening disease.
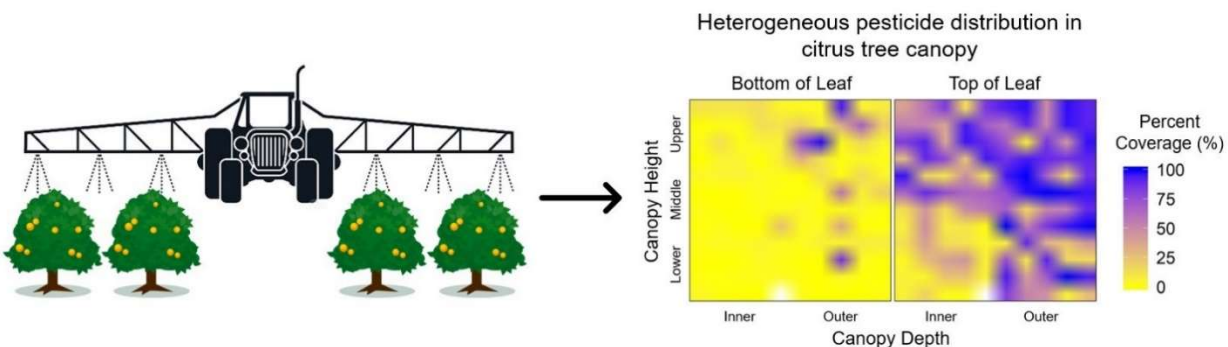
Figure 1.5 Schematic of measuring spatial distribution of pesticide in citrus trees (Chapter 3).

1.6 Mixing in Passive Flow Microfluidic Devices

My initial work in Chapters 2 and 3 about pesticide detection used a µPAD that can be read without a reagent performing a chemical reaction. However, there are few applications where a surrogate like the fluorescent dye can be used. Most chemical analysis requires chemical reactions and therefore also mixing. A disadvantage of most µPADs is that flow is dependent on the inherent

pore structure of the paper, making it difficult to control qualities of fluid flow other than direction.

Sample evaporation and paper swelling can occur, which contribute to unexpected changes in fluid

flow.[76-79] Rapid mixing is important for many complex reactions, especially for multi-step

reactions with multiple components. The mixing in µPADs cannot be manipulated due to the

reliance on the pore structure of the paper. Traditional microfluidic devices (not paper-based

devices), such as those made of materials like polydimethylsiloxane (PDMS), generate flow

through syringe pumps and can therefore manipulate mixing. These types of devices are unsuitable

for point-of-need settings due to the bulky size and electricity requirements of the associated

equipment.

In Chapter 4, a new passive flow device made of glass and double-sided adhesive is

described. The device keeps the advantages of microfluidic devices such as small sample size,

portability, and no external instrumentation while achieving full mixing of 2 sample droplets in <7

cm and <10s.[80] This device was modified for measuring organophosphate pesticides on the skin

of fruits and vegetables in Appendix 4.[81]

1.7 Detection of Perfluorinated Substances (This section is modified from a review article on
which I was the first author, with modifications and edits for this document)[82]

1.7.1 Overview

Per- and polyfluoroalkyl substances (PFAS) are a class of compounds that have recently

become an area of significant concern. Originating from a variety of materials like stain repellents,

nonstick coatings, cleaning products, and aqueous film forming foams (AFFFs), PFAS are

ubiquitous in environments all over the world, even in the Arctic.[83-85] They can be found in

drinking water, surface water, soils, wildlife, plants, the atmosphere, and human food sources as

well.[86-100] The high strength of the C-F bond makes PFAS thermodynamically stable and resistant

to typical environmental degradation pathways, like biodegradation and photolysis.[101, 102] This recalcitrance in the environment led to the moniker of "forever" chemicals.

Due to their widespread application and use, PFAS are continually released during production, product use, and disposal via point and nonpoint sources into the environment.[103] The highest PFAS concentrations have been recorded near wastewater treatment plants, firefighter training areas, landfill sites, and industrial sites.[104] These sources drain into environmental waters and ultimately our drinking water. Human exposure to PFAS is of high concern because they build up in the human body and have been linked to a variety of human health issues, including prostate and kidney cancer, thyroid disease, and diabetes.[93, 105-108] Studies have suggested that the toxicity comes from PFAS acting as an agonist for peroxisome proliferator-activated receptor alpha (PPARα). The activation of PPARα interferes with the proper transcription of many target genes, leading to cancer development and other diseases.[109-111]

The United States Environmental Protection Agency (EPA) has set a health advisory level of 70 ppt (70 ng L^{-1}) for lifetime exposure of perfluorooctanesulfonic acid (PFOS) and perfluorooctanoic acid (PFOA) in drinking water.[112] Despite this guideline (which is currently not legally regulated), drinking water levels of up to 3000 times the lifetime advisory level have been reported in Colorado, North Carolina, and other hotspots across the US.[113-115] It is estimated that 54 – 83% of the US population (179 – 272 million people) has been exposed to PFOS and PFOA contamination in their drinking water, indicating potential widespread contamination across the country.[116]

There are over 5000 CAS numbers that are classified under PFAS, and the identity of most of them is unknown.[117] PFOS and PFOA (Figure 1.6) have been studied the most since they have been manufactured the longest.[118, 119] The U.S. EPA lifetime health advisory level was determined based on exposure studies of these two PFAS.[120] However, there are so many other related compounds that contribute to overall PFAS occurrence and possible toxicity. Studies are ongoing to evaluate the cumulative toxicity of PFAS and also of newly developed short-chain alternatives like GenX (hexafluoropropylene oxide dimer acid, HFPO-DA) [93, 121, 122] As we begin to understand more about the global distribution of PFAS and replacement PFAS chemicals such as GenX and how toxic they can be, it is important to have a fast and cost-effective way to detect PFAS.[15]
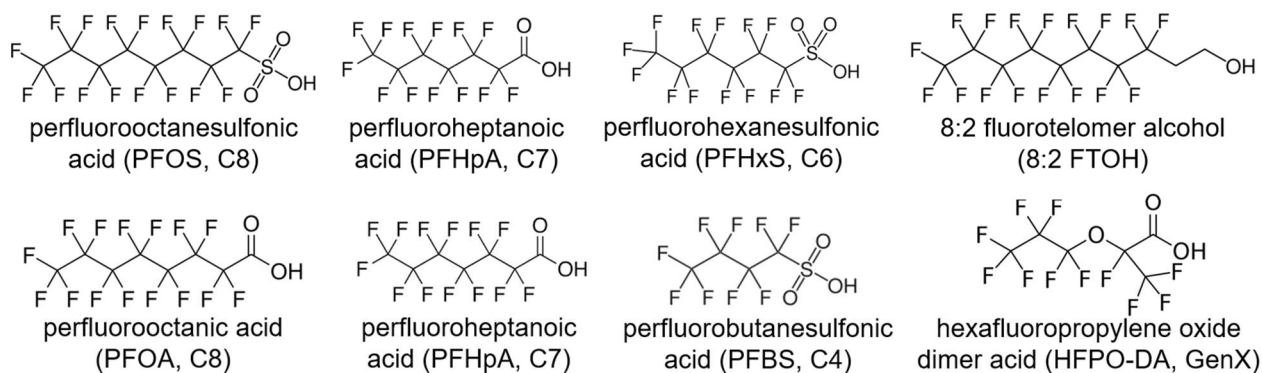
Figure 1.6 Example of common per and poly-fluoroalkyl substances (PFAS).

1.7.2 Current Methods for PFAS detection

Many laboratory-based techniques have been developed to detect PFAS using traditional analytical instruments.[104, 123-128] The EPA currently has three approved methods for PFAS analysis: Methods 533, 537, and 537.1.[129-131] These methods call for a polystyrene-divinylbenzene (SDVB) solid-phase extraction (SPE) step to concentrate the sample, followed by analysis with an LC-MS/MS fitted with a C18 column. All three methods are sensitive with LODs ranging from 0.71 – 16 ppt for 29 PFAS compounds but they are limited to drinking water samples and have a

minimum 35 min LC-MS/MS run time.[130, 131] As of May 2021, the EPA is working on validation to include other matrices like surface water, groundwater, wastewater, soil, sediment, and sludge.[132]

Other methods exist for the analysis of multiple PFAS in a variety of matrices, as recently reviewed by Amin *et al.*, although these methods have not been validated by the U.S. EPA.[128] For example, variations of liquid chromatography coupled with mass spectrometry offer targeted analysis with sensitive quantitative determination in aqueous matrices, including drinking water,[129, 133] groundwater,[134-136] surface water,[137, 138] river water,[139] seawater,[98] and wastewater.[135, 140] Ion chromatography[141-143] and fluorometric detection[144] can also provide LODs comparable to MS, but these methods require extensive pretreatment and/or derivatization with a fluorophore prior to analysis. Gas chromatography can only detect volatile, semi-volatile, and neutral PFAS which makes it less popular than LC[117, 123, 128] and the limits of detection are dependent on the detector. Capillary electrophoresis is portable but has poor detection limits (2-33 ppm).[145, 146]

While the instrumental methods are effective at the right time and place, they are limited by high instrument costs and the requirement of a laboratory with trained personnel. Costs of $300-$600 per sample are prohibitive in routine monitoring and do not allow for widespread sampling and testing of common PFAS.[147] To properly evaluate human risk of PFAS exposure, a simpler, faster, less expensive, and ideally field-based method is needed. Sensors, or devices that respond to an analyte and transform the chemical information into an analytically useful signal, have the potential to meet this demand for PFAS monitoring.[148] While PFAS exist in many matrices and detection therein is important, the detection of PFAS in aqueous matrices is a good first step to evaluate the risk of human exposure and the distribution of PFAS. Routine monitoring of water samples would allow more frequent testing to comply with regulations, providing actionable data

to water quality managers. A fast detection method can help identify critical areas of PFAS contamination where remediation efforts should be focused.[15] Without the need for a central laboratory, the general public could test their own drinking water using a fast and inexpensive test. A sensor for PFAS would not replace the traditional analytical techniques like LC-MS and GC-MS but instead complement their analysis by being able to provide real-time analysis at the point of decision.[15]

A colorimetric μPAD is ideal for PFAS analysis as it would provide a fast, easy-to-use, portable device. Currently, this does not exist. A variety of sensors have been developed but they often require long reaction times, multiple user steps, and/or external instrumentation for analysis.[82] The Naidu group in Australia has developed a colorimetric test kit for PFOA detection, the asktCARE kit, based on the complexation between ethyl violet and PFOA.[149, 150] After liquid-liquid extraction, the color of the resulting ion pair is measured by a smartphone. While the test kit is commercially available and is currently being used by Royal Australian Air Force defense bases,[149] it still requires many steps so running multiple samples at once would take up time and space. In Chapter 5, I present a colorimetric μPAD for the quantification of perfluorooctane sulfonate (PFOS) which achieves results in one step and <10 min.[151]

1.8 High Volume Heavy Metal Analysis

There has been much progress in the development of µPADs, especially given the massive increase in publications over the last few years. However, there is still the big limitation of high LODs which inhibits the use of µPADs in the real world.[47] One way to improve the limits of detection is to increase the number of moles of analyte that flow through the device. Moving from a color-changing spot test[152] to a distance-based device[153] to radial distance-based quantification[39] has increased the sample capacity from a few µL to 150 µL but the LODs are still high (Figure 1.7). Pretreatment steps like solid-phase extraction can concentrate a sample but this adds extra time, money, and user steps which is not necessarily desired for in-field and high-throughput analysis. There have been some reports of analyte concentration on µPADs, including heating[154-156] and ion concentration polarization,[157] but all of these methods require some degree of external instrumentation.

A. Spot test device for Fe, Ni, and Cu detection   B. Distance-based detection of Ni, Fe, and Cu   C. Radial distance-based detection cards for Zn, Fe, Mn, and Cu
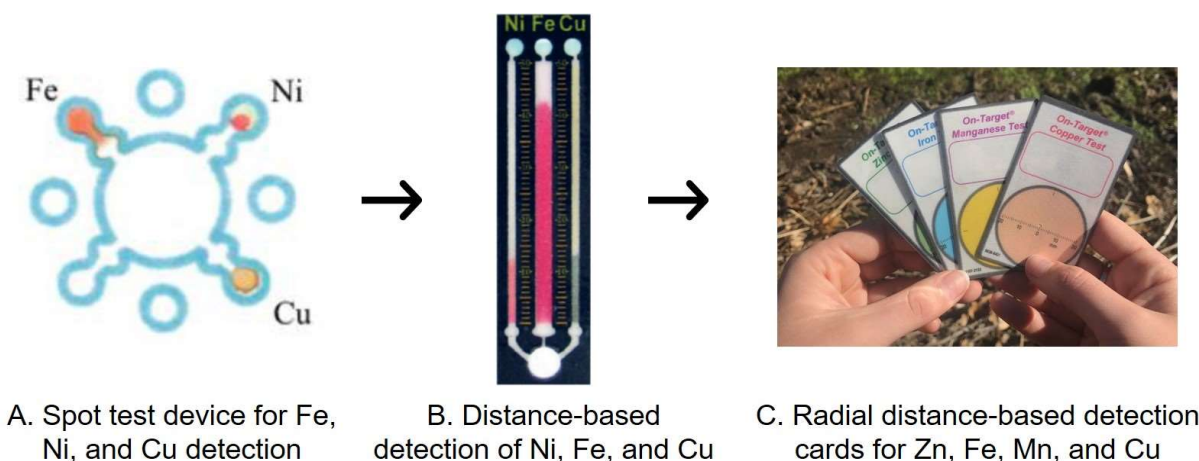
Figure 1.7 Examples of a spot test (A), distance-based device (B) and radial distance-based device (C). Figures obtained with permission from Mentele *et al.*, 2012, Cate *et al.*, 2015, and Hofstetter *et al.*, 2018.

Traditionally, µPADs are limited in terms of sample capacity, mostly requiring sample volumes of 1 – 100 µL. Some µPADs have been modified to accommodate higher volumes to

introduce more analyte molecules to the µPAD. For example, Kudo *et al.* quantified Zn^{2+} ions in a 1 mL sample on a colorimetric spot test with absorbent pads held together in a 3D-printed holder.[158] While the sample completed flow in 3 min, the holder increases the device cost, and high-throughput analysis would be challenging due to the device setup. The spot test needs to be removed from the holder and scanned for quantification. Shimada *et al.* used a distance-based format to detect Fe^{3+} but a sample volume of 1 mL took 9.5 hrs to flow through the device.[159]

Heavy metal detection by colorimetric µPADs especially suffers from high LODs, as heavy metals are only allowed at ppb or ppt levels by the Safe Drinking Water Act.[46] Colorimetric µPADs for heavy metals have achieved limits of detection of 0.1 – 100 ppm which are higher than recommended for drinking water.[23, 43, 47, 48, 160-162] A sample concentration step or higher sample volume is needed to detect contaminants in drinking water at their appropriate levels. Chapter 6, I present a new format for a colorimetric radial distance µPAD that does not require any holder or external instrumentation to increase the sample capacity by 10x. The results can be read in <1 hr by the naked eye and the LOD was decreased by 100x.[163]

1.9 Conclusion

In summary, the work described in this thesis is aimed towards developing and improving point-of-need µPADs for environmental contaminants. An improved method was developed to evaluate the spatial distribution of pesticides and support informed pest management decisions. In order to establish mixing by passive flow, a glass microfluidic device was designed and executed. PFAS, a class of contaminants of emerging concern, can now be detected and quantified with a colorimetric µPAD. Finally, heavy metal detection with µPADs suffers from high limits of

detection so a new device format has been proposed, improving colorimetric detection at the point of need.

REFERENCES

1.   Díaz, S.; Settele, J.; Brondízio, E. S.; Ngo, H. T.; Agard, J.; Arneth, A.; Balvanera, P.; Brauman, K. A.; Butchart, S. H. M.; Chan, K. M. A.; Garibaldi, L. A.; Ichii, K.; Liu, J.; Subramanian, S. M.; Midgley, G. F.; Miloslavich, P.; Molnár, Z.; Obura, D.; Pfaff, A.; Polasky, S.; Purvis, A.; Razzaque, J.; Reyers, B.; Chowdhury, R. R.; Shin, Y.-J.; Visseren-Hamakers, I.; Willis, K. J.; Zayas, C. N., Pervasive human-driven decline of life on Earth points to the need for transformative change. *Science* **2019,** *366* (6471), eaax3100.
2.   Chaudhry, F.; Malik, M., Factors affecting water pollution: a review. *J. Ecosyst. Ecography* **2017,** *7* (225), 1-3.
3.   Exposure to Environmental Contaminants. United States Environmental Protection Agency: 2020.
4.   Meredith, N. A.; Quinn, C.; Cate, D. M.; Reilly, T. H.; Volckens, J.; Henry, C. S., Paper-based analytical devices for environmental analysis. *The Analyst* **2016,** *141* (6), 1874-1887.
5.   Landrigan, P. J.; Fuller, R.; Acosta, N. J.; Adeyi, O.; Arnold, R.; Baldé, A. B.; Bertollini, R.; Bose-O'Reilly, S.; Boufford, J. I.; Breysse, P. N., The Lancet Commission on pollution and health. *The Lancet* **2018,** *391* (10119), 462-512.
6.   Wang, H.; Naghavi, M.; Allen, C.; Barber, R. M.; Bhutta, Z. A.; Carter, A.; Casey, D. C.; Charlson, F. J.; Chen, A. Z.; Coates, M. M., Global, regional, and national life expectancy, all-cause mortality, and cause-specific mortality for 249 causes of death, 1980–2015: a systematic analysis for the Global Burden of Disease Study 2015. *The Lancet* **2016,** *388* (10053), 1459-1544.
7.   Collaborators, G. R. F., Global, regional, and national comparative risk assessment of 79 behavioural, environmental and occupational, and metabolic risks or clusters of risks, 1990–2015: a systematic analysis for the Global Burden of Disease Study 2015. *Lancet (London, England)* **2016,** *388* (10053), 1659.
8.   Shaffer, R. M.; Sellers, S. P.; Baker, M. G.; De Buen Kalman, R.; Frostad, J.; Suter, M. K.; Anenberg, S. C.; Balbus, J.; Basu, N.; Bellinger, D. C.; Birnbaum, L.; Brauer, M.; Cohen, A.; Ebi, K. L.; Fuller, R.; Grandjean, P.; Hess, J. J.; Kogevinas, M.; Kumar, P.; Landrigan, P. J.; Lanphear, B.; London, S. J.; Rooney, A. A.; Stanaway, J. D.; Trasande, L.; Walker, K.; Hu, H., Improving and Expanding Estimates of the Global Burden of Disease Due to Environmental Health Risk Factors. *Environ. Health Perspect.* **2019,** *127* (10), 105001.
9.   *2017 Annual Report WHO/UNICEF Joint Monitoring Programme for Water Supply, Sanitation and Hygiene*; World Health Organization: 2017; pp 1-20.
10.   Approved Drinking Water Analytical Methods. United States Environmental Protection Agency: 2019.
11.   Creed, J. T.; Brockhoff, C. A.; Martin, T. D., Method 200.8: Determination of Trace Elements in Waters and Wastes By Inductively Coupled Plasma - Mass Spectrometry. 1994.
12.   Shoemaker, J., Development and Multi-laboratory Verification of US EPA Method 543 for the Analysis of Drinking Water Contaminants by Online Solid Phase Extraction-LC–MS-MS. *J. Chromatogr. Sci.* **2016,** *54* (9), 1532-1539.
13.   Hashim, M. A.; Mukhopadhyay, S.; Sahu, J. N.; Sengupta, B., Remediation technologies for heavy metal contaminated groundwater. *J. Environ. Manage.* **2011,** *92* (10), 2355-2388.

14.   Clement, T. P.; Truex, M. J.; Lee, P., A case study for demonstrating the application of U.S. EPA's monitored natural attenuation screening protocol at a hazardous waste site. *J. Contam. Hydrol.* **2002,** *59* (1-2), 133-162.

15.   Naidu, R.; Nadebaum, P.; Fang, C.; Cousins, I.; Pennel, K.; Conder, J.; Newell, C.; Longpré, D.; Warner, S.; Crosbie, N., Per-and poly-fluoroalkyl substances (PFAS) current status and research needs. *Environ. Technol. Inno.* **2020**, 100915.

16.   Banks, J.; Watt, J., On a Mew Method of Preparing a Test Liquor to Shew the Presence of Acids and Alkalies in Chemical Mixtures. *Phil. Trans. R. Soc. Lond.* **1784,** *74*, 419-422.

17.   Martinez, A. W.; Phillips, S. T.; Butte, M. J.; Whitesides, G. M., Patterned paper as a platform for inexpensive, low-volume, portable bioassays. *Angew. Chem. Int. Ed.* **2007,** *46* (8), 1318-20.

18.   Yetisen, A. K.; Akram, M. S.; Lowe, C. R., Paper-based microfluidic point-of-care diagnostic devices. *Lab Chip* **2013,** *13* (12), 2210.

19.   Rackus, D. G.; Shamsi, M. H.; Wheeler, A. R., Electrochemistry, biosensors and microfluidics: a convergence of fields. *Chem. Soc. Rev.* **2015,** *44* (15), 5320-5340.

20.   Xia, Y.; Si, J.; Li, Z., Fabrication techniques for microfluidic paper-based analytical devices and their applications for biological testing: A review. *Biosens. Bioelectron.* **2016,** *77*, 774-789.

21.   Byrnes, S.; Thiessen, G.; Fu, E., Progress in the development of paper-based diagnostics for low-resource point-of-care settings. *Bioanalysis* **2013,** *5* (22), 2821-2836.

22.   Yang, Y.; Noviana, E.; Nguyen, M. P.; Geiss, B. J.; Dandy, D. S.; Henry, C. S., Paper-Based Microfluidic Devices: Emerging Themes and Applications. *Anal. Chem.* **2017,** *89*, 71-91.

23.   Li, X.; Ballerini, D. R.; Shen, W., A perspective on paper-based microfluidics: Current status and future trends. *Biomicrofluidics* **2012,** *6* (1), 011301.

24.   Ahmed, S.; Bui, M.-P. N.; Abbas, A., Paper-based chemical and biological sensors: Engineering aspects. *Biosens. Bioelectron.* **2016,** *77*, 249-263.

25.   Akyazi, T.; Basabe-Desmonts, L.; Benito-Lopez, F., Review on microfluidic paper-based analytical devices towards commercialisation. *Anal. Chim. Acta* **2018,** *1001*, 1-17.

26.   Gong, M. M.; Sinton, D., Turning the Page: Advancing Paper-Based Microfluidics for Broad Diagnostic Application. *Chem. Rev.* **2017,** *117* (12), 8447-8480.

27.   Lim, W. Y.; Goh, B. T.; Khor, S. M., Microfluidic paper-based analytical devices for potential use in quantitative and direct detection of disease biomarkers in clinical analysis. *J. Chromatogr. B* **2017,** *1060*, 424-442.

28.   Morbioli, G. G.; Mazzu-Nascimento, T.; Stockton, A. M.; Carrilho, E., Technical aspects and challenges of colorimetric detection with microfluidic paper-based analytical devices (μPADs) - A review. *Anal. Chim. Acta* **2017,** *970*, 1-22.

29.   Cate, D. M.; Adkins, J. A.; Mettakoonpitak, J.; Henry, C. S., Recent Developments in Paper-Based Microfluidic Devices. *Anal. Chem.* **2015,** *87* (1), 19-41.

30.   Kung, C.-T.; Hou, C.-Y.; Wang, Y.-N.; Fu, L.-M., Microfluidic paper-based analytical devices for environmental analysis of soil, air, ecology and river water. *Sens. Actuators B Chem.* **2019,** *301*, 126855.

31.   Liana, D. D.; Raguse, B.; Gooding, J. J.; Chow, E., Recent Advances in Paper-Based Sensors. *Sensors* **2012,** *12* (9), 11505-11526.

32.   Carrilho, E.; Martinez, A. W.; Whitesides, G. M., Understanding Wax Printing: A Simple Micropatterning Process for Paper-Based Microfluidics. *Anal. Chem.* **2009,** *81* (16), 7091-7095.

33.   Martinez, A. W.; Phillips, S. T.; Whitesides, G. M.; Carrilho, E., Diagnostics for the Developing World: Microfluidic Paper-Based Analytical Devices. *Anal. Chem.* **2010,** *82* (1), 3-10.

34.   Dungchai, W.; Chailapakul, O.; Henry, C. S., Use of multiple colorimetric indicators for paper-based microfluidic devices. *Anal. Chim. Acta* **2010,** *674* (2), 227-33.

35.   Carrell, C. S.; Wydallis, R. M.; Bontha, M.; Boehle, K. E.; Beveridge, J. R.; Geiss, B. J.; Henry, C. S., Rotary manifold for automating a paper-based Salmonella immunoassay. *RSC Adv.* **2019,** *9* (50), 29078-29086.

36.   Noviana, E.; McCord, C. P.; Clark, K. M.; Jang, I.; Henry, C. S., Electrochemical paper-based devices: sensing approaches and progress toward practical applications. *Lab Chip* **2020,** *20* (1), 9-34.

37.   Noguez, C., Surface Plasmons on Metal Nanoparticles: The Influence of Shape and Physical Environment. *J. Phys. Chem. C* **2007,** *111* (10), 3806-3819.

38.   Gerold, C. T.; Bakker, E.; Henry, C. S., Selective Distance-Based K+ Quantification on Paper-Based Microfluidics. *Anal. Chem.* **2018,** *90* (7), 4894-4900.

39.   Hofstetter, J. C.; Wydallis, J. B.; Neymark, G.; Reilly, T. H.; Harrington, J.; Henry, C. S., Quantitative colorimetric paper analytical devices based on radial distance measurements for aqueous metal determination. *Analyst* **2018,** *143* (13), 3085-3090.

40.   Nguyen, M. P.; Kelly, S. P.; Wydallis, J. B.; Henry, C. S., Read-by-eye quantification of aluminum (III) in distance-based microfluidic paper-based analytical devices. *Anal. Chim. Acta* **2020,** *1100*, 156-162.

41.   Alsaeed, B.; Mansour, F. R., Distance-based paper microfluidics; principle, technical aspects and applications. *Microchem. J.* **2020,** *155*, 104664.

42.   Yamada, K.; Citterio, D.; Henry, C. S., "Dip-and-read" paper-based analytical devices using distance-based detection with color screening. *Lab Chip* **2018,** *18* (10), 1485-1493.

43.   Li, F.; Hu, Y.; Li, Z.; Liu, J.; Guo, L.; He, J., Three-dimensional microfluidic paper-based device for multiplexed colorimetric detection of six metal ions combined with use of a smartphone. *Anal. Bioanal. Chem.* **2019,** *411* (24), 6497-6508.

44.   Teengam, P.; Siangproh, W.; Tontisirin, S.; Jiraseree-amornkun, A.; Chuaypen, N.; Tangkijvanich, P.; Henry, C. S.; Ngamrojanavanich, N.; Chailapakul, O., NFC-enabling smartphone-based portable amperometric immunosensor for hepatitis B virus detection. *Sens. Actuators B Chem.* **2021,** *326*, 128825.

45.   Carrell, C.; Kava, A.; Nguyen, M.; Menger, R. F.; Munshi, Z.; Call, Z.; Nussbaum, M.; Henry, C., Beyond the lateral flow assay: A review of paper-based microfluidics. *Microelectron. Eng.* **2019,** *206*, 45-54.

46.   National Primary Drinking Water Regulations. In *816-F-09-004*, Agency, U. S. E. P., Ed. 2009.

47.   Almeida, M. I. G. S.; Jayawardane, B. M.; Kolev, S. D.; McKelvie, I. D., Developments of microfluidic paper-based analytical devices (µPADs) for water analysis: A review. *Talanta* **2018,** *177*, 176-190.

48.   Rattanarat, P.; Dungchai, W.; Cate, D.; Volckens, J.; Chailapakul, O.; Henry, C. S., Multilayer Paper-Based Device for Colorimetric and Electrochemical Quantification of Metals. *Analytical Chemistry* **2014,** *86* (7), 3555-3562.

49.   Meredith, N. A.; Volckens, J.; Henry, C. S., Paper-based microfluidics for experimental design: screening masking agents for simultaneous determination of Mn(ii) and Co(ii). *Anal. Methods* **2017,** *9*, 534-540.

50.   Jeon, J.; Kannan, K.; Lim, B. J.; An, K. G.; Kim, S. D., Effects of salinity and organic matter on the partitioning of perfluoroalkyl acid (PFAs) to clay particles. *J. Environ. Monitor.* **2011,** *13* (6), 1803.

51.   Niu, H.; Wang, S.; Zhou, Z.; Ma, Y.; Ma, X.; Cai, Y., Sensitive Colorimetric Visualization of Perfluorinated Compounds Using Poly(ethylene glycol) and Perfluorinated Thiols Modified Gold Nanoparticles. *Anal. Chem.* **2014,** *86* (9), 4170-4177.

52.   Zhang, F.; Zheng, Y.; Liang, J.; Long, S.; Chen, X.; Tan, K., A simple and highly sensitive assay of perfluorooctanoic acid based on resonance light scattering technique. *Spectrochim. Acta, Part A* **2016,** *159*, 7-12.

53.   Chen, Q.; Zhu, P.; Xiong, J.; Gao, L.; Tan, K., A new dual-recognition strategy for hybrid ratiometric and ratiometric sensing perfluorooctane sulfonic acid based on high fluorescent carbon dots with ethidium bromide. *Spectrochim. Acta, Part A* **2020,** *224*, 117362.

54.   Powley, C. R.; George, S. W.; Ryan, T. W.; Buck, R. C., Matrix Effect-Free Analytical Methods for Determination of Perfluorinated Carboxylic Acids in Environmental Matrixes. *Anal. Chem.* **2005,** *77* (19), 6353-6358.

55.   Cheng, J.; Vecitis, C. D.; Park, H.; Mader, B. T.; Hoffmann, M. R., Sonochemical Degradation of Perfluorooctane Sulfonate (PFOS) and Perfluorooctanoate (PFOA) in Landfill Groundwater: Environmental Matrix Effects. *Environ. Sci. Technol.* **2008,** *42* (21), 8057-8063.

56.   Taniyasu, S.; Kannan, K.; So, M. K.; Gulkowska, A.; Sinclair, E.; Okazawa, T.; Yamashita, N., Analysis of fluorotelomer alcohols, fluorotelomer acids, and short- and long-chain perfluorinated acids in water and biota. *J. Chromatogr. A.* **2005,** *1093* (1-2), 89-97.

57.   Medina-Sanchez, M.; Cadevall, M.; Ros, J.; Merkoci, A., Eco-friendly electrochemical lab-on-paper for heavy metal detection. *Anal. Bioanal. Chem.* **2015,** *407* (28), 8445-8449.

58.   Wang, H.; Li, Y.-J.; Wei, J.-F.; Xu, J.-R.; Wang, Y.-H.; Zheng, G.-X., Paper-based three-dimensional microfluidic device for monitoring of heavy metals with a camera cell phone. *Anal. Bioanal. Chem.* **2014,** *406* (12), 2799-2807.

59.   Jayawardane, B. M.; McKelvie, I. D.; Kolev, S. D., Development of a Gas-Diffusion Microfluidic Paper-Based Analytical Device (μPAD) for the Determination of Ammonia in Wastewater Samples. *Anal. Chem.* **2015,** *87* (9), 4621-4626.

60.   Jayawardane, B. M.; Wongwilai, W.; Grudpan, K.; Kolev, S. D.; Heaven, M. W.; Nash, D. M.; McKelvie, I. D., Evaluation and Application of a Paper-Based Device for the Determination of Reactive Phosphate in Soil Solution. *Journal of Environmental Quality* **2014,** *43* (3), 1081-1085.

61.   Hu, J.; Wang, S.; Wang, L.; Li, F.; Pingguan-Murphy, B.; Lu, T. J.; Xu, F., Advances in paper-based point-of-care diagnostics. *Biosens. Bioelectron.* **2014,** *54*, 585-597.

62.   Jayawardane, B. M.; McKelvie, I. D.; Kolev, S. D., Development of a Gas-Diffusion Microfluidic Paper-Based Analytical Device (mu PAD) for the Determination of Ammonia in Wastewater Samples. *Analytical Chemistry* **2015,** *87* (9), 4621-4626.

63.   Lopez-Ruiz, N.; Curto, V. F.; Erenas, M. M.; Benito-Lopez, F.; Diamond, D.; Palma, A. J.; Capitan-Vallvey, L. F., Smartphone-Based Simultaneous pH and Nitrite Colorimetric Determination for Paper Microfluidic Devices. *Anal. Chem.* **2014,** *86* (19), 9554-9562.

64.   Rehberg, R. A.; Trivedi, P.; Bahureksa, W.; Sharp, J.; Stokes, S. C.; Menger, R. F.; Borch, T., Quantification of insecticide application efficiency and Asian Citrus psyllid death within a citrus green disease infected grove. *Pest Manag. Sci.* **2021,** *77*, 1748-1756.

65.   Aktar, M. W.; Sengupta, D.; Chowdhury, A., Impact of pesticides use in agriculture: their benefits and hazards. *Interdiscip. Toxicol.* **2009,** *2* (1), 1.

66.   Mostafalou, S.; Abdollahi, M., Pesticides: an update of human exposure and toxicity. *Arch. Toxicol.* **2017,** *91* (2), 549-599.

67.   Water Sensitive Paper. Spraying Systems Co.

68.   3" x 2" Water Sensitive Paper – Sprayer Depot. Wheaton, IL.

69.   Hill, B. D.; Inaba, D. J., Use of Water-Sensitive Paper to Monitor the Deposition of Aerially Applied Insecticides. *J. Econ. Entomol.* **1989,** *82* (3), 974-980.

70.   Menger, R. F.; Bontha, M.; Beveridge, J. R.; Borch, T.; Henry, C. S., Fluorescent-based method for assessment of pesticide coverage on leaves and trees: A citrus grove case study. *J. Agric. Food Chem.* **2020,** *68* (47), 14009-14014.

71.   Menger, R. F.; Rehberg, R. A.; Trivedi, P.; Henry, C. S.; Borch, T., High spatial resolution fluorescence imagery for optimized pest management within a citrus grove. Submitted to *Phytopathology.* **2021**.

72.   Boina, D. R.; Bloomquist, J. R., Chemical control of the Asian citrus psyllid and of huanglongbing disease in citrus. *Pest Manag. Sci.* **2015,** *71* (6), 808-823.

73.   Singerman, A.; Rogers, M. E., The Economic Challenges of Dealing with Citrus Greening: The Case of Florida. *J. Integr. Pest Manag.* **2020,** *11* (1).

74.   Bové, J. M., Huanglongbing: a destructive, newly-emerging, century-old disease of citrus. *Journal of Plant Pathology* **2006**, 7-37.

75.   Grafton-Cardwell, E. E.; Stelinski, L. L.; Stansly, P. A., Biology and Management of Asian Citrus Psyllid, Vector of the Huanglongbing Pathogens. *Annu. Rev. Entomol.* **2012,** *58,* 413-432.

76.   Elizalde, E.; Urteaga, R.; Berli, C. L. A., Rational design of capillary-driven flows for paper-based microfluidics. *Lab Chip* **2015,** *15* (10), 2173-2180.

77.   Songok, J.; Toivakka, M., Controlling capillary-driven surface flow on a paper-based microfluidic channel. *Microfluid. Nanofluid.* **2016,** *20* (63), 1-9.

78.   Liu, M.; Wu, J.; Gan, Y.; Hanaor, D. A. H.; Chen, C. Q., Evaporation Limited Radial Capillary Penetration in Porous Media. *Langmuir* **2016,** *32* (38), 9899-9904.

79.   Chang, S.; Seo, J.; Hong, S.; Lee, D.-G.; Kim, W., Dynamics of liquid imbibition through paper with intra-fibre pores. *J. Fluid. Mech.* **2018,** *845,* 36-50.

80.   Channon, R. B.; Menger, R. F.; Wang, W.; Carrão, D. B.; Vallabhuneni, S.; Kota, A. K.; Henry, C. S., Design and application of a self-pumping microfluidic staggered herringbone mixer. *Microfluid. Nanofluid.* **2021,** *25* (4).

81.   Jang, I.; Carrão, D. B.; Menger, R. F.; Moraes De Oliveira, A. R.; Henry, C. S., Pump-Free Microfluidic Rapid Mixer Combined with a Paper-Based Channel. *ACS Sensors* **2020,** *5* (7), 2230-2238.

82.   Menger, R. F.; Funk, E.; Henry, C. S.; Borch, T., Sensors for Detecting Per- and Polyfluoroalkyl Substances (PFAS): A Critical Review of Development Challenges, Current Sensors, and Commercialization Obstacles. *Chem. Eng. J.* **2021**, 129133.

83.   Butt, C. M.; Berger, U.; Bossi, R.; Tomy, G. T., Levels and trends of poly- and perfluorinated compounds in the arctic environment. *Sci. Total Environ.* **2010,** *408* (15), 2936-2965.

84.   Yamashita, N.; Taniyasu, S.; Petrick, G.; Wei, S.; Gamo, T.; Lam, P. K. S.; Kannan, K., Perfluorinated acids as novel chemical tracers of global circulation of ocean waters. *Chemosphere* **2008,** *70* (7), 1247-1255.

85.   Ross, I.; McDonough, J.; Miles, J.; Storch, P.; Thelakkat Kochunarayanan, P.; Kalve, E.; Hurst, J.; S. Dasgupta, S.; Burdick, J., A review of emerging technologies for remediation of PFASs. *Remediation* **2018,** *28* (2), 101-126.

86.   Benskin, J. P.; Li, B.; Ikonomou, M. G.; Grace, J. R.; Li, L. Y., Per- and Polyfluoroalkyl Substances in Landfill Leachate: Patterns, Time Trends, and Sources. *Environ. Sci. Technol.* **2012,** *46* (21), 11532-11540.

87.   Domingo, J. L.; Nadal, M., Per-and polyfluoroalkyl substances (PFASs) in food and human dietary intake: a review of the recent scientific literature. *J. Agric. Food Chem.* **2017,** *65* (3), 533-543.

88.   Herzke, D.; Olsson, E.; Posner, S., Perfluoroalkyl and polyfluoroalkyl substances (PFASs) in consumer products in Norway - A pilot study. *Chemosphere* **2012,** *88* (8), 980-987.

89.   Hu, X. C.; Andrews, D. Q.; Lindstrom, A. B.; Bruton, T. A.; Schaider, L. A.; Grandjean, P.; Lohmann, R.; Carignan, C. C.; Blum, A.; Balan, S. A.; Higgins, C. P.; Sunderland, E. M., Detection of Poly- and Perfluoroalkyl Substances (PFASs) in U.S. Drinking Water Linked to Industrial Sites, Military Fire Training Areas, and Wastewater Treatment Plants. *Environ. Sci. Technol. Lett.* **2016,** *3* (10), 344-350.

90.   Goosey, E.; Harrad, S., Perfluoroalkyl substances in UK indoor and outdoor air: Spatial and seasonal variation, and implications for human exposure. *Environ. Int.* **2012,** *45*, 86-90.

91.   Loi, E. I. H.; Yeung, L. W. Y.; Mabury, S. A.; Lam, P. K. S., Detections of Commercial Fluorosurfactants in Hong Kong Marine Environment and Human Blood: A Pilot Study. *Environ. Sci. Technol.* **2013,** *47* (9), 4677-4685.

92.   Smithwick, M.; Norstrom, R. J.; Mabury, S. A.; Solomon, K.; Evans, T. J.; Stirling, I.; Taylor, M. K.; Muir, D. C. G., Temporal Trends of Perfluoroalkyl Contaminants in Polar Bears (Ursus maritimus) from Two Locations in the North American Arctic, 1972-2002. *Environ. Sci. Technol.* **2006,** *40* (4), 1139-1143.

93.   Sunderland, E. M.; Hu, X. C.; Dassuncao, C.; Tokranov, A. K.; Wagner, C. C.; Allen, J. G., A review of the pathways of human exposure to poly- and perfluoroalkyl substances (PFASs) and present understanding of health effects. *J. Exposure Sci. Environ. Epidemiol.* **2019,** *29* (2), 131-147.

94.   Szostek, B.; Prickett, K. B., Determination of 8:2 fluorotelomer alcohol in animal plasma and tissues by gas chromatography-mass spectrometry. *J. Chromatogr. B* **2004,** *813* (1-2), 313-21.

95.   Van de Vijver, K. I.; Hoff, P.; Das, K.; Brasseur, S.; Van Dongen, W.; Esmans, E.; Reijnders, P.; Blust, R.; De Coen, W., Tissue distribution of perfluorinated chemicals in harbor seals (Phoca vitulina) from the Dutch Wadden Sea. *Environ. Sci. Technol.* **2005,** *39* (18), 6978-84.

96.   Verreault, J.; Houde, M.; Gabrielsen, G. W.; Berger, U.; Hauks, M.; Letcher, R. J.; Muir, D. C. G., Perfluorinated Alkyl Substances in Plasma, Liver, Brain, and Eggs of Glaucous Gulls (Larus hyperboreus) from the Norwegian Arctic. *Environ. Sci. Technol.* **2005,** *39* (19), 7439-7445.

97.   Xiao, X.; Ulrich, B. A.; Chen, B.; Higgins, C. P., Sorption of Poly- and Perfluoroalkyl Substances (PFASs) Relevant to Aqueous Film-Forming Foam (AFFF)-Impacted Groundwater by Biochars and Activated Carbon. *Environ. Sci. Technol.* **2017,** *51* (11), 6342-6351.

98.   Yamashita, N.; Kannan, K.; Taniyasu, S.; Horii, Y.; Okazawa, T.; Petrick, G.; Gamo, T., Analysis of perfluorinated acids at parts-per-quadrillion levels in seawater using liquid chromatography-tandem mass spectrometry. *Environ. Sci. Technol.* **2004,** *38* (21), 5522-8.

99.   Place, B. J.; Field, J. A., Identification of Novel Fluorochemicals in Aqueous Film-Forming Foams Used by the US Military. *Environ. Sci. Technol.* **2012,** *46* (13), 7120-7127.

100. Backe, W.; Field, J. A., Zwitterionic, cationic, and anionic fluorinated chemicals in aqueous film forming foam formulations and groundwater at US militarty bases by non-aqueous large volume injection HPLC-MS/MS. *Environ. Sci. Technol.* **2013,** *47*, 5226-5234.

101. Liou, J. S. C.; Szostek, B.; Derito, C. M.; Madsen, E. L., Investigating the biodegradability of perfluorooctanoic acid. *Chemosphere* **2010,** *80* (2), 176-183.

102. Vaalgamaa, S.; Vähätalo, A. V.; Perkola, N.; Huhtala, S., Photochemical reactivity of perfluorooctanoic acid (PFOA) in conditions representing surface water. *Sci. Total Environ.* **2011,** *409* (16), 3043-3048.

103. Sharifan, H.; Bagheri, M.; Wang, D.; Burken, J. G.; Higgins, C. P.; Liang, Y.; Liu, J.; Schaefer, C. E.; Blotevogel, J., Fate and transport of per- and polyfluoroalkyl substances (PFASs) in the vadose zone. *Sci. Total Environ.* **2021**, 145427.

104. Dauchy, X., Per- and polyfluoroalkyl substances (PFASs) in drinking water: Current state of the science. *Curr. Opin. Environ. Sci. Health* **2019,** *7*, 8-12.

105. Ahrens, L.; Bundschuh, M., Fate and effects of poly- and perfluoroalkyl substances in the aquatic environment: A review. *Environ. Toxicol. Chem.* **2014,** *33* (9), 1921-1929.

106. Butenhoff, J. L.; Kennedy, G. L., Jr.; Frame, S. R.; O'Connor, J. C.; York, R. G., The reproductive toxicology of ammonium perfluorooctanoate (APFO) in the rat. *Toxicology* **2004,** *196* (1-2), 95-116.

107. Hekster, F. M.; Laane, R. W. P. M.; De Voogt, P., Environmental and Toxicity Effects of Perfluoroalkylated Substances. *Rev. Environ. Contam. Toxicol.* **2003,** *179*, 99-121.

108. Kudo, N.; Kawashima, Y., Toxicity and toxicokinetics of perfluorooctanoic acid in humans and animals. *J. Toxicol. Sci.* **2003,** *28* (2), 49-57.

109. Hurst, C. H.; Waxman, D. J., Activation of PPAR and PPAR by Environmental Phthalate Monoesters. *Toxicol. Sci.* **2003,** *74* (2), 297-308.

110. Shipley, J. M., trans-Activation of PPAR and Induction of PPAR Target Genes by Perfluorooctane-Based Chemicals. *Toxicol. Sci.* **2004,** *80* (1), 151-160.

111. Klaunig, J. E.; Babich, M. A.; Baetcke, K. P.; Cook, J. C.; Corton, J. C.; David, R. M.; DeLuca, J. G.; Lai, D. Y.; McKee, R. H.; Peters, J. M., PPARα agonist-induced rodent tumors: modes of action and human relevance. *Crit. Rev. Toxicol.* **2003,** *33* (6), 655-780.

112. Lifetime Health Advisories and Health Effects Support Documents for Perfluorooctanoic Acid and Perfluorooctane Sulfonate. U.S. Environmental Protection Agency: Washington, D.C., 2016; Vol. 81.

113. Finley, B., Colorado ramps up response to toxic "forever chemicals" after discovery of hot spots across metro Denver. *Denver Post* 2019.

114. White, D., Denver Post Article on Colorado Response to High Levels of PFAS. Association of State Drinking Water Administrators: 2019.

115. PFAS Contamination in the U.S. https://www.ewg.org/interactive-maps/2019_pfas_contamination/map/ (accessed November 1, 2020).

116. Andrews, D. Q.; Naidenko, O. V., Population-Wide Exposure to Per- and Polyfluoroalkyl Substances from Drinking Water in the United States. *Environ. Sci. Technol. Lett.* **2020,** *7* (12), 931-936.

117. Nakayama, S. F.; Yoshikane, M.; Onoda, Y.; Nishihama, Y.; Iwai-Shimada, M.; Takagi, M.; Kobayashi, Y.; Isobe, T., Worldwide trends in tracing poly- and perfluoroalkyl substances (PFAS) in the environment. *TrAC, Trends Anal. Chem.* **2019,** *121*, 115410.

118. Giesy, J. P.; Kannan, K., Perfluorochemical surfactants in the environment. *Environ. Sci. Technol.* **2002,** *36*, 147-152.

119.   Giesy, J. P.; Kannan, K., Global distribution of perfluorooctane sulfonate in wildlife. *Environ. Sci. Technol.* **2001,** *35* (7), 1339-1342.

120.   Cordner, A.; De La Rosa, V. Y.; Schaider, L. A.; Rudel, R. A.; Richter, L.; Brown, P., Guideline levels for PFOA and PFOS in drinking water: the role of scientific uncertainty, risk assessment decisions, and social factors. *J. Exposure Sci. Environ. Epidemiol.* **2019,** *29* (2), 157-171.

121.   Rice, P. A.; Aungst, J.; Cooper, J.; Bandele, O.; Kabadi, S. V., Comparative analysis of the toxicological databases for 6:2 fluorotelomer alcohol (6:2 FTOH) and perfluorohexanoic acid (PFHxA). *Food Chem. Toxicol.* **2020,** *138*, 111210.

122.   Cannon, R. E.; Richards, A. C.; Trexler, A. W.; Juberg, C. T.; Sinha, B.; Knudsen, G. A.; Birnbaum, L. S., Effect of GenX on P-Glycoprotein, Breast Cancer Resistance Protein, and Multidrug Resistance–Associated Protein 2 at the Blood–Brain Barrier. *Environ. Health Perspect.* **2020,** *128* (3), 037002.

123.   Trojanowicz, M.; Koc, M., Recent developments in methods for analysis of perfluorinated persistent pollutants. *Microchim. Acta* **2013,** *180* (11-12), 957-971.

124.   Coggan, T. L.; Anumol, T.; Pyke, J.; Shimeta, J.; Clarke, B. O., A single analytical method for the determination of 53 legacy and emerging per-and polyfluoroalkyl substances (PFAS) in aqueous matrices. *Anal. Bioanal. Chem.* **2019,** *411*, 3507 - 3520.

125.   McDonough, C. A.; Guelfo, J. L.; Higgins, C. P., Measuring total PFASs in water: The tradeoff between selectivity and inclusivity. *Curr. Opin. Environ. Sci. Health* **2019,** *7*, 13-18.

126.   Onghena, M.; Moliner-Martinez, Y.; Picó, Y.; Campíns-Falcó, P.; Barceló, D., Analysis of 18 perfluorinated compounds in river waters: Comparison of high performance liquid chromatography–tandem mass spectrometry, ultra-high-performance liquid chromatography–tandem mass spectrometry and capillary liquid chromatography–mass spectrometry. *J. Chromatogr. A.* **2012,** *1244*, 88-97.

127.   Pan, Y.; Wang, J.; Yeung, L. W. Y.; Wei, S.; Dai, J., Analysis of emerging per- and polyfluoroalkyl substances: Progress and current issues. *TrAC, Trends Anal. Chem.* **2020,** *124*, 115481.

128.   Al Amin, M.; Sobhani, Z.; Liu, Y.; Dharmaraja, R.; Chadalavada, S.; Naidu, R.; Chalker, J. M.; Fang, C., Recent advances in the analysis of per- and polyfluoroalkyl substances (PFAS) - A review. *Environ. Technol. Inno.* **2020,** *19*, 100879.

129.   Shoemaker, J. A.; Grimmett, P. E.; Boutin, B. K., Method 537: Determination of Selected Per- and Polyfluorinated Alkyl Substances in Drinking Water by Solid Phase Extraction and Liquid Chromatography/Tandem Mass Spectrometry (LC/MS/MS). U.S. Environmental Protection Agency, Office of Research and Development, National Exposure Research Laboratory: Washington, D.C., 2018.

130.   Shoemaker, J. A.; Tettenhorst, D. R., Method 537.1: Determination of selected per- and polyfluorinated alkyl substances in drinking water by solid phase extraction and liquid chromatography/tandem mass spectrometry (LC/MS/MS). U.S. Environmental Protection Agency, Office of Research and Development, National Center for Environmental Assessment: Washington, D.C., 2020.

131.   Rosenblum, L.; Wendelken, S. C., Method 533: Determination of per- and polyfluoroalkyl substances in drinking water by isotope dilution anion exchange solid phase extraction and liquid chromatography/tandem mass spectometry. U.S. Environmental Protection Agency, Office of Ground Water and Drinking Water: Cincinnati, OH, 2019.

132.   *EPA PFAS Action Plan: Program Update*; U.S. Environmental Protection Agency: Washington, D.C., 2020.

133.   Tröger, R.; Klöckner, P.; Ahrens, L.; Wiberg, K., Micropollutants in drinking water from source to tap - Method development and application of a multiresidue screening method. *Sci. Total Environ.* **2018,** *627*, 1404-1432.

134.   Wei, C.; Wang, Q.; Song, X.; Chen, X.; Fan, R.; Ding, D.; Liu, Y., Distribution, source identification and health risk assessment of PFASs and two PFOS alternatives in groundwater from non-industrial areas. *Ecotoxicol. Environ. Saf.* **2018,** *152*, 141-150.

135.   Field, J. A.; Schultz, M.; Barofsky, D., Fluorinated alkyl surfactants in groundwater and wastewater. *Chimia* **2003,** *57*, 22-34.

136.   Janda, J.; Nödler, K.; Brauch, H.-J.; Zwiener, C.; Lange, F. T., Robust trace analysis of polar (C2-C8) perfluorinated carboxylic acids by liquid chromatography-tandem mass spectrometry: method development and application to surface water, groundwater and drinking water. *Environ. Sci. Pollut. Res.* **2018,** *26*, 7326-7336.

137.   Simcik, M. F.; Dorweiler, K. J., Ratio of perfluorochemical concentrations as a tracer of atmospheric deposition to surface waters. *Environ. Sci. Technol.* **2005,** *39* (22), 8678-8683.

138.   Dalahmeh, S.; Tirgani, S.; Komakech, A. J.; Niwagaba, C. B.; Ahrens, L., Per- and polyfluoroalkyl substances (PFASs) in water, soil and plants in wetlands and agricultural areas in Kampala, Uganda. *Sci. Total Environ.* **2018,** *631-632*, 660-667.

139.   Takino, M.; Daishima, S.; Nakahara, T., Determination of perfluorooctane sulfonate in river water by liquid chromatography/atmospheric pressure photoionization mass spectrometry by automated on-line extraction using turbulent flow chromatography. *Rapid Commun. Mass Spectrom.* **2003,** *17* (5), 383-390.

140.   Gallen, C.; Eaglesham, G.; Drage, D.; Nguyen, T. H.; Mueller, J. F., A mass estimate of perfluoroalkyl substance (PFAS) release from Australian wastewater treatment plants. *Chemosphere* **2018,** *208*, 975-983.

141.   Hori, H.; Hayakawa, E.; Einaga, H.; Kutsuna, S.; Koike, K.; Ibusuki, T.; Kiatagawa, H.; Arakawa, R., Decomposition of environmentally persistent perfluorooctanoic acid in water by photochemical approaches. *Environ. Sci. Technol.* **2004,** *38* (22), 6118-24.

142.   Miyake, Y.; Yamashita, N.; Rostkowski, P.; So, M. K.; Taniyasu, S.; Lam, P. K.; Kannan, K., Determination of trace levels of total fluorine in water using combustion ion chromatography for fluorine: a mass balance approach to determine individual perfluorinated chemicals in water. *J. Chromatogr. A* **2007,** *1143* (1-2), 98-104.

143.   Janda, J.; Nödler, K.; Scheurer, M.; Happel, O.; Nürenberg, G.; Zwiener, C.; Lange, F. T., Closing the gap – inclusion of ultrashort-chain perfluoroalkyl carboxylic acids in the total oxidizable precursor (TOP) assay protocol. *Environ. Sci. Process Impacts* **2019,** *21* (11), 1926-1935.

144.   Poboży, E.; Król, E.; Wójcik, L.; Wachowicz, M.; Trojanowicz, M., HPLC determination of perfluorinated carboxylic acids with fluorescence detection. *Microchim. Acta* **2011,** *172* (3-4), 409-417.

145.   Wójcik, L.; Korczak, K.; Szostek, B.; Trojanowicz, M., Separation and determination of perfluorinated carboxylic acids using capillary zone electrophoresis with indirect photometric detection. *J. Chromatogr. A* **2006,** *1128* (1-2), 290-297.

146.   Wójcik, L.; Szostek, B.; Maruszak, W.; Trojanowicz, M., Separation of perfluorocarboxylic acids using capillary electrophoresis with UV detection. *Electrophoresis* **2005,** *26* (6), 1080-1088.

147.	Laboratory Testing. https://www.michigan.gov/pfasresponse/0,9038,7-365-86704_90691---,00.html (accessed November 1, 2020).

148.	Hulanicki, A.; Glab, S.; Ingman, F., Chemical Sensors Definitions and Classification. *Pure Appl. Chem.* **1991**, *63* (9), 1247-1250.

149.	astkCARE: anionic surfactant detection. https://www.crccare.com/products-and-services/technologies/astkcare (accessed November 1, 2020).

150.	Fang, C.; Zhang, X.; Dong, Z.; Wang, L.; Megharaj, M.; Naidu, R., Smartphone app-based/portable sensor for the detection of fluoro-surfactant PFOA. *Chemosphere* **2018**, *191*, 381-388.

151.	Menger, R. F.; Beck, J. J.; Borch, T.; Henry, C. S., Colorimetric paper-based analytical device for PFOS detection. submitted to *ACS ES&T Water,* **2021**.

152.	Mentele, M. M.; Cunningham, J.; Koehler, K.; Volckens, J.; Henry, C. S., Microfluidic paper-based analytical device for particulate metals. *Anal. Chem.* **2012,** *84* (10), 4474-80.

153.	Cate, D. M.; Noblitt, S. D.; Volckens, J.; Henry, C. S., Multiplexed paper analytical device for quantification of metals using distance-based detection. *Lab Chip* **2015**, *15* (13), 2808-2818.

154.	Ninwong, B.; Ratnarathorn, N.; Henry, C. S.; Mace, C. R.; Dungchai, W., Dual Sample Preconcentration for Simultaneous Quantification of Metal Ions Using Electrochemical and Colorimetric Assays. *ACS Sensors* **2020**, *5* (12), 3999-4008.

155.	Ninwong, B.; Sangkaew, P.; Hapa, P.; Ratnarathorn, N.; Menger, R. F.; Henry, C. S.; Dungchai, W., Sensitive distance-based paper-based quantification of mercury ions using carbon nanodots and heating-based preconcentration. *RSC Adv.* **2020**, *10* (17), 9884-9893.

156.	Wong, S. Y.; Cabodi, M.; Rolland, J.; Klapperich, C. M., Evaporative Concentration on a Paper-Based Device to Concentrate Analytes in a Biological Fluid. *Anal. Chem.* **2014,** *86* (24), 11981-11985.

157.	Yeh, S.-H.; Chou, K.-H.; Yang, R.-J., Sample pre-concentration with high enrichment factors at a fixed location in paper-based microfluidic devices. *Lab Chip* **2016**, *16* (5), 925-931.

158.	Kudo, H.; Yamada, K.; Watanabe, D.; Suzuki, K.; Citterio, D., Paper-Based Analytical Device for Zinc Ion Quantification in Water Samples with Power-Free Analyte Concentration. *Micromachines* **2017,** *8* (4), 127.

159.	Shimada, Y.; Kaneta, T., Highly Sensitive Paper-based Analytical Devices with the Introduction of a Large-Volume Sample via Continuous Flow. *Anal. Sci.* **2018,** *34* (1), 65-70.

160.	Kamnoet, P.; Aeungmaitrepirom, W.; Menger, R. F.; Henry, C. S., Highly selective simultaneous determination of Cu(ii), Co(ii), Ni(ii), Hg(ii), and Mn(ii) in water samples using microfluidic paper-based analytical devices. *Analyst* **2021,** (7), 1-25.

161.	Cate, D. M.; Dungchai, W.; Cunningham, J. C.; Volckens, J.; Henry, C. S., Simple, distance-based measurement for paper analytical devices. *Lab Chip* **2013**, *13* (12), 2397-404.

162.	Sun, X.; Li, B.; Qi, A.; Tian, C.; Han, J.; Shi, Y.; Lin, B.; Chen, L., Improved assessment of accuracy and performance using a rotational paper-based device for multiplexed detection of heavy metals. *Talanta* **2018**, *178*, 426-431.

163.	Menger, R. F.; Beck, J. J.; Fuller, K. Z.; Reilly III, T. H.; Henry, C. S., High volume radial detection paper-based device for trace metal analysis. submitted to *ACS* Sensors, **2021**.

CHAPTER 2: FLUORESCENT DYE PAPER-BASED METHOD FOR ASSESSMENT OF
PESTICIDE COVERAGE ON LEAVES AND TREES: A CITRUS GROVE CASE STUDY

Crop disease management depends on efficient and adequate pesticide distribution to reduce pest population. Instrument-based methods to evaluate the spatial distribution of pesticides are available, but they are not field-compatible because of instrument size, cost, and extensive sample preparation. The current standard of water-sensitive papers is field-compatible; however, these papers often produce false positives due to reaction with water from sources other than the pesticide mixture. Thus, we developed a novel method in which a fluorescent dye is sprayed over a crop with circles of filter paper (samplers) attached to the leaves. After collection, a lightbox is used to take pictures of the samplers, and an algorithm analyzes each image for percent coverage to visualize the pesticide distribution within the crop. This method produces results quickly and inexpensively compared to current methods and can be applied to any crop to inform best pesticide application strategies. This work was published in *Journal of Agricultural and Food Chemistry*.[1] Mridula Bontha (2nd author) developed the Python script to analyze the images of the samplers.

2.1 Introduction

The agricultural industry relies heavily on the application of pesticides for disease control and sustainable crop pest management.[2] Depending on the crop, 10-20% of crops are lost to insects.[3] Pesticide application is an inefficient process, with less than 0.1% of the volume sprayed actually reaching the target pest.[4] To prevent insect resistance, product loss, and environmental pollution, efficient and adequate distribution of pesticide is necessary.[5-7] Correct adjustment and calibration of sprayers or new types of applicators can help in optimizing pesticide application, but to quantify the improvement, a reliable and easy to use method is needed to determine pesticide distribution within the crop as well as how well the individual leaves are covered.

28

The current industry standard for evaluating insecticide distribution is water-sensitive papers (WSP, Figure 2.1A). These paper cards can be attached to any crop and react in the presence of water. The coating on the paper, bromophenol blue, changes from yellow at pH 3.0 to blue at pH 4.6.[8] While easy to use, these papers often result in false positives in that a blue spot appears from water other than the insecticide mixture, such as humidity in the air or dew on the crop, inaccurately representing insecticide distribution.[9-12] As a result, water-sensitive papers should not be used when the relative humidity is above 80%,[13] limiting their application in humid regions. For instance, in Florida, the relative humidity is above 80% approximately half the time.[14] As a result, a study where many WSP are distributed throughout a crop would result in inaccurate representations of insecticide presence due to reaction with the water vapor in the air as well as dew on the leaves. The cards cost approximately $1.40 USD per card,[15] which is costly when performing an in-depth study of a larger crop like a fruit orchard with hundreds to thousands of samples across multiple trees.

Beyond cost concerns, the water-sensitive papers can be used to provide qualitative results by naked eye analysis, but computer-based image analysis is needed to quantify the results. These programs (DropletScan, DepositScan, Drop-Vision Ag, SnapCard, and more) usually require scanning the water-sensitive paper and importing it to a mobile phone application or computer program.[16, 17] The analysis programs are limited by the resolution of the scanner or camera and the algorithms differ in how they differentiate droplets, producing different results for the same samples.[11, 16-19] Especially at heavier application rates, droplet overlapping causes problems when results are presented in terms of droplet size.[20] Because of this, percent area covered is the most reliable metric to report and evaluate as a measure of pesticide application efficiency.[10, 21]

To analyze pesticide residues on plant leaves, traditional laboratory-based methods are also common. For example, chromatographic, fluorometric, and spectroscopic methods are common to detect pesticide residues in and on a variety of substrates, like leaves, vegetables, soil, and human skin.[22-27] Gas or liquid chromatography in conjunction with mass spectrometry have been used to determine pesticide presence in leaves. This method requires sample pretreatment or leaf extraction.[28-30] For detection on leaves, a fluorescent tracer is mixed with the pesticide, sprayed on the leaves, washed off the leaf, and analyzed by fluorimetry.[31-34] In a similar fashion, a metal tracer (potassium nitrate, zinc nitrate, or magnesium chloride) can be sprayed onto filter papers attached to leaves. The filters are extracted in nitric acid and the tracer analyzed via atomic absorption spectrometry.[35] These methods are expensive, time-consuming, and labor-intensive, requiring sample preparation and instrumental analysis which limit field analysis. The rinsing and extraction processes also eliminate the ability to differentiate between coverage on the two sides of the leaf. This distinction is important in mapping pesticide coverage within a crop. In order to adequately target a certain pest, sometimes pesticide coverage on both sides of the leaf, or even specifically the bottom side, is essential, and a method that can treat each side of the leaf as independent samples is needed.

Here we present the development of a novel, fluorescent-based method that is easy to deploy and accurately measures pesticide distribution in any crop. The method uses circular discs of filter paper that are clipped to the leaves of the crop and allows for both sides of the leaf to be independently analyzed. A fluorescent dye is mixed with the pesticide to be sprayed over the crop and the samples. The method is not harmful to the environment and can be used in the field to quickly achieve results. Lab-based studies were used to develop the method in a controlled environment. However, it is not possible to truly recreate the environment in which a pesticide is

sprayed. While the temperature, humidity, and wind can be simulated, a spraying chamber cannot recreate the tractor or airplane that is used in the field. A spraying chamber does not have the capacity to spray at the same application rate due to the limited number of nozzles and pressure. Additionally, to perform an in-depth study of spatial distribution, hundreds of samples are needed for statistical significance. Thus, to demonstrate the validity and feasibility of the method developed in this study, we conducted a field-scale study within a large citrus grove in Venus, Florida.

2.2 Materials and Methods

2.2.1 Overview

An original method was developed to evaluate the spatial distribution of pesticides within crops. The method is shown in Figure 2.1D. Whatman filter paper Grade 1 (GE Healthcare Sciences) was used as an inexpensive, easily obtainable substrate for sample collection. Circles (diameter 47 mm) of filter paper were cut with an Epilog Zing CO_2 laser cutter. These filter circles (samplers) were clipped to the leaves of the crop with 9/16" binder clips (Figure 2.1C). A dye was added to the pesticide mixture which is sprayed onto the crop via different methods (e.g. tractor, airplane). Samplers were collected and analyzed with a homebuilt lightbox (Appendix 1.1) and simplified computer system with a camera (Raspberry Pi) (Figure 2.1B).
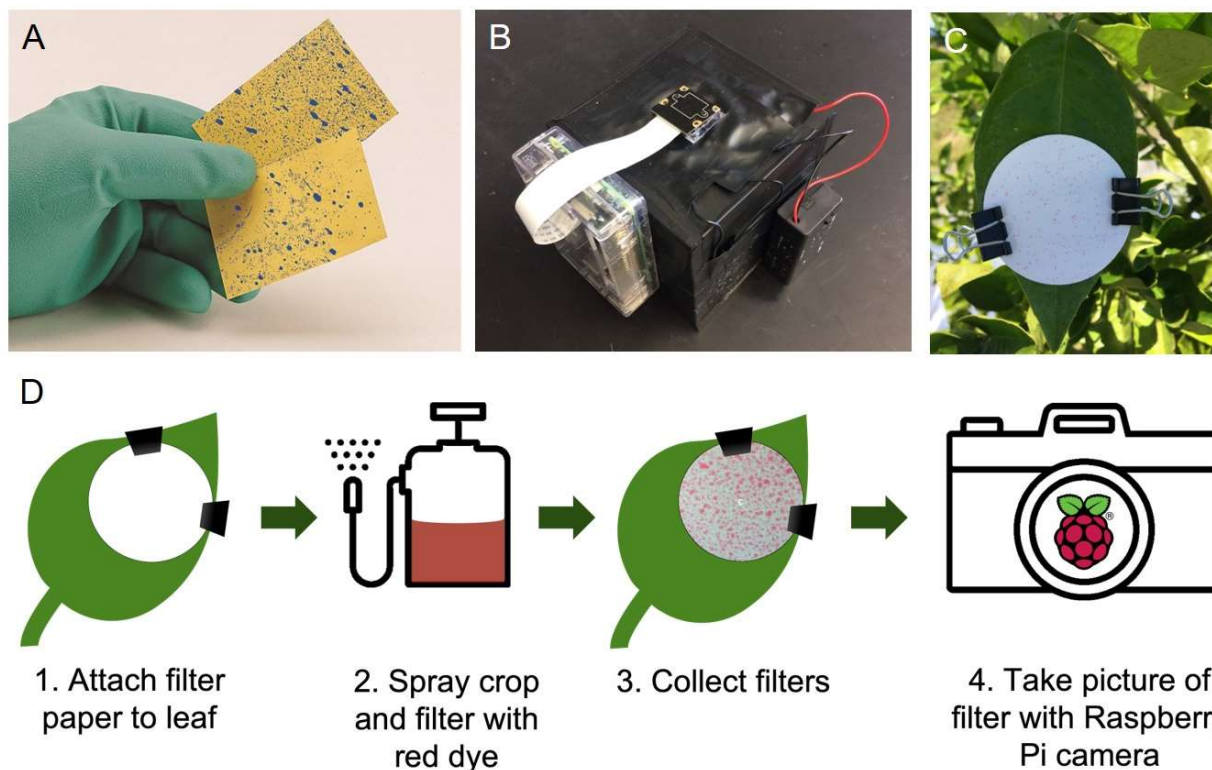
Figure 2.1 A. Water-sensitive paper. B. Lightbox with Raspberry Pi. C. A filter paper sampler clipped to the citrus leaf. D. Schematic of method.

2.2.2 Image Acquisition and Analysis

A Raspberry Pi single-board computer with a wide-angle camera attached to the computer with a 15-pin ribbon was used to collect images (Raspberry Pi 3 Model B, Keyestudio Camera).[36] The camera has a resolution of 5 MP and a pixel size of 1.4 x 1.4 μm. The Raspberry Pi was encased in a transparent case (KuGi) to protect the internal components and was controlled via VNC Viewer (Virtual Network Computing) and a laptop. The terminal window was used to enter commands to take pictures of the samplers (Appendix 1.4). After all the pictures were taken, they were analyzed in ImageJ (open source, NIH)[37] or by a custom Python script (Appendix 1.5). The degradation and benchmark experiments were analyzed in ImageJ. Briefly, the image was split into three channels, and the red channel was chosen. The thresholding command was used to select

just the droplets from the background. The 'Measure' command calculated the percent coverage (% area). The fieldwork images were analyzed with a custom Python script. Briefly, K-means clustering was used to identify three constituent colors (black, yellow, green) for each image. The RGB (red, green, blue) values were converted to their equivalent in HSV (hue, saturation, value) space. The thresholded values for each color generate a mask for the dye and background regions. Each mask was used to identify and then count the number of sample (yellow) and background (green) pixels, so the minimum spot size is 1 pixel. These counts were then converted into a percentage to determine the percent area that the dye covers on a sampler (Eq. 1). To count the number of particles and determine particle size, the colored image was converted to grayscale and a Gaussian blurring filter was applied to smooth the edges. Contouring, a curve joining all the continuous points along the boundary of a spot, was applied to identify individual droplets. A CSV (comma-separated value) file was generated containing the percent area coverage, number of particles, and particle size for each sampler image.

Equation 1. $$\textbf{\textit{Percent Coverage}} = \frac{\textit{sample}}{\textit{sample} + \textit{background}} \times \textbf{100}$$

2.2.3 Dye Selection and Degradation Test

To visualize the presence of pesticide collected on the filter paper samplers, three fluorescent tracer dyes were evaluated. A non-fluorescent dye could have been used but the contrast of the fluorescent dyes against the background was stronger, making the spots easier to see and analyze. Three fluorescent tracer dyes were tested for usability in the field: a yellow-green fluorescent dye (Risk Reactor IFWBC8), a red fluorescent dye (Risk Reactor IFWC7), and brilliant sulfaflavine (MP Biomedicals). The two dyes used from Risk Reactor are water-soluble, UV tracer

additives, NSF-certified and EPA-approved, meaning that the dye is bio- and photodegradable. The yellow-green dye fades in 2-3 days while the red dye fades in 5-7 days. Cai and Stark (1997) determined that brilliant sulfaflavine used as a pesticide tracer is relatively resistant to photodegradation compared to other dyes studied.[38] Because all three dyes would eventually degrade, it was necessary to test how fast the dye would degrade between spraying and collection time to ensure stability between deposition and analysis. Two degradation studies were performed: one in a solar simulator and one under actual field conditions in Florida.

A solar simulator (Atlas MTS Suntest CPS) was used with the following settings to mimic settings in Florida: temperature $= 25°C$, solar radiation $= 609 \ W/m^2$, 1500 W Xenon lamp. Samples were prepared by spotting 10 drops (1.25 µL) of each dye (1 ppm in water) on Whatman filter samplers with three replicates for each dye. Pictures were taken before exposure in the solar simulator and at the following time points after exposure: t = 15, 30, 45, 60, 90 min. Pictures were taken with the lightbox-Raspberry Pi set up and analyzed in ImageJ (NIH).[37] The red color intensity difference between before and after exposure was calculated for each time point. From this preliminary study, the red fluorescent dye was selected to move forward based on its properties of biodegradability, low cost, and light stability.

A second degradation study was performed in the field in Venus, Florida. Samples were prepared by dropping a total of 5 µl of a pesticide-dye mixture on each filter circle. The pesticide-dye mixture was a cocktail of 1500 ppm red dye, 3 µL/mL Malathion (insecticide), and 0.3 µL/mL Dyne-amic. A set of 4 samplers (1 blank and 3 samples) was prepared for each of the following time points: t = 0, 10, 20, 30, 45, 60, 75, 90, 120 min. Pictures were taken of all samplers prior to exposure in the sun. In Florida, all samplers (except t=0 min) were taped to a piece of cardboard and placed in direct sunlight. Weather data was provided by a weather station in Venus, Florida

(Table A.1.1). After each time point, a set of samplers was collected and stored in foil until analysis. After sun exposure, all samplers were imaged again and analyzed in ImageJ. The change in color intensity was calculated.

2.2.4 Benchmark to Water-Sensitive Paper (WSP)

To ensure that this method performs at least equal to or better than the existing method, a benchmark validation experiment was performed under controlled conditions. A DeVries Generation 4 Research Track Sprayer (DeVries Manufacturing, Hollandale, MN)[39] equipped with one TeeJet 8002EV8 nozzle (Spraying Systems Co., Wheaton, IL) were used to spray a dye solution (2500 ppm) on samplers and WSP at various nozzle pressure and speed combinations (5 – 40 psi, 1 – 3 mph). The nozzle was 26 inches above the samplers. After spraying, the samplers were collected and stored in foil until analysis. The lightbox-Raspberry Pi system was used to take pictures of the samplers, and a flatbed scanner was used to image the WSP. The pictures were analyzed using ImageJ for percent coverage.

2.2.5 Field Study Description

Samples were collected during four field campaigns at a citrus grove in Venus, Florida. Meteorological data for each trip was provided by the grove. Trips in February and May 2018 served as pilot studies to optimize the method. In October 2018, a full-scale field study was performed. For each field study, the samplers were hung in citrus trees in predetermined locations at various canopy heights, canopy depths, and sides of leaf (top and bottom). To evaluate the filter paper method with different application methods (aerial, ground), and trees ages (young, old), samplers were placed in four groups of trees: aerial young, aerial old, ground young, ground old.

With 48 samplers and 3 field blanks per tree, and 5 trees per treatment group, a total of 255 samplers were collected for each treatment group. For each field study, a dye was added to the sprayer tank with pesticide and water, mixed thoroughly, and sprayed on the citrus trees and samples with the appropriate sprayer. Field study, experimental, and weather details are found in Table A1.1. Samples were collected within an hour of spraying to minimize photodegradation and were stored in foil packets until analysis. Pictures were taken of each sampler in the lightbox - Raspberry Pi system and analyzed for percent coverage and droplet size with the custom Python script (Appendix 1.5).

2.2.6 Statistical Analysis

JMP Pro 13 (SAS Institute Inc., Cary, North Carolina, USA) was used for statistical analysis. A significance level of $p < 0.05$ was used to check statistical significance. The assumption of normality, homogeneity of variance, and linearity were checked with normal probability plots and residual plots, respectively.

2.3 Results and Discussion

2.3.1 Method Development and Optimization

To determine the optimal window for sample collection, a degradation study was performed under real conditions in Florida. From the initial study, a red rhodamine-based fluorescent dye was selected due to its resistance to photodegradation, environmental friendliness, low cost, and low reactivity towards pesticides (Figure A1.1).[40] Samplers with a pre-determined volume and concentration of dye were prepared and exposed to the sun. The samplers were analyzed at various time points with the lightbox-Raspberry Pi system. The change in red color

intensity from before and after sun exposure was calculated. There was a significant difference ($p < 0.05$) between before and after sun exposure starting at 20 min of exposure (Figure 2.2). However, with the sample size of the full-scale study, it was logistically impossible to collect all the samplers within 20 min of spraying, so 1 hr was accepted as the window to collect the samples without compromising them.
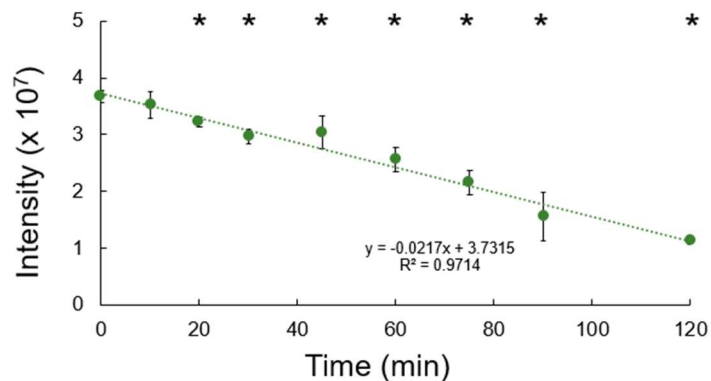
Figure 2.2 Color intensity of red dye droplets on filter paper versus time exposed to sun. The intensity was measured in ImageJ. Star (*) indicates significant difference between exposure and after exposure (n=3) ($p < 0.05$). Each point represents the average of 3 points, and the error bars are ±1σ around the mean.

2.3.2 Benchmark to Water-Sensitive Paper (WSP)

A benchmark study was performed to demonstrate that the developed filter paper method performs comparably to the existing method of water-sensitive papers (Figure 2.3, Table A1.3). The samplers and WSP were sprayed with 15 combinations of pressure and speed (5-40 psi, 1-3 mph). Multiple applications rates were used to replicate different settings that are used to apply pesticide in the field. At 5 psi (the lowest pressure tested), the dye dripped out of the nozzle, resulting in blotchy samplers and WSP. This pressure is not relevant to field settings, so those data were not reported. The other application rates are commonly used in the field.[41] The filter paper method performs comparably to the WSP (Figure 2.4), with similar coverage for each trial. At 3 mph, the filter samplers do have a significantly higher percent coverage compared to the WSP due to the absorbency of the Whatman filter paper compared to the WSP. The droplets spread more,

37

resulting in higher percent coverage (Figure A1.2). However, as long as the sampling method is consistent throughout a study (i.e. not mixing filters and WSP), the spatial distribution of pesticide can still be analyzed. In fact, the absorbency of the filter samplers contributes to even fewer false positives since they dry faster compared to the WSP, resulting in no smearing when the samples are collected. The WSP need 30-40 min to completely dry, compared to less than 10 min for the filter samplers.
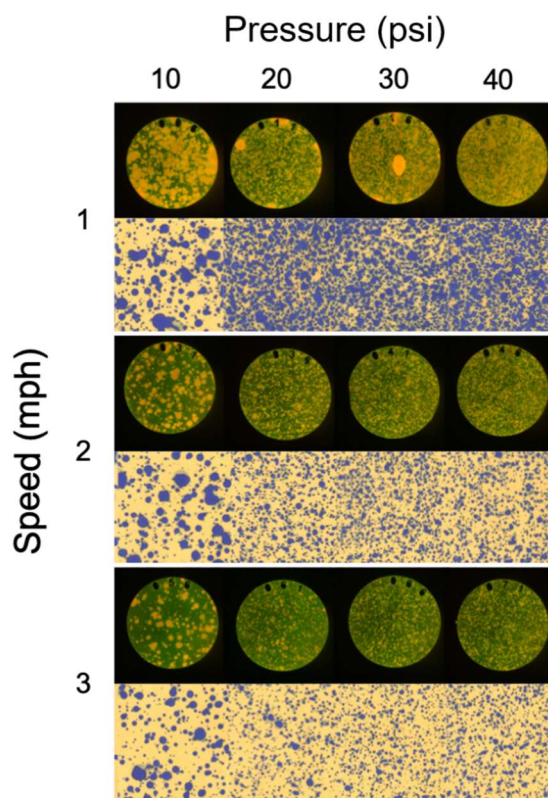
Figure 2.3 Representative images of filter samplers and water sensitive paper (WSP). The filter samplers are the top row of each set while the WSP are the bottom row of each set. A spraying chamber was used to spray a dye mixture on both the filter samplers and WSP. Images of the filter samplers were taken with the lightbox-Raspberry Pi camera system while the water-sensitive papers were scanned.

Both the filter samplers and WSP follow consistent trends when grouped by speed and pressure (Figure 2.4). As speed increases, percent coverage decreases, because there is less time for the dye to get on the filter samplers or WSP.[42, 43] As pressure increases, coverage also increases. It should be noted that this is not what happens in the field; droplet size decreases as pressure

increases, so the spray acts more like a mist. In the field, the spray is more subject to drift which will result in decreased coverage.[44] However, in the controlled environment of a spray chamber where there is very minimal drift, coverage does increase with pressure increase.
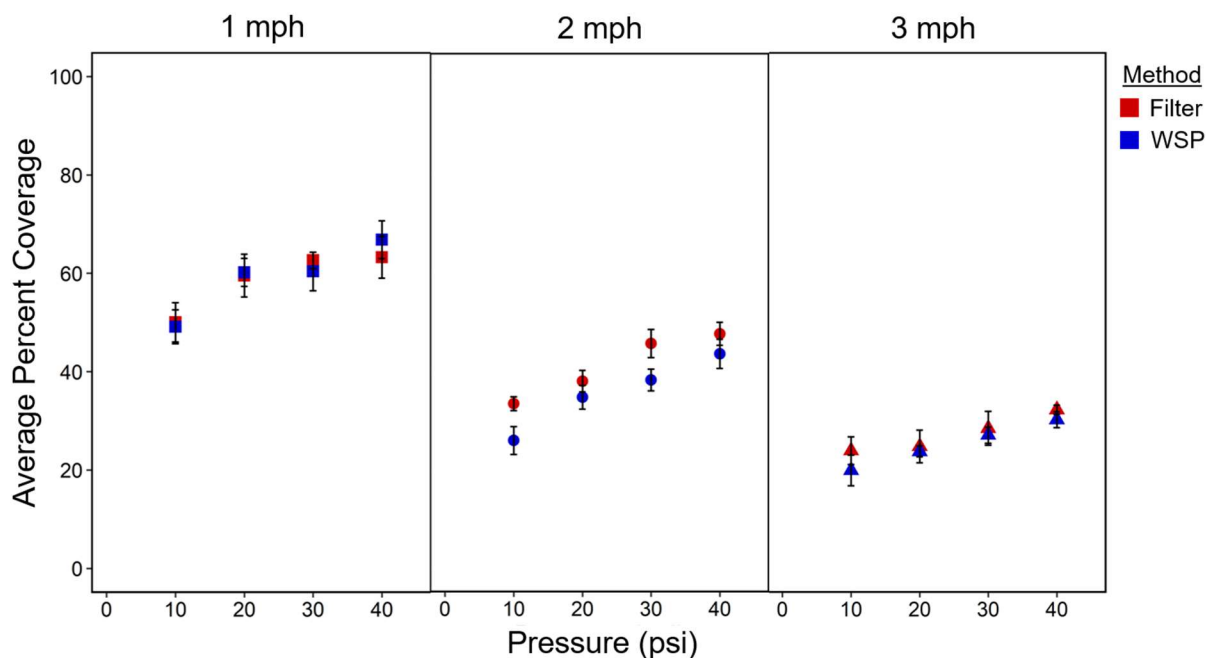
Figure 2.4 Average percent coverage by nozzle speed (mph) and nozzle pressure (psi). The red symbols are the filter paper samplers while the blue symbols are the water-sensitive papers (WSP). Each point represents the average of 5 replicates, and the error bars are ±1σ around the mean.

In addition to validating the filter paper sampler method against the WSP, this benchmark study demonstrates that the filter paper sampler method (as well as the water-sensitive papers) can discern differences in speed and pressure settings, making the filter paper method useful for nozzle calibrations. Each pesticide comes with a recommended application rate based on the crop. That rate, measured in gallons per acre (GPA), is achieved by the manipulation of the type of nozzle as well as the spraying speed and pressure (Figure A1.3, Appendix 1.2). Therefore, performing a nozzle calibration to ensure the proper GPA is necessary before each pesticide application. The filter paper method can discern between changes in speed and pressure and thus guide management decisions to achieve the correct application rate with adequate coverage for best pest management.

2.3.3 Field Studies

To demonstrate the feasibility of the newly developed filter paper method in real conditions instead of under the limitations of a spraying chamber, a field study was conducted in a citrus grove in Florida. During the first full field study in October 2018, four groups of trees were selected to evaluate the filter paper method: two application types (aerial vs ground) and two tree ages (young vs old). The filter paper samplers were clipped to the top and bottom of the leaves in various locations in the trees (Figure 2.1C). After spraying the dye over the citrus trees and the samplers, they were collected and analyzed with the lightbox. The samplers were grouped by application type, tree age, and side of leaf (top or bottom) to compare the coverage of the filter samplers (Figure 2.5, Table A1.4, Table A1.5). Percent coverage is defined as the percent of a sampler that is covered by the dye. There is a significant difference between all groups, as indicated by the stars across the box and whisker plot, except aerial young bottom and aerial old bottom, and ground young bottom and ground old bottom. In all cases, the tops of the leaves received significantly more pesticide than the bottom of the leaves. We are assuming that the presence of dye is consistent with the presence of pesticide based on ongoing studies.[45] In addition, trees with the pesticide mixture applied via tractors (ground application) had a significantly higher average percent coverage compared to the aerial application. This indicates that ground application gives more complete leaf coverage and thus a better application approach than aerial application. A more detailed discussion of the spatial distribution of pesticide within the citrus trees will be reported in the future.
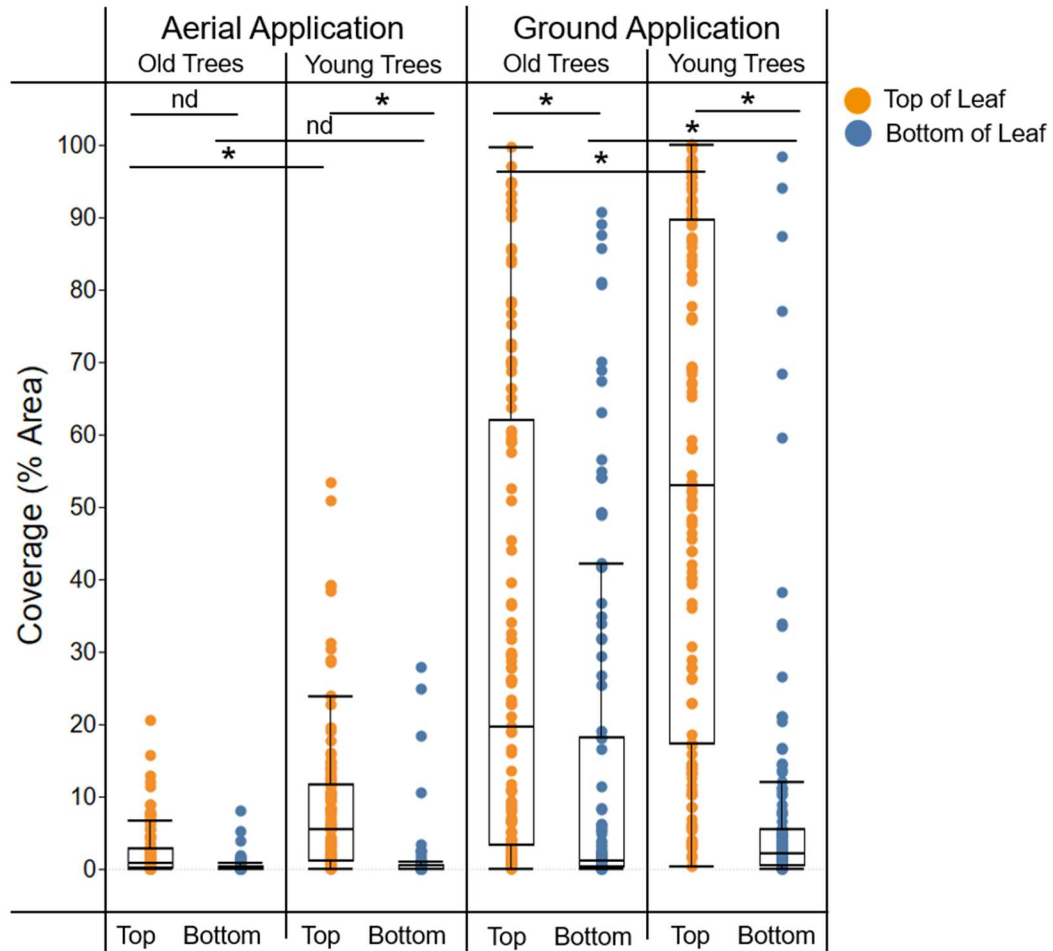
Figure 2.5 Box and whisker plot showing percent coverage of all samples, grouped by application type (aerial vs ground), age of tree (young vs old), and side of leaf (top vs bottom). The stars (*) indicate a significant difference (p < 0.05, n = 120) between the two groups connected by the line. No significant difference is indicated by "nd."

It should be noted that high percent coverage does not necessarily mean that the pesticide concentration is high enough to kill the pest that is targeted. Depending on the type of pesticide (systemic vs contact) as well as the time of pesticide degradation, 100% coverage is not necessarily warranted. There is also a limitation to this method at high coverage levels in that once the filter sampler is saturated with dye, the image analysis system will still report a coverage of 100%. However, of the 1020 samples that were analyzed in the field trial, only 4% (41 samplers) had a

coverage of 80%. Most samplers had a much lower coverage. "Adequate coverage" is often considered 15%,[46] so the upper limit of coverage (i.e. saturation) is not relevant.

2.4 Conclusions

We have developed a new method to evaluate pesticide distribution using a red fluorescent dye that is captured on a filter paper sampler and analyzed by a lightbox-camera system to achieve fast results, improving cost and ease of use over other methods. It is not subject to false positives like the water-sensitive papers, and dries much quicker as well, preventing smearing (<10 min vs 30-40 min). The sample substrate, Whatman filter paper, is inexpensive and easily obtainable. The samplers are clipped to the top and bottom of each leaf, which allows for independent analysis of each side of the leaf. This distinction is not possible with other fluorescent or spectroscopic methods. Since the fluorescent dye is added to the tank with the pesticide, a study of spatial distribution can be scaled as desired, with per sample cost decreasing as study size increases. The lightbox-camera system costs less than $100 to build and is a one-time cost. Together with the dye cost as the main consumable, this 1000 sample study cost $0.42 per sample, compared to $1.40 per sample if the water-sensitive paper had been used.[15] The lights inside the box provide a dependable and even light source, eliminating any interference or inconsistency from ambient light. Taking pictures of and analyzing 100 samples takes 10-15 minutes. With these improvements over current methods, this novel filter paper method can be used by farmers to evaluate the spatial distribution of pesticides within any crop and use that information to optimize spraying parameters and disease control.

REFERENCES

1.   Menger, R. F.; Bontha, M.; Beveridge, J. R.; Borch, T.; Henry, C. S., Fluorescent-based method for assessment of pesticide coverage on leaves and trees: A citrus grove case study. *J. Agric. Food Chem.* **2020,** *68* (47), 14009-14014.
2.   Giles, D. K.; Akesson, N. B.; Yates, W. E., Pesticide Application Technology: Research and Development and the Growth of the Industry. *Trans. ASABE* **2008,** *51* (2), 397-403.
3.   Deutsch, C. A.; Tewksbury, J. J.; Tigchelaar, M.; Battisti, D. S.; Merrill, S. C.; Huey, R. B.; Naylor, R. L., Increase in crop losses to insect pests in a warming climate. *Science* **2018,** *361*, 916-919.
4.   Pimentel, D., Amounts of Pesticides Reaching Target Pests: Environmental Impacts and Ethics. *J. Agric. Environ. Ethics* **1995,** *8* (1), 17-29.
5.   De Moor, A.; Langenakens, J.; Vereecke, E., Image analysis of water sensitive paper as a tool for the evaluation of spray distribution of orchard sprayers. *Asp. Appl. Biol.* **2000,** *57*, 329-342.
6.   Salyani, M.; Farooq, M.; Sweeb, R. D., Spray Deposition and Mass Balance in Citrus Orchard Applications. *Trans. ASABE* **2007,** *50* (6), 1963-1969.
7.   Giles, D.; Downey, D., Quality control verification and mapping for chemical application. *Precis. Agric* **2003,** *4* (1), 103-124.
8.   Turner, C. R.; Huntington, K. A., The Use of a Water Sensitive Dye for the Detection and Assessment of Small Spray Droplets. *J. Agric. Eng. Res.* **1970,** *15*, 385-387.
9.   Hill, B. D.; Inaba, D. J., Use of Water-Sensitive Paper to Monitor the Deposition of Aerially Applied Insecticides. *J. Econ. Entomol.* **1989,** *82* (3), 974-980.
10.   Salyani, M.; Fox, R. D., Evaluation of spray quality by oil- and water-sensitive papers. *Trans. ASAE* **1999,** *42* (1), 37-43.
11.   Hoffmann, W. C.; Hewitt, A. J.; Hoffmann, W. C., Comparison of three imaging systems for water-sensitive papers. *Appl. Eng. Agric.* **2005,** *21* (6), 961-964.
12.   Salyani, M.; Zhu, H.; Sweeb, R. D.; Pai, N., Assessment of spray distribution with water-sensitive paper. *Agric. Eng. Int.* **2013,** *15* (2), 101-111.
13.   Water Sensitive Paper. Spraying Systems Co.
14.   Relative Humidity - Florida Climate Center. https://climatecenter.fsu.edu/products-services/data/other-normals/relative-humidity (accessed June 10.
15.   3" x 2" Water Sensitive Paper – Sprayer Depot. Wheaton, IL.
16.   Zhu, H.; Salyani, M.; Fox, R. D., A portable scanning system for evaluation of spray deposit distribution. *Comput. Electron. Agric.* **2011,** *76*, 38-43.
17.   Ferguson, J. C.; Chechetto, R. G.; O'Donnell, C. C.; Fritz, B. K.; Hoffmann, W. C.; Coleman, C. E.; Chauhan, B. S.; Adkins, S. W.; Kruger, G. R.; Hewitt, A. J., Assessing a novel smartphone application SnapCard, compared to five imaging systems to quantify droplet deposition on artificial collectors. *Comput. Electron. Agric.* **2016,** *128*, 193-198.
18.   Cunha, J. P. A. R.; Farnese, A. C.; Olivet, J. J., Compare Programs for Analysis of Droplets Sprayed on Water Sensitive Papers. *Planta Daninha* **2013,** *31* (3), 715-720.
19.   Cunha, M.; Carvalho, C.; Marcal, A. R. S., Assessing the ability of image processing software to analyse spray quality on water-sensitive papers used as artificial targets. *Biosyst. Eng.* **2012,** *111*, 11-23.

20.	Williams, W. L.; Gardisser, D. G.; Wolf, R. E.; Whitney, R. W., Field and wind tunnel droplet spectrum data for the CP nozzle. *ASABE* **1999**.

21.	Panneton, B., Image analysis of water-sensitive cards for spray coverage experiments. *J. Agric. Saf. Health* **2012,** *18* (2), 179-182.

22.	Coly, A.; Aaron, J.-J., Fluorimetric analysis of pesticides: Methods, recent developments and applications. *Talanta* **1998,** *46* (5), 815-843.

23.	Hassoon, S.; Schechter, I., In situ fluorimetric determination of pesticides on vegetables. *Anal. Chim. Acta* **2000,** *405* (1-2), 9-15.

24.	Schobel, U.; Barzen, C.; Gauglitz, G., Immunoanalytical techniques for pesticide monitoring based on fluorescence detection. *Fresen. J. Anal. Chem.* **2000,** *366* (6-7), 646-658.

25.	Dougall, D. M., The use of fluorometric measurements for determination of pesticide residues. Springer New York: New York, NY, 1962; pp 24-36.

26.	Barber, J. A. S.; Parkin, C. S., Fluorescent tracer technique for measuring the quantity of pesticide deposited to soil following spray applications. *Crop Prot.* **2003,** *22*, 15-21.

27.	Aragon, A.; Blanco, L. E.; Funez, A.; Ruepert, C.; Liden, C.; Nise, F.; Wesseling, C., Assessment of Dermal Pesticide Exposure with Fluorescent Tracer: A Modification of a Visual Scoring System for Developing Countries. *Ann. Occup. Hyg.* **2005,** *50* (1), 75-83.

28.	Gonzalez-de-Soto, M.; Emmi, L.; Perez-Ruiz, M.; Aguera, J.; Gonzalez-de-Santos, P., Autonomous systems for precise spraying – Evaluation of a robotised patch sprayer. *Biosyst. Eng.* **2016,** *146*, 165-182.

29.	Lehotay, S. J.; Kok, A. d.; Hiemstra, M.; Bodegraven, P. v., Validation of a Fast and Easy Method for the Determination of Residues from 229 Pesticides in Fruits and Vegetables Using Gas and Liquid Chromatography and Mass Spectrometric Detection. *J. AOAC Int.* **2005,** *88* (2), 595-614.

30.	Harrison, R. B.; Holmes, D. C.; Roburn, J.; Tatton, J. O. G., The fate of some organochlorine pesticides on leaves. *J. Sci. Food Agric.* **1967,** *18* (1), 10-15.

31.	Hayden, J.; Ayers, G.; Gradius, E.; Hayden, N., Two Water-Soluble Optically Resolvable Dyes for Comparing Pesticide Spray Distribution. *J. Econ. Entomol.* **1990,** *83* (6), 2411-2413.

32.	Sharp, R. B., Spray deposit measurement by fluorescence. *Pestic. Sci.* **1974,** *5* (2), 197-209.

33.	Macintyre-Allen, J. K.; Tolman, J. H.; Scott-Dupree, C. D.; Harris, R., Confirmation by fluorescent tracer of coverage of onion leaves for control of onion thrips using selected nozzles, surfactants and spray volumes. *Crop Prot.* **2007,** *26*, 1625-1633.

34.	Himel, C. M., The Fluorescent Particle Spray Droplet Tracer Method. *J. Econ. Entomol.* **1969,** *50* (4), 912-916.

35.	Duga, A. T.; Ruysen, K.; Dekeyser, D.; Nuyttens, D.; Bylemans, D.; Nicolai, B. M.; Verboven, P., Spray deposition profiles in pome fruit trees: Effects of sprayer design, training system and tree canopy characteristics. *Crop Prot.* **2015,** *67*, 200-213.

36.	Boehle, K. E.; Doan, E.; Henry, S.; Beveridge, J. R.; Pallickara, S. L.; Henry, C. S., Single board computing system for automated colorimetric analysis on low-cost analytical devices. *Anal. Methods* **2018,** *10*, 5282-5290.

37.	Abràmoff, M. D.; Magalhães, P. J.; Ram, S. J., Image processing with ImageJ. *Biophotonics Int.* **2004,** *11* (7), 36-42.

38.	Cai, S.-S.; Stark, J., A method for the determination of rhodamine b and brilliant sulfaflavine on cotton string collectors and in a spray tank solution mixture. *J. Environ. Sci. Health B* **1997,** *32* (6), 985-1004.

39.   Generation 4 Research Track Sprayer. http://www.devriesmfg.com/ (accessed June 10, 2019).

40.   Runkel, R. L., On the use of rhodamine WT for the characterization of stream hydrodynamics and transient storage. *Water Resour. Res.* **2015,** *51* (8), 6125-6142.

41.   Nansen, C.; Ferguson, J. C.; Moore, J.; Groves, L.; Emery, R.; Garel, N.; Hewitt, A., Optimizing pesticide spray coverage using a novel web and smartphone tool, SnapCard. *Agron. Sustainable Dev.* **2015,** *35* (3), 1075-1085.

42.   Carvalho, F. K.; Chechetto, R. G.; Mota, A. A. B.; Antuniassi, U. R., Characteristics and challenges of pesticide spray applications in Mato Grosso, Brazil. *Outlooks Pest. Manag.* **2017,** *28* (1), 4-6.

43.   Bjugstad, N.; Torgrimsen, T., Operator safety and plant deposits when using pesticides in greenhouses. *J. Agric. Eng. Res.* **1996,** *65* (3), 205-212.

44.   Ferguson, J. C.; Hewitt, A. J.; O'Donnell, C. C., Pressure, droplet size classification, and nozzle arrangement effects on coverage and droplet number density using air-inclusion dual fan nozzles for pesticide applications. *Crop Prot.* **2016,** *89*, 231-238.

45.   Rehberg, R. A.; Trivedi, P.; Bahureksa, W.; Sharp, J.; Stokes, S. C.; Menger, R. F.; Borch, T., Quantification of insecticide application efficiency and Asian Citrus psyllid death within a citrus green disease infected grove. *Pest Manag. Sci.* **2021,** *77*, 1748-1756.

46.   Deveau, J. How to Confirm Coverage with Water-Sensitive Paper. https://sprayers101.com/confirm-coverage-wsp/ (accessed May 18, 2016).

CHAPTER 3: HIGH SPATIAL RESOLUTION FLUORESCENCE IMAGERY FOR OPTIMIZED PEST MANAGEMENT WITHIN A CITRUS GROVE

Huanglongbing (HLB), or citrus greening disease, has significantly decreased citrus production all over the world. The disease management currently depends on the efficient application and adequate distribution of insecticides to reduce the density of the disease vector, the Asian citrus psyllid. Here, we use a novel fluorescent-based method to evaluate insecticide distribution in an HLB-infected citrus grove in Florida. Specifically, we evaluated six different locations within citrus trees, the top and bottom sides of leaves, the effect of application approach (tractor vs airplane), and different application rates. We found that despite the insecticide distribution being highly variable among the different locations within a tree, the top of the leaves received an average increase of 21 times more than the bottom of the leaves. Application by tractor also resulted in a 4- to 87-fold increase in insecticide coverage compared to aerial application, depending on the location in the tree and side of leaf. When taken into context regarding the type of insecticide that is applied (systemic vs contact), these results can be used to optimize a pest management strategy to effectively target psyllids and other pests while minimizing the time and money spent on insecticide application and reducing risk to the environment. This work has been submitted for publication in *Phytopathology*.[1] Rachelle Rehberg (2nd author) assisted with sample collection during the field studies and is also currently working on quantifying pesticide concentration as a continuation of this work.[2] Dr. Hannah Miller and Dr. Daniel Blascke Carrao also assisted with the field studies.

3.1 Introduction

Crop protection depends on the efficient application of insecticide to control the insects, or vectors that spread crop diseases. For example, the Asian citrus psyllid, *Diaphorina citri*, serves as the vector for the bacterial pathogen *Candidatus* Liberibacter spp., which causes Huanglongbing (HLB). When the psyllids feed on the phloem sap, they infect the tree with HLB, resulting in citrus trees with blotchy, mottled leaves, discolored fruit, and a weakened root system.[3], HLB has significantly affected productivity and fruit quality, with severe economic effects.[4] In the United States, the production of oranges for processing decreased 72% between the 2007 and 2018 due to HLB.[5, 6] At present, there is not a "silver bullet cure" for HLB.[3] Management and reduction of this disease requires a systems approach, including destroying infected trees, using disease-free rootstock and scion grafts, and optimizing insecticide application.[7-9]

The use of insecticides is one of the main management strategies to reduce the Asian citrus psyllid population and therefore the transmission of HLB.[10, 11] As female psyllids prefer to lay their eggs on the underside of new flush,[4] protecting the bottom of those young leaves on the outside of the tree is vital for preventing the spread of HLB. However, insecticide application is expensive, with yearly costs of over $1,000 per acre for just insecticides, compared to pre-HLB costs of $800 per acre for both insecticides and fertilizers.[12] Ensuring adequate and efficient distribution of insecticides within the citrus tree can improve psyllid management as well as reduce the cost and environmental impact of insecticide application.[13, 14]

There are two types of insecticides, contact and systemic. Contact insecticides kill the insect by coming into contact with it and absorbing through the skin. It is very important for the leaves to receive a good distribution of insecticide to ensure the highest probability of actually hitting the pest. Systemic insecticides are absorbed by the roots or leaves (depending on drench or foliar application) and translocate through the plant via the xylem and the phloem.[15] It kills the

pest when the pest ingests the phloem sap. Systemic insecticides can reach other areas of the tree and still be effective against pests if the area with the pest did not initially get covered with insecticide. Full coverage of the leaves is not as imperative for the systemic insecticide to be effective.[16]

The spatial distribution of insecticides within crops has not been fully studied. Water-sensitive papers or Kromekote cards have been used to evaluate the effect of application rate, spray volume, droplet size, sprayer type, ground speed, and meteorological conditions on spray deposition on individual leaves.[17-22] However, the spatial distribution within the entire crop canopy has not been evaluated in full. Onions, tomato, pepper, oat, wheat, and pineapple plants have been analyzed for canopy penetration, but these are all small plants with sparse plant material to be covered with insecticide.[14, 23-28] The results from these studies cannot be translated to larger orchard crops like fruit trees as they have a larger and denser canopy which is more difficult to penetrate with insecticide. The canopy penetration in citrus trees specifically has been evaluated by a few studies, with the finding that the outer canopy has a higher spray deposition than the inner canopy.[21, 29-31] These studies applied metal or fluorescent tracers that were collected on the leaves or a cotton ribbon and then rinsed off for analysis.[21, 29] However, this approach does not account for differences between the top and bottom of the leaf. Differentiation between the side of the leaf is essential since psyllids are primarily located on the underside of the leaf.[31] Knowing exactly where the insecticide is distributed within the tree can inform better management practices for optimizing insecticide application and development of more efficient spraying technology.

Here we use the previously developed and validated filter paper method from Chapter 2 to evaluate the spatial distribution of pesticides in citrus trees in a citrus grove in Venus, Florida. With large scale studies with over 1000 samples, we show the heterogeneity of pesticide

application within the trees based on canopy height, canopy depth, and side of leaf. We also show how changing the application rate resulted in altered pesticide distribution within the trees and on either side of the leaf. Finally, the numerical results obtained by these studies provide conclusions that are used to inform best practices for applying systemic and contact pesticides in citrus trees. These best practices are recommended to properly target psyllids for the management of citrus greening disease but can also be applied towards other insects and pests.

3.2 Materials and Methods

3.2.1 Overview

A novel fluorescent-based method was used to evaluate the spatial distribution of insecticides.[32] The method was developed and validated in Chapter 2, and is briefly described here (Figure 3.1C). Details for the field studies can be found in Table A2.1. Circles (diameter 47 mm)
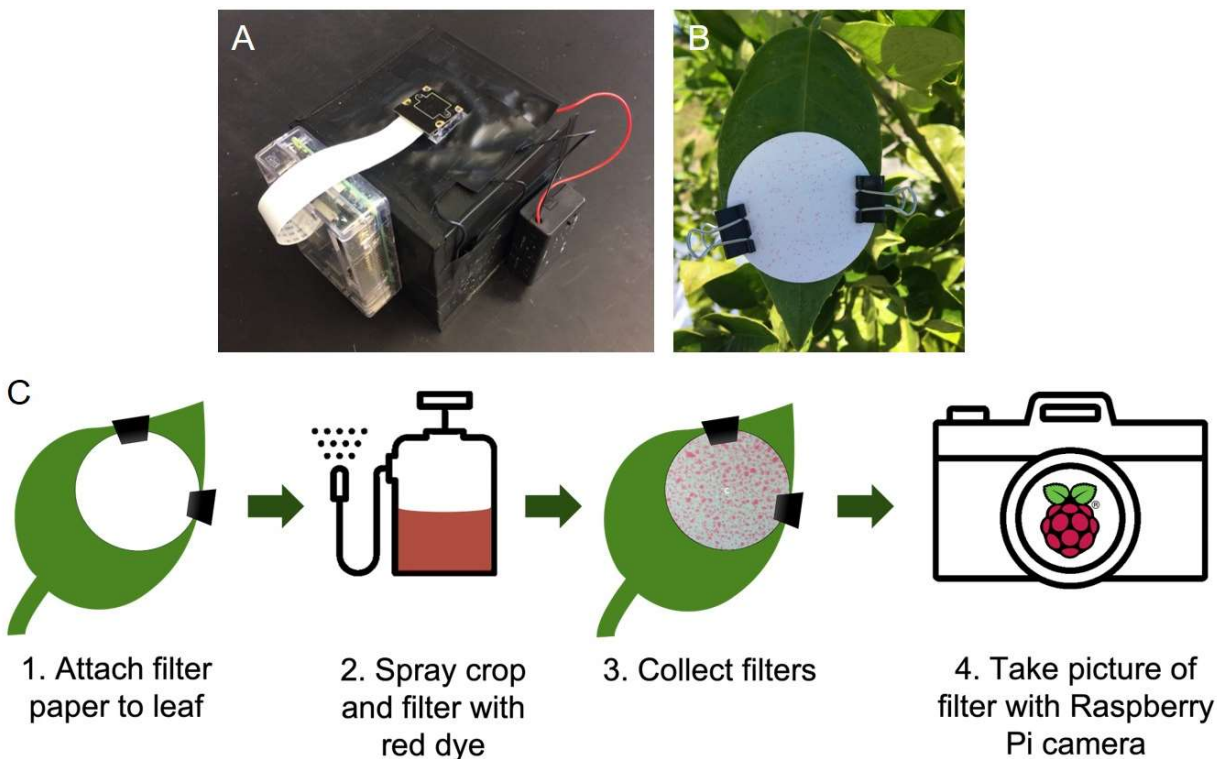

Figure 3.1 A. Lightbox with Raspberry Pi camera used to take pictures of filters. B. A filter paper sampler clipped to a citrus leaf. C. Schematic of method.

were cut out of Whatman Filter Paper No. 1 with an Epilog Zing CO_2 laser cutter. Numbers to label each circle were also cut during this step. These filter circles (samplers) were clipped to the leaves of the citrus tree with mini binder clips (9/16") (Filter 3.1B). A red fluorescent dye (Risk Reactor IFWBC7) was added to the insecticide mixture which was sprayed onto the crop via conventional sprayers attached to either a tractor or an airplane. Samplers were collected within an hour of spraying to minimize photodegradation and stored in foil packets until analysis. Pictures of each sampler were taken with a lightbox and simplified computer with a camera (Raspberry Pi) (Figure 3.1A). The pictures were analyzed for percent coverage with a custom Python script (Appendix 1.5).[32] Percent coverage is defined as the percent of a sampler that is covered by the dye – insecticide mixture.

3.2.2 Field Study Description

Samplers were collected during two field campaigns at a commercial citrus grove in Venus, Florida, in October 2018 and April 2019. Meteorological data for each trip was provided by the grove. Pesticide application details are summarized in Table A2.1. For all studies, the samplers were hung in citrus trees in various locations to test variables like canopy height (upper, middle, lower), canopy depth (inner, outer), and side of leaf (top, bottom) (Figure 3.2). With 48 samplers distributed amongst the 12 locations and 5 trees as replicates, 240 samplers were collected for each treatment group (20 samplers for each location). Two application approaches (aerial, ground) and two tree ages (young = 1 year old, old = 3 years old) were evaluated for a total of four treatment groups: aerial young, aerial old, ground young, ground old. All trees were sprayed aerially with an airplane equipped with 86 flat fan #15 nozzles (Figure 3.2A). For ground application, there were two different sprayers. The young trees (1 year old) were sprayed with a side sprayer (Newton

50

Crounch). The horizontal nozzle boom has 2 TXR80049VK nozzles (Teejet) facing down and each vertical boom has 4 TXR80017VK nozzles (Teejet) facing inward (Figure 3.2C). The older trees (3 years old) were sprayed with a speed sprayer (FM Copling) with 18 D3-C25 nozzles (Albuz/Teejet) on each side (Figure 3.2B).
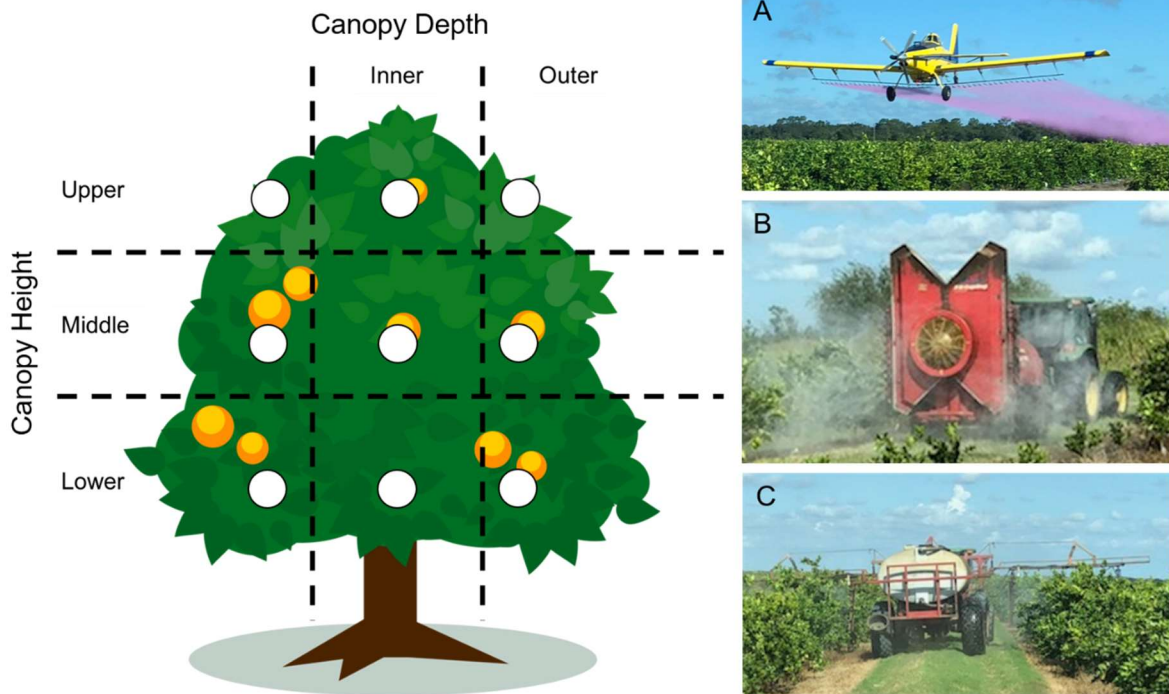
Figure 3.2. (Left) Representative citrus tree to show sampler locations. Trees were divided to investigate canopy depth (inner and outer) and height (upper, middle, and lower). Each sampler was attached on the top and bottom of a leaf in each canopy height and depth section, along with on each coordinate side of the tree (North, East, South, and West) for addition replicates. This scheme generated 48 samplers per tree. (Right) An airplane (A) was used to apply pesticide to both young and old trees. A speed sprayer (B) was used to spray pesticide on older trees (>2 years old) while the side sprayer (C) was used to spray young trees (<2 years old).

3.2.3 Statistical Analysis

Statistical analysis was performed using the JMP Pro 13 software package (SAS Institute Inc., Cary, North Carolina, USA). A significance level of $p < 0.05$ was used for statistical significance. The assumption of normality, homogeneity of variance, and linearity were checked with normal probability plots and residual plots, respectively. For October young top, October old top, and April old top, percent area coverage was selected to satisfy the normality assumption. For

all others, a base-10 logarithm transformation was selected. A mixed model was used to assess the significance of canopy depth and canopy height on percent coverage, by calendar month, tree age, and side of leaf. Factorial ANOVAs and Tukey post-hoc tests were done for each parameter combination to check for statistical significance. To determine the effect of the side of leaf on percent coverage at each location within a tree in each group, the student's t-test was used with significance at $p < 0.05$. To compare the results from the October and April field studies at a certain location within the tree, the student's t-test was used with significance at $p < 0.05$. Throughout all analyses, a random effect for leaf was included to account for measurements on both the top and bottom of each leaf.

3.3 Results and Discussion

3.3.1 Overview

In this study, we evaluated the spatial distribution within different locations in citrus trees as well as each side of the leaf. During the first field study in October 2018, four groups of trees were selected to evaluate the effect of application approach (aerial vs ground) and tree age (young vs old). Samplers were distributed throughout the tree as shown schematically in Figure 3.2. At an initial glance, the application pattern between ground and aerial application is quite different (Figure 3.3). The aerial application has individual and distinct droplets, while the ground application samplers are more evenly covered for both types of sprayers.
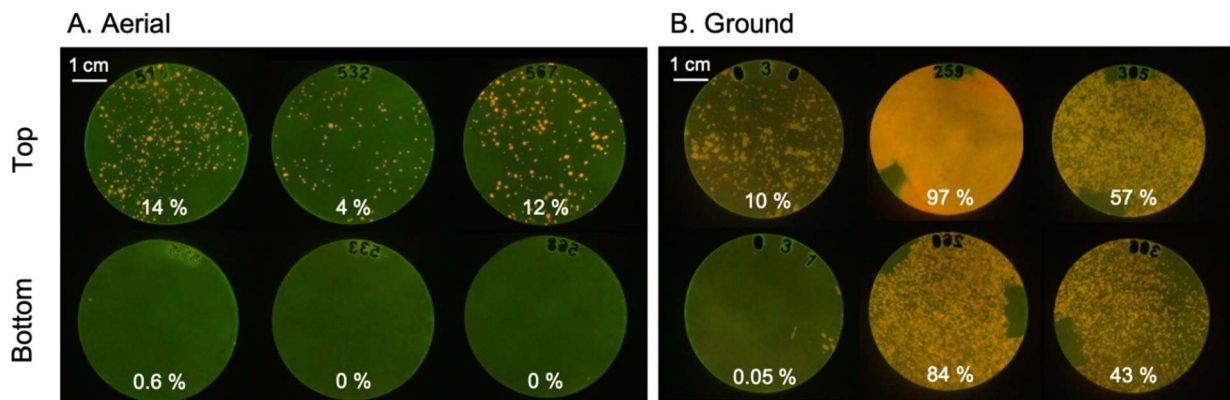
Figure 3.3 Representative images of Whatman filter paper circles (samplers) collected from the field demonstrating the varying spray pattern for insecticide sprayed via aerial (A) and ground (B) application, as well as the difference between the top and bottom of the leaf. The percent coverage (%) is labeled for each sampler.

Percent coverage is defined as the percent of a sampler that is covered by the dye – insecticide mixture. In 78% of the samplers, the top of the leaves received an average of 22 times more dye than the bottom of the leaves (Table A2.2). In addition, trees with insecticide applied via tractors (ground application) had a significantly higher average percent coverage compared to the aerial application, indicating that ground application results in more complete coverage of the leaves. The coverage on top of the leaves when sprayed by a tractor was 10 times higher than when sprayed by airplane, and the bottom of the leaves had 35 times higher coverage with tractor application (Table A2.3). However, the implication that ground application is a better application method compared to aerial application because it has a higher percent coverage needs to be taken into context with the type of insecticide being applied (i.e., contact versus systemic mode of action). Since contact insecticides need to come into direct contact with the insect to kill it by absorbing through its skin, the small distinct spots in Figure 3.3A are not ideal because the probability of hitting the insect with a small droplet is low. This also leaves unprotected areas on the leaves for the insect to avoid the insecticide.[33] It could still be effective if the insect walks through the spot to encounter the insecticide;[16] however, volatilization and degradation decrease the active concentration of insecticide over time.[34] Good coverage on the bottom of the leaf is very

important for contact insecticides to kill the Asian citrus psyllid since they primarily reside and feed on this side of the leaves. However, presence of insecticide and uniform coverage on the bottom of the leaf is less important for systemic insecticides since the insecticide will be absorbed into the leaf from both sides.

It is important to note that the variability of the field study data is quite high, and the error bars often overlap (Figures A2.2, A2.4). This is not a result of the method used for determining the spatial distribution of pesticides. It does, however, indicate the nonuniformity of insecticide application, even within each location in the tree, with percent relative standard deviation ranging from 24% to 346% among the treatment groups (Tables A2.5, A2.6).

3.3.2 Aerial Application

It is important to consider the distribution of insecticide within the citrus tree and how it is affected by the application approach and age of the tree. Figure 3.4 shows the percent coverage for the top (orange) and bottom (blue) of the leaf at the six locations evaluated in each tree with pesticide application by airplane. The samplers on the tops of leaves did not have a significant difference between any of the locations except for the inner lower location of the young trees. Equal coverage among all locations within the tree shows efficient application and is ideal for pest management to protect all parts of the tree. Systemic insecticides, like imidacloprid, can take days to weeks for full uptake in mature citrus trees, so insecticide coverage on the inside of the tree as well as the outside is recommended for full protection.[35]
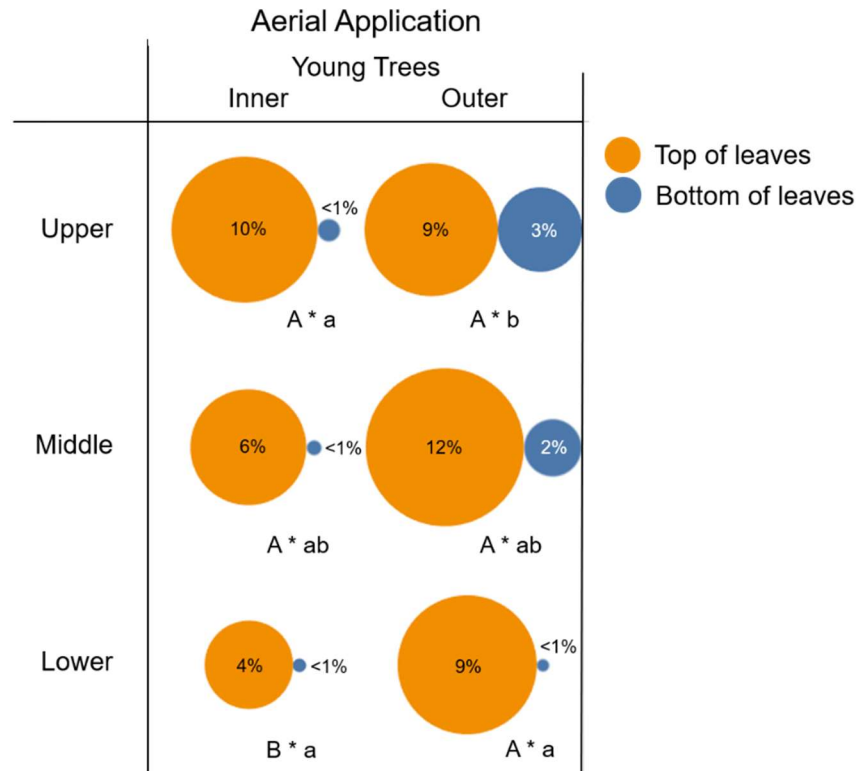
Figure 3.4. A bubble plot showing the percent area coverage of samplers with insecticide applied aerially to young trees. Samplers are grouped by canopy depth (outer, inner) and canopy height (upper, middle, lower). The left bubble (orange) of the pair is the top of the leaf, and the right bubble (blue) is the bottom of the leaf. The size of the bubbles corresponds to percent coverage, with the text in each bubble showing the average of 20 filter samplers. Letters indicate significant difference: bubbles connected by different letters are significantly different from one another, while bubbles with the same letter are not significantly different (Tukey HSD test, $p < 0.05$). Capital letters are only for the top of the leaf, while lowercase letters are for the bottom. A star (*) indicates a significant difference between the top and bottom side of the leaf at that location.

As would be expected with application from above, the top of the leaves of the young trees received significantly more insecticide than the bottom in most cases, by a factor of 47 (Figure A2.2, Table A2.2). For a systemic insecticide that absorbs into the leaf, higher coverage on the top of the leaf would suffice as long as the insecticide concentration inside the plant is high enough to kill the insect being targeted. The old trees were also sampled, but due to a miscommunication with the pilot, the trees were not sprayed properly. Therefore, those data are not presented.

3.3.3 Ground Application

For ground application, two sprayer types were evaluated: a side sprayer for the young trees (1 year old) (Figure 3.2C) and a speed sprayer for the older (3 years old) trees (Figure 3.2B). The two sprayers have different nozzle arrangements. The side sprayer has 3 panels of nozzles: a vertical panel on either side of the tree and a horizontal panel that passes over the tops of the trees. One would expect the outer and upper leaves of the young trees to get higher coverage than the inner, middle, and lower sections of the tree due to closer proximity to the nozzles.[21] However, our findings show no statistical difference among the top of the leaves for the different locations, but the general trend does match what is expected based on the arrangement of the nozzles. The outer and upper regions of the tree receive more pesticide (Figure 3.5). Due to the horizontal panel of nozzles traveling above the trees, the tops of the leaves receive 9 times more pesticide compared to the bottom, with significant differences at all locations except for the inner and outer upper locations (Table A2.4, Figure 3.5). The upper canopy is less dense compared to the rest of the tree, which means the samplers and leaves are not blocked by other leaves.
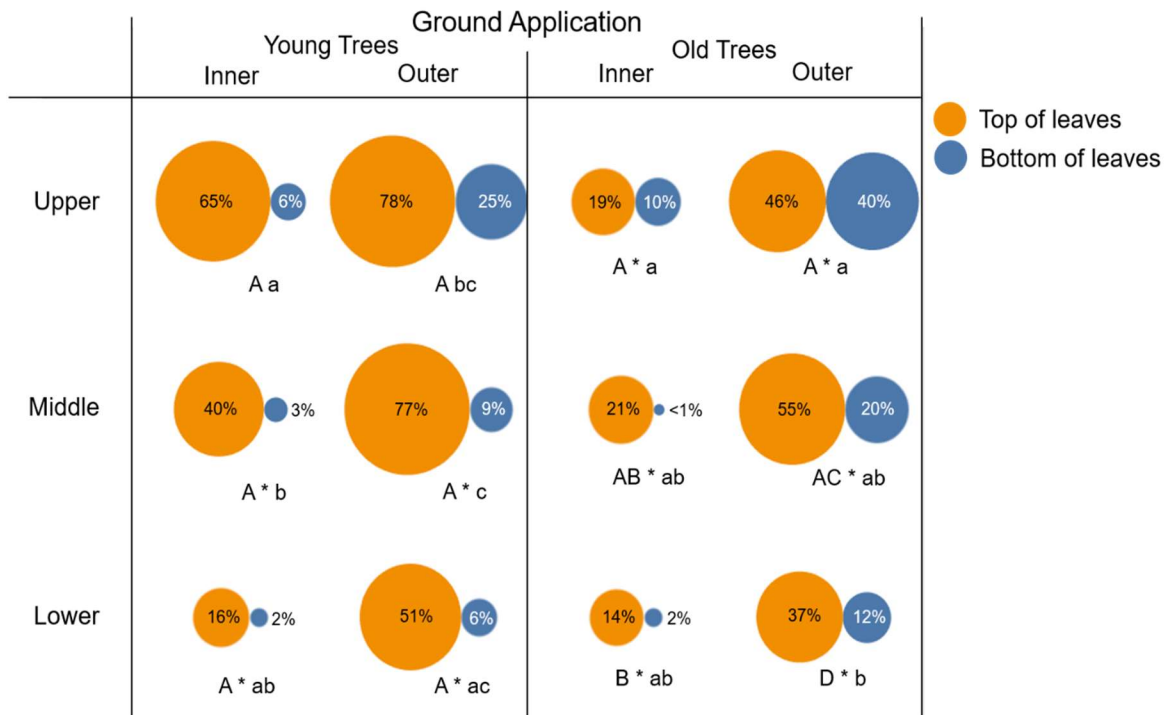
Figure 3.5. A bubble plot showing the percent area coverage of samplers with insecticide applied via tractors (ground application). Samplers are grouped by young (<1 year old) and old trees (2-3 years old), then by canopy depth (outer, inner) and canopy height (upper, middle, lower). The left bubble (orange) of the pair is the top of the leaf, and the right bubble (blue) is the bottom of the leaf. The size of the bubbles corresponds to percent coverage, with the text in each bubble showing the average of 20 samplers. Letters indicate significant difference: bubbles with different letters are significantly different from one another, while bubbles with the same letter are not significantly different (Tukey HSD test, $p < 0.05$). Capital letters are only for the top of the leaf, while lowercase letters are for the bottom. A star (*) indicates a significant difference between the top and bottom side of the leaf at that location.

The speed sprayer for the old trees has one vertical panel of nozzles that spray the insecticide with a high pressure and application rate (200 psi, 35 gallons per acre (GPA)) which is meant to increase the spray deposition to the inside of the tree.[31] Ideally, there would be no difference in canopy height (upper vs middle vs lower) due to the vertical panel or canopy depth (inner vs outer); however, this is not the case. There is a significant difference between the outer upper and lower locations, the outer middle and lower, as well as the inner upper and lower locations (Figure 3.5). This may be due to improper adjustment of the nozzle boom in relation to the canopy, where the end of the boom does not reach high or low enough. There is also a significant difference between the outer and inner canopy at the middle and lower locations, with

the outer canopy receiving on average 8.8 times more dye-insecticide mixture (Table A2.4). It has always been a challenge to reach the inside canopy of an orchard tree.[30, 31, 36] Our results show that an application rate of 35 GPA does not provide insecticide coverage on the inside of the tree. The force of spray is also meant to agitate the leaves enough so that more pesticide gets on the bottom of the leaves, but there is a significant difference between the top and the bottom of the leaves at each location. The tops of the leaves receive 8.9 times as much dye-insecticide mixture, indicating that pesticide application is not as uniform as it is thought to be (Table A2.2).

With both sprayers, the outer canopy receives more insecticide than the inner canopy, by a factor of 8.8 for the old trees (speed sprayer) and 3.0 for the young trees (side sprayer) (Table A2.4). Depending on where the insect prefers to reside, higher coverage on the outer canopy may suffice instead of having equal coverage throughout the tree. To target a specific insect, their movement within the crop should be used to inform the best application. For example, the psyllids that carry HLB prefer the underside of the new flush which is on the outer part of the tree but they can still move to the inside of the tree.[37] An application approach that effectively covers the bottom of the leaves is necessary for a contact insecticide, while adequate coverage on the top of the leaves would suffice for a systemic insecticide. However, while "adequate" coverage has been recommended as 15% coverage,[38] the concentration of the pesticide still needs to be high enough to actually kill the pest being targeted. Based on preliminary results, there is a significant correlation ($p = 2.2e\text{-}16$, Figure A2.5) between pesticide concentration and percent coverage).[2] Spraying the tree with low pesticide concentration but high spray coverage is ineffective as the pesticide concentration is likely not high enough to be toxic to the insect, leading to pesticide resistance.[2] The trees probably need to be sprayed again, increasing the time and money associated with pest management.[39]

3.3.4 Impact of Changing Spraying Settings

To evaluate the impact of changing the application rate on pesticide distribution, a second field study was performed in April 2019. The nozzle pressure was increased or decreased (thus changing the application rate) while all other sampling parameters remained the same. For the young trees, the application rate was decreased from 35 GPA to 20 GPA, resulting in a 2.3-fold decrease in coverage for the top of the leaves and a 5.8-fold decrease for the bottoms (Figure 3.6A, Table A2.5). There was a significant decrease in coverage on both the tops and bottoms of the leaves at most locations a result of the decreased application rate (Figure A2.6A).

For the old trees, the application rate was increased from 50 GPA to 90 GPA. This increased application rate resulted in higher coverage on both the top and bottom of the leaves (Figure 3.6B). Most notable is the statistically significant increase on the bottom of the leaves at each location (Figure A2.6B). The coverage on the bottom of the leaves increased by a factor of 12, most likely due to increased agitation of the leaves, while the top of the leaves only increased by a factor of 1.6 (Table A2.6). The top of the leaves at inner lower and middle locations also had a significant increase in coverage (Figure A2.6B).

Overall, the percent coverage of pesticide on the leaves improved using this higher application rate. While increasing the application rate may seem like an obvious choice to improve insecticide application, this higher application rate used with the same insecticide concentration cannot be used for every application because the insecticide concentration would reach the limits set by the Environmental Protection Agency. These regulations are in place to reduce health risks to humans and the environment.[40] In addition, intensive insecticide application can lead to insecticide resistance and have negative impacts on other insects that naturally help reduce the citrus population.[41] A higher application rate could be used with a lower insecticide concentration

to ensure that the bottom of the leaves and the inside of the leaves are targeted, but the insecticide

concentration might not be high enough to kill the psyllids. In addition, a higher application rate

results in smaller droplets that are more susceptible to drift, resulting in more insecticide lost to

the environment.[39]
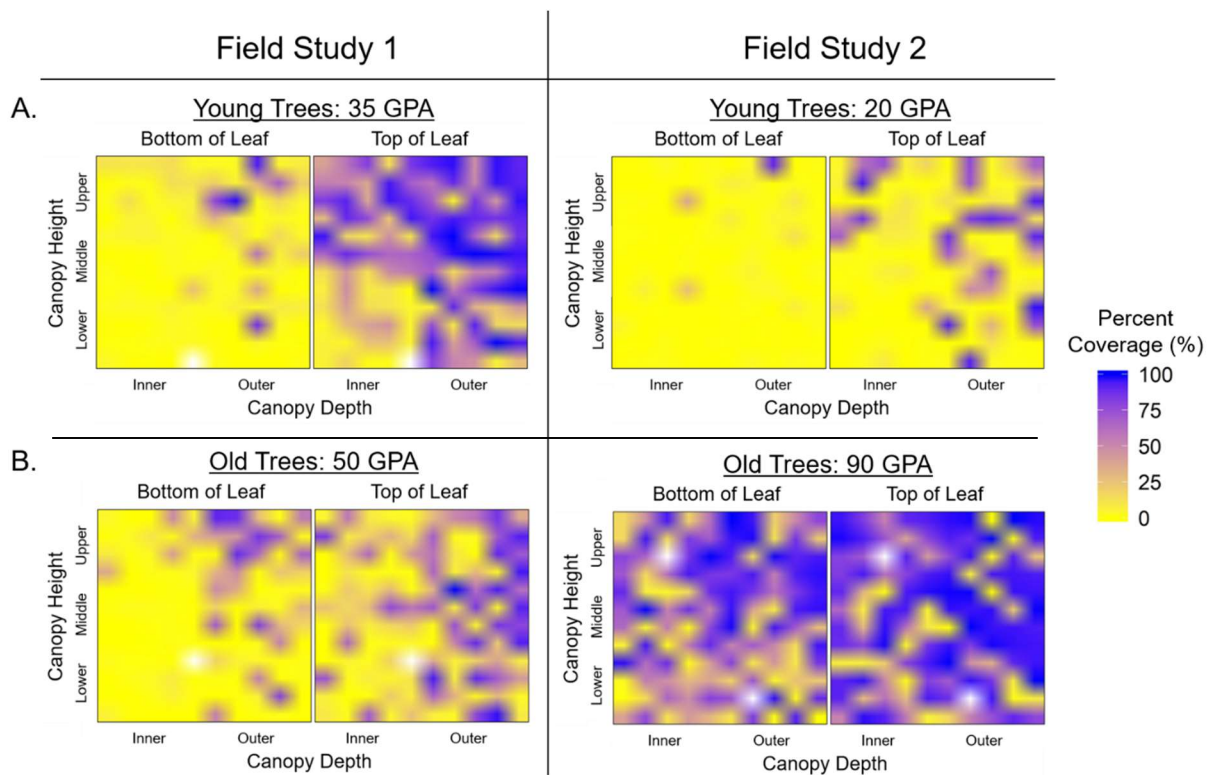
Figure 3.6 Comparison of Field Study 1 (Oct 2018) and 2 (Apr 2019) in young (A) and Old (B) trees. For the young trees, the application rat was decreased from 35 gallons per acre (GPA) to 20 GPA during Field Study 2. For the old trees, the application rate was increased from 50 GPA to 90 GPA during Field Study 2. Each 2D density plot is representative of half a tree, divided into the 6 sampling locations. Each cell corresponds to one sampler, with a total of 20 samplers per location. The percent coverage is represented by a color scale, from 0% (yellow) to 100% coverage (blue). The white cells are missing samplers.

3.4 Conclusions and Implications

In this study, we have demonstrated how application rate and type affect the pesticide

distribution within a citrus tree. Application by airplane resulted in significantly higher coverage

on the top of the leaves. The young trees were sprayed with a side sprayer which resulted in higher

pesticide coverage on the upper and outer parts of the tree as well as higher coverage on the top of

the leaves. When the application rate was decreased from 35 to 20 GPA, overall coverage decreased. The older trees were sprayed with a speed sprayer and a higher application rate (50 GPA). While there was still more coverage on the top of the leaves, the difference was not as great compared to application by the airplane or side sprayer. When the application rate was increased from 50 to 90 GPA, coverage on the bottom of the leaves significantly increased.

The results of a systematic study of pesticide application should be used to evaluate the effectiveness of current spraying techniques to make improvements given the pest to be targeted and which pesticide is being applied (Figure 3.7). For long-term protection of a large grove, a systemic insecticide applied by airplane is recommended. While it may take a few weeks for the insecticide to be fully taken up by a tree, it offers weeks to months of protection.[35] With a systemic insecticide, coverage on the bottom of the leaves and inner part of the tree is less critical, so the time saved by aerial application is more beneficial. When psyllids are present and a quick knockdown of the psyllid population is needed, the areas of high psyllid population, like the borders of the grove,[37] can be sprayed with a high application rate and high insecticide concentration.[2] For routine maintenance, contact insecticides should be applied on a rotating basis via tractor-based approaches to ensure high coverage within the entire tree and both sides of the leaf. High coverage will increase the probability of directly hitting the insect with pesticide. Care should be taken to rotate among different classes of insecticides to reduce the progression of resistance. While this study used the management of Huanglongbing in citrus trees as a case study, the fluorescent-based filter paper method can be used in any crop to evaluate the efficiency of any pest management approach.
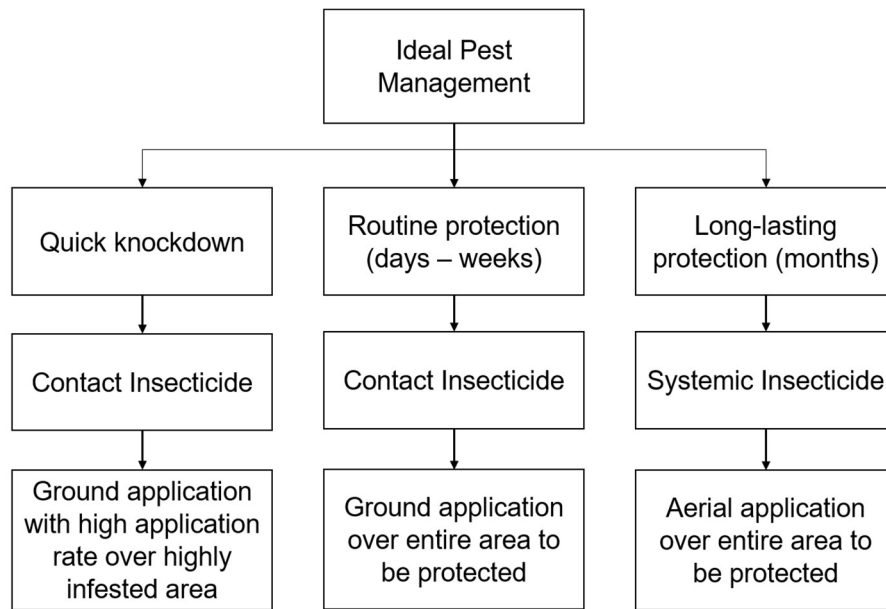
Figure 3.7 Decision tree for ideal pest management based on desired pesticide protection.

REFERENCES

1.   Menger, R. F.; Rehberg, R. A.; Trivedi, P.; Henry, C. S.; Borch, T., High spatial resolution fluorescence imagery for optimized pest management within a citrus grove. submitted to *Phytopathologypla.* **2021**.

2.   Rehberg, R. A.; Trivedi, P.; Bahureksa, W.; Sharp, J.; Stokes, S. C.; Menger, R. F.; Borch, T., Quantification of insecticide application efficiency and Asian Citrus psyllid death within a citrus green disease infected grove. *Pest Manag. Sci.* **2021,** *77*, 1748-1756.

3.   Wang, N.; Trivedi, P., Citrus Huanglongbing: A Newly Relevant Disease Presents Unprecedented Challenges. *Phytopathology* **2013,** *103* (7), 652-665.

4.   Halbert, S. E.; Manjunath, K. L., Asian citrus psyllids (Sternorrhyncha: psyllidae) and greening disease of citrus: A literature review and assessment of risk in Florida. *Fla. Entomol.* **2004,** *87* (3), 330-354.

5.   USDA-NASS *Citrus Fruits 2018 Summary*; USDA, National Agricultural Statistics Service: 2018.

6.   Dala-Paula, B. M.; Plotto, A.; Bai, J.; Manthey, J. A.; Baldwin, E. A.; Ferrarezi, R. S.; Gloria, M. B. A., Effect of Huanglongbing or Greening Disease on Orange Juice Quality, a Review. *Front. Plant Sci.* **2019,** *9*, 1-19.

7.   Martini, X.; Pelz-Stelinski, K. S.; Stelinski, L. L., Absence of windbreaks and replanting citrus in solid sets increase density of Asian citrus psyllid populations. *Agric. Ecosyst. Environ.* **2015,** *212*, 168-174.

8.   Quarles, W., IPM for Asian Citrus Psyllid and Huanglongbing Disease. *The IPM Practioner* **2013,** *34* (1).

9.   Gottwald, T. R.; Graça, J. V. d.; Bassanezi, R. B., Citrus Huanglongbing: The Pathogen and Its Impact. *Plant Health Prog.* **2007,** *8* (1), 1-36.

10.   Lopes, S. A.; Massari, C. A.; Barbosa, J. C.; Ayres, A. J. *Huanglongbing in the State of São Paulo-Brazil Current situation, regulation, management and economic impact*; 2009.

11.   Gottwald, T. R., Current Epidemiological Understanding of Citrus Huanglongbing. *Annu. Rev. Phytopathol* **2010,** *48*, 119-139.

12.   Farnsworth, D.; Grogan, K. A.; Van Bruggen, A. H. C.; Moss, C. B., The Potential Economic Cost and Response to Greening in Florida Citrus. *Choices* **2014,** *29* (3), 1-6.

13.   Uk, S.; Courshee, R. J., Distribution and likely effectiveness of spray deposits within a cotton canopy from ultralow-volume spray applied by aircraft. *Pestic. Sci.* **1982,** *13* (5), 529-536.

14.   Wolf, T. M.; Harrison, S. K.; Hall, F. R.; Cooper, J., Optimizing postemergence herbicide deposition and efficacy through application variables in no-till systems. *Weed Sci.* **2000,** *48* (6), 761-768.

15.   Cloyd, R. A.; Bethke, J. A.; Cowles, R. S., Systemic insecticides and their use in ornamental plant systems. *Floriculture Ornamental Biotech.* **2011,** *5*, 1-9.

16.   Boina, D. R.; Bloomquist, J. R., Chemical control of the Asian citrus psyllid and of huanglongbing disease in citrus. *Pest Manag. Sci.* **2015,** *71* (6), 808-823.

17.   Bretthauer, S. M.; Mueller, T. A.; Derkson, R. C.; Bode, L. E. In *The effects of spray application rate and droplet size on applications to control soybean rust*, 2008 ASABE Annual International Meeting, Providence, Rhode Island, June 28 - July 2, 2008; ASABE: Providence, Rhode Island, 2008.

18.   Pergher, G.; Gubiani, R., The Effect of Spray Application Rate and Airflow Rate on Foliar Deposition in a Hedgerow Vineyard. *J. Agric. Eng. Res.* **1995,** *61* (3), 205-216.

19.   Salyani, M.; Hoffman, W. C., Effects of Application Time and Spray Volume on Deposition. *Proc. Fla. State Hort. Soc.* **1996,** *109*, 46-50.

20.   Brusselman, E.; Beck, B.; Pollet, S.; Temmerman, F.; Spanoghe, P.; Moens, M.; Nuyttens, D., Effect of spray volume on the deposition, viability and infectivity of entomopathogenic nematodes in a foliar spray on vegetables. *Pest Manag. Sci.* **2012,** *68* (10), 1413-1418.

21.   Whitney, J. D.; Salyani, M.; Churchill, D. B.; Knapp, J. L.; Whiteside, J. O.; Littell, R. C., A field investigation to examine the effects of sprayer type, ground speed, and volume rate on spray deposition in Florida citrus. *J. Agric. Eng. Res.* **1989,** *42* (4), 275-283.

22.   Ferguson, J. C.; Hewitt, A. J.; O'Donnell, C. C.; Kruger, G. R., Comparison of water-sensitive paper, Kromekote and Mylar collectors for droplet deposition with a visible fluorescent dye solution. *J. Plant Prot. Res.* **2020**, 98-105.

23.   Macintyre-Allen, J. K.; Tolman, J. H.; Scott-Dupree, C. D.; Harris, R., Confirmation by fluorescent tracer of coverage of onion leaves for control of onion thrips using selected nozzles, surfactants and spray volumes. *Crop Prot.* **2007,** *26*, 1625-1633.

24.   Llop, J.; Gil, E.; Llorens, J.; Gallart, M.; Balsari, P., Influence of air-assistance on spray application for tomato plants in greenhouses. *Crop Prot.* **2015,** *78*, 293-301.

25.   Foqué, D.; Pieters, J. G.; Nuyttens, D., Spray deposition and distribution in a bay laurel crop as affected by nozzle type, air assistance and spray direction when using vertical spray booms. *Crop Prot.* **2012,** *41*, 77-87.

26.   Olivet, J. J.; Val, L.; Usera, G., Distribution and effectiveness of pesticide application with a cold fogger on pepper plants cultured in a greenhouse. *Crop Prot.* **2011,** *30*, 977-985.

27.   Ferguson, J. C.; Chechetto, R. G.; Hewitt, A. J.; Chauhan, B. S.; Adkins, S. W.; Kruger, G. R.; O'Donnell, C. C., Assessing the deposition and canopy penetration of nozzles with different spray qualities in an oat (Avena sativa L.) canopy. *Crop Prot.* **2016,** *81*, 14-19.

28.   Wang, J.; Lan, Y.; Wen, S.; Hewitt, A. J.; Yao, W.; Chen, P., Meteorological and flight altitude effects on deposition, penetration, and drift in pineapple aerial spraying. *Asia-Pac. J. Chem. Eng.* **2020,** *15* (1), e2382.

29.   Juste, F.; Sanchez, S.; Ibañez, R.; Val, L.; Garcia, C., Measurement of spray deposition and efficiency of pesticide application in citrus orchards. *J. Agric. Eng. Res.* **1990,** *46*, 187-196.

30.   Farooq, M.; Salyani, M., Modeling of Spray Penetration and Deposition on Citrus Tree Canopies. *Trans. ASAE* **2004,** *47* (3), 619-627.

31.   Farooq, M.; Salyani, M., Spray Penetration into the Citrus Tree Canopy from Two Air-Carrier Sprayers. In *ASAE Annual Conference*, ASAE Meeting Presentation: Key Largo, Florida, 2002.

32.   Menger, R. F.; Bontha, M.; Beveridge, J. R.; Borch, T.; Henry, C. S., Fluorescent-based method for assessment of pesticide coverage on leaves and trees: A citrus grove case study. *J. Agric. Food Chem.* **2020,** *68* (47), 14009-14014.

33.   Nansen, C.; Vaughn, K.; Xue, Y.; Rush, C.; Workneh, F.; Goolsby, J.; Troxclair, N.; Anciso, J.; Gregory, A.; Holman, D.; Hammond, A.; Mirkov, E.; Tantravahi, P.; Martini, X., A Decision-Support Tool to Predict Spray Deposition of Insecticides in Commercial Potato Fields and Its Implications for Their Performance. *J. Econ. Entomol.* **2011,** *104* (4), 1138-1145.

34.   Bedos, C.; Barriuso, E.; Cellier, P.; Calvet, R.; Gabrielle, B., Mass transfer of pesticides into the atmosphere by volatilization from soils and plants: Overview. *Agronomie* **2002,** *22*, 21-33.

35.   Grafton-Cardwell, E.; Lee, J.; Robillard, S.; Gorden, J., Role of imidacloprid in integrated pest management of California citrus. *J. Econ. Entomol.* **2014,** *101* (2), 451-460.

36.   Salyani, M.; Farooq, M.; Sweeb, R. D., Spray Deposition and Mass Balance in Citrus Orchard Applications. *Trans. ASABE* **2007,** *50* (6), 1963-1969.

37.   Sétamou, M.; Bartels, D. W., Living on the Edges: Spatial Niche Occupation of Asian Citrus Psyllid, Diaphorina citri Kuwayama (Hemiptera: Liviidae), in Citrus Groves. *PLOS One* **2015,** *10* (7), 1-21.

38.   Deveau, J. How to Confirm Coverage with Water-Sensitive Paper. https://sprayers101.com/confirm-coverage-wsp/ (accessed May 18, 2016).

39.   Nansen, C.; Ferguson, J. C.; Moore, J.; Groves, L.; Emery, R.; Garel, N.; Hewitt, A., Optimizing pesticide spray coverage using a novel web and smartphone tool, SnapCard. *Agron. Sustainable Dev.* **2015,** *35* (3), 1075-1085.

40.   Federal Insecticide, Fungicide, and Rodenticide Act. Agency, U. S. E. P., Ed. 1972.

41.   Tiwari, S.; Mann, R. S.; Rogers, M. E.; Stelinski, L. L., Insecticide resistance in field populations of Asian citrus psyllid in Florida. *Pest Manag. Sci.* **2011,** *67* (10), 1258-1268.

CHAPTER 4: DESIGN AND APPLICATION OF A SELF-PUMPING MICROFLUIDIC
STAGGERED HERRINGBONE MIXER

The rapid mixing of reagents is critical to a wide range of chemical and biological reactions but is difficult to implement in microfluidic devices, particularly in capillary action / passive pumping devices or in point-of-need environments. Here, we develop a self-pumping asymmetric staggered herringbone mixer made from only laser-ablated glass and tape. This lab-on-a-chip platform is capable of rapid flow (0.14 mL min^{-1}, 1 cm s^{-1}) and fast mixing (<10 s) without external forces or pumps and is amenable to the flow of non-aqueous solvents. Furthermore, the degree of mixing and flow rates are easily tunable through the length and depth of the herringbone grooves, and the thickness of the double-sided tape that defines the channel height, respectively. The device utility is demonstrated for chemical and biological assays through the reaction of Ni(II) and DMG in ethanol/water and the enzymatic reaction of o-dianisidine with peroxidase, respectively. This work has been published in *Microfluidics and Nanofluidics*.[1] Dr. Rob Channon developed the device and optimized the fabrication method. Dr. Wei Wang developed and fabricated the superomniphobic paper. I optimized and performed the mixing, Ni-DMG, and peroxidase reactions.

4.1 Introduction

Microfluidic and lab-on-a-chip devices are transformative tools for carrying out chemical and biological reactions across a wide range of disciplines, from drug discovery to biomarker monitoring.[2, 3] These applications are driven by the small sample volume requirements, high device portability, and inexpensive setup and reaction costs compared to conventional approaches. Three key current challenges in the microfluidics / lab-on-a-chip community are i) generating fluid flow

cheaply and easily in point-of-care environments, ii) the ability to transport non-aqueous solvents, and iii) the fast and complete mixing of reagents.[4-6]

The most common approach to generate fluid flow in microfluidic devices is through syringe pumps, but these are unsuitable for point-of-care flow generation due to the bulky size and requirement of electricity. Portable plug-and-play pumps or valves have been designed to overcome this challenge, though they are often application-specific (e.g., fixed flow rates).[7-9] Capillary action-based flow is also used with hydrophilic materials such as paper or glass, although the flow rates can be slow and integration of complex designs (e.g., mixing and sensing modules) can be challenging.[10, 11]

Many microfluidic devices are made of materials (like polydimethylsiloxane and paper) that are incompatible with non-aqueous solvents. This limits the scope of microfluidic devices.[12] Cyclic olefin copolymers and hybrid materials such as fluorinated polymers coated onto PDMS can accommodate non-aqueous solvents, but the preparation of these materials is often more complex and expensive.[4, 13] Paper-based devices are ideally suited for point-of-care environments, however, the flow rates are generally slow and the inks used to define channels are not stable in non-aqueous solvents.[14, 15]

Micromixers are critical components to conduct chemical or biological reactions and/or to sense analytes in microfluidic or lab-on-a-chip devices.[16] Micromixers can be divided into active and passive mixers. Active micromixers employ an external stimulus to mix fluids, including magnetic beads, temperature, pressure, acoustics, digital droplets or an electric field.[17-21] Active mixers typically provide a high degree of mixing and are especially useful for systems with low Reynolds numbers (Re < 1), to overcome low flow rates and high viscosity, but these mixers are unsuitable for point-of-care devices due to the added cost and increased size that comes with the

integration of an external power source to a microfluidic device.[22] Passive micromixers rely on shrewd device designs to enhance advective and diffusive mixing without external forces, for example, serpentines, splitting then recombination of streams, multiphase flow, and integration of obstacles, grooves or ridges.[17-19, 23-26] Compared to active mixers, passive micromixers typically require longer channel lengths and longer mixing times to achieve complete mixing. Furthermore, there are very few effective passive micromixers for capillary-based flow systems.[27-30]

Among passive mixers, herringbone mixers are particularly popular due to the efficient mixing over short channel lengths. Herringbone devices feature an array of grooves in the wall of a microfluidic channel.[31] Fluid enters these grooves and recirculates into the main channel, generating complex circulating flows that result in fluid mixing. The speed and extent of mixing are controlled by the length of the herringbone, the channel dimensions, and the flow rate.[32] Patterning herringbones into both the top and bottom channel walls has been shown to improve the mixing efficiency, although this is difficult to implement depending on the fabrication procedure and device materials.[23, 33, 34] Herringbone micromixers have been employed for micromixing in a range of applications,[35, 36] but rarely in point-of-care environments.

In this work, we demonstrate for the first time an asymmetric two-faced staggered herringbone passive micromixer combined with a passive/capillary action flow device. Our design is based on a self-pumping device made from glass and tape which is simple, inexpensive, and fast to manufacture. This novel fabrication approach provides fast flow rates and rapid mixing that have not been achieved previously in other passive flow herringbone devices. To demonstrate the scope of this point-of-care device, we investigate the application of the microfluidic device with two kinetically fast chemical and biological reactions.

4.2 Materials and Methods

4.2.1 Fabrication and Operation of Herringbone Device

Microfluidic devices with herringbone grooves were fabricated via a simple cutting and stacking method. Three sets of herringbone grooves were rastered onto each glass slide (Glass D, Nexterion) with a laser cutter (Epilog Zing), operated at a resolution of 500 dpi, 100% laser power, and 25% scanning speed. Each of the 3 sets of herringbones consisted of 15 herringbone grooves with a width of ~285 – 300 µm, depth of ~120 µm, and inter-groove spacing of ~530 µm (i.e., valley to valley), which was achieved through 8 laser engraving scans (Figure A3.1). The angle between the long and short grooves is 105.7°. The channel height, herringbone groove depth were optimized to provide the most efficient mixing.[32, 33] After fabrication, the glass slides were cleaned by ultrasonication in acetone for 10 min, rinsed with DI water and dried with nitrogen.

To join the glass slides and define the channel height and width, double-sided tape (3M Scotch) was carefully cut with a laser ablator and aligned on the glass slide to form a ~3 mm wide Y-shaped channel (~50 µm channel height) over the herringbone structures (Figure A3.2). A template was used to ensure proper alignment. Another glass slide with herringbone structures was placed on the tape layer and firmly pressed to form the microfluidic device. An asymmetric design was employed where the herringbone grooves in the top face of the channel were oriented in an offset pattern to the bottom face to enhance the mixing (Figure 4.1A).[33, 34] A coating of 3M instant adhesive (SF 100) was applied to the sidewall with the channel inlets to prevent undesired spreading of liquid droplets upon contacting the device entrance. Prior to experiments, the device was cleaned by flushing with ethanol, then water, and dried thoroughly with nitrogen.

To demonstrate the rapid mixing of our self-pumping microfluidic devices, Liquid droplets containing reagents were placed on a piece of superomniphobic paper, which displays extreme repellence to liquids with a wide range of surface tension.[37-40] The droplets were spaced

accordingly to line up with the entrance of the microfluidic device. The device was moved toward the droplets until contact with the glass initiated fluid flow into the channel. The experiments were recorded with a digital camera (Canon) and then analyzed using NIH ImageJ software (Appendix 3.1).

4.2.2 Fabrication of Superomniphobic Paper

Superomniphobic paper was fabricated through liquid phase silanization of Whatman filter paper 8, as previously described.[41, 42] The filter paper was exposed to oxygen plasma for 10 min and then immersed in a mixture of 20 mL hexane and 600 µL of heptadecafluoro-1,1,2,2-tetrahydrodecyltrichlorosilane (FDTS) for 3 days at room temperature. The paper was then washed with hexane and dried with nitrogen.

4.2.3 Ni-DMG Reaction

The colorimetric reaction of nickel with dimethylglyoxime (DMG) was used as a representative inorganic reaction (Figure A3.3). A solution of 2.25 mM nickel (nickel (II) sulfate hexahydrate, Sigma Aldrich) was prepared in 1:1 mix of ethanol and pH 5 acetate buffer. A solution of 4.5 mM DMG (Fluka) was prepared in 50% v/v ethanol: DI water. 50 µL droplets of each reagent were mixed in the device.

4.2.4 HRP-H_2O_2 Reaction

The enzymatic turnover of H_2O_2 by horseradish peroxidase was used as a representative biological reaction to evaluate enzyme kinetics using the herringbone device (Figure A3.4). Ten solutions of H_2O_2 (Sigma Aldrich) were prepared in DI water between 0.001 mM and 0.06 mM

(0.005% - 0.2% v/v). A 0.018 M solution of o-dianisidine dihydrochloride (Sigma Aldrich) in DI water was used for all experiments. A 32.5 U mL^{-1} solution of horseradish peroxidase (HRP, Sigma Aldrich, peroxidase from horseradish Type VI, >250 U mg^{-1}) was prepared in DI water immediately prior to use. All solutions were prepared in DI water instead of buffer due to the higher o-dianisidine (OD) solubility in DI water. In the device, a 30 µL droplet of a 50:50 mixture of OD and HRP was mixed with a 30 µL droplet of H_2O_2. Videos were recorded for each reaction and analyzed in ImageJ (Appendix 3.1). The determination of Michaelis-Menten constants is described in Appendix 3.2.

4.3 Results and Discussion

Given the challenges associated with mixing in passive flow devices, we sought to determine if we could use herringbone-based mixing devices to achieve mixing in a capillary flow device. Our device design (Figure 4.1A) was adapted from that used in multilayered paper-based microfluidic devices without mixers as well as the literature on staggered one- and two-faced herringbone microfluidic mixers.[31, 34, 42, 43] The device itself is fabricated using a laser cutter to etch the herringbone grooves into glass slides and sealing with double-sided adhesive to form the microfluidic channel. The device design, dimensions, and characterization by optical profilometry are provided in Appendix 3 (Figures A3.1 and A3.2). The number and depth of the herringbone sets, as well as the height of the tape, were previously optimized and chosen for both efficient mixing and consistency of the device.[32, 33] The staggered herringbone grooves in the top and bottom faces of the channel were offset yielding an asymmetric pattern. This provides enhanced mixing over herringbones in a single face or symmetric herringbones in two faces, and likely results in four circular flows across the channel cross-section as previously described.[34] To establish fluid flow, reactants were placed as droplets on superomniphobic paper (contact angle ≈

165° for ~10 µL, Figure 4.1C) which displays extreme repellence to liquids with a wide range of surface tension.[37-40] Moving the device toward the droplets until contact with the glass initiates fast fluid flow (0.14 mL min^{-1}, 1 cm s^{-1}) of the reactants into the channel due to capillarity.
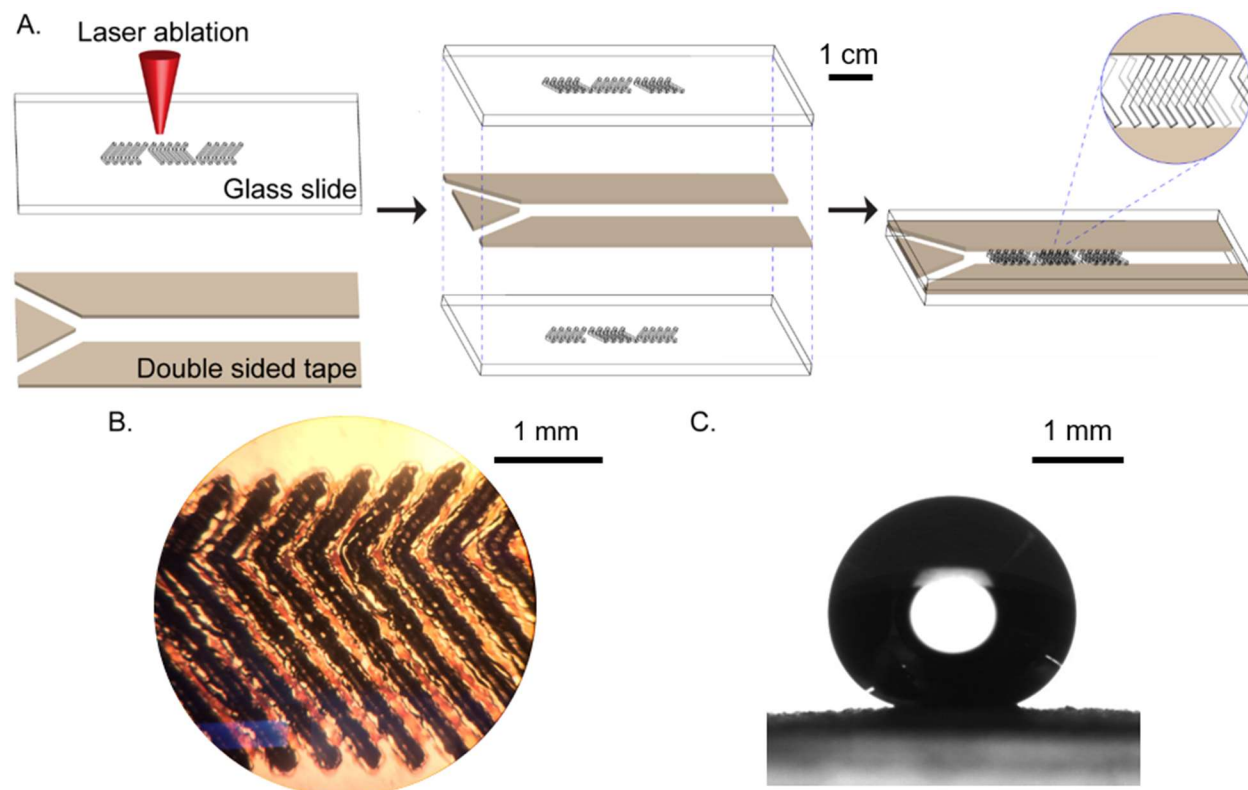
Figure 4.1 A. Schematic of device fabrication, B. Microscope image of lasered grooves, C. 10 µL droplet of water on superomniphobic paper (contact angle 165°).

To illustrate the enhanced mixing in the herringbone device, aqueous droplets of blue and yellow food dyes were mixed forming a green color. The pixel count for each color was measured in ImageJ before and after the herringbones (Figure A3.3). Three device configurations were evaluated: a control device with no herringbone grooves, a device with one slide with ablated herringbone grooves, and one with two slides with herringbone grooves in an asymmetric pattern (Figure 4.2, ESI videos 'BY dye control', 'BY dye 1 side herringbone', and 'BY dye 2 sides
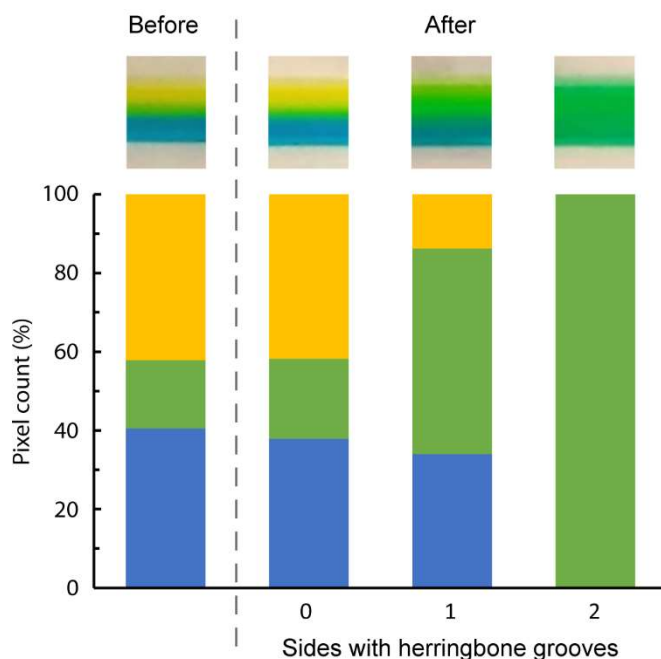
Figure 4.2 Analysis of mixing blue and yellow dyes to form a green color with 0, 1, and 2 slides with herringbone grooves. Images (top row) were taken just before and just after the herringbones.

herringbone'). In the absence of herringbone grooves, mixing only occurred at the interface of the two colors (20% green pixels). The Reynolds (Re) and Peclet (Pe) numbers for our system are 0.98 and 490, respectively. This suggests flow in the devices is laminar, and mass transport is likely mixed diffusive and convective. In fact, in the control device without herringbones, an 8 m long channel would be required to fully mix the two colors.[31] Partial mixing was achieved when one channel wall contained herringbone grooves (52% green pixels), but for complete mixing in the length of the herringbone grooves (3.3 cm), two faces with herringbone grooves were required (100% green pixels). This result is in line with previous studies on improved mixing efficiencies with multiple walls of herringbone grooves compared to a single set.[33, 34] As the three sets of herringbones deliver complete mixing, we anticipate most solvents and solvent mixtures would also mix satisfactorily through the current design. The fabrication method is designed as such to be able to tune the device to the application (i.e., choice of tape to define the channel height or

number of herringbones). The speed and degree of mixing can be tuned with these parameters depending on the miscibility and viscosity of the reagents and the application.

Manufacturing microfluidic devices with herringbone grooves in the top and bottom channel walls is challenging using traditional micromachining methods. Typically, microfluidic devices are made with a channel in one material, like PDMS, which is bonded to a base substrate, like a glass coverslip, using plasma treatment. It can be challenging to make herringbone grooves in PDMS since these devices typically require photolithography as a fabrication process.[31, 32] Our proposed device is made of two glass slides bonded with double-sided adhesive. The herringbone grooves are etched into each slide with a laser cutter, and the channel height and width are controlled by the placement and height of double-sided adhesive. Our device features a channel width of 3 mm and height of 50 µm, representing a hydraulic diameter of 98 µm. The use of wide channels with small heights is fairly common in microfluidic devices, e.g. in channel flow cells with electrochemical sensing.[44] Also, the flow and mixing of small sample volumes (ca. 40 µL) fit the definition of a microfluidic device. Given the benefits of the fabrication method (fast, easy, inexpensive), we envision these glass/tape herringbone devices as disposable mixers for point-of-care applications.

As proof of concept to demonstrate the device scope, two representative chemical and biological application reactions were chosen. First, the detection of Ni(II) in the environment, which is important due to the environmental abundance of Ni(II) and potential health issues like reduced lung function and cancer.[45] A common colorimetric assay for Ni(II) detection is the reaction with dimethylglyoxime (DMG) in ethanol:H_2O (Figure A3.4).[46, 47] This reaction produces a reddish-pink precipitate which is insoluble in water, as shown in Figure 3b (ESI video 'Ni-DMG herringbone'). Note, in the absence of the herringbones, no precipitate is observed (Figure 4.3A,
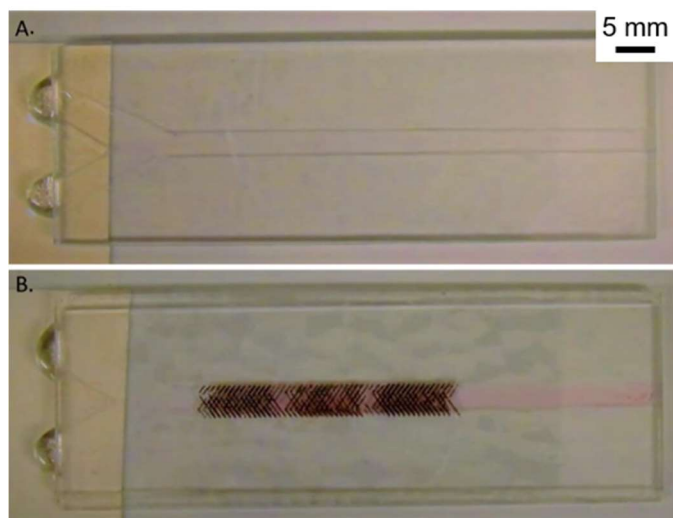
Figure 4.3 Nickel (top droplet) mixing with DMG (bottom droplet) in a device without herringbone grooves (A.) and with herringbone grooves (B.).

ESI video 'Ni-DMG control'). Since the DMG is dissolved in ethanol, this reaction also demonstrates that the device applicability for reactions in non-aqueous solvents, which are commonplace in industry. Many microfluidic materials (polydimethylsiloxane, PDMS, paper) are limited by incompatibility with non-aqueous solvents,[12] but with the herringbone device being made out of glass, it is compatible with organic solvents as there were no visible adverse effects like degradation or delamination.

The mixing device can also be used for biological assays such as the enzymatic reaction of hydrogen peroxide (H_2O_2) and horseradish peroxidase (HRP), using o-dianisidine (OD) as a colorimetric indicator (Figure A3.5). The reaction of HRP with H_2O_2 is important for many bioassays where HRP is a label.[48] H_2O_2 is turned over by the HRP, oxidizing the OD which turns from colorless to dark brown (Figure 4.4A, ESI video 'HRP herringbone'). Without the herringbone grooves, mixing only occurs at the interface of the two liquids due to diffusion (Figure 4.4B, ESI video 'HRP control'). To demonstrate that the herringbone device gives similar results to traditional microfluidic devices and bulk solution reactions, Michaelis-Menten kinetics were determined for this reaction using the micromixing device (Appendix 3.2, Figures A3.6 and A3.7).
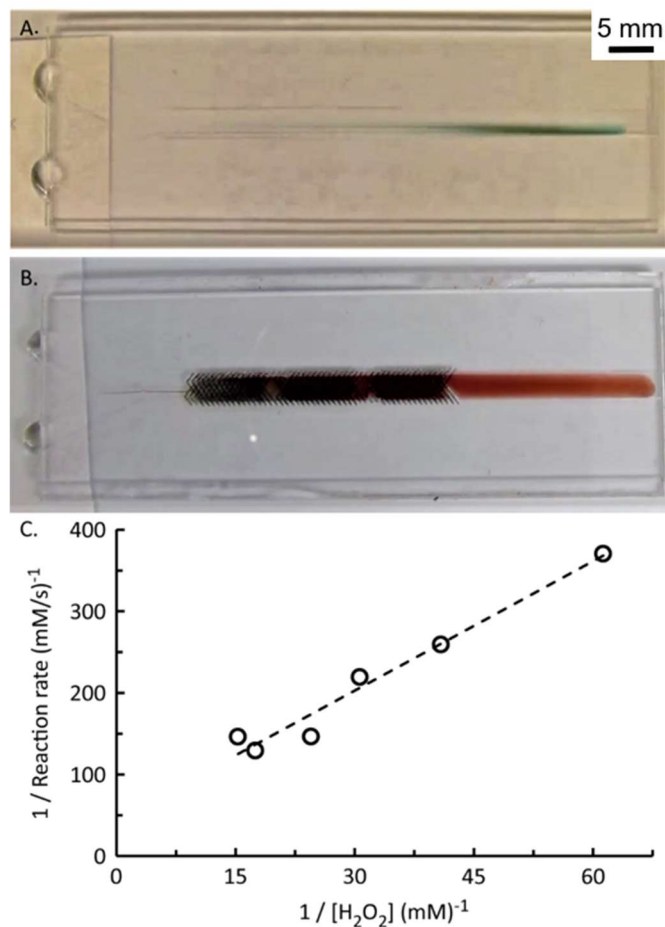
Figure 4.4 Reaction of hydrogen peroxide (top droplets) with o-dianisidine and horseradish peroxidase (bottom droplet) in a device without herringbone grooves (A.) and with herringbone grooves (B.). The reagents are fully mixed in B to produce to produce brown o-dianisidine. C. Lineweaver-Burk plot of the enzymatic turnover of hydrogen peroxide.

In short, videos with various concentrations of H_2O_2 were analyzed and the brown color intensity was measured in ImageJ over the course of each video (Figure A3.4). This yielded the reaction rate, and its inverse was plotted against the inverse of H_2O_2 concentration, generating a Lineweaver-Burk plot (Figure 4.4C). Values for K_m and k_{cat} were determined to be 0.119 mM and 7.61 s^{-1}, respectively, and are comparable to those found in the literature.[49] The similarity in measured values indicates the viability of this simple mixing system for carrying out kinetic reactions. In addition, the herringbone device could easily be used for other biological applications,

for example, investigating the binding kinetics between fluorescently tagged antibodies and antigens without needing surface plasmon resonance measurements.[50]

Previous herringbone devices have been fabricated using standard photolithography methods and a SU-8 photoresist, forming the channel when PDMS is plasma-bonded to a glass slip.[31, 32] This method is time-intensive and expensive in comparison to the described approach of laser ablating the glass slides and sealing with tape. Each device costs ~$0.40 and takes ~7 min to make by hand. Since the design is printed from a CAD file, changing the design to prototype new devices is fast and simple in comparison to making a new photoresist mold. Glass also has high solvent stability compared to other common materials used to make microfluidic devices. For example, PDMS swells in nonpolar solvents like hydrocarbons, toluene, and dichloromethane,[51] resulting in deformed channels and altered dimensions, which changes the fluid velocity and mixing capacity as well as affecting any sensing elements. Typically, paper-based devices use wax to form hydrophobic channels on the paper.[52] Wax is not compatible with organic solvents, leaving the device without any barriers to direct fluid flow. Conversely, glass is compatible with a wider range of solvents,[51] allowing this herringbone device to be used for a variety of reactions without compromising the integrity of the device.

4.4 Conclusion

A new herringbone microfluidic mixer is presented that can achieve complete mixing of small volumes over short times and distances. Crucially, these devices employ passive pumping (capillary action) and are capable of transporting both aqueous and organic solvents which are typically challenging to use in self-pumping devices. Laser cutting the asymmetric staggered herringbone grooves into glass slides as the channel walls delivers a fast, simple, inexpensive, and easily modifiable fabrication that has not been previously demonstrated as well as achieving fast

flow rates and rapid mixing. The flow rate can easily be changed through altering the channel height through the choice of double-sided tape thickness or number of tape layers (commercially available tapes range from 50 to 230 μm thicknesses).[42] The degree of mixing can be simply altered through the number of herringbone grooves, or the depth of the grooves (through the number of lasering rasters).[32-34, 53] The device can be used for a range of biological and environmental applications, including inorganic, organic, and enzymatic reactions. Furthermore, relevant data like enzyme kinetics can be easily deduced from the device through colorimetric image analysis and our devices are amenable to other microfluidic sensing formats such as fluorescence and electrochemical detection. This device has great potential as a disposable mixer for point-of-care applications. Future work will seek to expand the application of these devices to a wider range of reactions in non-aqueous solvents, as well as to conduct finite element modeling of the device to understand the mixing in a capillary flow-driven asymmetric staggered herringbone mixer and optimize the device design.[34, 54, 55]

REFERENCES

1.   Channon, R. B.; Menger, R. F.; Wang, W.; Carrão, D. B.; Vallabhuneni, S.; Kota, A. K.; Henry, C. S., Design and application of a self-pumping microfluidic staggered herringbone mixer. *Microfluid. Nanofluid.* **2021,** *25* (4).

2.   Regnault, C.; Dheeman, D.; Hochstetter, A., Microfluidic Devices for Drug Assays. *High-Throughput* **2018,** *7* (18), 1-13.

3.   Nahavandi, S.; Baratchi, S.; Soffe, R.; Tang, S.-Y.; Nahavandi, S.; Mitchell, A.; Khoshmanesh, K., Microfluidic platforms for biomarker analysis. *Lab Chip* **2014,** *14* (9), 1496-1514.

4.   Renckens, T. J. A.; Janeliunas, D.; Van Vliet, H.; Van Esch, J. H.; Mul, G.; Kreutzer, M. T., Micromolding of solvent resistant microfluidic devices. *Lab Chip* **2011,** *11* (12), 2035-2038.

5.   Cai, G.; Xue, L.; Zhang, H.; Lin, J.; Cai, G.; Xue, L.; Zhang, H.; Lin, J., A Review on Micromixers. *Micromachines* **2017,** *8* (9), 274-274.

6.   Chin, C. D.; Linder, V.; Sia, S. K., Commercialization of microfluidic point-of-care diagnostic devices. *Lab Chip* **2012,** *12* (12), 2118.

7.   Zhang, X.; Xia, K.; Ji, A., A portable plug-and-play syringe pump using passive valves for microfluidic applications. *Sens. Actuators B Chem.* **2020,** *304*, 127331.

8.   Park, J.; Park, J.-K., Integrated microfluidic pumps and valves operated by finger actuation. *Lab Chip* **2019,** *19*, 5.

9.   Feeny, R. M.; Puissant, N. L.; Henry, C. S., Degassed PDMS pump for controlled extraction from dried filter samples in microfluidic devices. *Anal. Methods* **2016,** *8*, 8243-8370.

10.   Iliescu, C.; Taylor, H.; Avram, M.; Miao, J.; Franssila, S., A practical guide for the fabrication of microfluidic devices using glass and silicon. *Biomicrofluidics* **2012,** *6* (1), 016505.

11.   Carrell, C.; Kava, A.; Nguyen, M.; Menger, R. F.; Munshi, Z.; Call, Z.; Nussbaum, M.; Henry, C., Beyond the lateral flow assay: A review of paper-based microfluidics. *Microelectron. Eng.* **2019,** *206*, 45-54.

12.   Channon, R. B.; Joseph, M. B.; Macpherson, J. V., Additive Manufacturing for Electrochemical (Micro)Fluidic Platforms. *Electrochem. Soc. Interface* **2016,** *25* (1), 63-68.

13.   Illa, X.; Ordeig, O.; Snakenborg, D.; Romano-Rodríguez, A.; Compton, R. G.; Kutter, J. P., A cyclo olefin polymer microfluidic chip with integrated gold microelectrodes for aqueous and non-aqueous electrochemistry. *Lab Chip* **2010,** *10* (10), 1254.

14.   Park, S. H.; Maruniak, A.; Kim, J.; Yi, G.-R.; Lim, S. H., Disposable microfluidic sensor arrays for discrimination of antioxidants. *Talanta* **2016,** *153*, 163-169.

15.   Cardoso, T. M. G.; De Souza, F. R.; Garcia, P. T.; Rabelo, D.; Henry, C. S.; Coltro, W. K. T., Versatile fabrication of paper-based microfluidic devices with high chemical resistance using scholar glue and magnetic masks. *Anal. Chim. Acta* **2017,** *974*, 63-68.

16.   Jeong, G. S.; Chung, S.; Kim, C.-B.; Lee, S.-H., Applications of micromixing technology. *Analyst* **2010,** *135* (3), 460-473.

17.   Ward, K.; Fan, Z. H., Mixing in microfluidic devices and enhancement methods. *J. Micromech. Microeng.* **2015,** *25* (9), 094001.

18.	Shanko, E.-S.; Van De Burgt, Y.; Anderson, P. D.; Den Toonder, J. M. J., Microfluidic Magnetic Mixing at Low Reynolds Numbers and in Stagnant Fluids. *Micromachines* **2019,** *10* (11), 731.

19.	Bayareh, M.; Ashani, M. N.; Usefian, A., Active and passive micromixers: A comprehensive review. *Chem. Eng. Process* **2020,** *147*, 107771.

20.	Lynn, N. S.; Henry, C. S.; Dandy, D. S., Microfluidic mixing via transverse electrokinetic effects in a planar microchannel. *Microfluid. Nanofluid.* **2008,** *5* (4), 493-505.

21.	Srinivasan, V.; Pamula, V. K.; Fair, R. B., An integrated digital microfluidic lab-on-a-chip for clinical diagnostics on human physiological fluids. *Lab Chip* **2004,** *4*, 310-315.

22.	Capretto, L.; Cheng, W.; Hill, M.; Zhang, X., Micromixing Within Microfluidic Devices. In *Microfluidics*, Lin, B., Ed. Springer Berlin Heidelberg: Berlin, Heidelberg, 2011; Vol. 304, pp 27-68.

23.	Feng, X.; Ren, Y.; Hou, L.; Tao, Y.; Jiang, T.; Li, W.; Jiang, H., Tri-fluid mixing in a microchannel for nanoparticle synthesis. *Lab Chip* **2019,** *19* (17), 2936-2946.

24.	Seong, G. H.; Crooks, R. M., Efficient Mixing and Reactions within Microfluidic Channels Using Microbead-Supported Catalysts. *J. Am. Chem. Soc.* **2002,** *124* (45), 13360-13361.

25.	Chen, C.; Zhao, Y.; Wang, J.; Zhu, P.; Tian, Y.; Xu, M.; Wang, L.; Huang, X., Passive Mixing inside Microdroplets. *Micromachines* **2018,** *9* (4), 160.

26.	Wang, J.; Zhang, N.; Chen, J.; Rodgers, V. G. J.; Brisk, P.; Grover, W. H., Finding the optimal design of a passive microfluidic mixer. *Lab Chip* **2019,** *19* (21), 3618-3627.

27.	Lillehoj, P. B.; Wei, F.; Ho, C.-M., A self-pumping lab-on-a-chip for rapid detection of botulinum toxin. *Lab Chip* **2010,** *10* (17), 2265-2270.

28.	Gervais, L.; Hitzbleck, M.; Delamarche, E., Capillary-driven multiparametric microfluidic chips for one-step immunoassays. *Biosens. Bioelectron.* **2011,** *27* (1), 64-70.

29.	Glavan, A. C.; Martinez, R. V.; Maxwell, E. J.; Subramaniam, A. B.; Nunes, R. M. D.; Soh, S.; Whitesides, G. M., Rapid fabrication of pressure-driven open-channel microfluidic devices in omniphobic RF paper. *Lab Chip* **2013,** *13* (15), 2922-2930.

30.	Taher, A. J., Benjamin; Fiorini, P.; Lagae, L., A valveless capillary mixing system usaing a novel approach for passive flow control. *Microfluid. Nanofluid.* **2017,** *21* (8), 10.

31.	Stroock, A. D.; Dertinger, S. K. W.; Ajdari, A.; Mezic, I.; Stone, H. A.; Whitesides, G. M., Chaotic Mixer for Microchannels. *Science* **2002,** *295* (5555), 647-651.

32.	Williams, M. S.; Longmuir, K. J.; Paul, Y., A practical guide to the staggered herringbone mixer. *Lab Chip* **2008,** *8*, 1121-1129.

33.	Hossain, S.; Husain, A.; Kim, K. Y., Optimization of micromixer with staggered herringbone grooves on top and bottom walls. *Eng. Appl. Comp. Fluid Mech.* **2011,** *5* (4), 506-516.

34.	Choudhary, R.; Bhakat, T.; Kumar Singh, R.; Ghubade, A.; Mandal, S.; Ghosh, A.; Rammohan, A.; Sharma, A.; Bhattacharya, S., Bilayer staggered herringbone micro-mixers with symmetric and asymmetric geometries. *Microfluid. Nanofluid.* **2011,** *10*, 271-286.

35.	Liu, B.; Wu, T.; Yang, X.; Wang, Z.; Du, Y., Portable Microfluidic Chip Based Surface-Enhanced Raman Spectroscopy Sensor for Crystal Violet. *Anal. Lett.* **2014,** *47* (16), 2682-2690.

36.	Wang, S.; Niu, H.; Cai, Y.; Cao, D., Multifunctional Au NPs-polydopamine-polyvinylidene fluoride membrane chips as probe for enrichment and rapid detection of organic contaminants. *Talanta* **2018,** *181*, 340-345.

37.   Movafaghi, S.; Cackovic, M. D.; Wang, W.; Vahabi, H.; Pendurthi, A.; Henry, C. S.; Kota, A. K., Superomniphobic Papers for On-Paper pH Sensors. *Adv. Mater. Interfaces* **2019,** *6* (13), 1900232.

38.   Vahabi, H.; Wang, W.; Davies, S.; Mabry, J. M.; Kota, A. K., Coalescence-induced self-propulsion of droplets on superomniphobic surfaces. *ACS Appl. Mater.* **2017,** *9* (34), 29328-29336.

39.   Vahabi, H.; Wang, W.; Mabry, J. M.; Kota, A. K., Coalescence-induced jumping of droplets on superomniphobic surfaces with macrotexture. *Sci. Adv.* **2018,** *4* (11), 3488.

40.   Wang, W.; Vahabi, H.; Movafaghi, S.; Kota, A. K., Superomniphobic surfaces with improved mechanical durability: Synergy of hierarchical texture and mechanical interlocking. *Adv. Mater. Interfaces* **2019,** *6* (18), 1900538.

41.   Wang, W.; Du, X.; Vahabi, H.; Zhao, S.; Yin, Y.; Kota, A. K.; Tong, T., Trade-off in membrane distillation with monolithic omniphobic membranes. *Nat. Commun.* **2019,** *10* (1), 3220.

42.   Channon, R. B.; Nguyen, M. P.; Henry, C. S.; Dandy, D. S., Multilayered Microfluidic Paper-Based Devices: Characterization, Modeling, and Perspectives. *Anal. Chem.* **2019,** *91* (14), 8966-8972.

43.   Lin, D.; He, F.; Liao, Y.; Lin, J.; Liu, C.; Song, J.; Cheng, Y., Three-dimensional staggered herringbone mixer fabricated by femtosecond laser direct writing. *J. Opt.* **2013,** *15* (2), 025601-025601.

44.   Channon, R. B.; Joseph, M. B.; Bitziou, E.; Bristow, A. W. T.; Ray, A. D.; Macpherson, J. V., Electrochemical Flow Injection Analysis of Hydrazine in an Excess of an Active Pharmaceutical Ingredient: Achieving Pharmaceutical Detection Limits Electrochemically. *Anal. Chem.* **2015,** *87* (19), 10064-10071.

45.   Denkhaus, E.; Salnikow, K., Nickel essentiality, toxicity, and carcinogenicity. *Crit. Rev. Oncol. Hemat.* **2002,** *42*, 35-56.

46.   Mentele, M. M.; Cunningham, J.; Koehler, K.; Volckens, J.; Henry, C. S., Microfluidic Paper-Based Analytical Device for Particulate Metals. *Anal. Chem.* **2012,** *84* (10), 4474-4480.

47.   Cate, D. M.; Noblitt, S. D.; Volckens, J.; Henry, C. S., Multiplexed paper analytical device for quantification of metals using distance-based detection. *Lab Chip* **2015,** *15* (13), 2808-2818.

48.   Hempen, C.; Karst, U., Labeling strategies for bioassays. *Anal. Bioanal. Chem.* **2006,** *384* (3), 572-583.

49.   Ugarova, N. N.; Lebedeva, O. V.; Berezin, I. V., Horseradish peroxidase catalysis I. Steady-state kinetics of peroxidase-catalyzed individual and co-oxidation of potassium ferrocyanide and o-dianisidine by hydrogen peroxide. *J. Mol. Catal.* **1981,** *13* (2), 215-225.

50.   Lago, S.; Nadai, M.; Rossetto, M.; Richter, S. N., Surface Plasmon Resonance kinetic analysis of the interaction between G-quadruplex nucleic acids and an anti-G-quadruplex monoclonal antibody. *BBA-Gen. Subjects* **2018,** *1862* (6), 1276-1282.

51.   Lee, J. N.; Park, C.; Whitesides, G. M., Solvent Compatibility of Poly(dimethylsiloxane)-Based Microfluidic Devices. *Anal. Chem.* **2003,** *75*, 6544-6554.

52.   Altundemir, S.; Uguz, A.; Ulgen, K., A review on wax printed microfluidic paper-based devices for international health. *Biomicrofluidics* **2017,** *11* (4), 1-26.

53.   Stroock, A. D.; McGraw, G. J., Investigation of the staggered herringbone mixer with a simple analytical model. *Phil. Trans. R. Soc. Lond. A* **2004,** *362*, 971-986.

54.   Hama, B.; Mahajan, G.; Fodor, P. S.; Kaufman, M.; Kothapalli, C. R., Evolution of mixing in a microfluidic reverse-staggered herringbone micromixer. *Microfluid. Nanofluid.* **2018,** *22* (5), 54.

55.   Hossain, S.; Husain, A.; Kim, K.-Y., Shape optimization of a micromixer with staggered-herringbone grooves patterned on opposite walls. *Chem. Eng. J.* **2010,** *162* (2), 730-737.

CHAPTER 5: COLORIMETRIC PAPER-BASED ANALYTICAL DEVICE FOR PFOS
DETECTION

Per- and polyfluoroalkyl substances (PFAS) are a class of environmental contaminants of emerging concern due to being highly persistent, bioaccumulative, ubiquitous, and potentially toxic. Multiple instrument-based methods exist for sensitive and somewhat selective detection of PFAS, but they suffer from high costs, laboratory equipment requirements, and the need for highly trained lab personnel. Since PFAS can cause adverse human health impacts, there is a need for fast, inexpensive, robust, and portable methods to detect PFAS outside the laboratory. This would enable identification of concentrated pollution sources as well as monitor contamination. Here we present a paper-based analytical device (PAD) for detection of perfluorooctane sulfonate (PFOS) which is one of the most widespread PFAS. Based on a color change from the ion-pairing between PFOS and methylene green, PFOS can be detected with the naked eye by measuring the diameter of the purple circle that is formed by the ion pair. A limit of detection (LOD) of 10 ppm was obtained. In this paper, we optimized the PAD and then evaluated it for interferences from perfluorooctanoic acid (PFOA) and surfactants commonly found in environmental samples as well as other potential co-existing ions. With the help of pretreatment and/or preconcentration steps, this PAD can serve as a tool to identify areas of high PFOS contamination. This work will be submitted for review to *ACS ES&T Water* pending analysis of real samples.[1] Josi Beck, my high school research assistant, helped with most of the experiments.

5.1 Introduction

Per- and polyfluoroalkyl substances (PFAS) have become known as contaminants of emerging concern.[2] The class includes over 5,000 different compounds that have a common fluoro-

carbon backbone with sulfonic acid or carboxylic acid head groups. The unique properties of the C-F bond produce water and oil resistance, which are beneficial in a variety of industries and products: non-stick pans, cleaning products, aqueous film-forming foams (AFFF), and stain repellents.[3] However, during the manufacture, use, and disposal of these products, PFAS are released into the environment where they bioaccumulate.[4, 5] The same properties that make them useful for industrial purposes unfortunately also make PFAS resistant to typical degradation pathways like photolysis[6], reductive defluorination,[7] and biodegradation.[8] For this reason, PFAS are known as "forever chemicals." PFAS have spread all over the world with continuously increasing concentrations —making their way into drinking water, surface water, soils, wildlife, plants, and the atmosphere.[9-15] In humans, PFAS have been linked to a variety of adverse health effects, including prostate and kidney cancer, immune effects, thyroid disease, and fetal development effects.[12, 16-19] It is estimated that 54-83% of the US population is exposed to PFAS contamination in their drinking water.[20] Thus, a rapid and cost-effective PFAS sensor is needed for rapid at-home and on-site uses.

Perfluorooctane sulfonate (PFOS) and perfluorooctanoic acid (PFOA) are the two most prevalent and thus widely studied PFAS. The United States Environmental Protection Agency (U.S. EPA) has set a health advisory level for lifetime exposure of PFOS and/or PFOA at 70 parts per trillion (ppt) in drinking water.[21] Despite this guideline, PFOS and PFOA levels of up to 3000 times the lifetime advisory level have been reported in drinking water in Colorado, North Carolina, and many other locations across the US.[20, 22-24] The current gold standard method to detect PFAS in drinking water is the EPA Method 537, which can quantify up to 25 PFAS compounds in drinking water. It calls for a polystyrene-divinylbenzene (SDVB) solid-phase extraction (SPE) step to concentrate the sample followed by analysis with an LC-MS/MS fitted with a reverse-phase C-

18 column.[25, 26] While the method is sensitive and selective with limits of detection (LOD) ranging 0.71 – 2.8 ppt, it suffers from instrument and power requirements, costs of $300-$600 per sample, and hours of analysis time.[27] This is not ideal for cost-effective and rapid detection of PFAS in remote locations or for near real-time monitoring.

In recent years, efforts have focused on developing faster, less expensive, and more easily usable sensors for PFAS detection that would enable more widespread sampling and testing for common PFAS.[28, 29] These include optical sensors based on small molecule complexation, nanoparticles, molecularly imprinted polymers (MIPs), optical fibers, and immunosensors.[28] Sensors with detection by colorimetry are ideal for field-based applications as they do not require much external instrumentation for detection. A color change can be quantified by the naked eye (semi-quantitative) a smartphone, or portable UV-Vis. Small molecules like ethyl violet[30] and methylene blue[31] as well as modified nanoparticles[32-34] have been applied towards colorimetric PFAS detection. Currently, these aqueous colorimetric reactions are performed as solution-based assays in the lab, but this approach doesn't allow for high-throughput and portable analysis.

The Naidu group in Australia has developed the astkCARE kit — the only test kit that is currently commercially available for PFOA detection.[30, 35] The process to use the kit involves adding a sample to the included reagents to perform liquid-liquid extraction, which purifies the sample by eliminating interferences. Then, after the addition of ethyl violet which complexes with the PFAS, a smartphone is used to read the color of the resulting ion pair. The smartphone compares the color to a built-in calibration curve that provides results in minutes. While the method is rather straightforward to use, there are still multiple steps involved, and running multiple samples at once would require time and space.

Paper-based analytical devices (PADs) have gained significant popularity in recent years due to their low cost, ease of manufacture and disposal, and wide range of applications. For environmental applications, heavy metals, pesticides, and particulate matter have been detected.[36] The paper platform is small and light, making it easy to perform analyses outside the laboratory. Colorimetric PADs in particular are ideal because analysis can be performed by the naked eye or a smartphone, eliminating the need for expensive instrumentation.[37] Here we present a colorimetric PAD for PFOS detection. In addition to being easy to use, the device allows for fast, robust, and quantitative detection of PFAS in aqueous environmental samples. While the LOD (10 ppm) of the device is currently above the recommended level for drinking water (70 ppt),[21] this device is an important step towards detecting PFOS in the field without any instrumentation.

5.2 Materials and Methods

5.2.1 Chemicals and Materials

All solutions were prepared using deionized (DI) water from a Milli-Q system (Merck Millipore Darmstadt, Germany, R 18.2 MΩ cm^{-1}). Methylene green zinc chloride double salt (MG), 3-(N,N-dimethyloctylammonio)propanesulfonate (8DAPS), 3-(decyldimethylammonio)-propanesulfonate (10DAPS), sodium dodecyl sulfate (SDS), sodium dodecylbenzene sulfonate (SDBS), and perfluorooctanoic acid (PFOA) sodium chloride, magnesium chloride, calcium chloride, sodium nitrite, sodium fluoride, potassium phosphate monobasic, copper(II) sulfate pentahydrate, and nickel(II) sulfate hexahydrate were acquired from Sigma-Aldrich (St. Louis, MO, USA). Phosphoric acid and glacial acetic were obtained from EMD Millipore (St. Louis, MO, USA). Hydrochloric acid, boric acid, sodium sulfate, sodium nitrate, sodium carbonate, and lead(II) nitrate were obtained from Fisher Scientific (Waltham, MA, USA). Iron(II) sulfate

heptahydrate and iron(III) chloride hexahydrate were obtained from Mallinckrodt (St. Louis, MO, USA). Potassium perfluorooctanesulfonate (PFOS) was obtained from Synquest Laboratories (Alachua, FL, USA). All chemicals were used without further purification. All PFOS solutions were prepared in DI water unless otherwise noted.

Whatman Grade 4 filter paper was purchased from GE Healthcare UK Limited (Buckinghamshire, U.K.). Universal 3M UNV84630 lamination (3 mil) was purchased from Amazon.

5.2.2 Device Fabrication

Device fabrication has been described in detail previously.[38] The devices were designed in CorelDRAW software. A 60 mm circle was printed on Whatman Grade 4 filter paper using a Xerox ColorQube 8570DN. The wax was melted into the paper using a hot plate at 150°C for 90s, forming a three-dimensional hydrophobic barrier. A piece of aluminum (4 x 5 x 1/8") was placed on top of the filter paper to ensure the paper kept uniform contact with the hot plate. The paper devices were dipped in a solution of methylene green (150 ppm in 0.7% hydrochloric acid + 1 g KH_2PO_4) and then dried in an oven at 65°C for 20 min. A 2 mm sample inlet was cut out of lamination sheets (3 mil) using an Epilog Zing CO2 laser cutter. The dried paper layers were sandwiched between a top lamination sheet with a cut-out sample inlet (2 mm) and a full sheet on the back. The paper devices were laminated at 230°C using a TruLam laminator (TL-320B). A sample of PFOS or other sample solution (300 µL) was added to the sample inlet. After complete device saturation (~15 min), the devices were scanned using a scanner (Xerox DocuMate 3220) and saved as a JPEG.

5.2.3 Image Analysis

Images were analyzed in ImageJ (NIH).[39] A profile of each image was obtained using the line profile function. This data was used to find the purple circle and calculate its diameter in R.[40] For experiments that evaluated the intensity of the purple color formed, the mean value was obtained from the red, green, and blue color channels. Details are found in Appendix 6.

5.2.4 Reaction Stability

The ionic strength of a 0.2 mM PFOS solution was adjusted with 0 – 2.0 M sodium chloride (NaCl). The same device preparation as described above was used.

The effect of pH on the reaction was studied by preparing 0.2 mM PFOS in Britton Robinson buffer at pHs ranging from 2 – 12. The buffer was prepared by mixing equal parts of 40 mM boric acid, 40 mM phosphoric acid, and 40 mM acetic acid. The pH of the buffer was adjusted with 1 M NaOH. Devices were prepared according to the procedure described above and then scanned after sample addition (300 μL).

5.2.5 Effects of surfactants and other ions

Perfluorooctanoic acid (PFOA), sodium dodecyl sulfate (SDS), sodium dodecylbenzene sulfonate (SDBS), 3-(N,N-dimethyloctylammonio)-propanesulfonate (8DAPS), and 3-(decyldimethylammonio)-propanesulfonate (10DAPS) were evaluated for interference with PFOS detection. Solutions of 0.2 mM of each surfactant alone in water were tested as well as 1:1 solutions of surfactant + PFOS (0.2 mM) in water.

5.2.6 Signal Stability Study

Devices were fabricated as described above (60 mm circle). After the addition of 300 µL PFOS (100 ppm), devices were scanned at multiple time points following the normal protocol. In between scanning, devices were set on the benchtop at room temperature.

5.2.7 Device Storage Condition Study

Devices were fabricated as described above (45 mm circle). Light and temperature storage conditions were evaluated over time: room temperature (25°C) vs fridge (4°C) vs freezer (-24°C) and light vs dark. Devices were prepared as described above, up through the lamination step. Devices kept in the dark were wrapped in aluminum foil and sealed in a Ziplock back. Devices exposed to light were kept in Ziplock bags. At various time points (1 day, 3 days, 7 days, 1 month), devices were removed and 150 µL of 200 ppm PFOS was added. The scanning procedure and image analysis were followed as described above.

5.3 Results and Discussion

5.3.1 Assay Principle

PFAS form colored ion pairs with cationic dyes like methylene green (MG) that can be optically quantified (Figure 5.1A). To perform the assay using a PAD, devices were fabricated by printing a circle design on Whatman filter paper using a printer where the ink is formulated out of
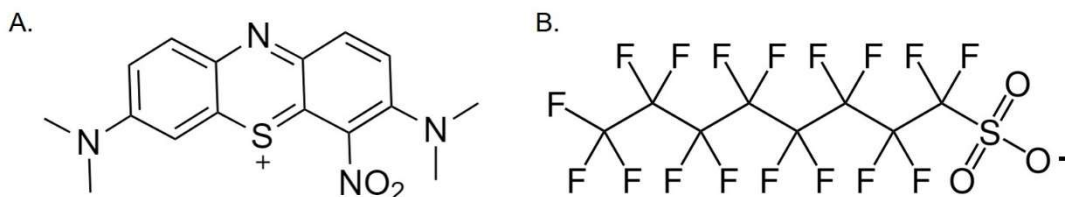

Figure 5.1 A. Structure of methylene green (MG). B. Structure of perfluorooctane sulfonate (PFOS).

wax. When the paper is set on a hot plate, the wax penetrates the paper, forming a hydrophobic

barrier that directs and controls fluid flow. The paper is laminated (with a cut-out sample inlet) to

prevent sample evaporation and protect the device from humidity changes (Figure A6.1).

After reagent optimization with a spot test (Figure A6.2), the MG-PFOS reaction was

converted to a radial detection device. With the ion pairing of MG and PFOS, a purple circle forms,

the diameter of which can be measured using a ruler or calipers. In our studies, the devices were

scanned using a desktop scanner. Image analysis was performed in ImageJ to obtain a line profile

of each image to objectively calculate the diameter of purple color formation (Figure A6.3). The

calibration curve shows the relationship between purple spot diameter and concentration of PFOS

(Figure 5.2). The curve is non-linear due to two factors: 1) evaporation at the sample inlet and 2)

mass transfer limitations of the device where analyte ions at the sample front are depleted (i.e.,

have formed an ion pair with methylene green) before reaching the outer edges of the device.[38] A

visual limit of detection of 10 ppm was determined (Figure 5.2).
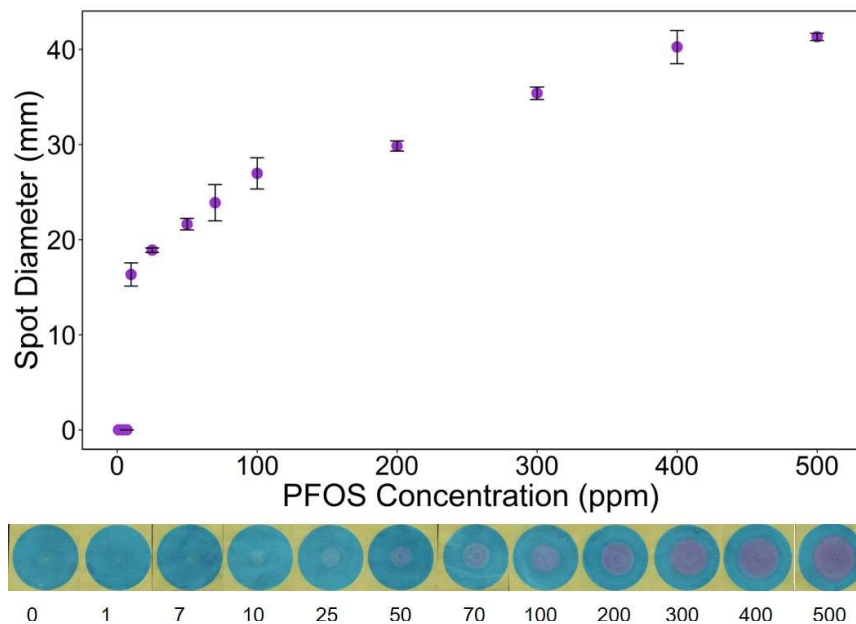
Figure 5.2 Calibration curve of spot diameter vs PFOS concentration (ppm). Each circle (60 mm in diameter) is prepared with 150 ppm methylene green. After lamination, 300 μL of PFOS sample is added. Each point on the plot spot represents 3 replicates and the error bars are one standard deviation around the mean.

5.3.2 Reaction Stability

Effect of ionic strength

As the ion pairing between PFOS and MG is dependent on electrostatic interactions, the effect of ionic strength was tested by preparing a 100 ppm solution of PFOS in various concentrations of NaCl (0 – 2.0 M). Above 1.0 M NaCl, there was a significant decrease in spot diameter—to the point where it is indistinguishable from the blank (Figure 5.3A, A6.4). This is likely because the sodium and chloride ions interfere with the electrostatic interaction between MG and PFOS. As seawater has a salt concentration of 0.5 M, detection of PFOS in seawater would be possible without affecting the PFOS response.[41]

Effect of pH

Solutions of 100 ppm PFOS were prepared in Britton-Robinson buffer (40 mM) at multiple pHs in the range of 2 – 12. At pH $\leq$ 4 and pH $\geq$ 8, the spot diameter was significantly decreased (Figure 5.3B, A6.5). This should not be a problem in real samples as drinking water will be within pH 6.5 – 8.5.[42] Environmental samples can have pHs outside that range,[43] but the sample can be neutralized to pH 7 with HCl or NaOH without impacting the assay. A test kit could include a dried buffer to which the sample would be added, ensuring consistent pH for each analysis.[38]
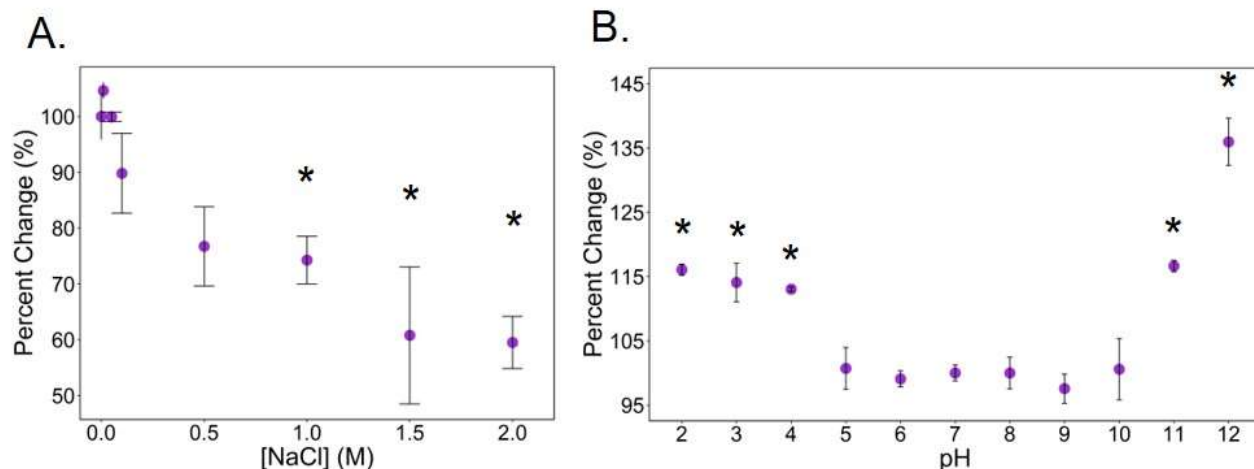
Figure 5.3 A. Effect of increasing ionic strength on spot diameter. Ionic strength was adjusted by preparing 100 ppm PFOS in different concentrations of NaCl. Stars (*) indicate significant different between that ionic strength and the control ([NaCl] = 0 M) ($p < 0.05$, n = 3). B. Effect of increasing pH. Solutions of 100 ppm PFOS were prepared in 40 mM Britton-Robinson buffer and pH was adjusted with 1 M NaOH. Stars (*) indicate significant difference between the pH and the control (PFOS in water, pH 7) ($p < 0.05$, n = 3).

5.3.3 Effects of surfactants and other ions

Since methylene green is a cationic dye that can form ion pairs with other anionic surfactants, the selectivity of the presented method was evaluated with solutions of only surfactant and also 1:1 surfactant + PFOS. Perfluorooctanoic acid (PFOA), a fluorinated surfactant similar in structure to PFOS, did not have a significant effect on PFOS detection (Figure 5.4). When tested on its own, PFOA did not form a purple circle with methylene green on paper like PFOS does (Figure A6.6). This is likely due to the difference in hydrophobicity between PFOA and PFOS: PFOS is more hydrophobic (solubility in water = 570 mg L^{-1} for PFOS vs 4340 mg L^{-1} for PFOA[44]), so the immiscible ion pair with PFOS is retained on the paper and can be measured whereas the less hydrophobic PFOA travels with the solvent front. In addition, the sulfonic acid headgroup of PFOS is a stronger acid (pKa = 1.0) than the carboxylic acid headgroup of PFOA (pKa = 1.30), so PFOS would form a stronger ion pair with methylene green.[45, 46]

Other non-fluorinated surfactants had little interaction on their own. SDBS and SDS on their own did produce a signal, but the circle did not have the same purple intensity as PFOS (Figure A6.7). In the presence of PFOS combined with surfactant, a larger circle was produced (98 – 142%) (Figure 5.4). 8DAPS, 10DAPS, SDBS, and SDS all have the same head group as PFOS. Since the ion pairing between MG and PFOS is due to the sulfonic acid headgroup interacting with the cationic dye, the presence of both the surfactant and PFOS increased the size of the purple circle.[47] These surfactant interferences can be eliminated by adding excess barium to the sample which can then be removed by cation exchange resin.[48]
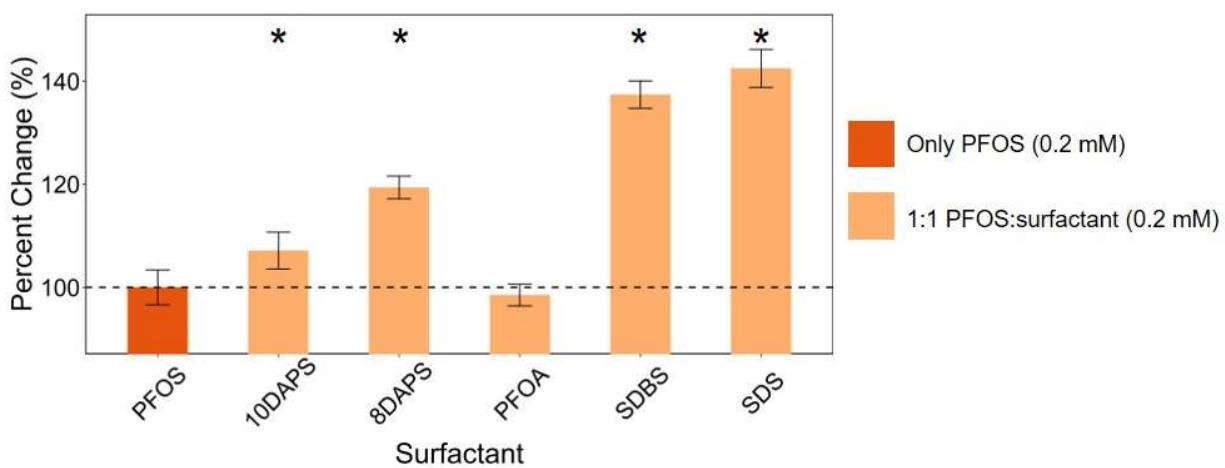
Figure 5.4 A. Effect of surfactant interference on PFOS detection. Aliquots of 0.2 mM PFOS (100 ppm) + 0.2 mM surfactant were added to 60 mm devices treated with 150 ppm methylene green. Stars (*) indicate a significant difference between surfactant + PFOS and only PFOS ($p < 0.05$, $n = 3$).

The impacts of other potentially co-existing substances on the detection of PFOS were also studied. Nine common environmental cations and anions were tested both individually (20 mM) and with PFOS (at 1x and 10x ratios). All results were compared to a control solution containing only PFOS as well as a negative control of a blank of deionized water. The response of 0.2 mM sulfate by itself was very similar to the response of only 0.2 mM PFOS (100 ppm), likely due to the same complexation mechanism of the sulfonate headgroup and MG (Figure A6.8). Carbonate

on its own also produced a purple response. Without the hydrophobic C-F tail, it is likely that carbonate acts as a moderately strong base that can still form a purple complex with MG (Figure A6.8). At 1:1 ion:PFOS (0.2 mM), there was a significant change in the diameter of the purple circle in the presence of some of ions in the range of 88 – 109 % (Figure 5.5). At 10:1 ion:PFOS (2.0 mM ion), the response was eliminated, and no purple circle appeared (Figure A6.8). While this is concerning, the concentrations of ions tested were higher than expected or allowed in environmental samples --- most ions are permitted at <1 mM.[42] Despite having an effect on PFOS detection at high concentrations, the ions can be removed by a filter-based cation exchange membrane.[48]
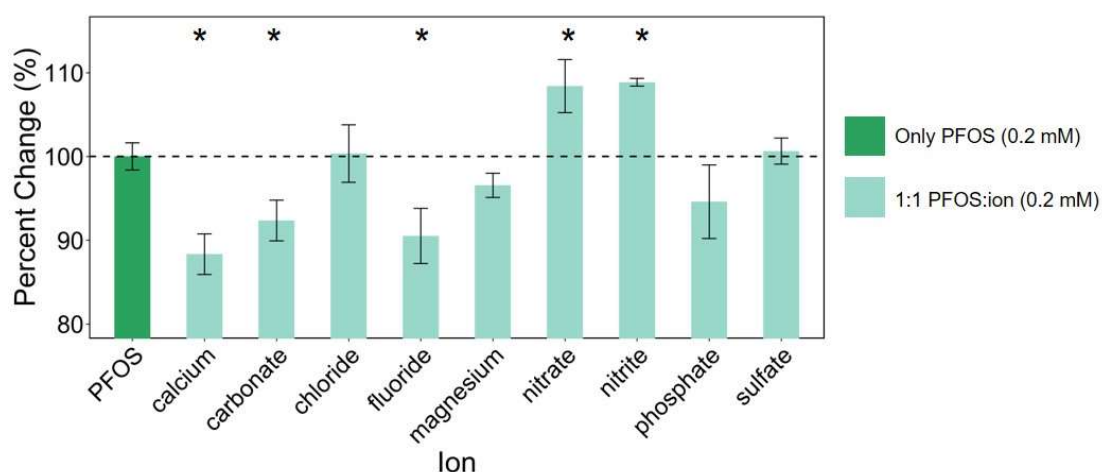
Figure 5.5 Effect of co-existing substances on PFOS detection. Aliquots of 0.2 mM PFOS (100 ppm) + 0.2 mM ion were added to 60 mm devices treated with 150 ppm methylene green. Stars (*) indicate a significant difference between ion + PFOS and only PFOS (p < 0.05, n = 3).

Heavy metal contamination is common in environmental samples,[38] so the effects of Cu(II), Fe(II), Fe(III), Ni(II), and Pb(II) on PFOS detection were studied (Figure A6.9). As iron is commonly found in the environment, both Fe(II) and Fe(III) were tested. At 1:1, there was not a significant difference between iron + PFOS and only PFOS (Figure 5.6). All other heavy metal + PFOS solutions had some decrease in signal due to interference from the heavy metal (50 – 95%, depending on the metal). As with the other potentially co-existing ions above, the decrease in the
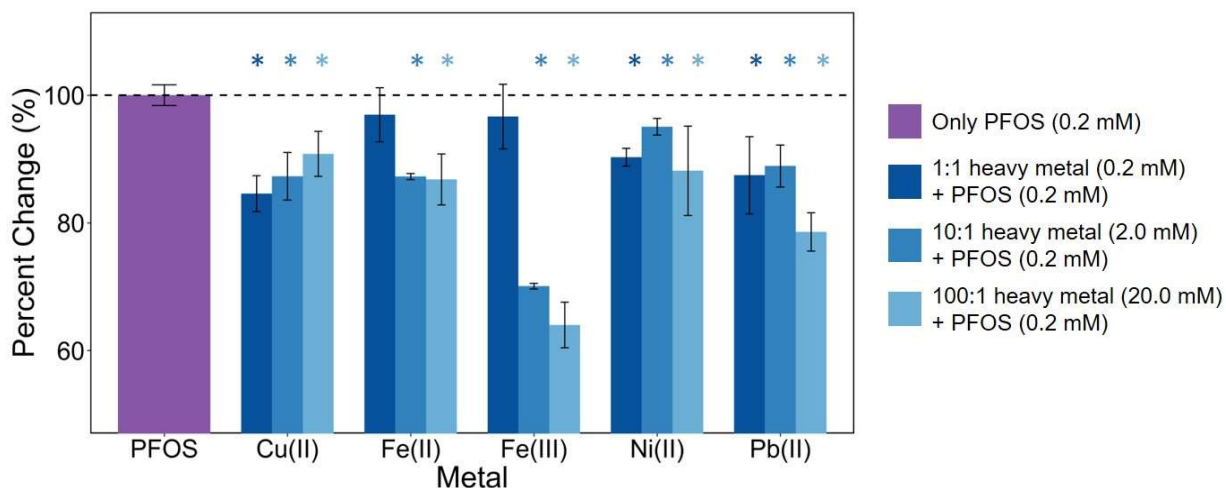
Figure 5.6 Effect of heavy metals on PFOS detection. Aliquots of 0.2 mM PFOS + heavy metal (0.2 mM, 2.0 mM, 20 mM) were added to 60 mm devices. Stars (*) indicate a significant difference between heavy metal + PFOS and only PFOS ($p < 0.05$, n = 3).

size of the purple circle is likely from interference with the electrostatic interaction between PFOS and MG. Fe(III) tends to form strong metal-organo complexes,[49] which would support why the Fe(III) resulted in the smallest diameter. As with the other coexisting ions above, the concentrations tested (0.2 mM, 2.0 mM, 20 mM) are higher than what is allowed in drinking water.[42] In environmental samples, higher concentrations could be found so the ratio of heavy metal to PFOS is relevant.[50] The effect of heavy metal interference can be removed by cation exchange resin.[51]

5.3.4 Signal Stability

The signal stability after the addition of PFOS was evaluated. In some instances, reading the results might occur well after sample addition. Devices were prepared with a 100 ppm aliquot (300 µL) of PFOS. After flow stopped, as indicated by a fully saturated circle (15 min), the devices were scanned multiple times. In between scans, the devices were exposed to ambient light at room temperature for up to 4 h. After 1 h, there was a significant decrease in the purple color intensity (Figure 5.7A, S10). However, the spot diameter was consistent 4 h after the addition of PFOS

despite the decrease in purple color intensity (Figure 5.7B). Still, it is recommended that results be recorded as soon as possible after sample addition.
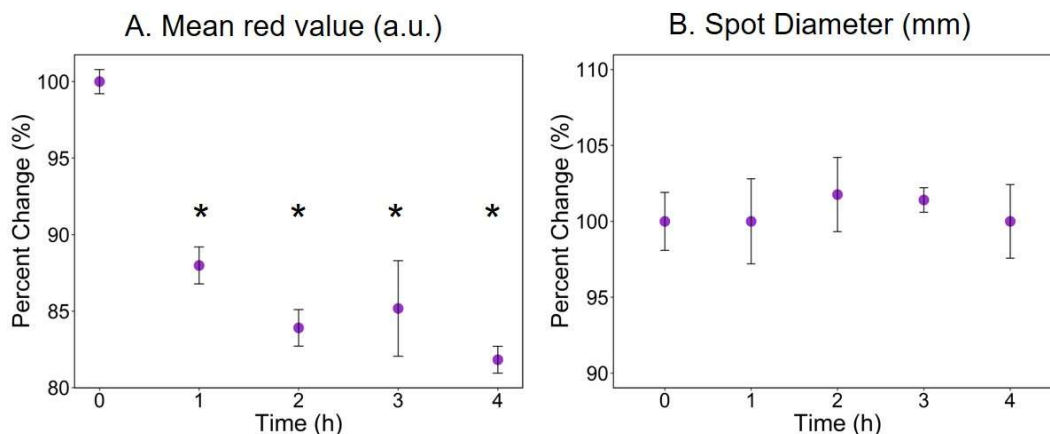
Figure 5.7 Percent change in mean red value (A.) and spot diameter (B.) of purple circle over time after addition of 100 ppm PFOS. Stars (*) indicate a significant different between the control (t = 0) and later time points ($p <$ 0.05, n = 3). The mean red value of the purple circle was 154 at t = 0.

5.3.5 Device Storage Condition Stability Study

The stability of prepared devices was evaluated under different storage conditions: light vs dark and room temperature vs fridge vs freezer over 1 month. Devices kept in the dark were wrapped in aluminum foil and stored in a Ziplock bag at the different temperatures: freezer (-24°C), fridge (4°C), room temperature (25°C). At each time point, devices were removed and an aliquot of PFOS (200 ppm) was added. Under all conditions except RT dark, the intensity of the purple circle (measured as mean red value) decreased significantly compared to the control (day 0, $p < 0.05$) (Figure 5.8A). Despite the decreasing intensity over time, the diameter of the purple circles remained constant under all conditions (Figure 5.8B). It is recommended to store the devices in the dark (using a Mylar bag) to prevent degradation due to light and/or humidity.
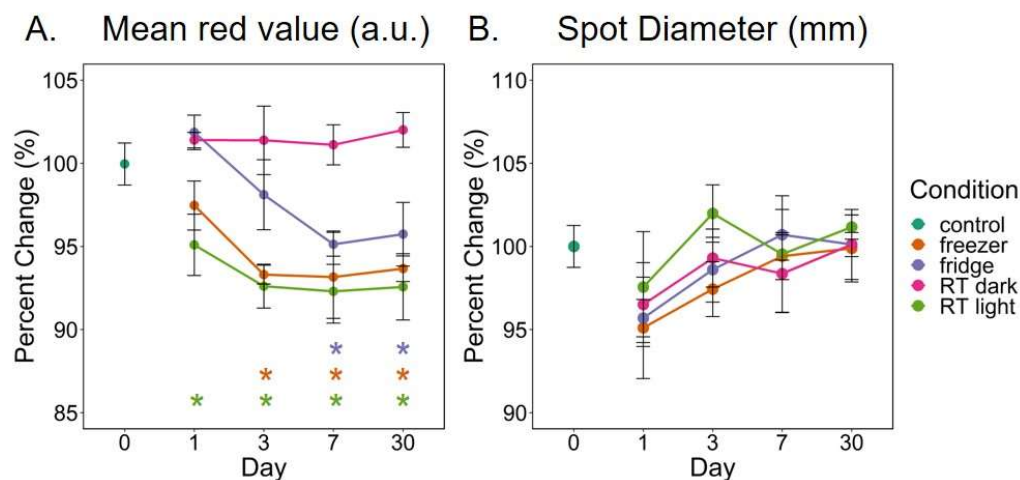
Figure 5.8 A. Percent change of the mean red value of the purple circle over time by different storage conditions. The mean red value of the control on Day = 0 was 154. B. Spot diameter (200 ppm PFOS) over time. Stars (*) indicate a significant different between that day and the control (day 0) for each condition by color ($p < 0.05$, $n = 3$). Conditions: freezer (-24°C), fridge (4°C), RT (room temperature, 25°C).

5.4 Conclusion

A paper-based analytical device has been presented for the detection of PFOS in simulated environmental samples. This approach achieves similar detection limits (10 ppm) to other colorimetric assays for PFOS in much less time (<15 min), cost (< $1), and user steps.[31, 52] To improve the LOD and enable the measurement of ppb levels of PFOS, a sample preconcentration step like SPE should be used.[53] Fluoro-SPE, a technique developed for concentrating and separating PFAS from environmental samples, can be used.[53] With the addition of traditional and fluoro-SPE, a 1000-fold sample enrichment can be obtained, lowering the LOD to 10 ppb. Each of these SPE steps involves a vacuum pump and manifold which is not ideal for in-field analysis, future work should focus on incorporating a concentration step into the PAD to maintain portability. Future work will include testing real samples as well as optimizing the device fabrication to include inkjet printing the methylene green on the paper. While the LOD is still relatively high for detection of PFOS in drinking water samples, this method is a first step towards a paper-based device for PFOS detection at heavily polluted military or industrial sites.

REFERENCES

1.   Menger, R. F.; Beck, J. J.; Borch, T.; Henry, C. S., Colorimetric paper-based analytical device for PFOS detection. submitted to *ACS ES&T Water,* **2021**.
2.   Technical Fact Sheet - Perfluorooctane Sulfonate (PFOS) and Perfluorooctanoic Acid (PFOA). United States Environmental Protection Agency: 2017.
3.   Prevedouros, K.; Cousins, I. T.; Buck, R. C.; Korzeniowski, S. H., Sources, Fate and Transport of Perfluorocarboxylates. *Environ. Sci. Technol.* **2006,** *40* (1), 32-44.
4.   Fujii, S.; Polprasert, C.; Tanaka, S.; Lien, N. P. H.; Qiu, Y., New POPs in the water environment: distribution, bioaccumulation and treatment of perfluorinated compounds - a review paper. *J. Water Supply Res. T.* **2007,** *56* (5), 313-326.
5.   Sharifan, H.; Bagheri, M.; Wang, D.; Burken, J. G.; Higgins, C. P.; Liang, Y.; Liu, J.; Schaefer, C. E.; Blotevogel, J., Fate and transport of per- and polyfluoroalkyl substances (PFASs) in the vadose zone. *Sci. Total Environ.* **2021**, 145427.
6.   Vaalgamaa, S.; Vähätalo, A. V.; Perkola, N.; Huhtala, S., Photochemical reactivity of perfluorooctanoic acid (PFOA) in conditions representing surface water. *Sci. Total Environ.* **2011,** *409* (16), 3043-3048.
7.   Blotevogel, J.; Giraud, R. J.; Borch, T., Reductive defluorination of perfluorooctanoic acid by zero-valent iron and zinc: A DFT-based kinetic model. *Chem. Eng. J.* **2018,** *335*, 248-254.
8.   Liou, J. S. C.; Szostek, B.; Derito, C. M.; Madsen, E. L., Investigating the biodegradability of perfluorooctanoic acid. *Chemosphere* **2010,** *80* (2), 176-183.
9.   Domingo, J. L.; Nadal, M., Per-and polyfluoroalkyl substances (PFASs) in food and human dietary intake: a review of the recent scientific literature. *J. Agric. Food Chem.* **2017,** *65* (3), 533-543.
10.   Hu, X. C.; Andrews, D. Q.; Lindstrom, A. B.; Bruton, T. A.; Schaider, L. A.; Grandjean, P.; Lohmann, R.; Carignan, C. C.; Blum, A.; Balan, S. A.; Higgins, C. P.; Sunderland, E. M., Detection of Poly- and Perfluoroalkyl Substances (PFASs) in U.S. Drinking Water Linked to Industrial Sites, Military Fire Training Areas, and Wastewater Treatment Plants. *Environ. Sci. Technol. Lett.* **2016,** *3* (10), 344-350.
11.   Smithwick, M.; Norstrom, R. J.; Mabury, S. A.; Solomon, K.; Evans, T. J.; Stirling, I.; Taylor, M. K.; Muir, D. C. G., Temporal Trends of Perfluoroalkyl Contaminants in Polar Bears (Ursus maritimus) from Two Locations in the North American Arctic, 1972-2002. *Environ. Sci. Technol.* **2006,** *40* (4), 1139-1143.
12.   Sunderland, E. M.; Hu, X. C.; Dassuncao, C.; Tokranov, A. K.; Wagner, C. C.; Allen, J. G., A review of the pathways of human exposure to poly- and perfluoroalkyl substances (PFASs) and present understanding of health effects. *J. Exposure Sci. Environ. Epidemiol.* **2019,** *29* (2), 131-147.
13.   Yamashita, N.; Kannan, K.; Taniyasu, S.; Horii, Y.; Okazawa, T.; Petrick, G.; Gamo, T., Analysis of perfluorinated acids at parts-per-quadrillion levels in seawater using liquid chromatography-tandem mass spectrometry. *Environ. Sci. Technol.* **2004,** *38* (21), 5522-8.
14.   Place, B. J.; Field, J. A., Identification of Novel Fluorochemicals in Aqueous Film-Forming Foams Used by the US Military. *Environ. Sci. Technol.* **2012,** *46* (13), 7120-7127.

15.   Rauert, C.; Shoieb, M.; Schuster, J. K.; Eng, A.; Harner, T., Atmospheric concentrations and trends of poly- and perfluoroalkyl substances (PFAS) and volatile methyl siloxanes (VMS) over 7 years of sampling in the Global Atmospheric Passive Sampling (GAPS) network. *Environ. Pollut.* **2018,** *238*, 94-102.

16.   Ahrens, L.; Bundschuh, M., Fate and effects of poly- and perfluoroalkyl substances in the aquatic environment: A review. *Environ. Toxicol. Chem.* **2014,** *33* (9), 1921-1929.

17.   Butenhoff, J. L.; Kennedy, G. L., Jr.; Frame, S. R.; O'Connor, J. C.; York, R. G., The reproductive toxicology of ammonium perfluorooctanoate (APFO) in the rat. *Toxicology* **2004,** *196* (1-2), 95-116.

18.   Hekster, F. M.; Laane, R. W. P. M.; De Voogt, P., Environmental and Toxicity Effects of Perfluoroalkylated Substances. *Rev. Environ. Contam. Toxicol.* **2003,** *179*, 99-121.

19.   Kudo, N.; Kawashima, Y., Toxicity and toxicokinetics of perfluorooctanoic acid in humans and animals. *J. Toxicol. Sci.* **2003,** *28* (2), 49-57.

20.   Andrews, D. Q.; Naidenko, O. V., Population-Wide Exposure to Per- and Polyfluoroalkyl Substances from Drinking Water in the United States. *Environ. Sci. Technol. Lett.* **2020,** *7* (12), 931-936.

21.   Lifetime Health Advisories and Health Effects Support Documents for Perfluorooctanoic Acid and Perfluorooctane Sulfonate. U.S. Environmental Protection Agency: Washington, D.C., 2016; Vol. 81.

22.   Finley, B., Colorado ramps up response to toxic "forever chemicals" after discovery of hot spots across metro Denver. *Denver Post* 2019.

23.   White, D., Denver Post Article on Colorado Response to High Levels of PFAS. Association of State Drinking Water Administrators: 2019.

24.   PFAS Contamination in the U.S. https://www.ewg.org/interactive-maps/2019_pfas_contamination/map/ (accessed November 1, 2020).

25.   Shoemaker, J. A.; Grimmett, P. E.; Boutin, B. K., Method 537: Determination of Selected Per- and Polyfluorinated Alkyl Substances in Drinking Water by Solid Phase Extraction and Liquid Chromatography/Tandem Mass Spectrometry (LC/MS/MS). U.S. Environmental Protection Agency, Office of Research and Development, National Exposure Research Laboratory: Washington, D.C., 2018.

26.   Shoemaker, J. A.; Tettenhorst, D. R., Method 537.1: Determination of selected per- and polyfluorinated alkyl substances in drinking water by solid phase extraction and liquid chromatography/tandem mass spectrometry (LC/MS/MS). U.S. Environmental Protection Agency, Office of Research and Development, National Center for Environmental Assessment: Washington, D.C., 2020.

27.   Laboratory Testing. https://www.michigan.gov/pfasresponse/0,9038,7-365-86704_90691---,00.html (accessed November 1, 2020).

28.   Menger, R. F.; Funk, E.; Henry, C. S.; Borch, T., Sensors for Detecting Per- and Polyfluoroalkyl Substances (PFAS): A Critical Review of Development Challenges, Current Sensors, and Commercialization Obstacles. *Chem. Eng. J.* **2021**, 129133.

29.   Naidu, R.; Nadebaum, P.; Fang, C.; Cousins, I.; Pennel, K.; Conder, J.; Newell, C.; Longpré, D.; Warner, S.; Crosbie, N., Per-and poly-fluoroalkyl substances (PFAS) current status and research needs. *Environ. Technol. Inno.* **2020**, 100915.

30.   Fang, C.; Zhang, X.; Dong, Z.; Wang, L.; Megharaj, M.; Naidu, R., Smartphone app-based/portable sensor for the detection of fluoro-surfactant PFOA. *Chemosphere* **2018,** *191*, 381-388.

31.   Coll, C.; Martínez-Máñez, R.; Marcos, M. D.; Sancenón, F.; Soto, J., A Simple Approach for the Selective and Sensitive Colorimetric Detection of Anionic Surfactants in Water. *Angew. Chem. Int. Ed.* **2007,** *46* (10), 1675-1678.

32.   Niu, H.; Wang, S.; Zhou, Z.; Ma, Y.; Ma, X.; Cai, Y., Sensitive Colorimetric Visualization of Perfluorinated Compounds Using Poly(ethylene glycol) and Perfluorinated Thiols Modified Gold Nanoparticles. *Anal. Chem.* **2014,** *86* (9), 4170-4177.

33.   Takayose, M.; Akamatsu, K.; Nawafune, H.; Murashima, T.; Matsui, J., Colorimetric detection of perfluorooctanoic acid (PFOA) utilizing polystyrene-modified gold nanoparticles. *Anal. Lett.* **2012,** *45* (18), 2856-2864.

34.   Liu, J.; Du, J.; Su, Y.; Zhao, H., A facile solvothermal synthesis of 3D magnetic MoS2/Fe3O4 nanocomposites with enhanced peroxidase-mimicking activity and colorimetric detection of perfluorooctane sulfonate. *Microchem. J.* **2019,** *149*, 104019.

35.   astkCARE: anionic surfactant detection. https://www.crccare.com/products-and-services/technologies/astkcare (accessed November 1, 2020).

36.   Kung, C.-T.; Hou, C.-Y.; Wang, Y.-N.; Fu, L.-M., Microfluidic paper-based analytical devices for environmental analysis of soil, air, ecology and river water. *Sens. Actuators B Chem.* **2019,** *301*, 126855.

37.   Ozer, T.; McMahon, C.; Henry, C. S., Advances in Paper-Based Analytical Devices. *Annu. Rev. Anal. Chem.* **2020,** *13*, 85-109.

38.   Hofstetter, J. C.; Wydallis, J. B.; Neymark, G.; Reilly, T. H.; Harrington, J.; Henry, C. S., Quantitative colorimetric paper analytical devices based on radial distance measurements for aqueous metal determination. *Analyst* **2018,** *143* (13), 3085-3090.

39.   Abràmoff, M. D.; Magalhães, P. J.; Ram, S. J., Image processing with ImageJ. *Biophotonics Int.* **2004,** *11* (7), 36-42.

40.   Team, R. C. *R: A language and environment for statistical computing*, R Foundation for Statistical Computing: Vienna, Austria, 2017.

41.   Low, S., Preliminary studies of seawater desalination using forward osmosis. *Desalination and Water Treatment* **2009,** *7* (1-3), 41-46.

42.   National Primary Drinking Water Regulations. In *816-F-09-004*, Agency, U. S. E. P., Ed. 2009.

43.   McLaughlin, M. C.; Borch, T.; McDevitt, B.; Warner, N. R.; Blotevogel, J., Water quality assessment downstream of oil and gas produced water discharges intended for beneficial reuse in arid regions. *Sci. Total Environ.* **2020,** *713*, 136607.

44.   Rahman, M. F.; Peldszus, S.; Anderson, W. B., Behaviour and fate of perfluoroalkyl and polyfluoroalkyl substances (PFASs) in drinking water treatment: A review. *Water Res.* **2014,** *50*, 318-340.

45.   Cheng, J.; Psillakis, E.; Hoffmann, M. R.; Colussi, A. J., Acid Dissociation versus Molecular Association of Perfluoroalkyl Oxoacids: Environmental Implications. *J. Phys. Chem. A* **2009,** *113* (29), 8152-8156.

46.   Kutsuna, S.; Hori, H., Experimental determination of Henry's law constant of perfluorooctanoic acid (PFOA) at 298K by means of an inert-gas stripping method with a helical plate. *Atmos. Environ.* **2008,** *42* (39), 8883-8892.

47.   Zhang, D.; Zeng, G.; Huang, J.; Bi, W.; Xie, G., Spectroscopic studies of dye-surfactant interactions with the co-existence of heavy metal ions for foam fractionation. *J. Environ. Sci.* **2012,** *24* (12), 2068-2074.

48.   Liang, J.; Deng, X.; Tan, K., An eosin Y-based "turn-on" fluorescent sensor for detection of perfluorooctane sulfonate. *Spectrochim. Acta, Part A* **2015**, *150*, 772-777.

49.   Daugherty, E. E.; Gilbert, B.; Nico, P. S.; Borch, T., Complexation and Redox Buffering of Iron(II) by Dissolved Organic Matter. *Environ. Sci. Technol.* **2017**, *51* (19), 11096-11104.

50.   Rodriguez-Freire, L.; Avasarala, S.; Ali, A.-M. S.; Agnew, D.; Hoover, J. H.; Artyushkova, K.; Latta, D. E.; Peterson, E. J.; Lewis, J.; Crossey, L. J.; Brearley, A. J.; Cerrato, J. M., Post Gold King Mine Spill Investigation of Metal Stability in Water and Sediments of the Animas River Watershed. *Environ. Sci. Technol.* **2016,** *50* (21), 11539-11548.

51.   Cheng, Z.; Dong, H.; Liang, J.; Zhang, F.; Chen, X.; Du, L.; Tan, K., Highly selective fluorescent visual detection of perfluorooctane sulfonate via blue fluorescent carbon dots and berberine chloride hydrate. *Spectrochim. Acta, Part A* **2019**, *207*, 262-269.

52.   Anionic Surfactants as MBAS. In *Standard Methods for the Examination of Water and Wastewater*, 20th ed.; Association, A. P. H.; Association, A. W. W.; Federation, W. E., Eds. American Public Health Association: Washington, DC, 1998; pp (5-47)-(5-49).

53.   Al Amin, M.; Sobhani, Z.; Chadalavada, S.; Naidu, R.; Fang, C., Smartphone-based / Fluoro-SPE for selective detection of PFAS at ppb level. *Environ. Technol. Inno.* **2020,** *18*, 100778.

CHAPTER 6: HIGH VOLUME RADIAL DETECTION PAPER-BASED DEVICE FOR
TRACE METAL ANALYSIS

Colorimetric microfluidic paper-based analytical devices (μPADs) are ideal for environmental analysis because of benefits of low cost, portability, and instrument-free analysis. However, a significant limitation of colorimetric μPADs is not being able to achieve low enough limits of detection (LOD) to match government regulations without extensive sample pretreatment. Current μPADs for heavy metal detection typically have LODs in the ppm range, but governmental allowances for heavy metals in drinking water are in the ppb range. Furthermore, most μPADs rely on measuring spot intensity to quantify analyte concentration. Radial devices offer fast detection where a colored circle is measured to determine analyte concentration. Here we present a new format for μPADs that combines a previously reported radial distance-based device for heavy metals with a high-volume system to improve detection limits. Multiple layers of filter paper and double-sided adhesive are stacked under the detection layer to accommodate a substantially increased sample volume. With the new format, the LOD for radial detection of copper was decreased by 2 orders of magnitude, to 5 ppb. This work has been submitted for publication in *ACS Sensors*.[1] Josi Beck, my high school research assistant, helped with most of the experiments. Our collaborators at Access Sensor Technologies, LLC., Kai Fuller and Thomas H. Reilly, provided the Cu detection cards.

6.1 Introduction

Microfluidic paper-based analytical devices (μPADs) have become popular as point-of-care and point-of-need devices with benefits of low cost, portability, ease of use, versatility, and fast results. Initially developed by the Whitesides group in 2007,[2] μPADs have been developed for

a variety of analytes including environmental contaminants, medical diagnostics, foodborne pathogens, and biological particles.[3, 4] Detection methods include colorimetry, fluorescence, or electrochemistry.[4, 5] Colorimetry is often favored for fast on-site analysis because a color change can be measured by the naked eye, or a smartphone can be used to aid in more quantitative analysis reducing the need for equipment like a spectrometer or potentiostat.[4, 6]

Colorimetric μPADs for heavy metals started as spot tests where a wax ring is printed on filter paper and a colorimetric reagent that is specific to the analyte of interest is added. After sample addition, changes in color hue and/or intensity can be measured.[7] While this is a simple approach, there is subjectivity in determining changes in the color and intensity on the paper by the user, even with help of a smartphone or scanner.[6] Changing the spot test to a distance-based format where the sample flows along a channel in the paper makes quantification more objective. In this format, the sample reacts with the colorimetric reagent and develops color until the analyte is consumed. For quantification, the color length is measured, eliminating the need to differentiate between minute differences in color hue or intensity.[8-10] A limitation of distance-based detection is that analysis can take 30 min – 1 hr depending on the size of the device.[8, 9, 11, 12] As the length of the channel increases, the assay time will increase since the sample flow rate decreases with distance traveled based on the Lucas-Washburn equation.[13] Radial devices fix this issue, as the sample flows radially outward in all directions at once. Results are achieved in <5-10 min.[14, 15]

A major limitation of μPADs in general, and especially colorimetric devices, is that LODs can be higher than levels found in samples.[5] For example, heavy metals are allowed at only very low concentrations (ppb range) in drinking water, so low LODs are desired.[16] While μPADs benefit from only needing small sample volumes (10 - 100 μL), this does not provide enough analyte molecules to make a signal that is detectable by the naked eye, like a color change.[6]

Increasing the sample capacity increases the moles of analyte that pass through the device and should increase signal. There has been some work to increase the volume capacity of µPADs, but those require an extra 3D-printed holder[17] or take almost 10 hours to flow through the device.[18]

µPADs are promising for on-site environmental analysis, especially for heavy metals. The devices are light, portable, and disposable, eliminating the need to transport water samples back to the lab for analysis by traditional instrumental analysis like atomic absorption spectroscopy (AAS) or inductively coupled plasma (ICP) coupled with mass spectrometry (MS).[19, 20] Kung *et al.* recently covered the newest developments in µPADs for environmental analysis.[21] Colorimetric devices for heavy metals have achieved limits of detection of 0.11 – 100 ppm.[8, 22-26] A radial µPAD has been developed for different heavy metals (Cu, Fe, Zn, Cd, Mn).[14, 27] The diameter is measured and correlated back to a calibration curve and thus the concentration of metal in the sample.[14] These cards have a limit of detection (LOD) of as low as 0.5 ppm, depending on the metal.

Here we demonstrate a new device format for the previously mentioned radial devices (single-layer device) for heavy metal detection. The new device consists of multiple layers of paper and tape (multi-layer device) to increase sample volume and reduce detection limits. The new format was compared against the existing single-layer device radial detection µPADs. While the assay time increased from 5 min to 1 hr, the LOD was decreased by 2 orders of magnitude, to 5 ppb.

6.2 Materials and Methods

6.2.1 Reagents

2-(N-morpholino)ethanesulfonic acid (MES), Zincon monosodium salt, and tetraoctylammonium bromide were obtained from Sigma-Aldrich (St. Louis, MO, USA). Copper

(II) nitrate ($Cu(NO_3)_2$) was obtained from Mallinckrodt (St. Louis, MO, USA) and used without further purification. Copper solutions were prepared in 150 mM MES buffer (pH 4.5) and used immediately. Ultrapure water (18.2 MΩ·cm) from a Mill-Q system was used to prepare solutions (Merck Millipore, Darmstadt, Germany).

6.2.2 Device Fabrication

Single-layer radial detection μPADs were fabricated as previously described.[14] Briefly, 44 black rings were printed on an 8.5 x 11'' sheet of Whatman 4 filter paper (GE Healthcare Life Sciences) with a Xerox ColorQube 8570 wax printer. The wax was melted through the depth of the paper by placing the paper in a 150°C oven for 4 min. An Epson R280 inkjet printer was modified to print a solution of 50 mM Zincon and 75 mM tetraoctylammonium bromide within the 44 mm wax circles.[14] The sheets of printed paper were laminated with 7 mil lamination sheets (Oregon Laminations Co.) that have a 2 mm sample inlet cut out with a CO_2 laser cutter (Trotec Speedy 100). Finished devices were cut into individual cards using the CO_2 laser cutter.

To modify the single-layer μPADs for the multi-layer configuration, the same process as described was followed up until the lamination step. For the multi-layer devices, devices were assembled as shown in Figures A7.1, A7.3, A7.4, or 6.2, layering pieces of filter paper or superabsorbent material and double-sided adhesive (DSA, 467MP, 3M), depending on the experiment. Devices were sealed by laminating the stack of paper and tape with 3 mil lamination sheets (Universal 3M UNV84630) with a 2 mm sample inlet cut out of it and centered on the reagent circle. An Eppendorf pipette was used to deliver the appropriate sample volume: 150 μL for single layer cards and 1000 μL for the multi-layer cards. The volume for the single-layer cards has been previously optimized.[14]

6.3 Results and Discussion

In order to reduce the LOD of a μPAD, the chemistry of the device could be modified to improve analyte:reagent interactions. Alternatively, to use existing cards, the form factor and/or sample volume can be increased, which allows for more analyte molecules to react. First, the size of the card was increased. While this did lower the LOD to 50 ppb, the form factor of an 8.5 x 11 in. sheet of paper is not conducive to field analysis. To increase the sample volume of a paper-based device without significantly increasing the size of the device, various superabsorbent materials were evaluated: Whatman 1 and Whatman 4 filter paper with absorbencies of ~ 27 and 35 μL cm^{-2}, respectively, and GelMax, Hexasorb, PIG, and Pride with absorbencies of $10 - 67$ mL cm^{-2} (data not shown). Devices were assembled by stacking a sheet of Whatman 4 filter paper (which is normally used to fabricate the single layer radial devices) that had a wax ring printed on it, double-sided adhesive, and then a square of superabsorbent material (Figure A7.1). The stack was sealed by lamination with a 2 mm sample inlet cut out. Initial trials with water containing blue dye were unsuccessful (Figure A7.2): once the dye reached the superabsorbent layer after flowing through the filter paper, fluid flow slowed down drastically, and the dye collected between the paper and the lamination. The flow rate in each of the materials was evaluated by timing how long it takes blue-colored water to flow through each material. Whatman 4 filter paper (W4) had the fastest flow rate, so this material was used in subsequent experiments (Figure 6.1). For clarity, error bars have been removed from the plot but can be found in Figure A7.3.
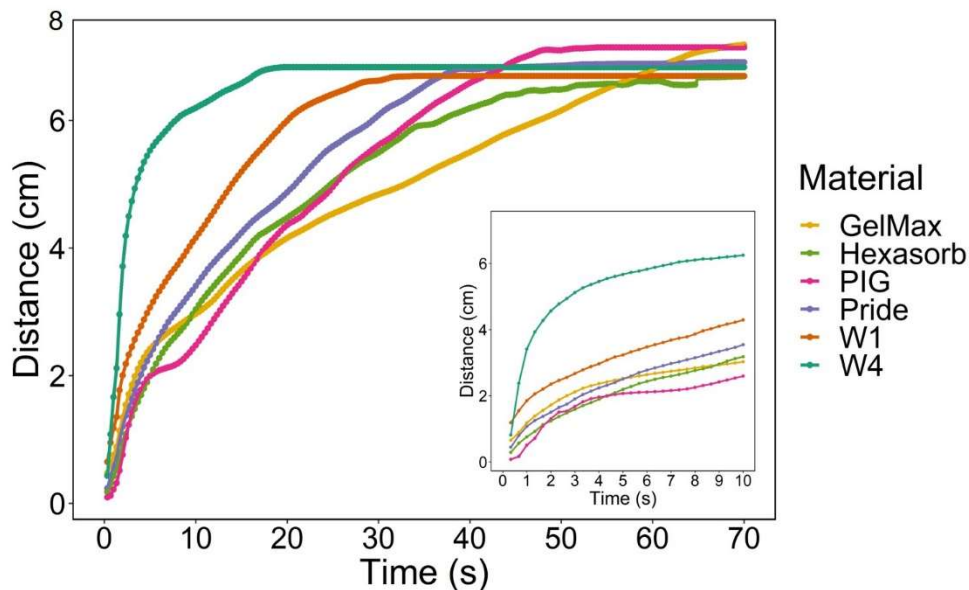
Figure 6.1 Evaluation of flow velocity in different materials. W1 = Whatman 1 filter paper, W4 = Whatman 4 filter paper. Each line is the average of 3 replicates. The same plot with error bars can be found in Figure A7.1.

In order to further increase the sample capacity, multiple pieces of W4 paper were stacked under the detection layer (Figure A7.4A). The contact between the layers of W4 was poor and the flow slowed down as more layers of paper were added (Figure A7.4B). Instead of simply stacking the layers of paper, double-sided adhesive (DSA) can be used to connect the paper layers, improving contact, but also forming a consistent gap. This gap between paper layers has been shown to significantly increase the flow rate in the paper.[13] Multiple configurations of DSA were evaluated (Figure A7.5, A7.6), with design 2 turning out the best: In addition to being the easiest to assemble, the grate-like design of the DSA enhanced the contact between the W4 layers and also increased flow to the lower layers of the device.

With the device configuration optimized (Figure 6.2), the multi-layer "high volume" device was compared to the single-layer radial µPADs. Single-layer µPADs were fabricated for copper detection.[14] The top detection layer of just Zincon printed on paper was used to assemble the multi-layer devices. To the single-layer devices, 150 µL of Cu^{2+} was added and 1 mL was added to the multi-layer devices. The devices were scanned after the flow stopped (5 min for single layer, 1 hr
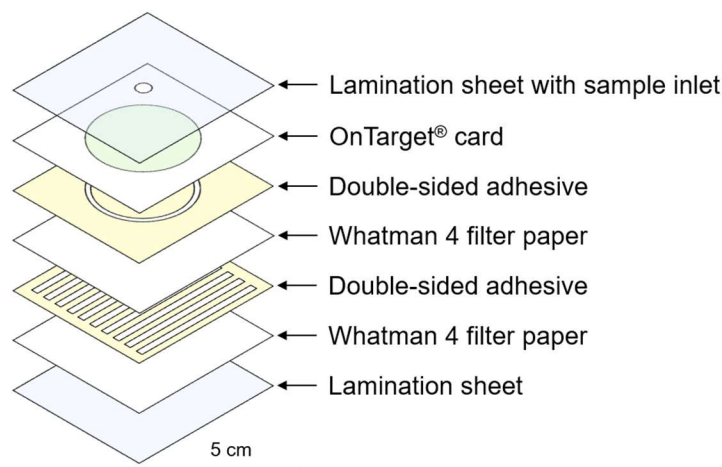
Figure 6.2 Scheme of device layers and assembly for multi-layer On-Target® cards.

for multi-layer), and the diameter of the blue circle was measured (Figure 6.3). With the new device configuration, the multi-layer devices were able to detect Cu down to 5 ppb (Figure 6.4), which is a significant improvement over the previous detection limit of 500 ppb (0.5 ppm). The cards are still the size of a business card, which is better suited for in-field analysis. Despite a run time of 1 hr, the sample preparation time is minimal as all the run time is passive. An external preconcentration step is not necessary unless sub-ppb levels of detection are desired.
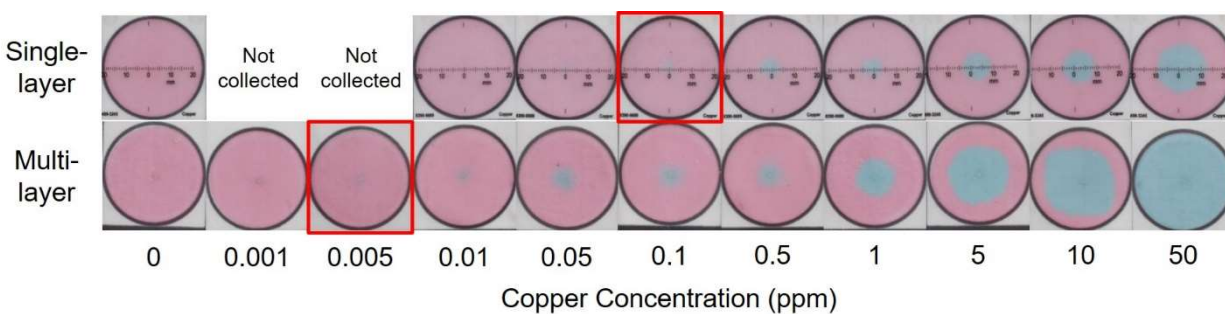
Figure 6.3 A selection of single and multi-layer devices by Cu concentration. The visual limits of detection are outlined in a red box. Sample addition volumes: 150 μL to single-layer, 1000 μL to multi-layer devices.
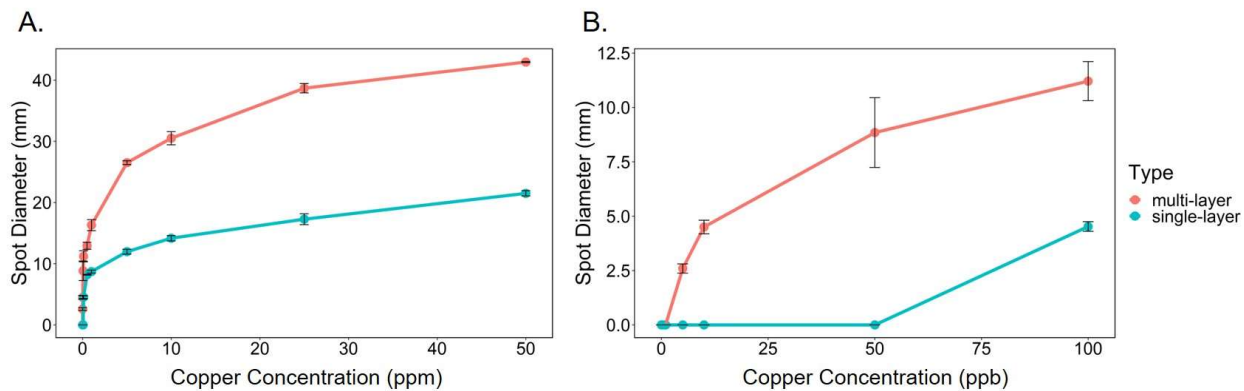
Figure 6.4 Circle diameter vs Cu concentration for both multi and single layer devices. Each point represents the average of 3 replicates, and the error bars are ±1σ around the mean. The left panel (A) shows the full calibration curve (0 – 500 ppm) while the right panel (B.) shows just the low concentrations (0 – 100 ppb). Please note the differences in units for the x-axis and scale on the y-axis.

REFERENCES

1.   Menger, R. F.; Beck, J. J.; Fuller, K. Z.; Reilly III, T. H.; Henry, C. S., High volume radial detection paper-based device for trace metal analysis. submitted to *ACS Sensors,* **2021**.

2.   Martinez, A. W.; Phillips, S. T.; Butte, M. J.; Whitesides, G. M., Patterned paper as a platform for inexpensive, low-volume, portable bioassays. *Angew. Chem. Int. Ed.* **2007,** *46* (8), 1318-20.

3.   Carrell, C.; Kava, A.; Nguyen, M.; Menger, R. F.; Munshi, Z.; Call, Z.; Nussbaum, M.; Henry, C., Beyond the lateral flow assay: A review of paper-based microfluidics. *Microelectron. Eng.* **2019,** *206*, 45-54.

4.   Ozer, T.; McMahon, C.; Henry, C. S., Advances in Paper-Based Analytical Devices. *Annu. Rev. Anal. Chem.* **2020,** *13*, 85-109.

5.   Noviana, E.; McCord, C. P.; Clark, K. M.; Jang, I.; Henry, C. S., Electrochemical paper-based devices: sensing approaches and progress toward practical applications. *Lab Chip* **2020,** *20* (1), 9-34.

6.   Morbioli, G. G.; Mazzu-Nascimento, T.; Stockton, A. M.; Carrilho, E., Technical aspects and challenges of colorimetric detection with microfluidic paper-based analytical devices (μPADs) - A review. *Anal. Chim. Acta* **2017,** *970*, 1-22.

7.   Martinez, A. W.; Phillips, S. T.; Carrilho, E.; Thomas, S. W., 3rd; Sindi, H.; Whitesides, G. M., Simple telemedicine for developing regions: camera phones and paper-based microfluidic devices for real-time, off-site diagnosis. *Anal. Chem.* **2008,** *80* (10), 3699-707.

8.   Cate, D. M.; Dungchai, W.; Cunningham, J. C.; Volckens, J.; Henry, C. S., Simple, distance-based measurement for paper analytical devices. *Lab Chip* **2013,** *13* (12), 2397-404.

9.   Cate, D. M.; Noblitt, S. D.; Volckens, J.; Henry, C. S., Multiplexed paper analytical device for quantification of metals using distance-based detection. *Lab Chip* **2015,** *15* (13), 2808-2818.

10.   Nguyen, M. P.; Kelly, S. P.; Wydallis, J. B.; Henry, C. S., Read-by-eye quantification of aluminum (III) in distance-based microfluidic paper-based analytical devices. *Anal. Chim. Acta* **2020,** *1100*, 156-162.

11.   Pratiwi, R.; Nguyen, M. P.; Ibrahim, S.; Yoshioka, N.; Henry, C. S.; Tjahjono, D. H., A selective distance-based paper analytical device for copper(II) determination using a porphyrin derivative. *Talanta* **2017,** *174*, 493-499.

12.   Quinn, C. W.; Cate, D. M.; Miller-Lionberg, D. D.; Reilly, T.; Volckens, J.; Henry, C. S., Solid-Phase Extraction Coupled to a Paper-Based Technique for Trace Copper Detection in Drinking Water. *Environ. Sci. Technol.* **2018,** *52* (6), 3567-3573.

13.   Channon, R. B.; Nguyen, M. P.; Scorzelli, A. G.; Henry, E. M.; Volckens, J.; Dandy, D. S.; Henry, C. S., Rapid flow in multilayer microfluidic paper-based analytical devices. *Lab Chip* **2018,** *18* (5), 793-802.

14.   Hofstetter, J. C.; Wydallis, J. B.; Neymark, G.; Reilly, T. H.; Harrington, J.; Henry, C. S., Quantitative colorimetric paper analytical devices based on radial distance measurements for aqueous metal determination. *Analyst* **2018,** *143* (13), 3085-3090.

15.   Luo, K.; Ryu, J.; Seol, I.-H.; Jeong, K.-B.; You, S.-M.; Kim, Y.-R., Paper-Based Radial Chromatographic Immunoassay for the Detection of Pathogenic Bacteria in Milk. *ACS Appl. Mater.* **2019,** *11* (50), 46472-46478.

16.   Drinking Water Contaminants. http://water.epa.gov/drink/ (accessed April 2021.

17.   Kudo, H.; Yamada, K.; Watanabe, D.; Suzuki, K.; Citterio, D., Paper-Based Analytical Device for Zinc Ion Quantification in Water Samples with Power-Free Analyte Concentration. *Micromachines* **2017,** *8* (4), 127.

18.   Shimada, Y.; Kaneta, T., Highly Sensitive Paper-based Analytical Devices with the Introduction of a Large-Volume Sample via Continuous Flow. *Anal. Sci.* **2018,** *34* (1), 65-70.

19.   Creed, J. T.; Brockhoff, C. A.; Martin, T. D., Method 200.8: Determination of Trace Elements in Waters and Wastes By Inductively Coupled Plasma - Mass Spectrometry. 1994.

20.   Jain, R.; Thakur, A.; Kaur, P.; Kim, K.-H.; Devi, P., Advances in imaging-assisted sensing techniques for heavy metals in water: Trends, challenges, and opportunities. *TrAC, Trends Anal. Chem.* **2020,** *123*, 115758.

21.   Kung, C.-T.; Hou, C.-Y.; Wang, Y.-N.; Fu, L.-M., Microfluidic paper-based analytical devices for environmental analysis of soil, air, ecology and river water. *Sens. Actuators B Chem.* **2019,** *301*, 126855.

22.   Kamnoet, P.; Aeungmaitrepirom, W.; Menger, R. F.; Henry, C. S., Highly selective simultaneous determination of Cu(ii), Co(ii), Ni(ii), Hg(ii), and Mn(ii) in water samples using microfluidic paper-based analytical devices. *Analyst* **2021,** (7).

23.   Rattanarat, P.; Dungchai, W.; Cate, D.; Volckens, J.; Chailapakul, O.; Henry, C. S., Multilayer Paper-Based Device for Colorimetric and Electrochemical Quantification of Metals. *Anal. Chem.* **2014,** *86* (7), 3555-3562.

24.   Sun, X.; Li, B.; Qi, A.; Tian, C.; Han, J.; Shi, Y.; Lin, B.; Chen, L., Improved assessment of accuracy and performance using a rotational paper-based device for multiplexed detection of heavy metals. *Talanta* **2018,** *178*, 426-431.

25.   Li, X.; Ballerini, D. R.; Shen, W., A perspective on paper-based microfluidics: Current status and future trends. *Biomicrofluidics* **2012,** *6* (1), 011301.

26.   Li, F.; Hu, Y.; Li, Z.; Liu, J.; Guo, L.; He, J., Three-dimensional microfluidic paper-based device for multiplexed colorimetric detection of six metal ions combined with use of a smartphone. *Anal. Bioanal. Chem.* **2019,** *411* (24), 6497-6508.

27.   Access Sensor Technologies. https://www.accsensors.com/ (accessed April 5, 2021).

CHAPTER 7: CONCLUSIONS AND FUTURE DIRECTIONS

Paper-based sensors, or µPADs, offer many advantages for environmental analyses. Their low cost, portability, disposability, and ability to be manufactured in bulk make µPADs ideal for in-field analysis, especially in remote settings where instrumentation and power may not be accessible or desired. While there has been significant progress in developing µPADs for many environmental analytes,[1] there are still many challenges that need to be overcome for the devices to be used regularly in the field.[2] The LODs of µPADs are often higher than regulatory limits or concentrations commonly found in the environment. Also, developing a device that is specific for one analyte without interference from other competing substances is challenging due to similar complexation mechanisms. Adding extra steps to concentrate a sample or treating it to remove interferences reduces the usability of the device in the field. The chapters in this thesis have discussed the development of new µPADs as well as addressed some of those challenges.

The spatial distribution of pesticides has not been well studied in large orchard trees like citrus trees. As the application of pesticides is critical for managing crop diseases, it is important to study the spatial distribution with the trees. The commonly used method of water-sensitive papers (WSP) is not ideal because it is difficult to use and will react to any source of water, in addition to the pesticide. In Chapter 2, a novel method that uses a fluorescent dye and a paper substrate was developed, compared to the previous method (WSP), and used to measure pesticide application.[3] The use of the fluorescent dye allows the method to be used with (or even without) any pesticide. Then in Chapter 3, the method was applied in a citrus grove to evaluate the spatial distribution within citrus trees as applied by different equipment and under various application settings.[4] In addition, the new method is easy to scale up to thousands of samples at a time, cheaper,

and faster than the commonly used method of water-sensitive paper. We envision that the fluorescent dye and paper-based method will be used in other crops to optimize pesticide application, effectively improving crop yield and profits. The quantitative data obtained from the field studies provide a scientific basis for designing an optimized pesticide application approach.

While my initial work with paper-based devices used static conditions (no flow), this limits the potential applications. Fluid flow qualities in paper microfluidic devices – other than direction – are difficult to manipulate as the fluid flow is dependent on the inherent pore structure of the paper. In Chapter 4, a passive flow mixer was developed, where a staggered herringbone pattern is rastered into a glass slide to induce chaotic mixing in a microfluidic channel.[5] The device is inexpensive to fabricate, disposable, and compatible with organic solvents. Mixing was demonstrated and quantified by a few representative reactions. In Appendix 4, a similar capillary-driven mixer was developed, using layers of laminated transparency film and the cross-sectional overlap of two solutions to induce mixing.[6] The transparency-based device was used to detect pesticide residues on the skin of fruits and vegetables based on an acetylcholinesterase inhibition assay. This device has been developed further by other members of the lab into an at-home test for COVID-19.[7]

My research interests expanded to developing μPADs for other environmental analytes. For example, PFAS, or per- and polyfluoroalkyl substances, have arisen as environmental contaminants of emerging concern. It is important to detect PFAS – especially in aqueous samples – to monitor the spread of PFAS contamination.[8] Currently, PFAS detection relies on instrumental analyses, which are not techniques easily accessible to the general public. In Chapter 5, I developed a PAD for the detection of PFOS.[9] Although the LOD of the device (10 ppm) is higher than the concentration allowed in water (70 ppt) (although higher concentrations can be expected),[10] it

represents a first step towards fast, inexpensive, and accessible detection of PFOS using a µPAD. We will continue optimizing the device to include PFOA detection as well as improve the device fabrication (by inkjet printing the reagent[11]) to improve consistency and reduce variability. In addition, the image analysis process will be improved to determine the diameter of the purple circle more accurately. To lower the LOD to the appropriate range (at least <10 ppb), the device shape and size can be modified to accommodate a higher sample volume. Alternatively, a preconcentration step like solid-phase extraction could be applied to concentrate a sample.[12, 13]

As with the PFOS PAD, the sensitivity and LODs of colorimetric µPADs in general hinder their use in the real world. Environmental contaminants are often found at very low concentrations in water (ppt – ppb range). Most PADs can accommodate sample volumes of $1 – 100$ µL, but this often does not provide enough analyte molecules to react with the reagent stored on the paper. Other attempts to concentrate a sample require external instrumentation, extra user steps, and time, adding complexity to the device. A new device fabrication was proposed in Chapter 6 which uses an existing radial detection card for copper as the detection layer, and stacks of filter paper and double-sided adhesive underneath.[14] The device can hold a sample volume of 1 mL and potentially even more with an increase of paper layers and/or device size. The detection limit for copper was reduced from 100 ppb to 0.5 ppb, which is appropriate for testing copper contamination in drinking water.[15] Multiple samples can be run side-by-side with minimal user input aside from the sample addition.

The aforementioned method of preconcentration using a multi-layer device is promising over other methods like solid-phase extraction,[16] membrane concentration,[12] or heating,[17] in that the method does not have any power or instrument requirements. Even though the devices take up to an hour to complete, the majority of analysis time is passive. After sample addition, the device

can be left unmonitored for an hour and then checked for results. In addition, the µPAD is small and light, so multiple analyses can be performed outside the laboratory at any location, provided that the device can be protected from elements like wind and rain.

Figure 7.1 Selection of radial detection cards for zinc, iron, manganese, and copper from Access Sensor Technologies, LLC.

The multi-layer device fabrication is also straightforward to extend to radial detection cards other than those for Cu. Access Sensor Technologies offers a suite of radial detection cards for heavy metal detection (Figure 7.1).[18] With the addition of the multi-layer preconcentration method, the limit of detection of these cards can be lowered by three orders of magnitude, enabling quantification of metals at levels that are common in drinking water.[15] Currently, the dimensions of the multi-layer device are designed to match the existing On-Target cards, but these can easily be altered for other devices, either existing or new. A problem of the PFOS µPAD mentioned in Chapter 5 is that the current LOD is too high to be relevant for drinking water. When the PFOS µPAD was combined with the multi-layer preconcentration system, results were mixed. At a high concentration (200 ppm PFOS), the diameter of the purple circle was much larger than that on the single-layer device, as expected based on the results from Chapter 6 (Figure 7.2A). At a low concentration (30 ppm PFOS), the purple circle is visible to the naked eye on the single-layer

device; however, on the multi-layer device, the purple color is not intense enough to be visible (Figure 7.2B). There are not enough PFOS molecules forming purple ion pairs with the MG to overcome the baseline blue color. Further device and reagent optimization are necessary to improve the response of the purple color at low PFOS concentrations.
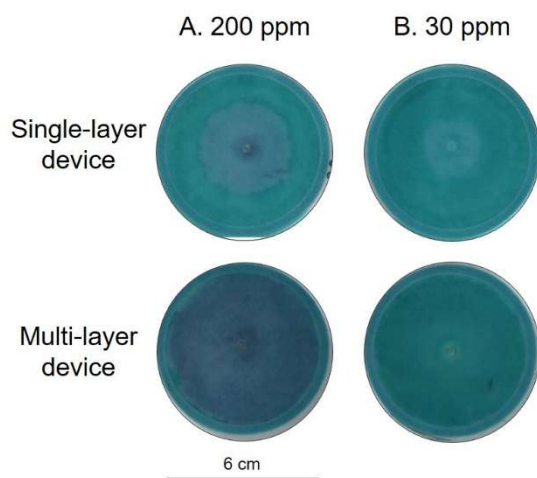
Figure 7.2 Top: single layer devices (45 mm) treated with 150 ppm methylene green to which 150 μL PFOS was added (A. 200 ppm, B. 30 ppm). Bottom row: multi-layer devices (45 mm) treated with 150 ppm methylene green. Layers of Whatman 4 and double-sided adhesive were stacked under the detection layer following Figure 6.2. 1 mL PFOS was added (A. 200 ppm, B. 30 ppm).

Overall, the work in this thesis has contributed to the development of μPADs for environmental analysis, maintaining beneficial properties like low cost, ease of use, and applicability while addressing the challenges of achieving relevant limits of detection. μPADs are not meant to replace traditional instrumental analyses but instead offer alternative and/or complementary analysis. The technologies presented in this dissertation look towards the idea of the "citizen scientist" – a movement that has recently gained popularity as devices like μPADs and other test kits have become accessible to the general public. Instead of a researcher or laboratory technician making house calls to evaluate drinking water quality or sending a sample out for analysis, anyone can use a μPAD to evaluate their water, providing peace of mind. Like the Flint,

Michigan water crisis beginning in 2014, a µPAD for multiplex heavy metal analysis would have been a great first step in identifying what kind of pollution was present instead of waiting for months for government officials to step in.[19] µPADs are a great opportunity to involve children with the analysis, introducing them to science in their own homes. In addition to the individual user, the data obtained from multiple homes across a region can be aggregated to potentially identify sources of pollution. A smartphone app can easily achieve this, where the app is used to take a picture of the µPAD, analyze, and upload the results with GPS coordinates to a central server or cloud. The data is plotted on a map by an algorithm or the next eager graduate student.

The use of µPADs in the home extends beyond the United States. As mentioned in the Introduction (Chapter 1), most water pollution occurs in resource-limited countries like Africa, India, and Southeast Asia.[20, 21] In these countries, where clean drinking water is not readily available, a tool like a µPAD can help identify whether water is safe to drink or not with respect to a certain analyte. While the µPAD will not magically clean up the water, it is a first step in providing drinking water quality analysis where instrumental analysis is not achievable due to cost, infrastructure, and personnel requirements.

Environmental research (monitoring and remediation) would also benefit from the use of µPADs. For example, the 2015 Gold King Mine spill in Silverton, CO released 3 million gallons of acid mine drainage into the Animas River, turning the river orange from the oxidation of dissolved iron (Figure 7.3). The acid mine drainage contained heavy metals like lead, copper, zinc, iron, and arsenic.[22] While there were many samples collected and subsequently analyzed in the lab, there was a delay in reporting resorts due to the turnaround time between sample collection, transportation, preparation, and analysis.[22] µPADs could have been used to monitor the progress of the contamination on a daily or even hourly basis, as well as multiple sampling locations

downstream from the spill. The analysis is much more complete with high temporal and spatial resolution, as well as results in almost real time. Deploying even 100 cards at a time costs less than a single lab analysis, and the use of a smartphone app to analyze the μPAD makes the entire process much faster and less expensive than lab analysis.

Figure 7.3 2015 Gold King Mine Spill near Silverton, CO.

While the Gold King Mine spill was an obvious contamination event with the river turning orange, water pollution is not necessarily visible. Heavy metals can be inconspicuously released into the water through many other processes, as can PFAS. The ease of use, straightforward analysis, and low cost make μPADs ideal for identifying hotspots of pollution, not necessarily in drinking water. For example, high PFAS contamination has been found in ground and surface water near wastewater treatment plants, firefighter training areas, landfill sites, and industrial sites.[23] After a hotspot has been identified, further analysis can be requested if needed, or at the very least, a decision can be made regarding next steps, whether further action is needed or not. With some more optimization, I believe the technologies that I developed for PFOS and heavy metal detection have the ability to make a big impact on society and access to safe drinking water.

The colorimetric platform has the potential to be expanded to an entire suite of common contaminants in water.

REFERENCES

1.   Kung, C.-T.; Hou, C.-Y.; Wang, Y.-N.; Fu, L.-M., Microfluidic paper-based analytical devices for environmental analysis of soil, air, ecology and river water. *Sens. Actuators B Chem.* **2019,** *301*, 126855.
2.   Carrell, C.; Kava, A.; Nguyen, M.; Menger, R. F.; Munshi, Z.; Call, Z.; Nussbaum, M.; Henry, C., Beyond the lateral flow assay: A review of paper-based microfluidics. *Microelectron. Eng.* **2019,** *206*, 45-54.
3.   Menger, R. F.; Bontha, M.; Beveridge, J. R.; Borch, T.; Henry, C. S., Fluorescent-based method for assessment of pesticide coverage on leaves and trees: A citrus grove case study. *J. Agric. Food Chem.* **2020,** *68* (47), 14009-14014.
4.   Menger, R. F.; Rehberg, R. A.; Trivedi, P.; Henry, C. S.; Borch, T., High spatial resolution fluorescence imagery for optimized pest management within a citrus grove. submitted to *Phytopathology.* **2021**.
5.   Channon, R. B.; Menger, R. F.; Wang, W.; Carrão, D. B.; Vallabhuneni, S.; Kota, A. K.; Henry, C. S., Design and application of a self-pumping microfluidic staggered herringbone mixer. *Microfluid. Nanofluid.* **2021,** *25* (4).
6.   Jang, I.; Carrão, D. B.; Menger, R. F.; Moraes De Oliveira, A. R.; Henry, C. S., Pump-Free Microfluidic Rapid Mixer Combined with a Paper-Based Channel. *ACS Sensors* **2020,** *5* (7), 2230-2238.
7.   Carrell, C.; Link, J.; Jang, I.; Terry, J.; Scherman, M.; Call, Z.; Panraksa, Y.; Dandy, D. S.; Geiss, B. J.; Henry, C., Point-of-Need Disposable ELISA System for COVID-19 Serology Testing. *ChemRxiv* **2020**.
8.   Naidu, R.; Nadebaum, P.; Fang, C.; Cousins, I.; Pennel, K.; Conder, J.; Newell, C.; Longpré, D.; Warner, S.; Crosbie, N., Per-and poly-fluoroalkyl substances (PFAS) current status and research needs. *Environ. Technol. Inno.* **2020**, 100915.
9.   Menger, R. F.; Beck, J. J.; Borch, T.; Henry, C. S., Colorimetric paper-based analytical device for PFOS detection. submitted to *ACS ES&T Water,* **2021**.
10.   Lifetime Health Advisories and Health Effects Support Documents for Perfluorooctanoic Acid and Perfluorooctane Sulfonate. U.S. Environmental Protection Agency: Washington, D.C., 2016; Vol. 81.
11.   Hofstetter, J. C.; Wydallis, J. B.; Neymark, G.; Reilly, T. H.; Harrington, J.; Henry, C. S., Quantitative colorimetric paper analytical devices based on radial distance measurements for aqueous metal determination. *Analyst* **2018,** *143* (13), 3085-3090.
12.   Quinn, C. W.; Cate, D. M.; Miller-Lionberg, D. D.; Reilly, T.; Volckens, J.; Henry, C. S., Solid-Phase Extraction Coupled to a Paper-Based Technique for Trace Copper Detection in Drinking Water. *Environ. Sci. Technol.* **2018,** *52* (6), 3567-3573.
13.   Meredith, N. A.; Quinn, C.; Cate, D. M.; Reilly, T. H.; Volckens, J.; Henry, C. S., Paper-based analytical devices for environmental analysis. *The Analyst* **2016,** *141* (6), 1874-1887.
14.   Menger, R. F.; Beck, J. J.; Fuller, K. Z.; Reilly III, T. H.; Henry, C. S., High volume radial detection paper-based device for trace metal analysis. submitted to *ACS Sensors*, **2021**.
15.   National Primary Drinking Water Regulations. In *816-F-09-004*, Agency, U. S. E. P., Ed. 2009.

16.   Calderilla, C.; Maya, F.; Leal, L. O.; Cerdà, V., Recent advances in flow-based automated solid-phase extraction. *TrAC, Trends Anal. Chem.* **2018,** *108*, 370-380.

17.   Ninwong, B.; Sangkaew, P.; Hapa, P.; Ratnarathorn, N.; Menger, R. F.; Henry, C. S.; Dungchai, W., Sensitive distance-based paper-based quantification of mercury ions using carbon nanodots and heating-based preconcentration. *RSC Adv.* **2020,** *10* (17), 9884-9893.

18.   Access Sensor Technologies. https://www.accsensors.com/ (accessed April 2021.

19.   Roy, S.; Tang, M.; Edwards, M. A., Lead release to potable water during the Flint, Michigan water crisis as revealed by routine biosolids monitoring data. *Water Res.* **2019,** *160*, 475-483.

20.   Landrigan, P. J.; Fuller, R.; Acosta, N. J.; Adeyi, O.; Arnold, R.; Baldé, A. B.; Bertollini, R.; Bose-O'Reilly, S.; Boufford, J. I.; Breysse, P. N., The Lancet Commission on pollution and health. *The Lancet* **2018,** *391* (10119), 462-512.

21.   *2017 Annual Report WHO/UNICEF Joint Monitoring Programme for Water Supply, Sanitation and Hygiene*; World Health Organization: 2017; pp 1-20.

22.   Rodriguez-Freire, L.; Avasarala, S.; Ali, A.-M. S.; Agnew, D.; Hoover, J. H.; Artyushkova, K.; Latta, D. E.; Peterson, E. J.; Lewis, J.; Crossey, L. J.; Brearley, A. J.; Cerrato, J. M., Post Gold King Mine Spill Investigation of Metal Stability in Water and Sediments of the Animas River Watershed. *Environ. Sci. Technol.* **2016,** *50* (21), 11539-11548.

23.   Dauchy, X., Per- and polyfluoroalkyl substances (PFASs) in drinking water: Current state of the science. *Curr. Opin. Environ. Sci. Health* **2019,** *7*, 8-12.

APPENDIX 1: SUPPLEMENTARY INFORMATION – FLUORESCENT DYE PAPER-BASED METHOD FOR ASSESSMENT OF PESTICIDE COVERAGE ON LEAVES AND TREES: A CITRUS GROVE CASE STUDY

1.1 Lightbox Fabrication

Pieces of black poly(methyl methacrylate) (PMMA) were cut with an Epilog Zing CO_2 laser cutter to make a 10 x 10 cm box (Figure 2.1B). Pieces were glued together with general use epoxy. The bottom PMMA piece had a 47 mm circle rastered into the center to ensure consistent placement of the samplers. The top piece had a 1.7 cm circle cut out of it to fit the Raspberry Pi camera (Raspberry Pi 3 Model B, Keyestudio 5 MP Camera). LED lights provided a consistent light source inside the box. LEDs were purchased at the appropriate wavelength for the dye used. For the red fluorescent dye (maximum absorption 550 nm), UV LED lights (Chanzon, 395 nm) were used for excitation. To fit the LED lights, five circles were laser cut into each side (5 mm in diameter), as well as eight circles around the camera in the top piece of PMMA. Two LEDs were wired together in series, with 14 pairs wired in parallel for a total of 28 LEDs. The anodes and cathodes of the LEDs were soldered to two strips of copper tape to eliminate excess wiring. One wire of each pair was soldered to the "anode tape" and the other was soldered to the "cathode tape." The circuit was completed by wiring a rechargeable 9V battery to the LED lights in parallel. The battery is located in a plastic holder with an on/off switch. A 9.2-ohm resistor was soldered to the negative input of the battery to limit the current through the LED lights. Black electrical tape was used to cover all exposed wire and copper tape. Holders for the camera and the Raspberry Pi system were designed in Onshape and 3D printed using a Form 2: Stereolithography 3D Printer (Formlabs) and were glued to the box with general use epoxy.

Table A1.1 Weather data for benchmark experiment.

Date	10/17/2018
Temperature (°C)	31.3
Wind Speed (mph)	7.0
Wind Direction	ESE
Humidity	70%
Heat Index	38.4
Time of Experiment	11 am - 1 pm

Table A1.2 Field study details

Date	2/14/2018	2/14/2018	2/15/2018	2/15/2018	5/9/2018	5/9/2018	5/10/2018	5/10/2018	10/16/2018	10/16/2018	10/18/2018	10/18/2019
Tree Age (yr)*	~1	~3	~1	~3	~1	~3	~1	~3	~1	~3	~1	~3
Aerial/Ground Spray	Ground	Ground	Aerial	Aerial	Ground	Ground	Aerial	Aerial	Ground	Ground	Aerial	Aerial
Sprayer Type	Side	Speed	Airplane	Airplane	Side	Speed	Airplane	Airplane	Side	Speed	Airplane	Airplane
Sprayer Name	Newton Crounch	FM Copling	Air Tractor	Air Tractor	Newton Crounch	FM Copling	Air Tractor	Air Tractor	Newton Crounch	FM Copling	Air Tractor	Air Tractor
Nozzle Type (#)	TXR80049VK (3) TXR80017VK (6)	D3-C25 (18)	Flat Fan #15 (86)	Flat Fan #15 (86)	TXR80049VK (3) TXR80017VK (6)	D3-C25 (18)	Flat Fan #15 (86)	Flat Fan #15 (86)	TXR80049VK (3) TXR80017VK (6)	D3-C25 (18)	Flat Fan #15 (86)	Flat Fan #15 (86)
Application Rate (gallons per acre)	35	50	5	5	35	50	5	5	35	50	5	5
Dye	Yellow-green	Yellow-green	Yellow-green	Yellow-green	Red	Red	Red	Red	Red	Red	Red	Red
Dye Concentration (ppm)	1	1	1	1	1,500	1,500	4,300	4,300	1,500	1,500	4,300	4,300
Temperature (°C)	74.3	74.3	79.9	79.9	28.3	28.3	26.9	26.9	32.8	29.8	26.8	26.8
Wind Speed (mph)	6.0	6.0	3.0	3.0	5.0	5.0	5.0	5.0	10.5	11.3	6.9	6.9
Wind Direction	ENE	ENE	SE	SE	ENE	ENE	ENE	ENE	ESE	ESE	ENE	ENE
Humidity	83%	83%	60%	60%	55%	55%	63%	63%	62%	75%	88%	88%
Heat Index	76.6	76.6	81.2	81.2	28.8	28.8	28.1	28.1	39.8	35.6	30.7	30.7
Time of application	11:30 AM	11:30 AM	1:00 PM	1:00 PM	11:30 AM	11:30 AM	11:00 AM	11:00 AM	1:30 PM	10:30 AM	9:30 AM	9:30 AM

*at time of experiment
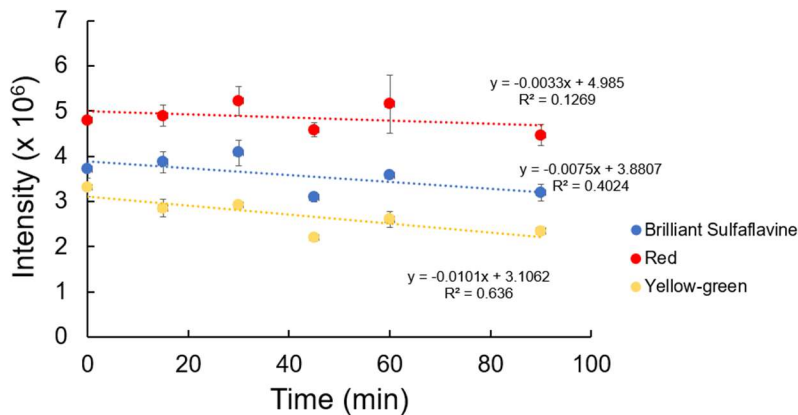
Figure A1.1 Color intensity vs time of 3 different dyes.
Table A1.3 Comparison of percent coverage from filter paper method and WSP

123

|			Filter Paper Method			WSP		
Trial	Speed (mph)	Pressure (psi)	Average	Standard Deviation	%RSD	Average	Standard Deviation	%RSD
1	1	10	50.05%	4.00	8.00%	49.13%	3.45	7.02%
2	1	20	59.54%	4.36	7.32%	60.19%	2.84	4.72%
3	1	30	62.64%	1.66	2.65%	60.39%	3.92	6.49%
4	1	40	63.26%	4.27	6.74%	66.83%	3.87	5.79%
5	2	10	33.48%	1.42	4.24%	25.96%	2.86	11.02%
6	2	20	38.08%	2.21	5.80%	34.79%	2.40	6.91%
7	2	30	45.75%	2.87	6.28%	38.30%	2.19	5.72%
8	2	40	47.73%	2.35	4.92%	43.62%	2.97	6.80%
9	3	10	23.92%	2.79	11.67%	19.91%	3.11	15.60%
10	3	20	24.77%	3.32	13.42%	23.75%	1.11	4.67%
11	3	30	28.47%	3.44	12.09%	27.09%	1.63	6.03%
12	3	40	32.23%	0.93	2.90%	30.22%	1.60	5.29%
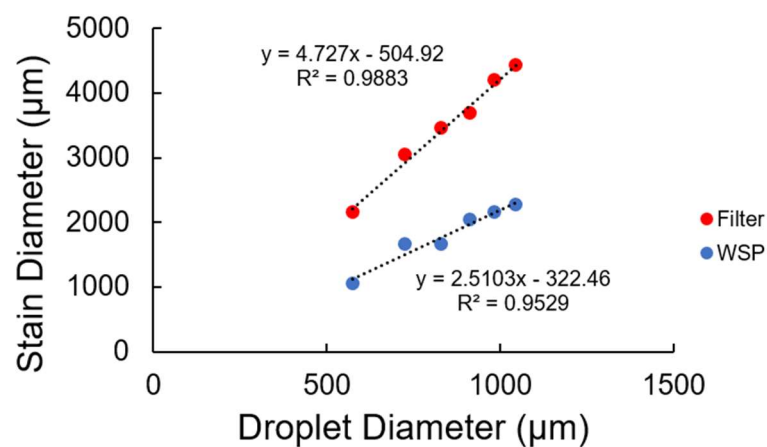
Figure A1.2 Stain diameter vs droplet diameter of filters and water-sensitive paper.
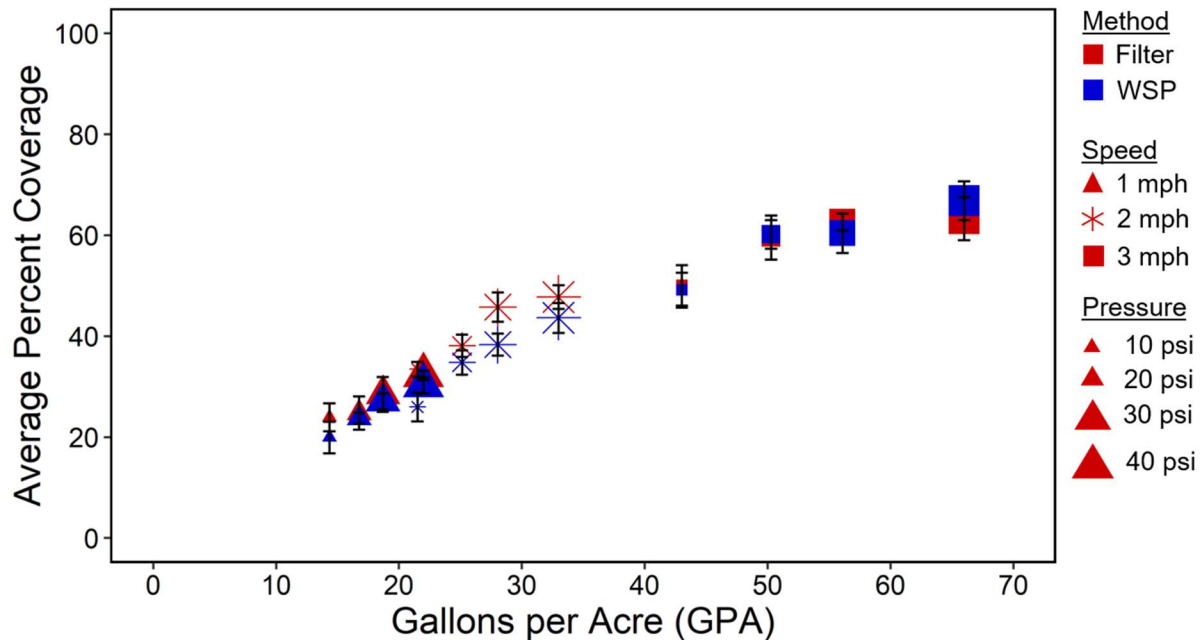
Figure A1.3 Average percent coverage vs gallons per acre (GPA) of the filter paper method (red) and water sensitive paper (WSP) (blue). The nozzle speed is differentiated by symbol shape while the size of the point correlates to symbol pressure. Each point represents the average of 5 replicates and the error bars are ±1σ around the mean.

1.2 Gallon per acre Calculation

The gallons per acre (GPA) was calculated with the following equation:

$$GPA = \frac{5940 \; x \; GPM}{mph \; x \; W}$$

where GPM is gallons per minute (capacity of one nozzle), mph is the speed of the nozzle in miles per hour, and W is the width between the nozzles in inches. The DeVries Generation 4 Research Track Sprayer (DeVries Manufacturing, Hollandale, MN) used to perform the benchmark experiment is equipped with one TeeJet 8002EV8 nozzle (Spraying Systems Co., Wheaton, IL). The nozzle output (in GPM) for each pressure was determined and provided by TeeJet.

1.3 Field Study Overview

An analysis of variance (ANOVA) yielded significant variation among the application groups, $F_{(7, 942)} = 113.8$, $p < 2e\text{-}16$. A post-hoc Tukey test showed a significant difference ($p < 0.05$) between multiple groups (Table A2.4).

Table A2.4 Average percent coverage and standard deviation of filters collected in the October 2018 field study. Filter samplers are grouped by application method, tree age, and side of leaf. Each group is the average of 120 samplers.

Application Method	Tree Age	Side of Leaf	Average	Standard Deviation
Aerial	Old	Bottom	0.34%	0.99%
Aerial	Old	Top	2.32%	3.53%
Aerial	Young	Bottom	0.94%	3.90%
Aerial	Young	Top	8.45%	10.49%
Ground	Old	Bottom	14.49%	24.64%
Ground	Old	Top	32.32%	32.76%
Ground	Young	Bottom	8.57%	18.41%
Ground	Young	Top	54.71%	34.51%

Table A2.5 Results of post-hoc Tukey HSD. p < 0.05 indicates a significant difference.

Group 1	Group 2	Difference	p-value
Aerial Old Top	Aerial Old Bottom	-2.1551	0.9638
Aerial Young Bottom	Aerial Old Bottom	0.0698	1.0000
Aerial Young Top	Aerial Old Bottom	-8.6092	0.0006
Ground Old Bottom	Aerial Old Bottom	-23.1533	0.0000
Ground Old Top	Aerial Old Bottom	-31.6277	0.0000
Ground Young Bottom	Aerial Old Bottom	-4.4645	0.3489
Ground Young Top	Aerial Old Bottom	-38.2034	0.0000
Aerial Young Bottom	Aerial Old Top	2.2249	0.9575
Aerial Young Top	Aerial Old Top	-6.4541	0.0324
Ground Old Bottom	Aerial Old Top	-20.9982	0.0000
Ground Old Top	Aerial Old Top	-29.4726	0.0000
Ground Young Bottom	Aerial Old Top	-2.3094	0.9476
Ground Young Top	Aerial Old Top	-36.0483	0.0000
Aerial Young Top	Aerial Young Bottom	-8.6790	0.0006
Ground Old Bottom	Aerial Young Bottom	-23.2231	0.0000
Ground Old Top	Aerial Young Bottom	-31.6975	0.0000
Ground Young Bottom	Aerial Young Bottom	-4.5343	0.3311
Ground Young Top	Aerial Young Bottom	-38.2732	0.0000
Ground Old Bottom	Aerial Young Top	-14.5441	0.0000
Ground Old Top	Aerial Young Top	-23.0185	0.0000
Ground Young Bottom	Aerial Young Top	4.1447	0.4528
Ground Young Top	Aerial Young Top	-29.5943	0.0000
Ground Old Top	Ground Old Bottom	-8.4745	0.0008
Ground Young Bottom	Ground Old Bottom	18.6887	0.0000
Ground Young Top	Ground Old Bottom	-15.0502	0.0000
Ground Young Bottom	Ground Old Top	27.1632	0.0000
Ground Young Top	Ground Old Top	-6.5757	0.0263
Ground Young Top	Ground Young Bottom	-33.7389	0.0000

1.4 Raspberry Pi Commands

The following commands were used to take pictures of the samples in the lightbox.

raspistill -p 0.5,0.5,0.5,0.5 -roi 0.25,0.25,0.5,0.5 -t 3000 -o /home/pi/CutralePictures/001.jpg

-p sets the preview window with x,y,w,h
-roi sets the region of interest
-t sets the time the preview window is open in milliseconds
-o sets the file path and file name

1.5 Python Script

The following code was used to analyze images of samples for percent coverage.

```
#Import the required packages
import glob
import math
import os
from os.path import isfile, join
import cv2
import numpy as np
from sklearn.cluster import KMeans


__author__ = "mridula@colostate.edu"

#Set folder and starting file names
images_folder = "G55"
#reading first file for kmeans clustering
first_file = "G55_260.jpg"
first_image = cv2.imread(images_folder + "/" + first_file)
first_image = cv2.cvtColor(first_image, cv2.COLOR_BGR2RGB)

#number of clusters
num_clusters = 3

image_for_clustering = first_image.reshape((first_image.shape[0] * first_image.shape[1], 3))
#represent as row*column,channel number
clt = KMeans(n_clusters=num_clusters) #cluster number
clt.fit(image_for_clustering)

#finding cluster enters
clusters = clt.cluster_centers_
```

```python
print(clusters)
#filtering out black and white as we are concentrating only on colored components of images
flatten  = [item for sublist in clusters for item in sublist]
print(min(flatten))
colors_of_interest = [row for row in clusters if ((min(flatten) < row[0] < 254) and (min(flatten) <
row[1] < 254) and (min(flatten) < row[2] < 254))]

#creating a list of (R,G,B) values of colors
color_list = sorted(list(list(math.floor(float(x)) for x in color.astype("uint8").tolist()) for color in
colors_of_interest),reverse=True)

print(color_list)
with open("csv_files/percentage_coverage_file.csv", 'w+') as f:
    f.write('image_name,sample(no. of pixels) ,backgroud (no. of
pixels),sample_percentage_coverge,particle count,background_percentage\n')
    for file in glob.glob(images_folder+"/*.jpg"):
        original_img = cv2.imread(file)
        original_img = cv2.cvtColor(original_img,cv2.COLOR_BGR2RGB)
        resized_image = cv2.resize(original_img, (400, 400))
        #hsv format of image
        img_hsv = cv2.cvtColor(resized_image, cv2.COLOR_RGB2HSV)

        hsv_sample = cv2.cvtColor(np.uint8([[color_list[0]]]), cv2.COLOR_RGB2HSV)
        hsv_background = cv2.cvtColor(np.uint8([[color_list[1]]]), cv2.COLOR_RGB2HSV)

#defining lower and upper limit for sample color for the purpose of masking (yellow color spots)
        lowerLimit_sample = (int(hsv_sample[0][0][0] - 10), 100, 20)
        upperLimit_sample = (int(hsv_sample[0][0][0] + 10), 255, 255)

#defining lower and upper limit for background color for the purpose of masking (green)
        lowerLimit_background = (int(hsv_background[0][0][0] - 10), 100, 20)
        upperLimit_background = (int(hsv_background[0][0][0] + 10), 255, 255)

#creating mask for sample
        mask_sample = cv2.inRange(img_hsv, lowerLimit_sample, upperLimit_sample)
        output_sample = cv2.bitwise_and(resized_image, resized_image, mask=mask_sample)

#creating mask for background
        mask_background = cv2.inRange(img_hsv, lowerLimit_background,
upperLimit_background)
        output_background = cv2.bitwise_and(resized_image, resized_image,
mask=mask_background)

#masking background, so as to count number of non-zero pixels left that define the sample
        sample_count = np.count_nonzero(output_sample)
```

```
    background_count = np.count_nonzero(output_background)

#using pixel count for both background and sample, calculating the percentage of pixels
belonging to the sample
    sample_percentage = (sample_count*100)/(sample_count+background_count)
    gray_sample = cv2.cvtColor(output_sample, cv2.COLOR_BGR2GRAY)

    _, contours, _ = cv2.findContours(gray_sample, cv2.RETR_LIST,
cv2.CHAIN_APPROX_SIMPLE)
    particle_count = sum(cv2.contourArea(cnt) > 0.5 for cnt in contours)

#writing into a file
    print('{0},{1},{2},{3},{4},{5}\n'.format(file.split("\\")[1], sample_count,
background_count,sample_percentage,particle_count,100-sample_percentage ))
    f.write('{0},{1},{2},{3},{4},{5}\n'.format(file.split("\\")[1], sample_count,
background_count,round(sample_percentage,2),particle_count,round(100-sample_percentage,2
)))
f.close()
```

Table A2.1 Field study details.

| Date	10/16/2018	10/16/2018	10/18/2018	10/18/2019	4/17/2019	4/17/2019
Tree Age (yr)*	~1	~3	~1	~3	~1	~3
Aerial/Ground Spray	Ground	Ground	Aerial	Aerial	Ground	Ground
Sprayer Type	Side	Speed	Airplane	Airplane	Side	Speed
Sprayer Name	Newton Crounch	FM Copling	Air Tractor	Air Tractor	Newton Crounch	FM Copling
Nozzle Type (#)	TXR80049VK (3) TXR80017VK (6)	D3-C25 (18)	Flat Fan #15 (86)	Flat Fan #15 (86)	TXR80049VK (3) TXR80017VK (6)	D3-C25 (18)
Application Rate (gallons per acre)	35	50	5	5	20	90
Dye	Red	Red	Red	Red	Red	Red
Dye Concentration (g/L)	1.5	1.5	4.3	4.3	3.12	2.8
Temperature (°C)	32.8	29.8	26.8	26.8	29.2	28.1
Wind Speed (mph)	10.5	11.3	6.9	6.9	5.0	4.0
Wind Direction	ESE	ESE	ENE	ENE	ESE	ESE
Humidity	62%	75%	88%	88%	54%	55%
Heat Index	39.8	35.6	30.7	30.7	30.6	28.9
Time of application	1:30 PM	10:30 AM	9:30 AM	9:30 AM	2:00 PM	12:30 PM
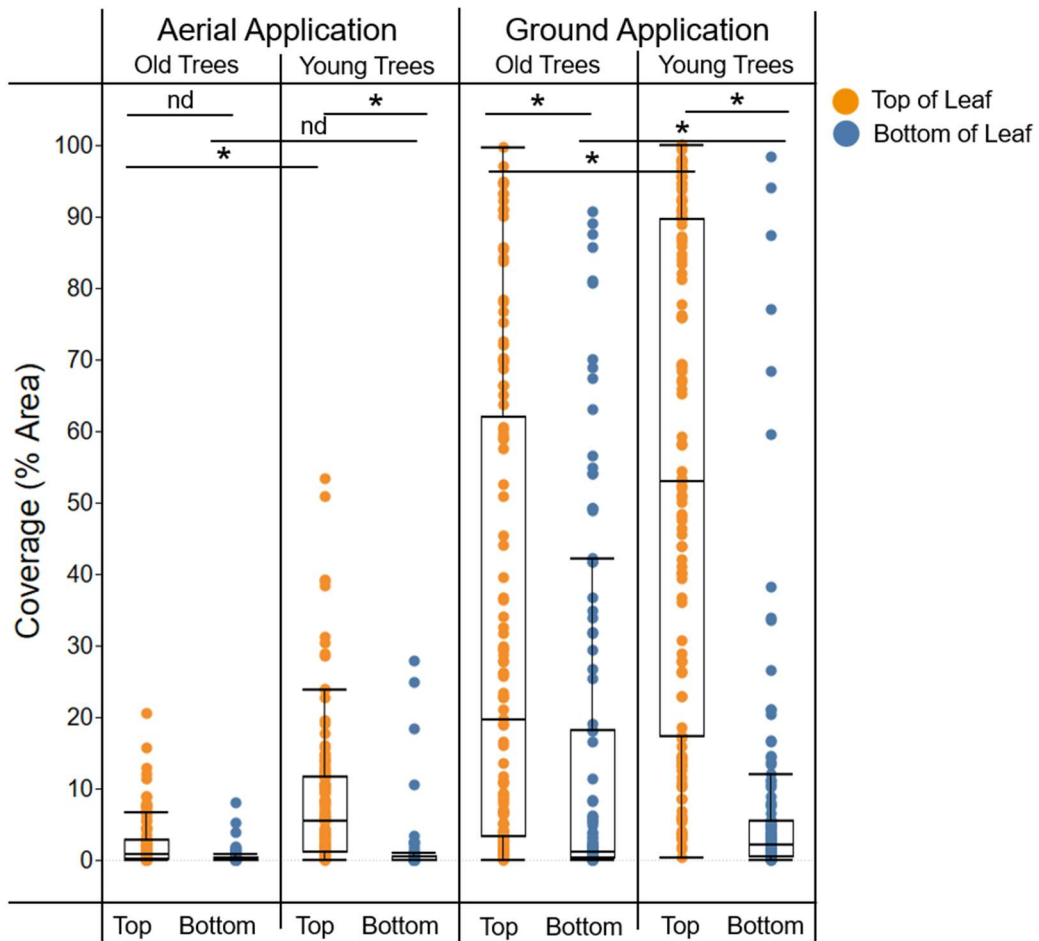
Figure A2.1 Box and whisker plot showing percent coverage of all samples from Field Study 1 (n = 1020 samplers), grouped by application type (aerial vs ground application), age of tree (young vs old), side of leaf (top vs bottom). Stars (*) indicate a significant difference (p < 0.05, n = 120) between the two groups connected by the line. No significant difference is indicated by "nd."

Table A2.2 Comparison of percent coverage between top and bottom of leaf from Field Study 1 (October 2018), sorted by application type and tree age.

Application Type	Tree Age	Canopy Depth	Canopy Height	Top of Leaf		Bottom of Leaf		Factor (Top/Bottom)	Avg. ± St. Dev.
				Avg.	St. Dev.	Avg.	St. Dev.		
Aerial	Young	Inner	Lower	3.76	9.01	0.09	0.17	42.24	46.66 ± 43.86
Aerial	Young	Inner	Middle	6.47	11.94	0.11	0.25	61.35	
Aerial	Young	Inner	Upper	10.26	7.19	0.24	0.43	42.83	
Aerial	Young	Outer	Lower	9.31	9.97	0.08	0.16	123.42	
Aerial	Young	Outer	Middle	12.03	10.80	1.58	6.19	7.62	
Aerial	Young	Outer	Upper	8.52	12.44	3.44	6.73	2.48	
Ground	Old	Inner	Lower	14.29	21.42	1.60	2.39	8.92	8.87 ± 13.25
Ground	Old	Inner	Middle	20.74	22.59	0.59	0.62	35.33	
Ground	Old	Inner	Upper	19.39	24.83	10.27	15.91	1.89	
Ground	Old	Outer	Lower	36.99	33.97	11.54	23.15	3.21	
Ground	Old	Outer	Middle	55.29	36.91	19.88	25.76	2.78	
Ground	Old	Outer	Upper	46.32	34.05	42.44	32.58	1.09	
Ground	Young	Inner	Lower	15.56	14.68	1.57	1.35	9.89	9.13 ± 3.77
Ground	Young	Inner	Middle	40.01	30.58	2.74	5.80	14.62	
Ground	Young	Inner	Upper	64.82	27.43	6.13	5.10	10.57	
Ground	Young	Outer	Lower	50.65	33.71	6.34	19.25	7.99	
Ground	Young	Outer	Middle	77.23	27.21	8.95	15.25	8.63	
Ground	Young	Outer	Upper	78.06	25.18	25.36	32.35	3.08	

Table A2.3 Comparison of percent coverage between aerial and ground application from Field Study 1 (October 2018), sorted by side of leaf.

| Side of Leaf	Tree Age	Canopy Depth	Canopy Height	Aerial Application		Ground Application		Factor (Ground/Aerial)	Avg. ± St. Dev.
				Avg.	St. Dev.	Avg.	St. Dev.		
Top	Old	Inner	Lower	0.67	0.92	14.29	21.42	21.28	10.62 ± 5.26
Top	Old	Inner	Middle	1.33	2.08	20.74	22.59	15.57	
Top	Old	Inner	Upper	1.69	2.17	19.39	24.83	11.50	
Top	Old	Outer	Lower	2.59	2.82	36.99	33.97	14.31	
Top	Old	Outer	Middle	3.54	4.50	55.29	36.91	15.60	
Top	Old	Outer	Upper	4.02	5.52	46.32	34.05	11.53	
Top	Young	Inner	Lower	3.76	9.01	15.56	14.68	4.13	
Top	Young	Inner	Middle	6.47	11.94	40.01	30.58	6.19	
Top	Young	Inner	Upper	10.26	7.19	64.82	27.43	6.32	
Top	Young	Outer	Lower	9.31	9.97	50.65	33.71	5.44	
Top	Young	Outer	Middle	12.03	10.80	77.23	27.21	6.42	
Top	Young	Outer	Upper	8.52	12.44	78.06	25.18	9.16	
Bottom	Old	Inner	Lower	0.15	0.32	1.60	2.39	10.96	35.44 ± 30.38
Bottom	Old	Inner	Middle	0.09	0.13	0.59	0.62	6.78	
Bottom	Old	Inner	Upper	0.14	0.18	10.27	15.91	73.98	
Bottom	Old	Outer	Lower	0.13	0.24	11.54	23.15	86.49	
Bottom	Old	Outer	Middle	0.56	1.81	19.88	25.76	35.38	
Bottom	Old	Outer	Upper	0.93	1.40	42.44	32.58	45.42	
Bottom	Young	Inner	Lower	0.09	0.17	1.57	1.35	17.65	
Bottom	Young	Inner	Middle	0.11	0.25	2.74	5.80	25.96	
Bottom	Young	Inner	Upper	0.24	0.43	6.13	5.10	25.60	
Bottom	Young	Outer	Lower	0.08	0.16	6.34	19.25	84.03	
Bottom	Young	Outer	Middle	1.58	6.19	8.95	15.25	5.67	
Bottom	Young	Outer	Upper	3.44	6.73	25.36	32.35	7.37	
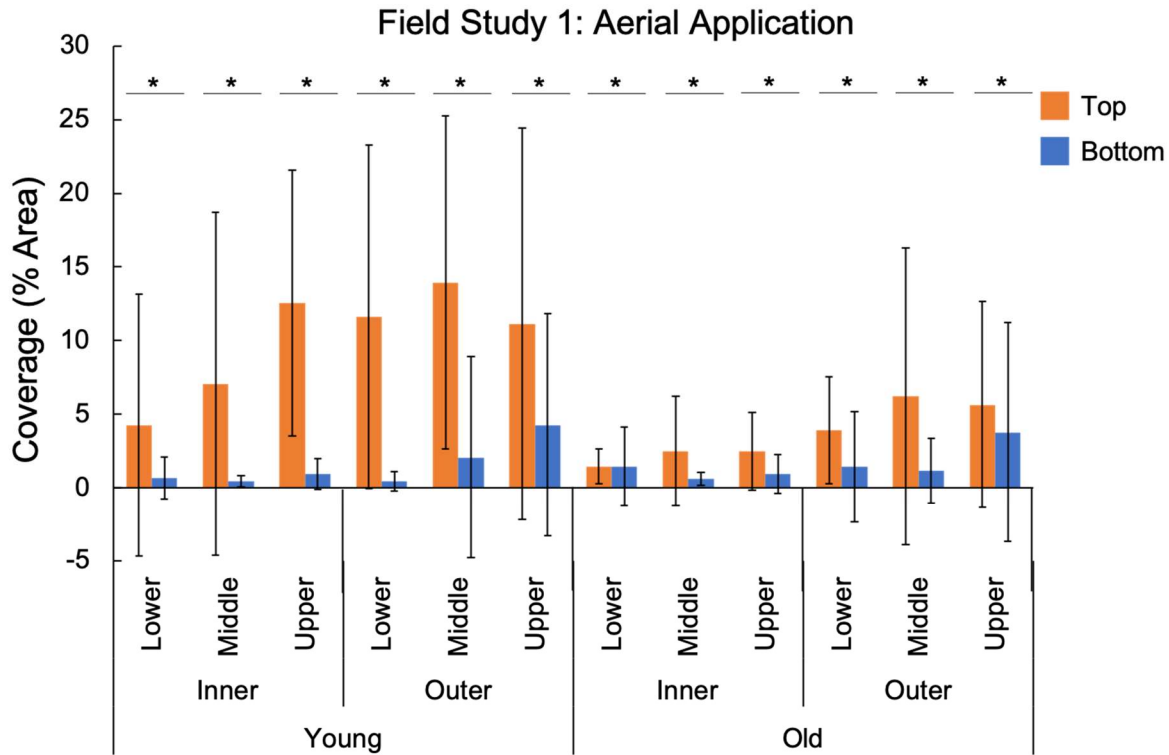
Figure A2.2 Bar graph of percent coverage of dye on top (orange) and bottom (blue) of leaves from Field Study 1: aerial application, divided into locations within young and old trees. Each bar is the average of 20 samplers, and the error bars represent $\pm 1\sigma$ around the mean. Stars (*) indicate a significant difference ($p < 0.05$, $n = 20$) between the two groups connected by the line ($p < 0.05$).
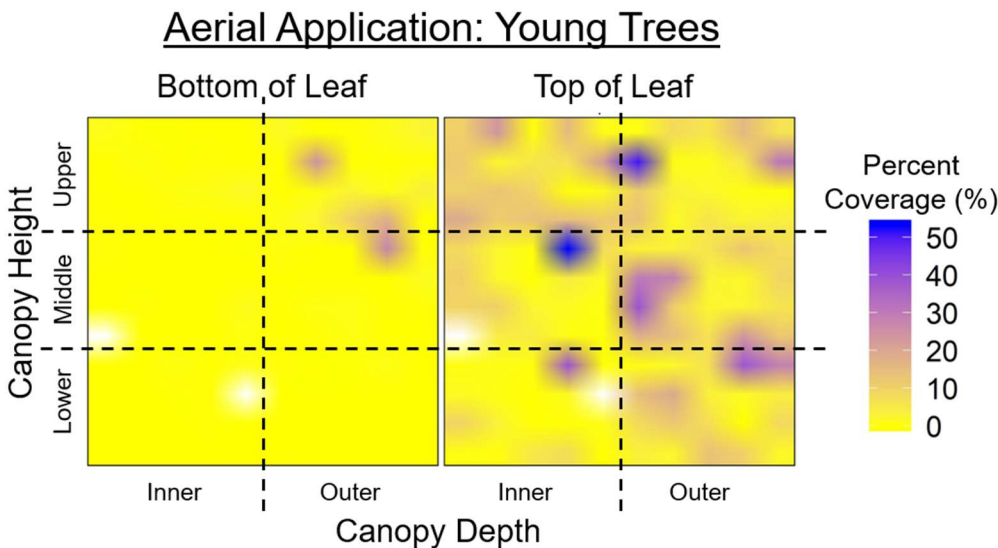

Figure A2.3 2D density plot of percent coverage of dye on bottom (left) and top (right) of leaves from Field Study 1: aerial application. Each plot is divided into 6 sampling locations. Each cell corresponds to one sampler, for a total of 20 samplers per location. The percent coverage is represented by a color scale, from 0% (yellow) to 50% coverage (blue). The white cells are missing samplers.

Table A2.4 Comparison of percent coverage between outer and inner canopy from Field Study 1 (October 2018) as applied by ground tractor and sorted by tree age.

Tree Age	Side of Leaf	Canopy Height	Inner Canopy		Outer Canopy		Factor (Outer/Inner)	Avg. ± St. Dev.
			Avg.	St. Dev.	Avg.	St. Dev.		
Old	Top	Lower	14.29	21.42	36.99	33.97	2.59	
Old	Top	Middle	20.74	22.59	55.29	36.91	2.67	
Old	Top	Upper	19.39	24.83	46.32	34.05	2.39	8.81 ± 12.41
Old	Bottom	Lower	1.60	2.39	11.54	23.15	7.20	
Old	Bottom	Middle	0.59	0.62	19.88	25.76	33.86	
Old	Bottom	Upper	10.27	15.91	42.44	32.58	4.13	
Young	Top	Lower	15.56	14.68	50.65	33.71	3.26	
Young	Top	Middle	40.01	30.58	77.23	27.21	1.93	
Young	Top	Upper	64.82	27.43	78.06	25.18	1.20	2.97 ± 1.17
Young	Bottom	Lower	1.57	1.35	6.34	19.25	4.03	
Young	Bottom	Middle	2.74	5.80	8.95	15.25	3.27	
Young	Bottom	Upper	6.13	5.10	25.36	32.35	4.14	
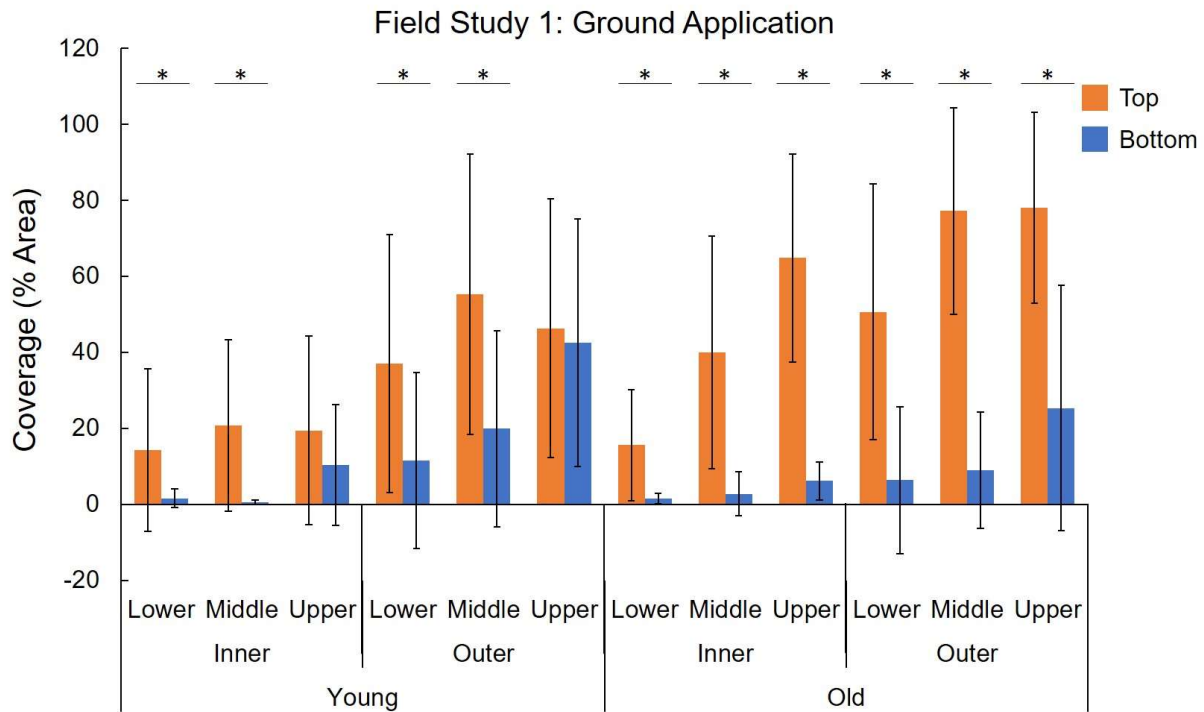
Figure A2.4 Bar graph of percent coverage of dye on top (orange) and bottom (blue) of leaves from Field Study 1: ground application, divided into locations within young and old trees. Each bar is the average of 20 samplers, and the error bars represent ±1σ around the mean. Stars (*) indicate a significant difference (p < 0.05, n = 20) between the two groups connected by the line.

136
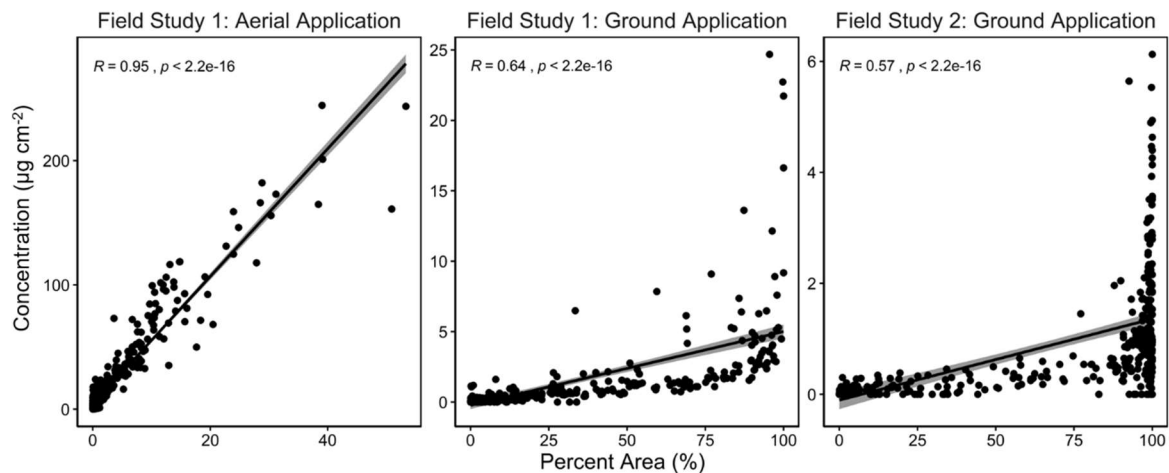
Figure A2.5 Correlation plots of pesticide amount vs percent area for Field Study 1 (October 2018) and Field Study 2 (April 2019). n = 510 samplers per application group.
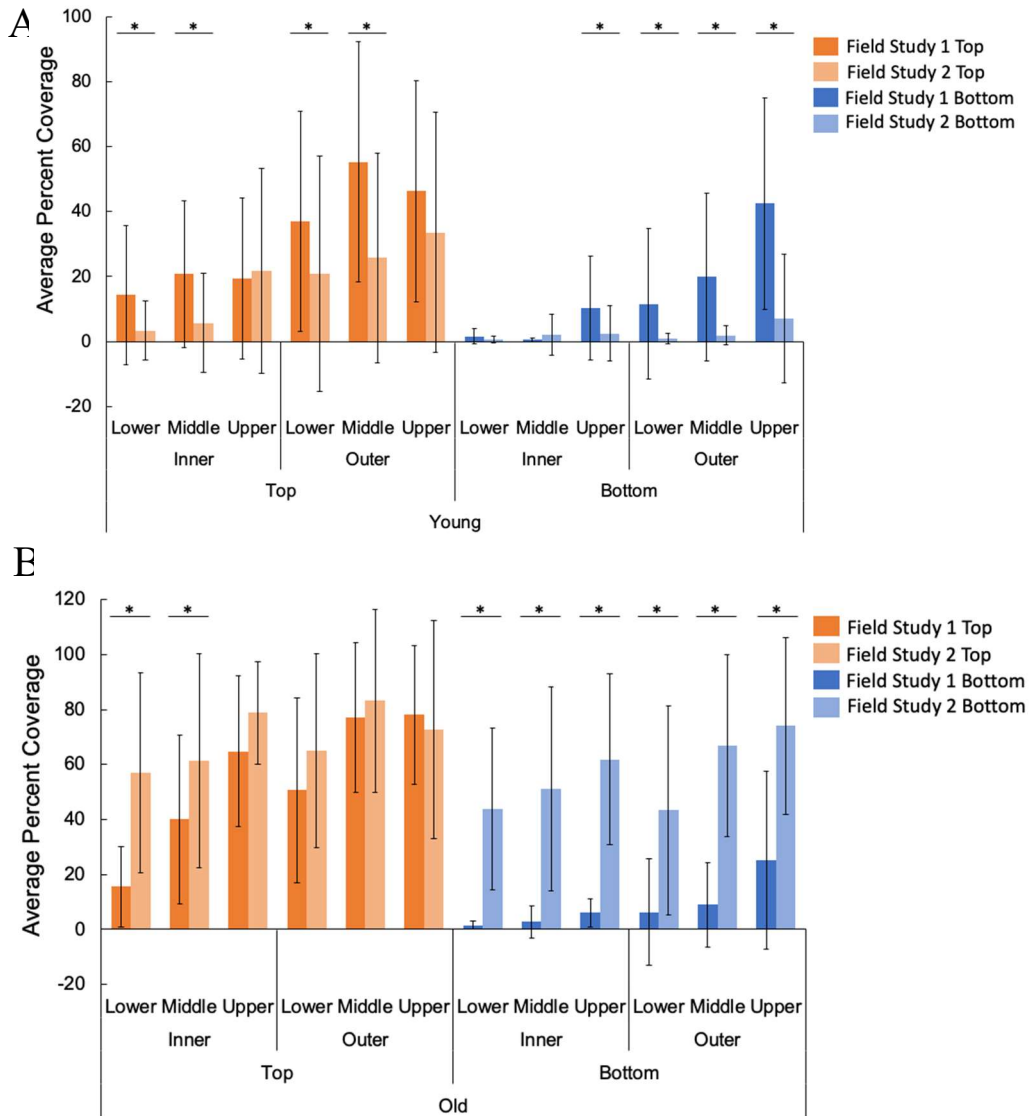
Figure A2.6 Comparison of Field Study 1 (Oct 2018) and 2 (Apr 2019) in young (A) and old (B) trees. For the young trees, the application rate was decreased from 35 GPA to 20 GPA during Field Study 2. For the old trees, the application rate was increased from 50 GPA to 90 GPA during Field Study 2. The tops of the leaves are the orange bars while the bottom of the leaves are the blue bars. Each bar is the average of 20 samplers, and the error bars represent $\pm 1\sigma$ around the mean. Stars (*) indicate a significant difference between field studies at that location in the tree ($p < 0.05$, n = 20).

Table A2.5 Comparison of Field Study 1 and Field Study 2 for the young trees with insecticide and dye applied by a side sprayer (ground application).

Tree Age	Side of Leaf	Canopy Depth	Canopy Height	Field Study 1 (Oct '18 – 35 GPA)			Field Study 2 (Apr '19 – 20 GPA)			Factor (Oct/Apr)	Avg. ± St. Dev.
				Avg.	St. Dev.	%RSD	Avg.	St. Dev.	%RSD		
Young	Top	Inner	Lower	14.29	21.42	149.90	3.39	9.03	266.72	4.22	2.34 ± 1.31
Young	Top	Inner	Middle	20.74	22.59	108.90	5.71	15.28	267.44	3.63	
Young	Top	Inner	Upper	19.39	24.83	128.05	21.73	31.54	145.14	0.89	
Young	Top	Outer	Lower	36.99	33.97	91.83	21.01	36.23	172.48	1.76	
Young	Top	Outer	Middle	55.29	36.91	66.75	25.71	32.34	125.77	2.15	
Young	Top	Outer	Upper	46.32	34.05	73.51	33.58	36.97	110.10	1.38	
Young	Bottom	Inner	Lower	1.60	2.39	148.87	0.57	0.99	174.54	2.83	5.84 ± 4.32
Young	Bottom	Inner	Middle	0.59	0.62	104.79	2.07	6.20	300.05	0.28	
Young	Bottom	Inner	Upper	10.27	15.91	154.88	2.45	8.48	345.75	4.19	
Young	Bottom	Outer	Lower	11.54	23.15	200.60	1.02	1.64	160.04	11.28	
Young	Bottom	Outer	Middle	19.88	25.76	129.57	1.91	2.92	153.25	10.43	
Young	Bottom	Outer	Upper	42.44	32.58	76.76	7.06	19.83	280.71	6.01	

Table A2.6 Comparison of Field Study 1 and Field Study 2 for the old trees with the insecticide and dye applied by a speed sprayer (ground application).

Tree Age	Side of Leaf	Canopy Depth	Canopy Height	Field Study 1 (Oct '18 – 50 GPA)			Field Study 2 (Apr '19 – 90 GPA)			Factor (Apr/Oct)	Avg. ± St. Dev.
				Avg.	St. Dev.	%RSD	Avg.	St. Dev.	%RSD		
Old	Top	Inner	Lower	15.56	14.68	94.37	57.01	36.34	63.74	3.66	1.62 ± 1.02
Old	Top	Inner	Middle	40.01	30.58	76.44	61.41	38.88	63.30	1.53	
Old	Top	Inner	Upper	64.82	27.43	42.31	78.80	18.68	23.71	1.22	
Old	Top	Outer	Lower	50.65	33.71	66.55	64.97	35.37	54.44	1.28	
Old	Top	Outer	Middle	77.23	27.21	35.23	83.20	33.31	40.04	1.08	
Old	Top	Outer	Upper	78.06	25.18	32.26	72.74	39.63	54.48	0.93	
Old	Bottom	Inner	Lower	1.57	1.35	85.89	43.81	29.35	66.99	27.85	12.31 ± 9.25
Old	Bottom	Inner	Middle	2.74	5.80	211.98	51.11	37.10	72.59	18.67	
Old	Bottom	Inner	Upper	6.13	5.10	83.11	61.86	31.12	50.30	10.09	
Old	Bottom	Outer	Lower	6.34	19.25	303.84	43.40	38.07	87.71	6.85	
Old	Bottom	Outer	Middle	8.95	15.25	170.39	66.75	33.10	49.58	7.46	
Old	Bottom	Outer	Upper	25.36	32.35	127.55	74.03	32.19	43.48	2.92	
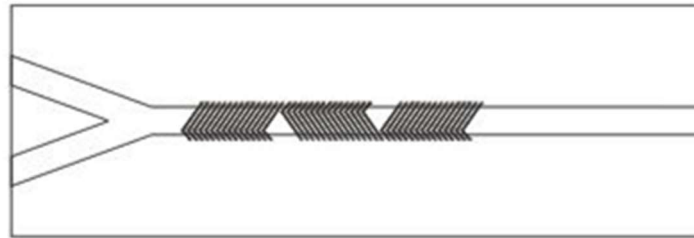
Figure A3.1 Schematic of herringbone grooves design overlaid with design for tape channels, made in CorelDraw and fabricated into glass and tape with an Epilog Zing laser cutter.
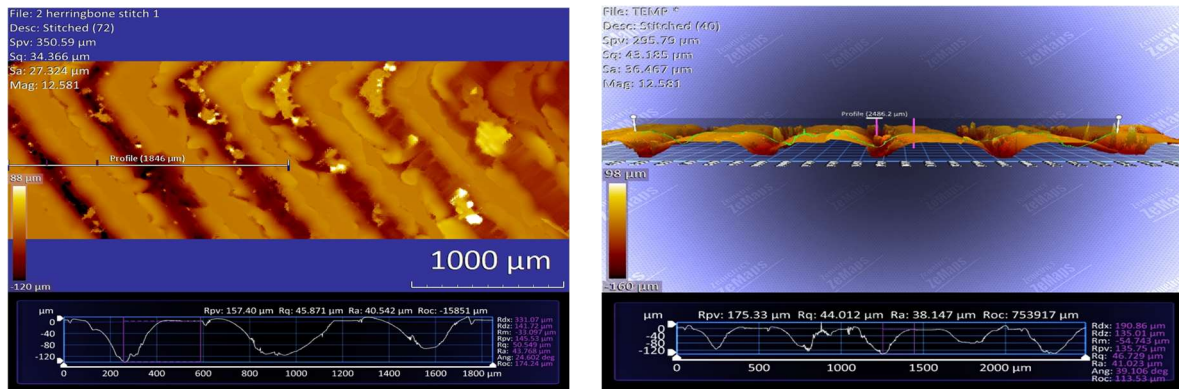
Figure A3.2 Optical profilometer data of the herringbone grooves.

To evaluate the degree of mixing, a still image of the blue and yellow dye reaction was analyzed. A rectangle before the herringbone and after the herringbone was selected for analysis (Figure A3.3). Briefly, the color threshold function in ImageJ (Image → Adjust → Color Threshold) was used to isolate each color (blue, yellow, and green). The number of thresholded
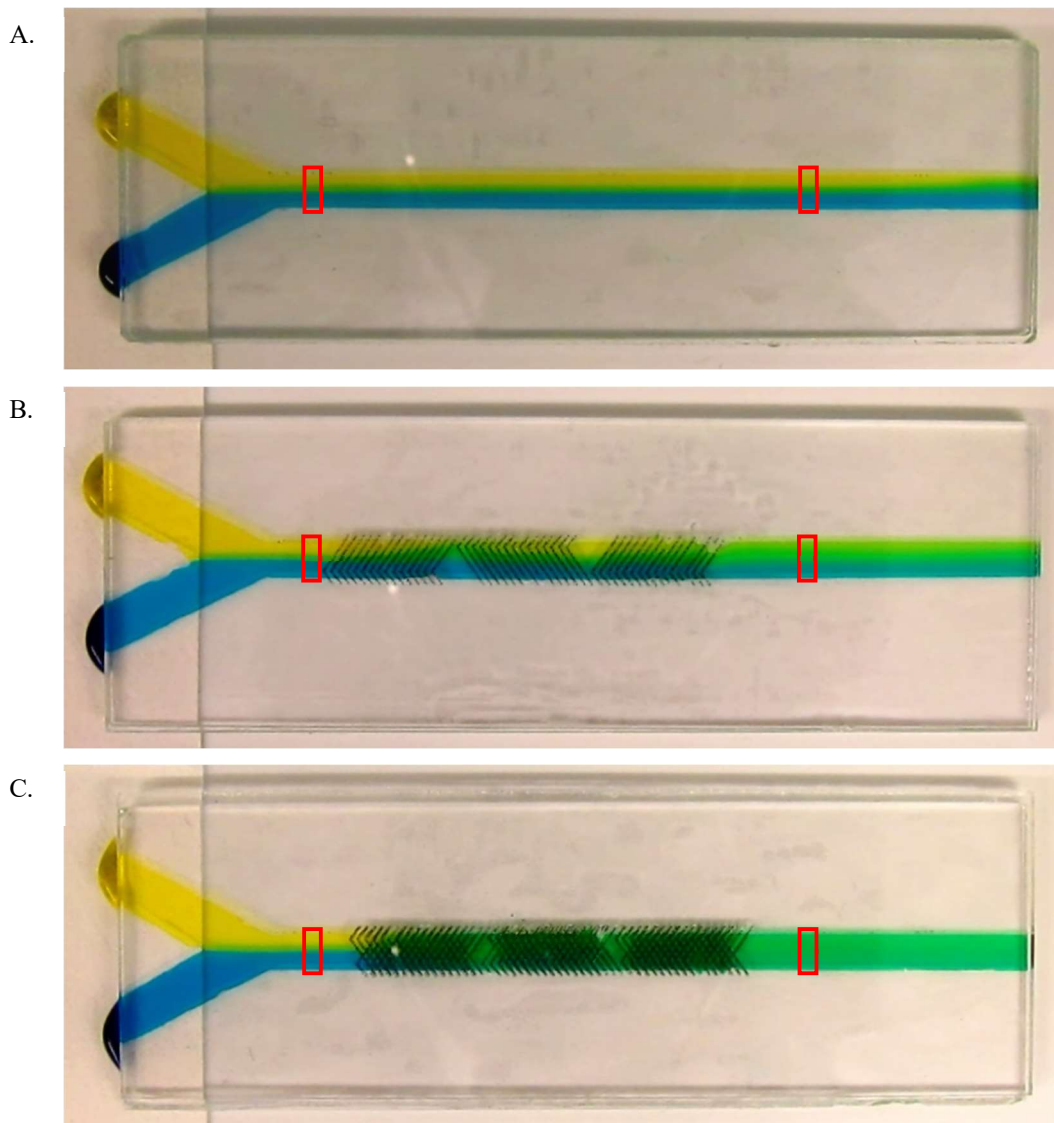
Figure A3.3 ImageJ analysis regions, marked by red boxes, to evaluate degree of mixing before and after herringbone grooves for 3 devices: A. 0 slides with herringbone grooves (straight channel) B. 1 slide with herringbone grooves, 1 slide without grooves C. 2 slides with mirrored herringbone grooves.

pixels was counted for each color in the rectangle before and after the herringbones (Analyze →

Histogram) and converted to a percent of the total number of pixels in the rectangle.
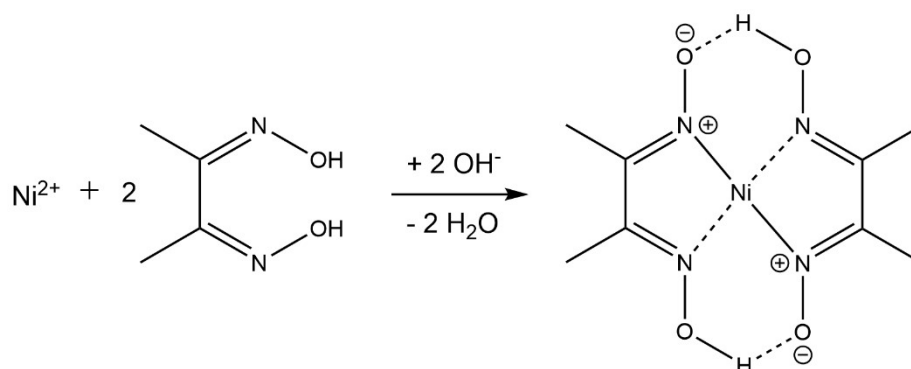
Figure A3.4 Reaction of nickel (Ni) and dimethylglyoxime (DMG).
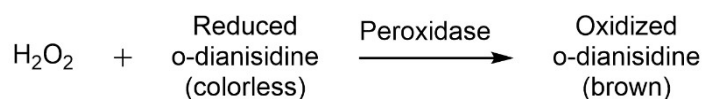
Figure A3.5 Reaction of hydrogen peroxide, o-dianisidine, and hydrogen peroxidase.

A3.2 Determining Michaelis-Menten Constants

To determine Michaelis-Menten constants of the enzymatic reaction, videos of the reaction

were analyzed. First, the videos were spliced into frames using Adapter. A rectangle right after the

herringbone grooves was analyzed for the average red, green, and blue (RGB) pixel values (Figure

A3.6). The color change was measured by calculating the Euclidean distance between the RGB

values of just the channel (baseline) and the RGB values of the channel with product to give a

graph of distance in RGB space *vs.* time for each substrate concentration (Figure A3.7). The

reaction rate for each concentration was determined by taking the slope of the linear portion of

each curve. The average color intensity was converted to substrate concentration using a

calibration curve. The calibration curve was generated by plotting maximum color intensity *vs.*

known substrate concentration and plotting a linear regression line. From this, a graph of reaction

rate (mmol s^{-1}) vs H_2O_2 concentration was generated. V_{max} and K_m values were calculated by

generating a Lineweaver-Burk plot. 1/[S] was plotted *vs*. 1/v and the inverse x- and y-intercepts were obtained.

Figure A3.6 ImageJ analysis regions of the reaction of hydrogen peroxide (top droplet) with hydrogen peroxide and o-dianisidine (bottom droplet).
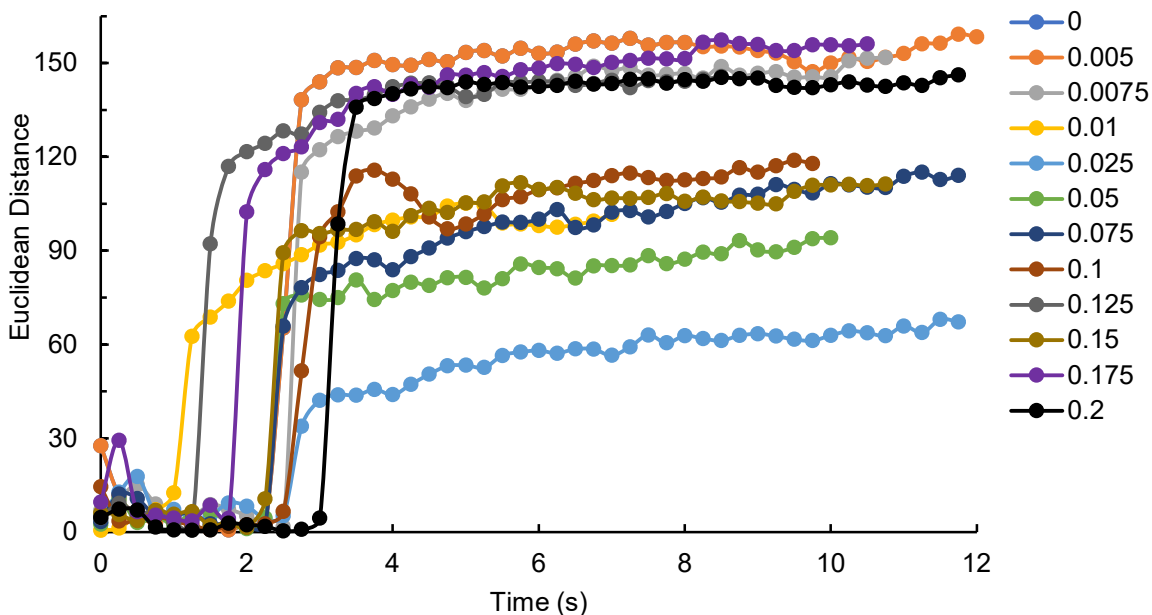
Figure A3.7 Graph of Euclidean distance in RGB space vs time for each substrate (hydrogen peroxide) concentration (mM).

APPENDIX 4: PUMP-FREE MICROFLUIDIC RAPID MIXER COMBINED WITH A
PAPER-BASED CHANNEL

Capillary forces are commonly employed to transport fluids in pump-free microfluidic platforms such as paper-based microfluidics. However, since paper is a porous material consisting of nonuniform cellulose fibers, it has some limitations in performing stable flow functions like mixing. Here we developed a pump-free microfluidic device that enables rapid mixing by combining paper and plastic. The device was fabricated by laminating transparency film and double-sided adhesive and is composed of an overlapping inlet ending in a paper-based reaction area. The mixing performance of the developed device was confirmed experimentally using aqueous dyes and pH indicators. In addition, the absolute mixing index was evaluated by numerically calculating the concentration field across the microfluidic channels. To demonstrate the utility of the new approach, the detection of an organophosphate pesticide was carried out using a colorimetric enzymatic inhibition assay. The developed device and a smartphone application were used to detect organophosphate pesticide on food samples, demonstrating the potential for on-site analysis. This work was published in *ACS Sensors*.[1] Dr. Ilhoon Jang developed the mixing device and performed the numerical modeling. Dr. Daniel Blascke Carrão and I developed and performed the organophosphate detection reaction. I also assisted with the initial pH mixing experiment as well as the editing of the manuscript.

A4.1 Introduction

Microfluidic devices that use capillary action to drive flow in a microchannel have attracted attention as on-site analytical devices because they do not require an external pump system.[2] Paper is a well-known material used to fabricate microfluidic channels and reaction areas in capillary-driven microfluidic devices, also called microfluidic paper-based analytical devices (μPADs).[3-5]

In these devices, colorimetric or electrochemical detection of analytes occurs when a fluid flows through the paper layer, driven by capillary forces, into a reaction area.[6-9] While paper has shown great potential as a substrate for analytical devices, flow is based on the inherent pore structure of the specific paper and therefore can be difficult to control. For example, sample evaporation and paper swelling can occur, resulting in unexpected changes in flow.[10-13] In addition, the mixing performance of single-layer μPADs cannot be manipulated by changing the flow rate or diffusion coefficient due to the mechanical dispersion characteristics of the paper.[14]

Rapid mixing in a microfluidic platform is important for many applications like complex chemical reactions, drug delivery, and nucleic acid synthesis, among others.[15, 16] However, the implementation of rapid mixing has been a challenge because the flow within microfluidic channels is laminar, and mixing is only achieved by diffusion at the fluid interface. Various methods have been used to enhance mixing and can be categorized as active and passive micromixers.[17, 18] Active micromixers employ an external force such as pressure, temperature, or acoustic waves to achieve high mixing performance. Passive mixers improve mixing performance by increasing the interface area of the different liquids or by manipulating the laminar flow within the microchannel using serpentine or herringbone structures. Passive mixing systems also have the advantage of not requiring external equipment for mixing. Various active and passive mixing systems have also been applied to improve mixing performance in μPADs.[14, 19, 20] Among these mixing systems, the lamination method, where overlapping channels increase the interface area of two fluids, has shown promise to significantly improve mixing performance.

The concept of laminating layers to form microfluidic channels was first introduced in 2001, for low-cost rapid prototyping of microfluidic channels.[21] In the lamination method, the channel geometry of each layer was formed before aligning and bonding with each other. Different

materials, such as polyester film,[22, 23] acrylic sheets,[24] glass slides,[25] paper,[26] and transparency film,[27, 28] have been bonded by double-sided adhesive (DSA), ethylene-vinyl acetate, oxygen plasma, or toner. The availability of various materials implies that the channel characteristics can be adjusted by changing the top and bottom layers covering the microchannel. In addition, the channel height can be adjusted by changing the thickness and number of DSA layers. Another feature of the lamination method is that multi-layered channels can be fabricated simply by stacking each layer. Although the lamination method has some advantages, it has seldomly been used for making microfluidic channels due to the low resolution of the channel geometry and the possibility of leakage between layers in pressure-driven devices.[29] However, capillary-driven devices that employ pressure drop on the fluid front decrease in pressure within the channel, and the pressure gradient along the channel decreases as flow distance increases.[30] Therefore, lamination-based channels can be employed in capillary-driven devices without worrying about leakage due to pressure.

Organophosphate pesticides (OPs) are the most commonly used insecticides worldwide, making up over 35 % of the applied insecticides in the US.[31] However, since the toxicity of OPs is related to several health conditions such as neurotoxicity,[32] infertility,[33] Alzheimer's disease,[34] Parkinson's disease,[35] and cancer,[36] the ingestion of food contaminated by OPs presents a potential risk to human health.[37-39] Therefore, the development of an on-site OP analysis platform is essential for food safety. Traditional analytical techniques such as high-performance liquid chromatography (HPLC), gas chromatography (GC), and capillary electrophoresis (CE) have been applied to evaluate the presence of OPs in food samples.[40-42] Although traditional techniques can sensitively detect OPs, they are not suitable for field-based analysis because of the need for trained analysts and expensive equipment in a centralized laboratory.[43] Enzymatic reactions are popular

for the rapid detection of OPs, due to their sensitivity and selectivity.[44] Recent studies using μPADs have shown acetylcholinesterase (AChE) activity can be used for OP detection based on AChE inhibition.[45-47] In these studies, each μPAD used different channel geometries to mix the AChE and OP in the device. Despite successful OP detection (6 nmol L^{-1} limit of detection),[45] mixing in previous studies was not efficient or rapid because it occurred in a single-layer paper-based channel.

In this study, we report a new, highly efficient, pump-free microfluidic mixer and demonstrate its use for the analysis of OPs on food samples. The passive mixer was fabricated by laminating transparency film and double-sided adhesive to form overlapping inlets, with colorimetric detection realized on a paper layer. First, we confirmed the mixing performance of the developed capillary-driven microfluidic device with dyed fluids and a pH indicator. The absolute mixing index in the mixing devices was numerically calculated. Then, we used the mixer for the determination of OPs using a colorimetric acetylcholinesterase inhibition assay.[48, 49] Different concentrations of one OP (malathion) were measured by analyzing the color of the mixed eluent collected on paper. Finally, we demonstrated OP detection on food samples (apple, cucumber, and tomato) and analysis with a smartphone application to show the potential as an on-site device.

A4.2 Materials and Methods

A4.2.1 Materials

Ultrapure water (R ≥ 18.2 MΩ cm at 25 °C, Milli-Q, Millipore) or methanol (HPLC grade) were used for preparing all solutions. Blue dye (erioglaucine, 800 μmol L^{-1}), yellow dye (tartrazine, 1870 μmol L^{-1}), phenol red (10 mmol L^{-1}, pH 4), and sodium hydroxide (10 mmol L^{-1},

pH 12) solutions were used for the mixing performance experiments. The organophosphate pesticide solution was prepared in an aqueous methanol solution (70 % v/v MeOH: H_2O) with different concentrations of malathion ($\geq$98.0 %) ranging from 0.001 to 5 µmol L^{-1}. Acetylcholinesterase from *Electrophorus electricus* (electric eel) was used as an enzyme. The acetylcholinesterase solution was prepared in tris(hydroxymethyl)aminomethane/potassium chloride (Tris-KCl) buffer (20 mmol L^{-1}, pH 7.4) + 10 % (m/v) bovine serum albumin (BSA) at 200 U mL^{-1}. The indicator solution was prepared with indoxyl acetate ($\geq$98.0 %) in methanol at 100 µmol L^{-1}. All chemicals were purchased from Sigma Aldrich (St. Louis, Missouri), except as noted above. The prepared solutions were stored at –20 °C and brought to 25 °C for 30 minutes before the experiment. The malathion insect spray concentrate (Spectracide) and food samples such as apple, cucumber, and tomato were purchased from a local grocery market in Fort Collins, CO, USA 1 day before the spray experiment.

A4.2.2 Device Fabrication

Figure A4.1a shows the developed capillary-driven microfluidic mixer consisting of two inlets, two microfluidic channels, and one outlet connected to a fan-shaped paper layer. The mixing device composed of 5 layers was fabricated by laminating transparency film (PP2500, 3M) and double-sided adhesive (467MP, 3M), as shown in Figure A4.1b and 1c. The top and bottom layers of transparency (light grey) cover the channel area, while the middle layers of transparency and tape define the channel geometry and height. Two inlet channels are formed in the 2nd and 4th layers out of tape and separated with transparency film (3rd layer, light grey). Two different geometries of the 3rd layer form a side-by-side inlet or overlapping inlet channels. These are
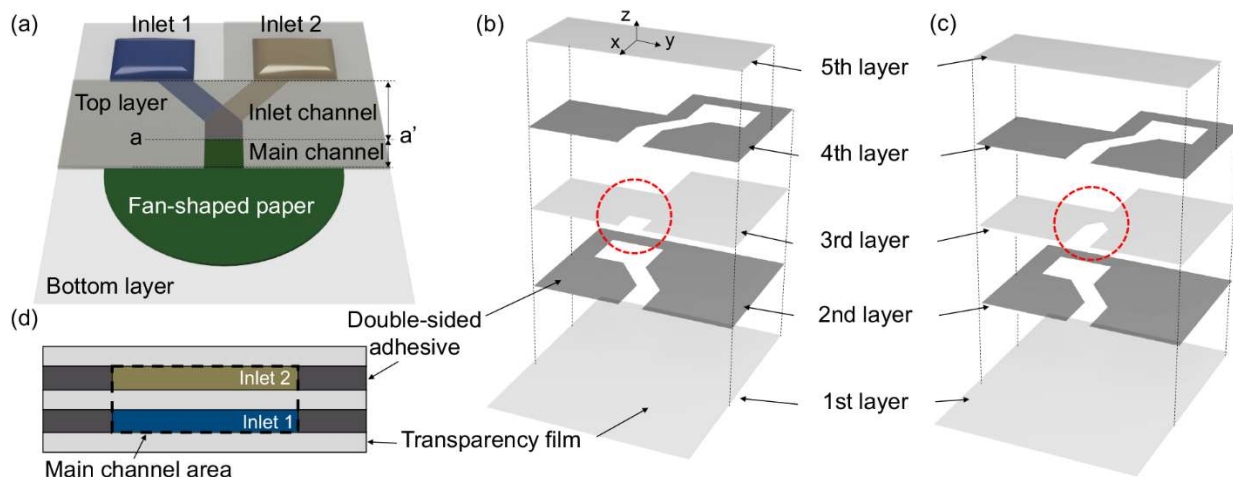
Figure A4.1 Schematics of the capillary-driven microfluidic mixer. (a) Assembled mixing device. The geometry of double-sided adhesives and transparency films for (b) overlapping inlet and (c) side-by-side inlet channels. Layers 1, 3, and 5 consist of transparency film (light grey) while layers 2 and 4 are made of double-sided adhesive (dark grey). The red circle indicates the different geometry of each channel type. (d) Cross-sectional view along the a-a' line in Figure A4.1a.

distinguished by whether a third layer exists in the main channel after the junction area or not, as marked with red circles in Figure A4.1b and c. For both geometries, the inlet channel has a height of 65 μm which is formed with one layer of DSA, and the main channel is 230 μm tall which includes 100 μm of height from one layer of transparency film with two layers of DSA. All channels are 3 mm wide. Chromatography paper (Grade 1 CHR, Whatman) was used to fabricate the fan-shaped paper which has a 9.5 mm radius with 180 degrees. The fan-shaped paper also has a rectangular area (3 mm x 1 mm) at the center of the half-circle which is inserted at the outlet of the mixing device after assembling the DSA and transparency film layers. All channel areas and fan-shaped paper were designed using design software (CorelDRAW X4, Corel) and cut using a laser cutter (Zing 10000, Epilog Laser).

A4.2.3 Numerical Analysis Method

Numerical analysis was performed using in-house MATLAB code. The main channel region with a 3 mm width, 6 mm length, and 0.23 mm height was generated with 200,000

hexahedral meshes. We used the first-order forward discretization in the time and x-direction and the second-order central discretization in the y-direction and z-direction to obtain the finite difference equation. The time interval for the calculation was 0.001 s and the total flow time was 30 s. A constant concentration, zero-gradient, and zero-flux were used to represent inlet, outlet, and wall boundary conditions, respectively. We set all regions of interest to zero concentration initially and applied boundary conditions such as side-by-side inlet and overlapping inlet.

A4.2.4 Acetylcholinesterase Inhibition Assay

The concentrations and volumes of the indoxyl acetate solution, the concentration of the acetylcholinesterase solution, and reaction time were previously optimized. The fan-shaped paper was prepared by dropcasting 20 µL of indoxyl acetate solution (25 µmol L^{-1} in methanol) onto the paper and placing it in the fridge for 10 min to dry the methanol before inserting in the device. For the assay, 15 µL of the acetylcholinesterase solution and 15 µL of water: methanol solution (70:30 v/v), pesticide solution (malathion), or sample solution were pipetted on the device inlet areas. After 15 min of reaction, a picture of the fan-shaped paper was taken using a smartphone camera.

A4.2.5 Image Analysis

The images of the fan-shaped papers were taken using a smartphone camera under laboratory conditions. To analyze the images, we evaluated which color channel presented the best correlation vs malathion concentration. The entire area of each fan-shaped paper was averaged after splitting the image into the red, blue, green, and gray color components using ImageJ software (NIH). The intensity values of each color component range from 0 to 255. The red channel was selected for the analysis since it had the best correlation with the malathion concentration. Finally,

the normalized intensities were calculated based on the mean red intensity of the blank paper (221.86). Details are described in Appendix 5.1.

A4.2.6 Malathion Determination in Food Samples

To simulate the presence of pesticides on food samples, a malathion insect spray concentrate (Spectracide) solution was sprayed on apples, cucumbers, and tomatoes using a spray chamber (Devries Generation 4 Research Track Sprayer, Hollandale, MN, USA) equipped with a TeeJet 8002EV8 spray nozzle (Glendale Heights, IL, USA). Details are described in Appendix A5.4. The sprayed malathion on apples, cucumbers, and tomatoes was extracted from a total of nine different samples using a "paste, peel off, solubilize" procedure similarly as described by Jiang et al.[50] The adhesive tape (Scotch, 3M) with 12 x 12 cm was pasted in the peel of the food. After then, the tape was peeled off and solubilize in water: methanol solution (70:30 v/v).

A4.2.7 Smartphone Application

The smartphone application was developed for an iPhone 11 Pro through Xcode (Apple). The first step is to capture or load an image from the library. We prepared the images of the fan-shaped paper by cutting out the outer area of the paper so that the application can recognize the fan-shaped area. The color analysis steps consisted of image select, image analysis, and display results. The application splits the original image into the red, green, and blue color channels and calculated the grayscale values (R + G + B /3). Each color component was displayed on the smartphone screen after averaging over the paper area. Finally, the pesticide concentration was calculated based on the calibration curve.

A4.3 Results and Discussion

A4.3.1 Mixing Experiments

A capillary-driven microfluidic mixer consisting of two inlets, two microfluidic channels, and one outlet connected to a fan-shaped paper layer was fabricated from transparency film and double-sided adhesive (DSA) (Figure A4.1). The inlet and main channels have heights of 65 and 230 μm, respectively, and surface tension acts to transport the fluid from the inlet through the device. In the capillary-driven mixer system, which consists of a closed channel, the two fluids should enter the main channel area at the same time to ensure mixing. If one fluid enters the main channel before the other, air is trapped between the two fluids, causing the second fluid to stop at the inlet channel. An abrupt change in channel geometry has been used to halt the flow in capillary-driven microfluidic channels in a concept called a trigger valve.[51] This geometry can be used to simultaneously release multiple fluids into the downstream channel.[52] Since our device has a large height difference between the inlet and main channels, the inlet channel worked as a simultaneous inflow system. Therefore, even though each fluid was injected manually, two fluids can flow simultaneously without air trapping problems (Figure A4.2).
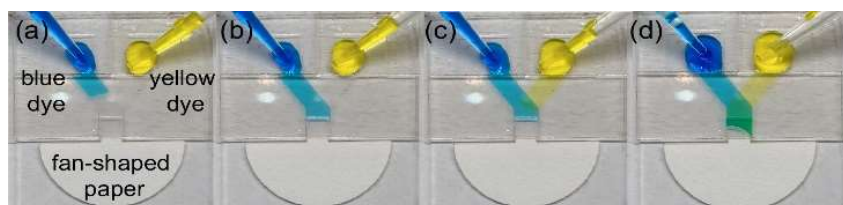
Figure A4.2 Sequential images after injecting blue and yellow dyes on each inlet of the mixer device. The blue dye (a) flows first and (b) stops at the junction until (c) the yellow dye arrives. (d) Finally, both fluids meet each other and flow the main channel. The flow time between (a) and (d) was about 1 s.

After the fluid front reaches the fan-shaped paper at the outlet, the paper layer acts as a capillary pump to sustain flow. Since the fan-shaped paper can provide a constant flow to its upstream, as introduced previously,[53-56] flow in the main channel is maintained as the fluid wets the paper layer. The constant flow rate implies that the mixer can continuously mix the two fluids

153

without interfering with mixing performance. Alternatively, the outlet of the main channel can be considered a reservoir for supplying fluid to the fan-shaped paper. This configuration enables the fast wetting of the paper because the flow length from the source to the end of the paper is short. The total flow time to wet a paper was about 40 s which is much shorter than the paper-based mixer (5 min) developed by Kang et al. with a similar length and geometry.[57]

Mixing of the two fluids occurs at their interface in the main channel. To increase the interface area[17, 18] between the two solutions, we devised a method of fabricating overlapping inlet channels by laminating DSA and transparent films. The method also provides the ability to define the channel geometry during the cutting process as well as easily constructing multi-layer geometries through lamination. The overlapping inlet channels are separated using transparency film in the center (Figure A4. 1d) and are connected to the main channel without interference with each other. Two inlet channels placed in different vertical positions establish a long interface between the two solutions while maintaining a short mixing distance in the horizontal direction, resulting in rapid mixing.

To confirm the mixing performance of the overlapping inlet channels, we compared the mixing flow of overlapping inlet channels to side-by-side inlet channels. The dimensions of the two channel types are the same; just the inlet geometry was changed. The side-by-side inlet channel was fabricated by replacing the 3rd layer (transparency film) with a different design. Aqueous droplets of blue and yellow dye (15 µL) were placed at the entrance of the inlet channels (Figure A4.3a). Since the two fluids are mixed in the main channel and flow into the fan-shaped paper for both configurations, we can confirm the mixing performance by comparing colors in the main channel and fan-shaped paper. As shown in Figure A4.3a, mixing only occurs at the interface of the blue and yellow dye in the side-by-side inlet channel (i). In contrast, the overlapping inlet

154
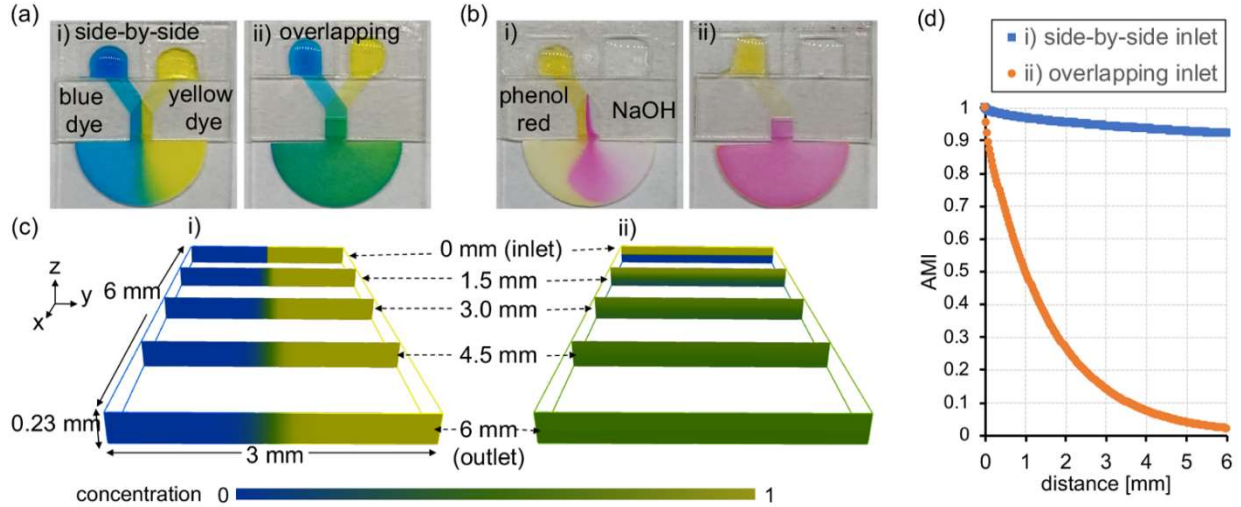
Figure A4.3 Images of mixing experiment for (a) blue and yellow dye and (b) phenol red (pH 4) and sodium hydroxide (pH 12) solutions. All images were captured right after the fan-shaped paper was fully wetted. (c) Concentration fields of a cross-sectional plane along the main channel. Concentrations are represented with colors. (d) Absolute mixing index (AMI) plot along the distance from the junction. In Figure A4.3b, side-by-side inlet and overlapped inlet channel marked by i) and ii), respectively.

channel (ii) mixes completely, producing a green color in the entire area of the main channel and fan-shaped paper. To further prove mixing is occurring, phenol red and sodium hydroxide solutions were used to demonstrate a simple chemical reaction (Figure A4.3b). Like the dye experiments, the overlapping inlet channel shows a much higher mixing performance than the side-by-side inlet channel, resulting in a uniform color change in both the main channel and paper layer. Interestingly, uniform green and pink colors appeared immediately at the main channel entrance along the entire channel width for both mixing experiments. This demonstrates that the long interface formed by the overlapping inlets dramatically improves mixing performance.

A4.3.2 Numerical Analysis of Mixing Performance

The quantitative mixing performance of the laminated devices was compared by performing a numerical simulation for each device. To describe the concentration fields in the main channel, we used the following three-dimensional convection-diffusion (C-D) equation:

$$\partial\emptyset/\partial t = D(\partial^2\emptyset/\partial y^2 + \partial^2\emptyset/\partial z^2) - U\,\partial\emptyset/\partial x \qquad (1)$$

155

where Ø is concentration, t is time, D is diffusivity, and U is flow velocity in the x-direction.[58] The C-D equation has previously been used to describe the mixing flow in microfluidic channels.[14, 19] The main channel geometry of the actual mixing device is 6 mm long, 3 mm wide, and 0.23 mm tall. Velocity and diffusivity in the C-D equation were obtained from the phenol red/sodium hydroxide experiments. Details of numerical simulation are described in Appendix 5.2. Figure A4.3c shows the simulated concentration fields of cross-sectional views of the side-by-side inlet (i) and overlapping inlet (ii) channels. The 0 mm plane represents the inlet conditions formed for each geometry. Although the occupied area of each fluid is the same at the inlet, the concentration field develops differently as the fluid moves downstream. This is because the overlapping inlet channel has a long interfacial length as well as a short mixing distance. We calculated an absolute mixing index (AMI) that indicates the mixing performance with values from 0 (perfect mixing) to 1 (non-mixing). Details of the AMI are described in Appendix A5.3. Figure A4.3d shows the AMI variation vs distance from the junction for two mixing channels. At the inlet area (0 mm), both channels have an AMI value of 1 (no mixing). However, the AMI values of the overlapping inlet channel decrease rapidly as distance increases, unlike the side-by-side inlet channel. For example, at 3 mm from the inlet, the AMI of the overlapping inlet channel is less than 0.15, while the side-by-side inlet channel still has a value greater than 0.9. Since the AMIs were calculated based on the phenol red/sodium hydroxide experiments, the AMI result does not indicate the absolute performance of the mixer. The mixing result will vary with the flow characteristics such as the diffusivity and velocity. However, the results of the mixing experiments and numerical simulations show that the mixing device consisting of the overlapping inlet can mix the two fluids extremely fast in a short distance and transport it to the fan-shaped paper without using an external pump.

A4.3.3 Pesticide Determination

The developed capillary-driven microfluidic mixer was used for the determination of organophosphate pesticides (OPs) through a colorimetric enzymatic inhibition assay.[49, 59, 60] We employed acetylcholinesterase as the enzyme and indoxyl acetate as the indicator.[61, 62] The indicator is converted into a blue product in a reaction catalyzed by the enzyme. The presence of OPs inhibits the activity of the enzyme, causing decreased blue product formation which correlates to the concentration of OPs. To implement the colorimetric OP analysis in the capillary-driven mixing device, OP sample (malathion) and enzyme solutions are mixed in the overlapping inlet channel and then react with the indoxyl acetate indicator infused on the fan-shaped paper to form a blue product. In this assay, the fan-shaped paper functions as a capillary pump as well as the reaction area. The fan-shaped paper was completely wetted by the mixed solution within 1 min, and the color change of the fan-shaped paper was analyzed 15 min after the droplets were introduced to the device. All experiments were carried out with a new mixing device because the flow characteristics can change after the channel is wet.

Figure A4.4 shows the results of OP determination using the capillary-driven microfluidic mixer. We used nine different concentrations of the malathion ranging from 0 to 5.00 µmol L^{-1}. Figure A4.4a presents the images of the fan-shaped paper for all malathion concentrations. Since malathion inhibits acetylcholinesterase, the blue color intensity decreases as the concentration of malathion increases. In addition, the blue product is distributed uniformly on the paper due to the rapid and complete mixing of malathion and enzyme solutions. The degree of inhibition could also be affected by the incubation time between the malathion and the enzyme.[63] In our mixing device, the incubation time was about 6s before reaching the paper. The incubation time can be adjusted by changing the length of the main channel or the shape of the paper layer. Since the changes in

channel and paper size can affect the distribution of the blue product, the volume of each solution should be optimized before performing the analysis.
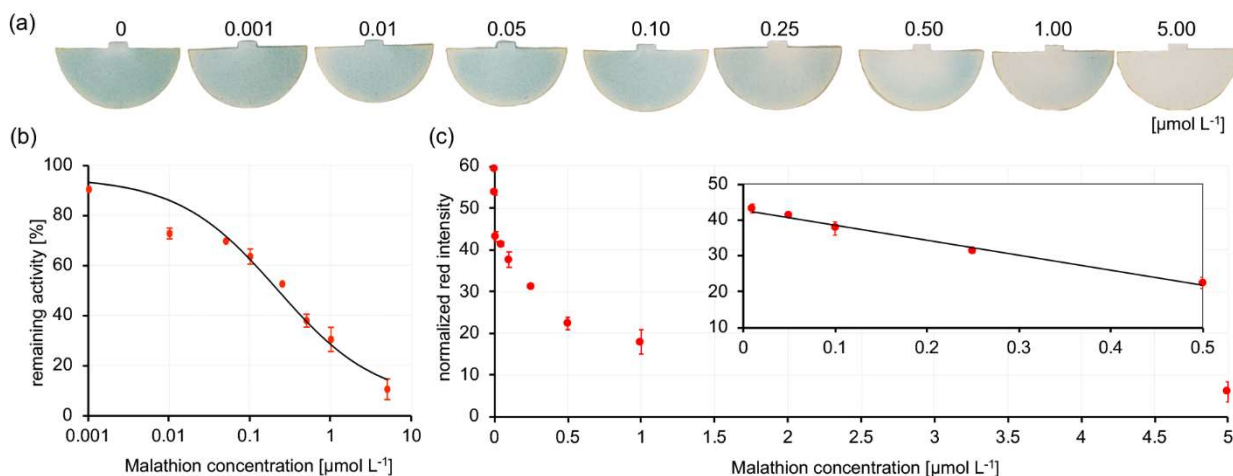

Figure A4.4 (a) Images of the fan-shaped paper for all evaluated concentrations of malathion. All images were taken 15 minutes after the droplets were introduced to the device. (b) Plot of the remaining enzyme activity versus malathion concentration and the dose-response graph to determine the IC_{50} value. (c) Normalized red intensity values with respect to malathion concentration ranging from 0 to 5 µmol L^{-1}. The inset shows the enlarged range of malathion concentration from 0.1 to 0.5 µmol L^{-1}. The calibration curve is $y = -42.27(\pm1.82)\, x + 42.82(\pm0.46)$ with an R^2 of 0.9875. All data points and error bars show the averages and standard deviations of 3 repeated experimental results, respectively.

To demonstrate an application of the capillary-driven mixer using the enzymatic inhibition assay, the concentration of malathion responsible for 50% inhibition of the enzymatic activity (IC_{50}) was determined.[64] The IC_{50} value was based on the remaining activity values listed in Table S1 in the Supporting Information. The remaining enzymatic activity was calculated using the normalized mean red intensity of the entire fan-shaped paper. Figure A4.4b shows the dose-response plot used to determine the IC_{50} value for the inhibition of acetylcholinesterase activity by malathion. The remaining activity follows the IC_{50} curve with $R^2 = 0.9581$. The obtained IC_{50} value was 0.22 ± 0.06 µmol L^{-1}, which is within the literature values ($0.05 - 25$ µmol L^{-1}) reported for acetylcholinesterase inhibition by malathion.[65-68] This result demonstrates the potential application of the capillary-driven microfluidic mixer for the determination of OPs. Next, the normalized red intensity vs malathion concentration was plotted to evaluate the calibration curve.

While the full evaluated range did not have a linear fit (Figure A4.4c), an acceptable linear calibration curve was obtained using the concentration range from 10 to 500 nmol L^{-1}. The limit of quantification (LOQ) was 10 nmol L^{-1}, which was determined based on the linear range of the calibration curve. Below 10 nmol L^{-1}, the response, although detectable, was non-linear. The obtained results were comparable to previous pesticide sensors using paper that showed the LOD of 6 nmol L^{-1}.[45]

A4.3.4 Demonstration of Field-Based Organophosphate Detection

Finally, the developed method was applied to determine malathion on apples, cucumbers, and tomatoes. Samples were sprayed with malathion, and a "paste, peel off, solubilize" procedure using adhesive tape was used to extract the OP from the peel of the samples as shown in Figure A4.5a.[50] The "paste and peel off" procedure allows pesticides to be easily extracted from the surface of the vegetable and fruit peels due to the sticky and flexible feature of the adhesive tape. The advantages of using this procedure are adhesive tape is an inexpensive and accessible material, the extraction procedure is fast, and the procedure can be performed outside of laboratories by
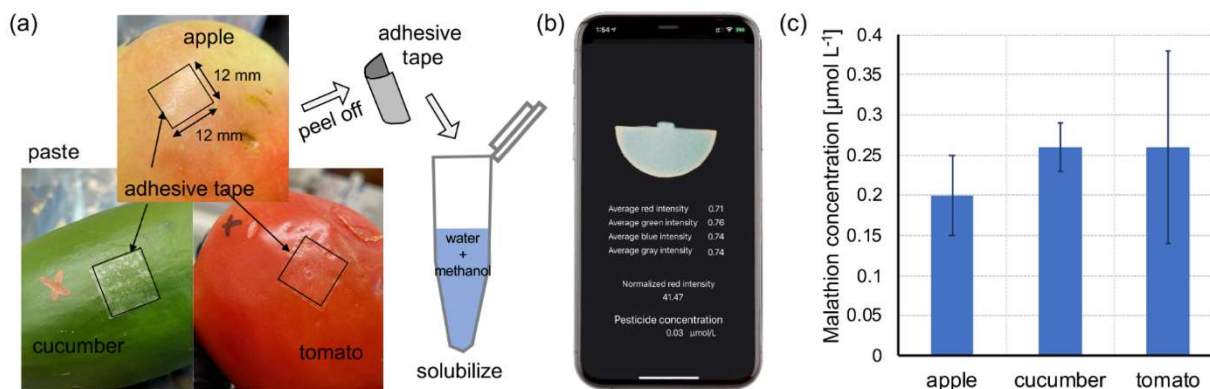
Figure A4.5 (a) Schematics of the "paste, peel off, solubilize" method used for extracting pesticides from food samples such as apple, cucumber, and tomato. The solubilized solution was used as a sample solution. (b) Captured image of the smartphone screen indicating the color analysis results and pesticide concentration. (c) Malathion concentrations measured from the food samples. All data and error bar show the averages and standard deviations of 3 different experimental results, respectively.

anyone. To confirm the lack of interference from the adhesive tape in the colorimetric enzymatic inhibition assay, a control experiment was performed, and it was confirmed that there is no significant interference from the tape (Appendix A5.5, Figure A5.5).

Food samples sprayed with malathion were subjected to the extraction procedure using adhesive tape and the colorimetric enzymatic inhibition assay using the capillary-driven microfluidic mixer was performed. The color change of fan-shaped paper was analyzed using a developed smartphone application for iPhone. Since the smartphone application contained the color analysis function with a calibration curve, the concentration of malathion could be determined without using a computer (Figure A4.5b). Although the smartphone application displayed all color components of the image, it used only the red intensity to determine the pesticide concentration. Figure A4.5c and Table A4.1 present the determined concentration of malathion in each food sample (apple, cucumber, and tomato). The concentration of solubilized samples was determined using the color of the fan-shaped paper and calibration curve (Figure A4.4c). The measured concentration indicates the concentration of extract solution by adhesive tape, and the concentration per unit area of the peel was calculated based on the area of adhesive tape used for the extraction process. The converted mass-to-area ratio of the malathion on the apple was 9.24 ng cm^{-2} (calculated by the molar mass of malathion, 330 g mol^{-1}) which was lower than the literature value of 28.8 ng cm^{-2} confirmed to be sufficient for actual applications.[50]

Table A4.1 Results of malathion determination on the food sample.

Food	Measured concentration [μmol L^{-1}]	Concentration per unit area [nmol cm^{-2}]
Apple	0.20 ± 0.05	0.028 ± 0.007
Cucumber	0.26 ± 0.03	0.036 ± 0.004
Tomato	0.26 ± 0.12	0.036 ± 0.017

Although all samples were exposed to the same experimental conditions, the pesticide on the apple was ~20% lower than the cucumber and tomato. Also, the standard deviation for the tomato is relatively large compared to others. This could be caused by differences in food sample smoothness, shell thickness, or the nonuniformity of pesticide spraying.[50] Also, large sampling could help to improve the standard deviation. Improvement in the extraction process might increase the performance of on-site pesticide analysis, allowing the accurate determination of food safety. However, we confirmed that the extraction process, as well as a smartphone application, have been successfully utilized with a colorimetric enzymatic inhibition assay in the mixer device for the pesticide determination of food samples for the first time. This result shows that our method has potential as an on-site device.

A4.4 Conclusion

In this work, we reported a capillary-driven microfluidic mixer for the analysis of organophosphate pesticides (OPs). All the functions of the device, such as mixing, sample transport, and analysis, were developed in consideration of an environment where the use of equipment is limited. We employed simple paper, transparency film, and double-sided adhesive to fabricate mixing devices, resulting in increased accessibility at low cost. The developed device was fabricated by laminating transparency film and double-sided adhesive and consisted of an overlapping inlet geometry. A fan-shaped paper was used at the end of the microfluidic channel to maintain upstream flow and to provide a reaction/detection area. The mixing performance was confirmed by comparing the overlapping inlet to a side-by-side inlet experimentally as well as numerically. Combining the lamination-based and paper-based channel allows for stable flow functions such as rapid mixing as well as a decreased wetting time of the paper layer. After that,

we used the developed device to analyze OPs by a colorimetric acetylcholinesterase inhibition assay. The pesticide determination was evaluated using the IC_{50} curve and a linear calibration curve was obtained ranging from 10 to 500 nmol L^{-1}. Finally, OP determination in food samples was successfully performed using the pump-free rapid mixer, a "paste, peel off, solubilize" extraction procedure, and a smartphone application.

REFERENCES

1.   Jang, I.; Carrão, D. B.; Menger, R. F.; Moraes De Oliveira, A. R.; Henry, C. S., Pump-Free Microfluidic Rapid Mixer Combined with a Paper-Based Channel. *ACS Sensors* **2020,** *5* (7), 2230-2238.

2.   Boyd-Moss, M.; Baratchi, S.; Di Venere, M.; Khoshmanesh, K., Self-contained microfluidic systems: a review. *Lab Chip* **2016,** *16* (17), 3177-3192.

3.   Nilghaz, A.; Guan, L.; Tan, W.; Shen, W., Advances of Paper-Based Microfluidics for Diagnostics—The Original Motivation and Current Status. *ACS Sensors* **2016,** *1* (12), 1382-1393.

4.   Carrell, C.; Kava, A.; Nguyen, M.; Menger, R. F.; Munshi, Z.; Call, Z.; Nussbaum, M.; Henry, C., Beyond the lateral flow assay: A review of paper-based microfluidics. *Microelectron. Eng.* **2019,** *206*, 45-54.

5.   Cate, D. M.; Adkins, J. A.; Mettakoonpitak, J.; Henry, C. S., Recent Developments in Paper-Based Microfluidic Devices. *Anal. Chem.* **2015,** *87* (1), 19-41.

6.   Liu, B. W.; Du, D.; Hua, X.; Yu, X. Y.; Lin, Y. H., Paper-Based Electrochemical Biosensors: From Test Strips to Paper-Based Microfluidics. *Electroanalysis* **2014,** *26* (6), 1214-1223.

7.   Mettakoonpitak, J.; Boehle, K.; Nantaphol, S.; Teengam, P.; Adkins, J. A.; Srisa-Art, M.; Henry, C. S., Electrochemistry on Paper-based Analytical Devices: A Review. *Electroanalysis* **2016,** *28* (7), 1420-1436.

8.   Morbioli, G. G.; Mazzu-Nascimento, T.; Stockton, A. M.; Carrilho, E., Technical aspects and challenges of colorimetric detection with microfluidic paper-based analytical devices (μPADs) - A review. *Anal. Chim. Acta* **2017,** *970*, 1-22.

9.   Noviana, E.; McCord, C. P.; Clark, K. M.; Jang, I.; Henry, C. S., Electrochemical paper-based devices: sensing approaches and progress toward practical applications. *Lab Chip* **2020,** *20* (1), 9-34.

10.   Elizalde, E.; Urteaga, R.; Berli, C. L. A., Rational design of capillary-driven flows for paper-based microfluidics. *Lab Chip* **2015,** *15* (10), 2173-2180.

11.   Songok, J.; Toivakka, M., Controlling capillary-driven surface flow on a paper-based microfluidic channel. *Microfluid. Nanofluid.* **2016,** *20* (63), 1-9.

12.   Liu, M.; Wu, J.; Gan, Y.; Hanaor, D. A. H.; Chen, C. Q., Evaporation Limited Radial Capillary Penetration in Porous Media. *Langmuir* **2016,** *32* (38), 9899-9904.

13.   Chang, S.; Seo, J.; Hong, S.; Lee, D.-G.; Kim, W., Dynamics of liquid imbibition through paper with intra-fibre pores. *J. Fluid. Mech.* **2018,** *845*, 36-50.

14.   Jang, I.; Kim, G.; Song, S., Mathematical model for mixing in a paper-based channel and applications to the generation of a concentration gradient. *Int. J. Heat Mass Tranf.* **2018,** *120*, 830-837.

15.   Nguyen, N.-T.; Wu, Z., Micromixers—a review. *J. Micromech. Microeng.* **2004,** *15* (2), 1-16.

16.   Suh, Y. K.; Kang, S., A Review on Mixing in Microfluidics. *Micromachines* **2010,** *1* (3), 82-111.

17.   Hessel, V.; Löwe, H.; Schönfeld, F., Micromixers—a review on passive and active mixing principles. *Chem. Eng. Sci.* **2005,** *60* (8), 2479-2501.

18.   Lee, C.-Y.; Chang, C.-L.; Wang, Y.-N.; Fu, L.-M., Microfluidic Mixing: A Review. *Int. J. Mol. Sci.* **2011,** *12* (5), 3263-3287.

19.   Schaumburg, F.; Urteaga, R.; Kler, P. A.; Berli, C. L. A., Design keys for paper-based concentration gradient generators. *J. Chromatogr. A.* **2018,** *1561*, 83-91.

20.   Osborn, J. L.; Lutz, B.; Fu, E.; Kauffman, P.; Stevens, D. Y.; Yager, P., Microfluidics without pumps: reinventing the T-sensor and H-filter in paper networks. *Lab Chip* **2010,** *10* (20), 2659-2665.

21.   Weigl, B. H.; Bardell, R.; Schulte, T.; Battrell, F.; Hayenga, J., Design and Rapid Prototyping of Thin-Film Laminate-Based Microfluidic Devices. *Biomed. Microdevices* **2001,** *3* (4), 267-274.

22.   Taylor, A. W.; Harris, D. M., Optimized commercial desktop cutter technique for rapid-prototyping of microfluidic devices and application to Taylor dispersion. *Rev. Sci. Instrum.* **2019,** *90* (11), 116102.

23.   Moreira, N. S.; Chagas, C. L. S.; Oliveira, K. A.; Duarte-Junior, G. F.; de Souza, F. R.; Santhiago, M.; Garcia, C. D.; Kubota, L. T.; Coltro, W. K. T., Fabrication of microwell plates and microfluidic devices in polyester films using a cutting printer. *Anal. Chim. Acta* **2020,** *1119*, 1-10.

24.   Islam, M.; Natu, R.; Martinez-Duarte, R., A study on the limits and advantages of using a desktop cutter plotter to fabricate microfluidic networks. *Microfluid. Nanofluid.* **2015,** *19* (4), 973-985.

25.   da Costa, E. T.; Mora, M. F.; Willis, P. A.; do Lago, C. L.; Jiao, H.; Garcia, C. D., Getting started with open-hardware: Development and control of microfluidic devices. *Electrophoresis* **2014,** *35* (16), 2370-2377.

26.   Channon, R. B.; Nguyen, M. P.; Scorzelli, A. G.; Henry, E. M.; Volckens, J.; Dandy, D. S.; Henry, C. S., Rapid flow in multilayer microfluidic paper-based analytical devices. *Lab Chip* **2018,** *18* (5), 793-802.

27.   Yuen, P. K.; Goral, V. N., Low-cost rapid prototyping of flexible microfluidic devices using a desktop digital craft cutter. *Lab Chip* **2010,** *10* (3), 384-387.

28.   Ouyang, Y.; Wang, S.; Li, J.; Riehl, P. S.; Begley, M.; Landers, J. P., Rapid patterning of 'tunable' hydrophobic valves on disposable microchips by laser printer lithography. *Lab Chip* **2013,** *13* (9), 1762-1771.

29.   Gale, B. K.; Jafek, A. R.; Lambert, C. J.; Goenner, B. L.; Moghimifam, H.; Nze, U. C.; Kamarapu, S. K., A Review of Current Methods in Microfluidic Device Fabrication and Future Commercialization Prospects. *Inventions* **2018,** *3* (60), 1-25.

30.   Berg, J. C., *An Introduction to Interfaces and Colloids*. 2010.

31.   Basheer, A. A., Chemical chiral pollution: impact on the society and science and need of the regulations in the 21st century. *Chirality* **2018,** *30* (4), 402-406.

32.   Jokanović, M.; Kosanović, M., Neurotoxic effects in patients poisoned with organophosphorus pesticides. *Environ. Toxicol. Pharmacol.* **2010,** *29* (3), 195-201.

33.   Melgarejo, M.; Mendiola, J.; Koch, H. M.; Moñino-García, M.; Noguera-Velasco, J. A.; Torres-Cantero, A. M., Associations between urinary organophosphate pesticide metabolite levels and reproductive parameters in men from an infertility clinic. *Environ. Res.* **2015,** *137*, 292-298.

34.   Sanchez-Santed, F.; Colomina, M. T.; Hernández, E. H., Organophosphate pesticide exposure and neurodegeneration. *Cortex* **2016,** *74*, 417-426.

35.   Manthripragada, A. D.; Costello, S.; Cockburn, M. G.; Bronstein, J. M.; Ritz, B., Paraoxonase 1 (PON1), agricultural organophosphate exposure, and Parkinson disease. *Epidemiology* **2010,** *21* (1), 87-94.

36.   Lerro, C. C.; Koutros, S.; Andreotti, G.; Friesen, M. C.; Alavanja, M. C.; Blair, A.; Hoppin, J. A.; Sandler, D. P.; Lubin, J. H.; Ma, X., Organophosphate insecticide use and cancer incidence among spouses of pesticide applicators in the Agricultural Health Study. *Occup. Environ. Med.* **2015,** *72* (10), 736-744.

37.   Hu, Y.; Chiu, Y.-H.; Hauser, R.; Chavarro, J.; Sun, Q., Overall and class-specific scores of pesticide residues from fruits and vegetables as a tool to rank intake of pesticide residues in United States: a validation study. *Environ. Int.* **2016,** *92*, 294-300.

38.   Donkor, A.; Osei-Fosu, P.; Dubey, B.; Kingsford-Adaboh, R.; Ziwu, C.; Asante, I., Pesticide residues in fruits and vegetables in Ghana: a review. *Environ. Sci. Pollut. Res.* **2016,** *23* (19), 18966-18987.

39.   Ingenbleek, L.; Hu, R.; Pereira, L. L.; Paineau, A.; Colet, I.; Koné, A. Z.; Adegboye, A.; Hossou, S. E.; Dembélé, Y.; Oyedele, A. D., Sub-Saharan Africa total diet study in Benin, Cameroon, Mali and Nigeria: Pesticides occurrence in foods. *Food Chemistry: X* **2019,** *2*, 100034.

40.   Huang, X. C.; Ma, J. K.; Feng, R. X.; Wei, S. L., Simultaneous determination of five organophosphorus pesticide residues in different food samples by solid-phase microextraction fibers coupled with high-performance liquid chromatography. *J. Sci. Food Agric.* **2019,** *99* (15), 6998-7007.

41.   Fernandes, V. C.; Freitas, M.; Pacheco, J. P.; Oliveira, J. M.; Domingues, V. F.; Delerue-Matos, C., Magnetic dispersive micro solid-phase extraction and gas chromatography determination of organophosphorus pesticides in strawberries. *J. Chromatogr. A.* **2018,** *1566*, 1-12.

42.   Li, D.; Jiang, M.; Xu, L.; Qiao, X.; Xu, Z., Simultaneous determination of acephate and isocarbophos in vegetables by capillary electrophoresis using ionic liquid and sodium dodecyl sulfate as modifiers. *Food Anal. Methods* **2017,** *10* (10), 3368-3374.

43.   Kung, C.-T.; Hou, C.-Y.; Wang, Y.-N.; Fu, L.-M., Microfluidic paper-based analytical devices for environmental analysis of soil, air, ecology and river water. *Sens. Actuators, B* **2019,** *301*, 126855.

44.   Yan, X.; Li, H.; Su, X., Review of optical sensors for pesticides. *TrAC, Trends Anal. Chem.* **2018,** *103*, 1-20.

45.   Jahanshahi-Anbuhi, S.; Henry, A.; Leung, V.; Sicard, C.; Pennings, K.; Pelton, R.; Brennan, J. D.; Filipe, C. D. M., Paper-based microfluidics with an erodible polymeric bridge giving controlled release and timed flow shutoff. *Lab Chip* **2014,** *14* (1), 229-236.

46.   Yang, N.; Shaheen, N.; Xie, L.; Yu, J.; Ahmad, H.; Mao, H., Pesticide Residues Identification by Optical Spectrum in the Time-Sequence of Enzyme Inhibitors Performed on Microfluidic Paper-Based Analytical Devices (µPADs). *Molecules* **2019,** *24* (13), 2428.

47.   Kim, H. J.; Kim, Y.; Park, S. J.; Kwon, C.; Noh, H., Development of Colorimetric Paper Sensor for Pesticide Detection Using Competitive-inhibiting Reaction. *BioChip Journal* **2018,** *12* (4), 326-331.

48.   Ellman, G. L.; Courtney, K. D.; Andres Jr, V.; Featherstone, R. M., A new and rapid colorimetric determination of acetylcholinesterase activity. *Biochem. Pharmacol* **1961,** *7* (2), 88-95.

49.   Pundir, C. S.; Chauhan, N., Acetylcholinesterase inhibition-based biosensors for pesticide determination: A review. *Anal. Biochem.* **2012,** *429* (1), 19-31.

50.   Jiang, J.; Zou, S.; Ma, L.; Wang, S.; Liao, J.; Zhang, Z., Surface-Enhanced Raman Scattering Detection of Pesticide Residues Using Transparent Adhesive Tapes and Coated Silver Nanorods. *ACS Appl. Mater.* **2018,** *10* (10), 9129-9135.

51.   Olanrewaju, A.; Beaugrand, M.; Yafia, M.; Juncker, D., Capillary microfluidics in microchannels: from microfluidic networks to capillaric circuits. *Lab Chip* **2018,** *18* (16), 2323-2347.

52.   Zimmermann, M.; Hunziker, P.; Delamarche, E., Valves for autonomous capillary systems. *Microfluid. Nanofluid.* **2008,** *5* (3), 395-402.

53.   Mendez, S.; Fenton, E. M.; Gallegos, G. R.; Petsev, D. N.; Sibbett, S. S.; Stone, H. A.; Zhang, Y.; López, G. P., Imbibition in Porous Membranes of Complex Shape: Quasi-stationary Flow in Thin Rectangular Segments. *Langmuir* **2010,** *26* (2), 1380-1385.

54.   Adkins, J. A.; Noviana, E.; Henry, C. S., Development of a Quasi-Steady Flow Electrochemical Paper-Based Analytical Device. *Anal. Chem.* **2016,** *88* (21), 10639-10647.

55.   Noviana, E.; Klunder, K. J.; Channon, R. B.; Henry, C. S., Thermoplastic Electrode Arrays in Electrochemical Paper-Based Analytical Devices. *Anal. Chem.* **2019,** *91* (3), 2431-2438.

56.   Pradela-Filho, L. A.; Noviana, E.; Araújo, D. A. G.; Takeuchi, R. M.; Santos, A. L.; Henry, C. S., Rapid Analysis in Continuous-Flow Electrochemical Paper-Based Analytical Devices. *ACS Sensors* **2020,** *5* (1), 274-281.

57.   Kang, H.; Jang, I.; Song, S.; Bae, S.-C., Development of a Paper-Based Viscometer for Blood Plasma Using Colorimetric Analysis. *Anal. Chem.* **2019,** *91* (7), 4868-4875.

58.   Toh, A. G. G.; Wang, Z. P.; Yang, C.; Nguyen, N.-T., Engineering microfluidic concentration gradient generators for biological applications. *Microfluid. Nanofluid.* **2014,** *16* (1), 1-18.

59.   Apilux, A.; Isarankura-Na-Ayudhya, C.; Tantimongcolwat, T.; Prachayasittikul, V., based acetylcholinesterase inhibition assay combining a wet system for organophosphate and carbamate pesticides detection. *EXCLI journal* **2015,** *14*, 307.

60.   Getz, M. E.; Friedman, S. J., Organophosphate pesticide residues: A spot test for detecting cholinesterase inhibitors. *J. AOAC* **1963,** *46* (4), 707-710.

61.   Wu, Y.; Sun, Y.; Xiao, F.; Wu, Z.; Yu, R., Sensitive inkjet printing paper-based colormetric strips for acetylcholinesterase inhibitors with indoxyl acetate substrate. *Talanta* **2017,** *162*, 174-179.

62.   Guilbault, G. G.; Sadar, M.; Glazer, R.; Skou, C., N-Methyl indoxyl esters as substrates for cholinesterase. *Anal. Lett.* **1968,** *1* (6), 365-379.

63.   Hossain, S. M. Z.; Luckham, R. E.; McFadden, M. J.; Brennan, J. D., Reagentless Bidirectional Lateral Flow Bioactive Paper Sensors for Detection of Pesticides in Beverage and Food Samples. *Anal. Chem.* **2009,** *81* (21), 9055-9064.

64.   Sebaugh, J., Guidelines for accurate EC50/IC50 estimation. *Pharm. Stat.* **2011,** *10* (2), 128-134.

65.   Krstić, D. Z.; Čolović, M.; Bavcon kralj, M.; Franko, M.; Krinulović, K.; Trebše, P.; VASIĆ, V., Inhibition of AChE by malathion and some structurally similar compounds. *J. Enzyme Inhib. Med.* **2008,** *23* (4), 562-573.

66.   Sabullah, K., An Inhibitive Assay for Insecticides using The Acetylcholinesterase from Osteochillus hasselt. *Bull. Environ. Sci. Sustain. Manag.* **2013,** *1* (1), 1-4.

67.   Pavelkić, V. M.; Krinulović, K. S.; Savić, J. Z.; Ilić, M. A., Malathion-induced inhibition of human plasma cholinesterase studied by the fluorescence spectroscopy method. *Russ. J. Phys. Chem. A* **2008,** *82* (5), 870-874.

68.   Ahmed, M.; Rocha, J. B. T.; Mazzanti, C. M.; Morsch, A. L.; Cargnelutti, D.; Corrêa, M.; Loro, V.; Morsch, V. M.; Schetinger, M. R., Malathion, carbofuran and paraquat inhibit Bungarus sindanus (krait) venom acetylcholinesterase and human serum butyrylcholinesterase in vitro. *Ecotoxicology* **2007,** *16* (4), 363.

A5.1 Image analysis

The red channel was selected for further analysis since it had the best correlation with the

malathion concentration. The normalized intensities were calculated based on the mean red

intensity of the blank paper (221.86) as follows:

$Normalized\ Mean\ Intensity = Mean\ Intensity\ of\ Blank - Mean\ Intensity\ of\ Sample$ (Eq. A5.1)
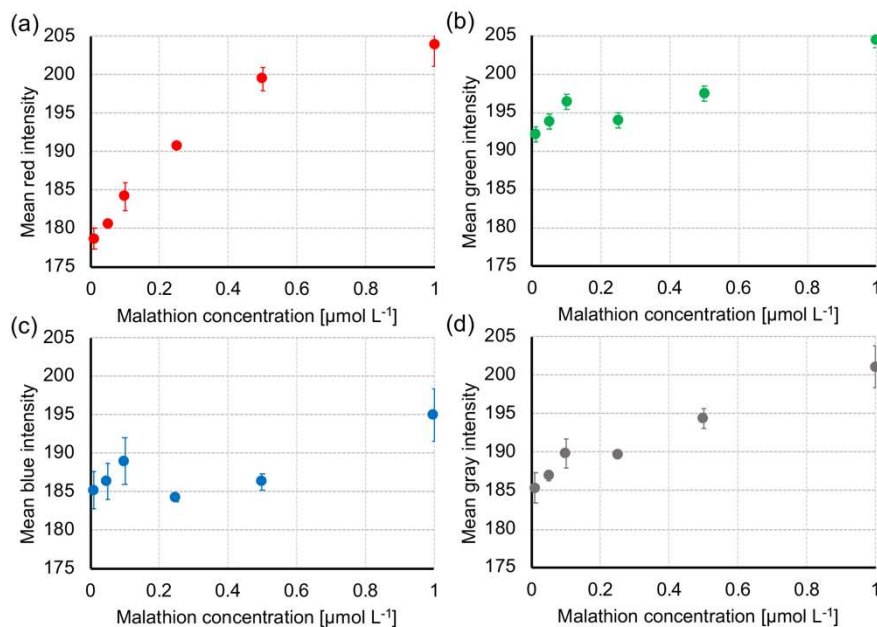
Figure A5.1 Mean intensity values of (a) red, (b) green, (c) blue, and (d) gray color channels for the various
concentrations of malathion (0.01 – 1 μM). All data and error bar indicate the averages and standard deviations
of 3 replicates.

Finally, we assumed the 0 μM concentration has 100% remaining activity and calculated

the remaining activity (%RA) using normalized mean intensity as follows:

$$\%RA = \frac{Normalized\ Mean\ Intensity\ of\ Sample}{Normalized\ Mean\ Intensity\ of\ 0\ \mu M} \times 100 \qquad \text{(Eq. A5.2)}$$

All values of normalized red intensity and remaining activity are shown in Table A5.1. The dose-response graph, that represents the remaining activity versus the logarithm of pesticide concentration, was applied to determine the concentration of malathion responsible for the inhibition of 50% of the enzymatic activity (IC50). The calibration curve was obtained through GraphPad Prism 8 software.

Table A5.1 Analysis results of captured images for different concentrations of malathion.

Concentration [μM]	Normalized red intensity	Remaining activity [%]
0	59.48 ± 0.3	100.0 ± 0.52
0.001	50.8 ± 0.6	90.2 ± 1.08
0.01	39.9 ± 1.1	72.5 ± 2.18
0.05	37.7 ± 0.8	69.5 ± 0.89
0.1	34.8 ± 2.0	63.3 ± 3.07
0.25	27.8 ± 0.2	52.3 ± 0.67
0.5	19.3 ± 0.2	37.6 ± 2.58
1	13.8 ± 3.4	30.0 ± 4.84
5	3.6 ± 2.5	10.1 ± 4.13

A5.2 Obtaining the constant for the numerical analysis

To express the mixing performance of real devices, we calculated the mean velocity and mixing diffusivity of the pH indicator experiment and used them as a mean velocity (U) and diffusivity (D) in Eq 1, respectively. First, the velocity in the main channel was calculated by analyzing the wetting area of the fan-shaped paper that was connected to the outlet and worked as a pump to draw the fluid through the channel. For the wetting area analysis, we utilized the overlapping inlet result that shows the wetting area much more clearly. Figure A5.2a and b show the variation in the wetting area over time in the fan-shaped paper of the pH indicator experiment. After the mixed fluid begins to flow into the fan-shaped paper layer, the wetting area increases linearly with a rate of 2.9 mm^2 s^{-1} ranging from 5 s to 35 s of flow time. Since the wetting area represents the volume of fluid within a paper layer, we considered the paper height (0.16 mm) and porosity (0.68) to determine the flow rate (0.316 mm^3 s^{-1}) and the mean velocity (U, 0.46 mm s^{-1})

at the outlet of the main channel. Next, the mixing diffusivity was calculated by analyzing the interdiffusion width which increases in the streamwise direction.

The interdiffusion width (σ) in a 2-dimensional microfluidic channel can be analytically estimated by assuming constant mixing diffusivity and mean velocity as follows:[1-3]

$$\sigma \sim \sqrt{xD/U} \qquad\qquad \text{(Eq. A5.3)}$$

where x is the distance from the inlet junction where both fluids meet. We used the side-by-side inlet result after assuming a 2-dimensional flow to determine the mixing diffusivity (Figure A5.2c). Figure A5.2d shows the analysis results of the interdiffusion width after the junction area of the side-by-side inlet channel. We confirmed that the square of interdiffusion width increases linearly with respect to distance, as shown in Eq. A5.3. However, we couldn't calculate the mixing diffusivity directly using Eq. A5.3, even knowing the relationship between distance and interdiffusion width as well as the mean velocity. Therefore, we performed an iterative method to determine the mixing diffusivity (D, 0.00135 mm^2 s^{-1}) which shows the same numerical results as the experimental results.
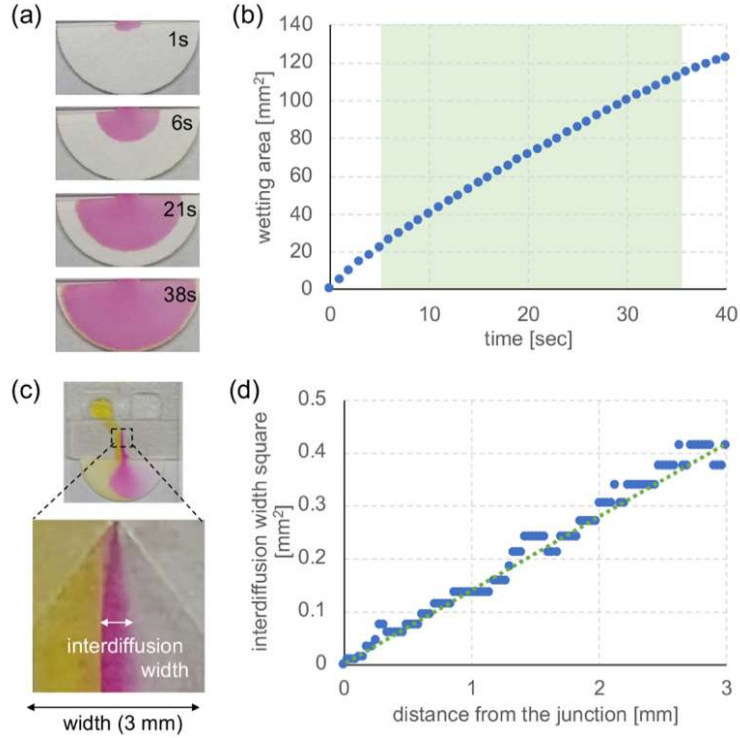
Figure A5.2 (a) Images of fan-shaped paper connected to the main channel, showing the increasing wetting area with time. (b) Wetting area analysis data for every second, measured until the paper is completely wet. (c) Enlarged image for analyzing the interdiffusion width of the side-by-side inlet channel. The image was captured after the fan-shaped paper completely wetted. (d) Variation plot of the interdiffusion width square with respect to distance from the junction.

A5.3. Absolute mixing index (AMI)

To quantify the mixing performance along the channel, we calculated an Absolute mixing index (AMI) on cross-sectional planes along the main channel. Since the concentration value of each node ranges from 0 to 1, we applied concentration values directly to calculate the AMIs. AMI is calculated by comparing the standard deviation of concentrations to the mean concentration at the same plane as follows:

$$AMI = \frac{\sigma}{<c>} = \frac{\sqrt{\frac{1}{N}\sum_{i=1}^{N}(C_i - <c>)^2}}{<c>}$$

(Eq. A5.4)

where σ is the standard deviation of the concentrations, C_i is the local concentration, $< C >$ is the average of the concentrations, and N is the total number of pixels on the interested plane.[4]

A5.4 Pesticide spraying in the food samples

All food samples were marked 'x' on the upper side and then placed along the spray line on the spray chamber platform, 100 cm from the nozzle (Figure A5.3). The nozzle sprayed the malathion solution (3 tablespoons per gallon of water) with 30 psi, traveling at 2 mph. After spraying pesticide once, the food samples were left inside the spray chamber to dry for 10 min (Figure A5.4). Finally, the food samples were taken from the spray chamber and stored individually prior to analysis.

Figure A5.3 Apples, cucumbers, and tomatoes placed in the spray chamber.
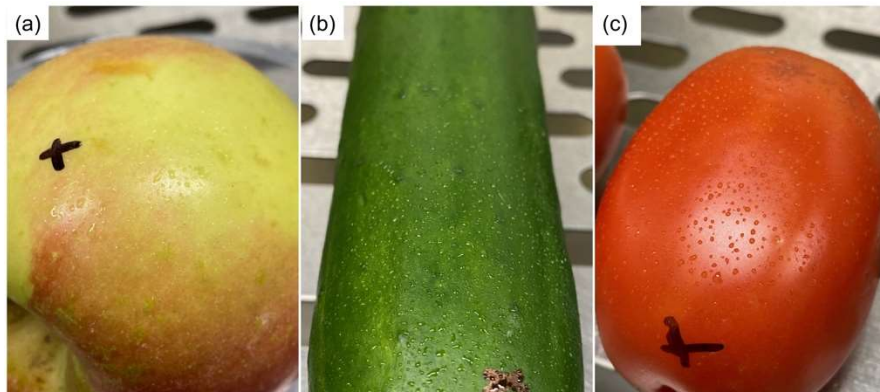
Figure A5.4 Food samples after pesticide spraying. (a) apple, (b) cucumber, and (c) tomato.

A5.5 Confirming the interference of the adhesive tape

172

We employed a "paste, peel off, solubilize" procedure to extract pesticides similarly as described by Jiang et al.[5] Since the peeled-off tape is solubilized in the sample solution, the impact of the tape on the colorimetric acetylcholinesterase assay should be evaluated. For a control experiment, two sample solutions of water: methanol (70:30 v/v) were prepared, and the adhesive tape (Scotch, 3M) of the same size (12x12 mm) as used in the food experiment was solubilized in one solution. Each sample solution was analyzed using the capillary-driven microfluidic mixer. The obtained results were compared using the t-Student unpaired test (Figure A5.5). There was no difference in mean red intensity using the tape.
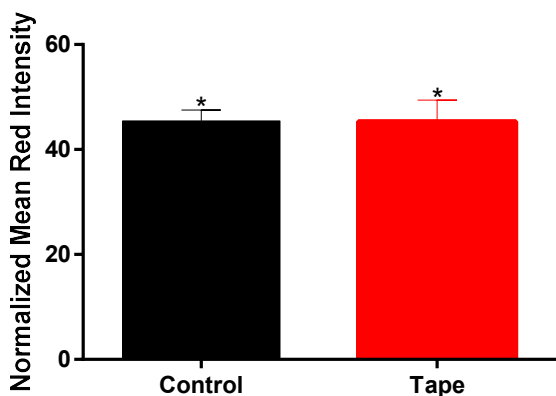
Figure A5.5 Control experiment to evaluate the effect of the tape constituents in the colorimetric acetylcholinesterase assay (n = 3, p < 0.05).

173

REFERENCES

1.   Kamholz, A. E.; Weigl, B. H.; Finlayson, B. A.; Yager, P., Quantitative Analysis of Molecular Interaction in a Microfluidic Channel: The T-Sensor. *Anal. Chem.* **1999,** *71* (23), 5340-5347.

2.   Ismagilov, R. F.; Stroock, A. D.; Kenis, P. J. A.; Whitesides, G.; Stone, H. A., Experimental and theoretical scaling laws for transverse diffusive broadening in two-phase laminar flows in microchannels. *Appl. Phys. Lett.* **2000,** *76* (17), 2376-2378.

3.   JIMÉNEZ, J., The growth of a mixing layer in a laminar channel. *J. Fluid. Mech.* **2005,** *535*, 245-254.

4.   Hashmi, A.; Xu, J., On the Quantification of Mixing in Microfluidics. *J. Lab. Autom.* **2014,** *19* (5), 488-491.

5.   Jiang, J.; Zou, S.; Ma, L.; Wang, S.; Liao, J.; Zhang, Z., Surface-Enhanced Raman Scattering Detection of Pesticide Residues Using Transparent Adhesive Tapes and Coated Silver Nanorods. *ACS Appl. Mater.* **2018,** *10* (10), 9129-9135.

APPENDIX 6: SUPPLEMENTARY INFORMATION – COLORIMETRIC PAPER-BASED ANALYTICAL DEVICE FOR PFOS DETECTION
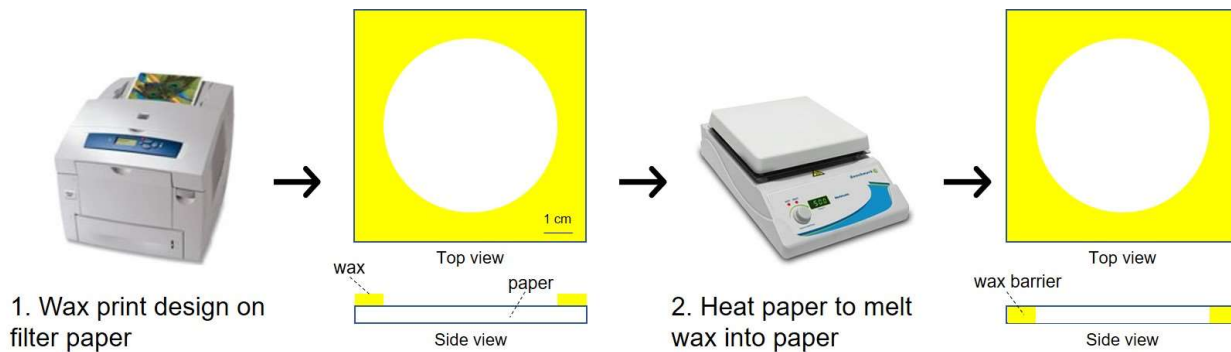
Figure A6.1 Device fabrication schematic.
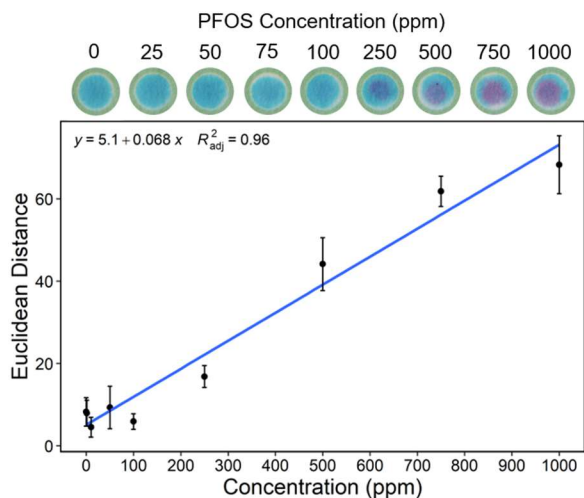
Figure A6.2 Spot test calibration curve of PFOS detection by methylene green (top). Calibration curve of color change as measured by Euclidean distance vs PFOS concentration (bottom). The Euclidean distance was calculated by the change in color between blue and purple in red-green-blue (RGB) color space. The data points are the average of 3 replicates for each PFOS concentration and the associated error bars are ± 1 standard deviation (1 σ) around the mean.
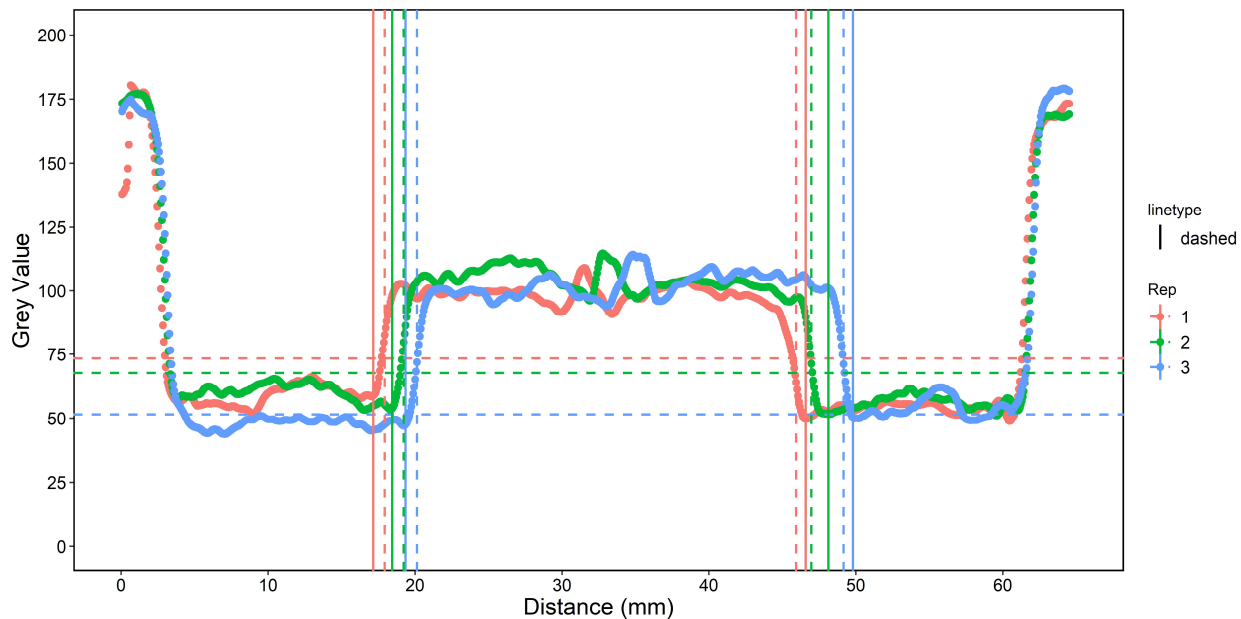
Figure A6.3 Sample ImageJ profile. The dashed horizontal lines correspond to the signal threshold that was determined for each profile by 3*standard deviation of the baseline. The dashed vertical lines are the maximum increase (on the left side) or maximum decrease (on the right side) to find a point to start looking for a continuous increase (or decrease) in grey value. The solid vertical lines represent where the purple color starts and ends.
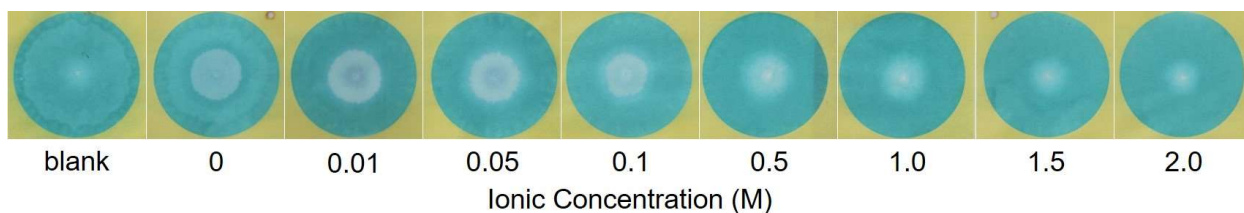
Figure A6.4 Representative device pictures of increasing ionic strength with 100 ppm PFOS. Ionic strength was adjusted by changing the NaCl concentration.
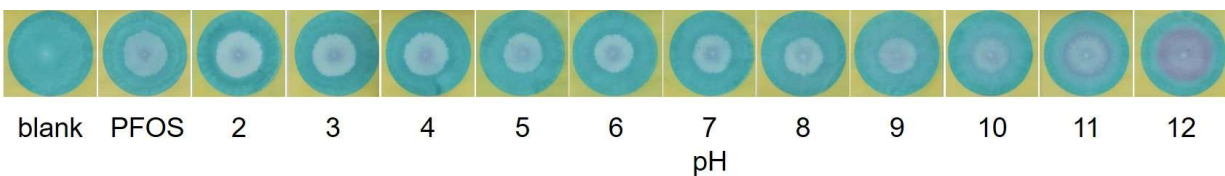
Figure A6.5 Representative device pictures of 100 ppm PFOS prepared in 40 mM Britton Robinson buffer. The pH of each solution was adjusted with 1 M NaOH.
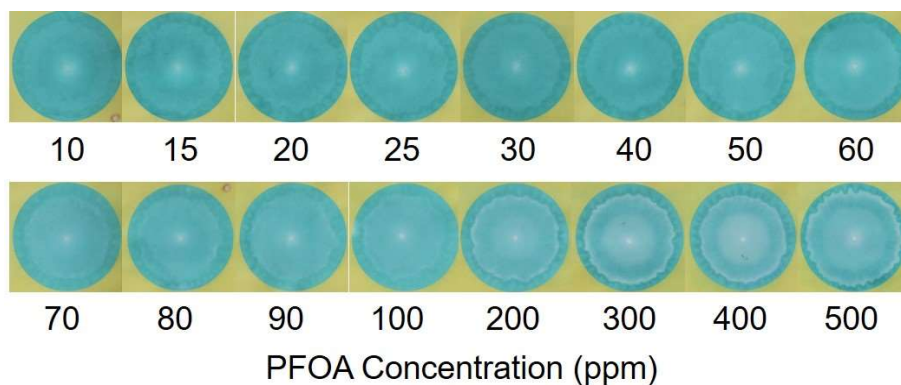
Figure A6.6 Representative device pictures of W4 filter paper prepared with 150 ppm methylene green. An aliquot (300 µL) of PFOA prepared in water was added to each device.
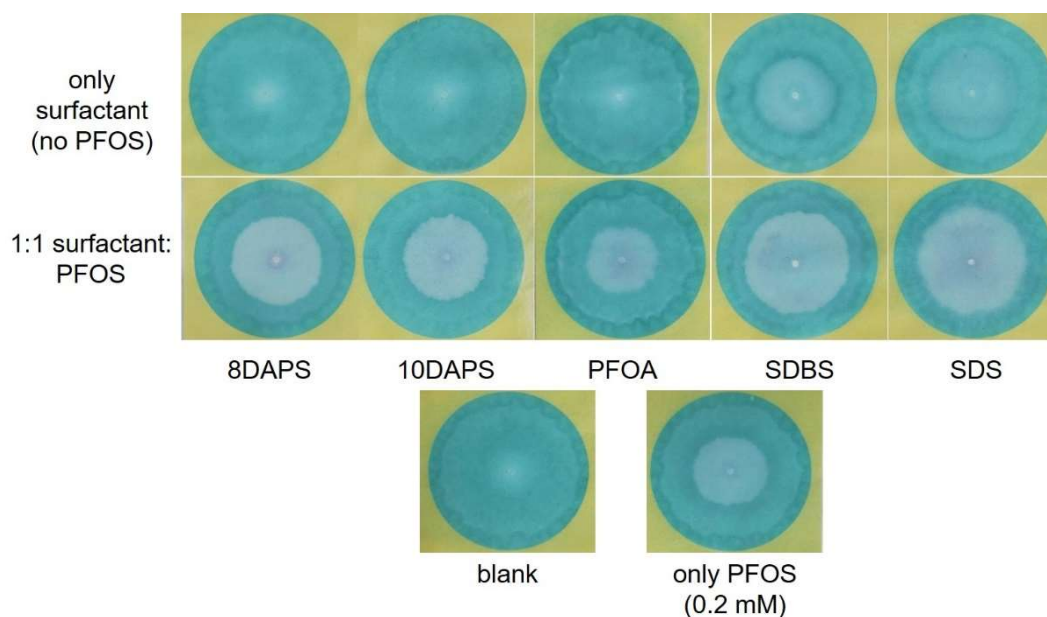
Figure A6.7 Representative device pictures of surfactant interference study. Top row: only 0.2 mM surfactant prepared in water was added to each device. Second row: 0.2 mM surfactant + 0.2 mM PFOS. Bottom row: blank and only PFOS (100 ppm = 0.2 mM). 300 µL were added to each device (60 mm).
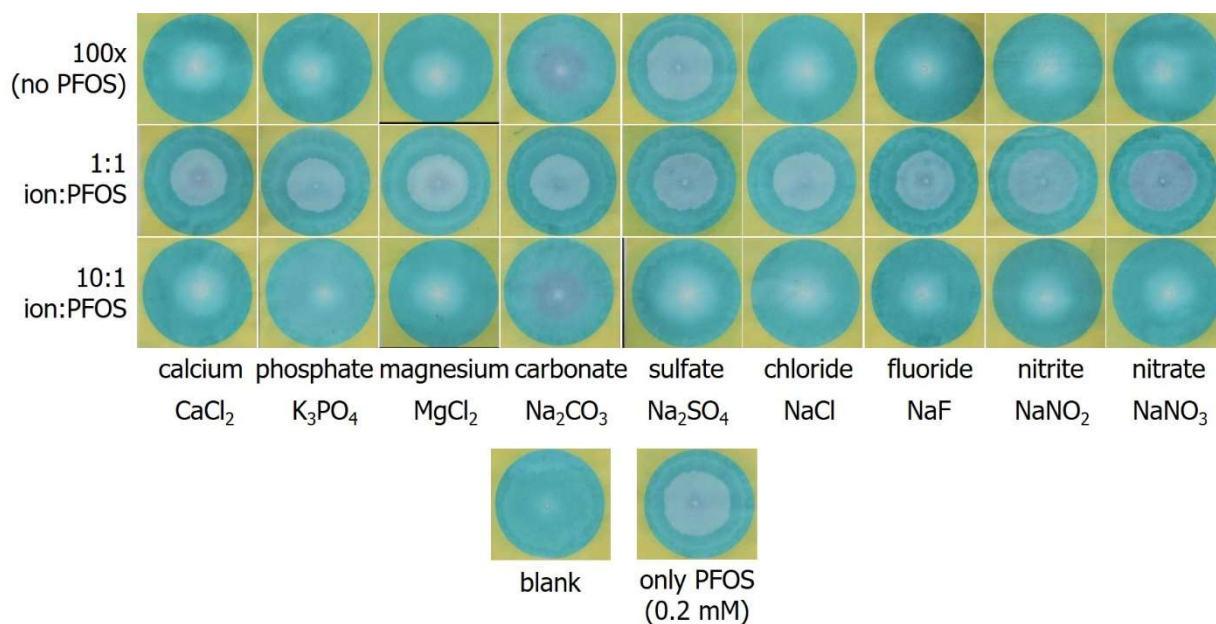
Figure A6.8 Representative device pictures of common ion interferences. Top row: 20 mM (100x) ion prepared in water was added to each device. Second row: 0.2 mM (1x) + 0.2 mM PFOS. Third row: 2.0 mM (10x) + 0.2 mM PFOS. Bottom row: blank and just PFOS (0.2 mM = 100 ppm). 300 µL were added to each device.
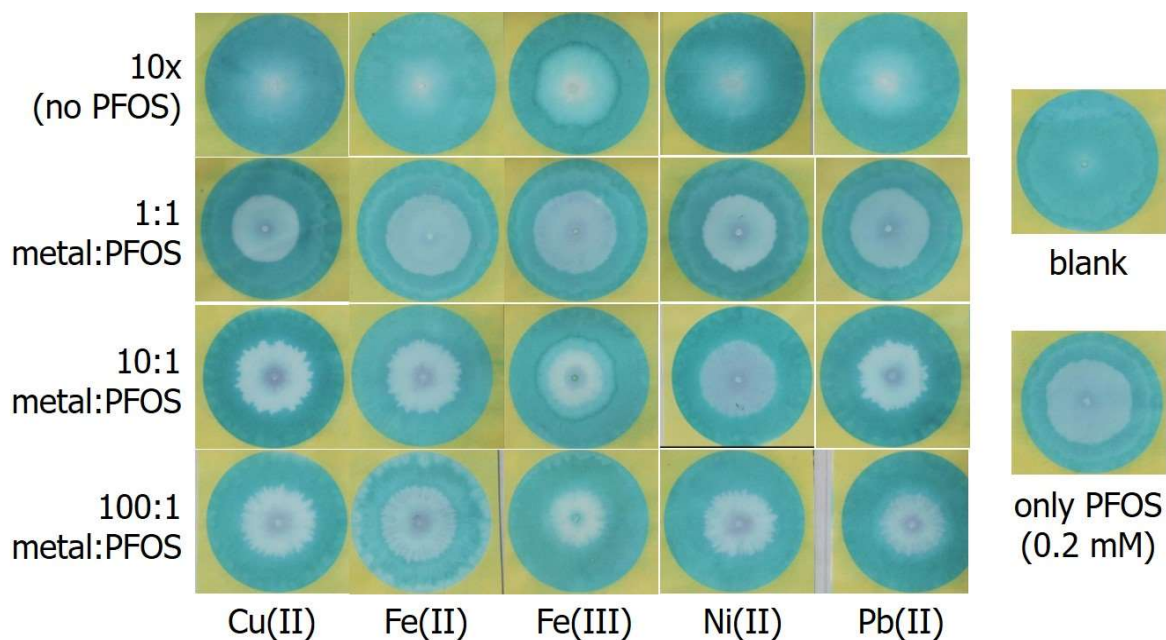

Figure A6.9 Representative device pictures of heavy metal interferences. Top row: just 2 mM (10x) heavy metal prepared in water was added to each device. Second row: 0.2 mM (1x) + 0.2 mM PFOS. Third row: 2.0 mM (10x) + 0.2 mM PFOS. Bottom row: 20.0 mM (100x) + 0.2 mM PFOS. Right panel: blank and just PFOS (0.2 mM = 100 ppm). 300 µL were added to each device.

178
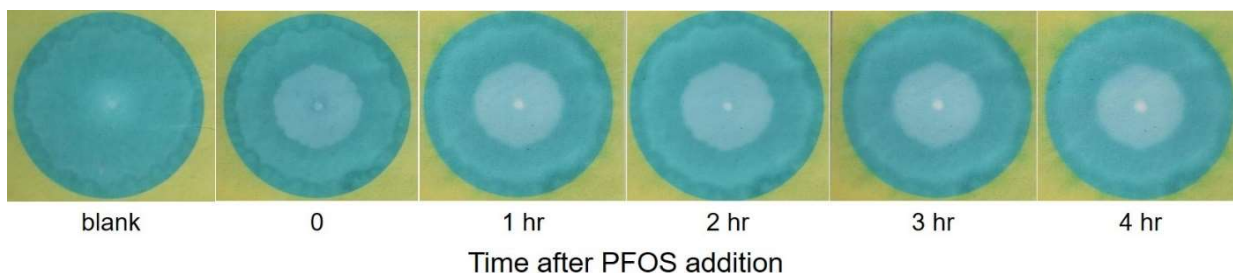
Figure A6.10 Representative device pictures of signal stability after PFOS (100 ppm) addition.

ImageJ Macro

```
imageTitle=getTitle();
run("Split Channels");
selectWindow(imageTitle+" (green)");
close();
selectWindow(imageTitle+" (blue)");
close();
selectWindow(imageTitle+" (red)");
run("Specify...", "width=1000 height=30 x=0 y=470");

run("Clear Results");
 profile = getProfile();
 for (i=0; i<profile.length; i++)
    setResult("Value", i, profile[i]);
 updateResults;
for (i=0; i<profile.length; i++)
        setResult("Label", i, imageTitle);
        updateResults;

 // Plot profile
 Plot.create("Profile", "X", "Value", profile);
selectWindow("Profile");
close();

run("Read and Write Excel", "stack_results");
```
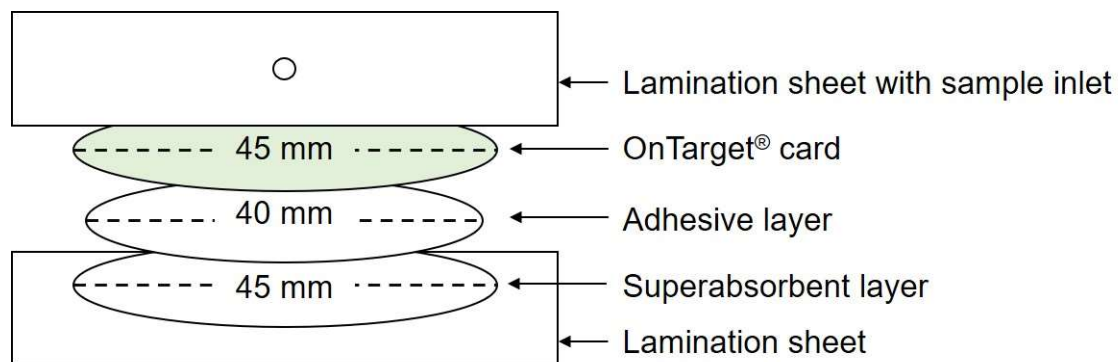
Figure A7.1 Scheme of device configuration with superabsorbent material underneath the radial detection layer. The detection layer and superabsorbent layer are connected with double-sided adhesive. The entire stack of paper is sealed with a lamination sheet.
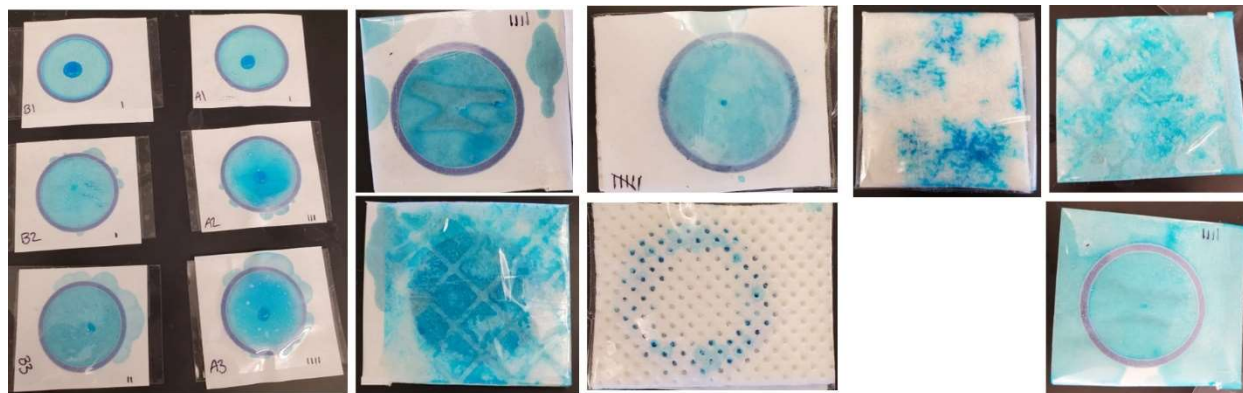

Figure A7.2 Example of devices with superabsorbent materials as the backing, following device scheme in Figure A7.1.
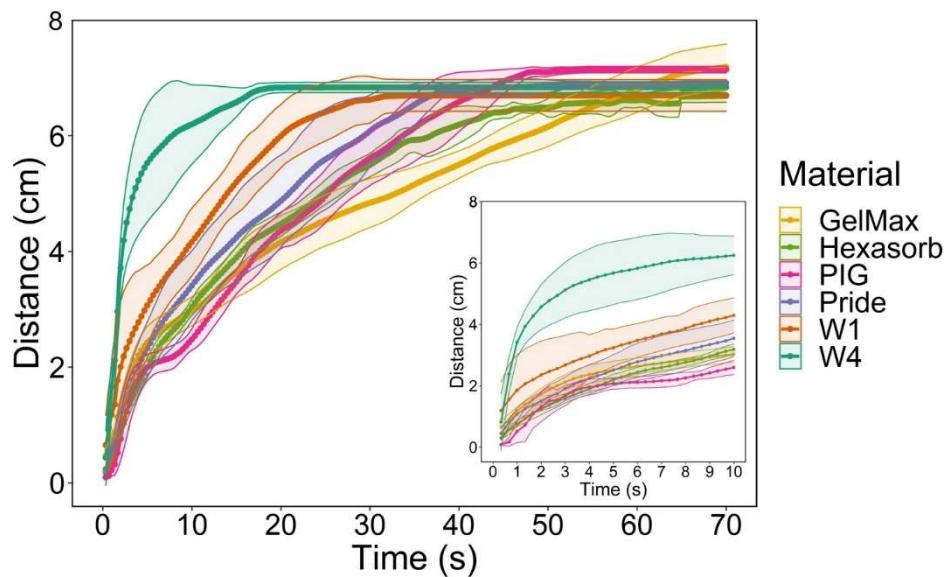
Figure A7.3 Evaluation of flow velocity in different materials. W1 = Whatman 1 filter paper, W4 = Whatman 4 filter paper. Each line is the average of 3 replicates and the shading represents ±1σ around the mean.
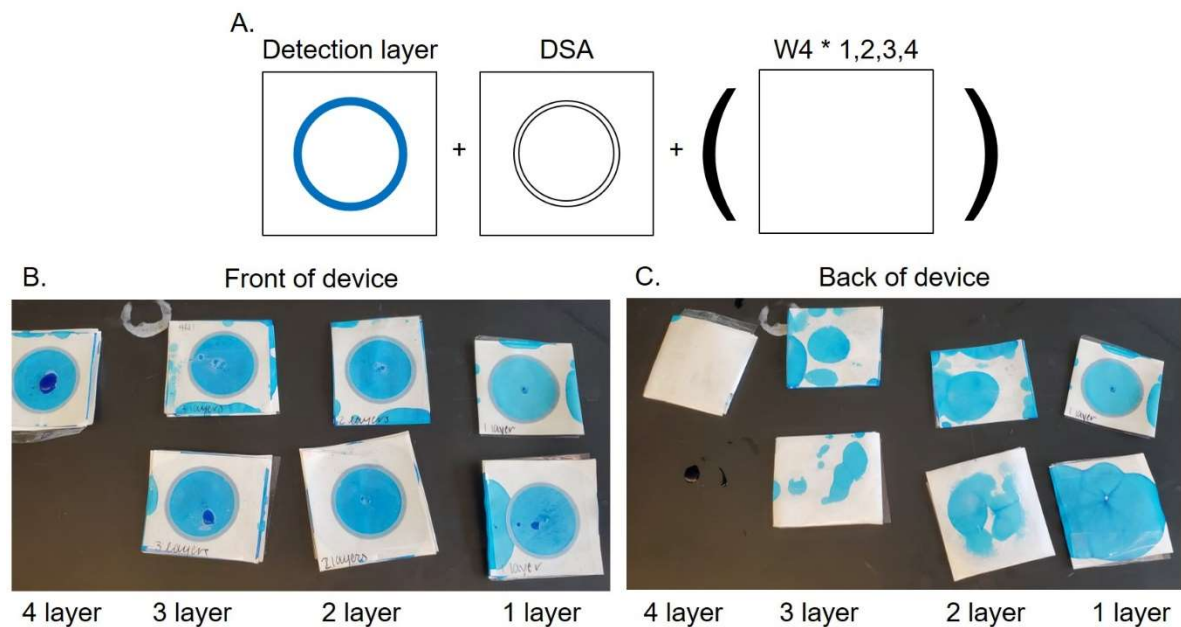
Figure A7.4 A. Device scheme of stacking multiple layers of Whatman 4 (W4) filter paper underneath the detection layer. B. Evaluation of multiple layers of W4 with the addition of blue dye.

181
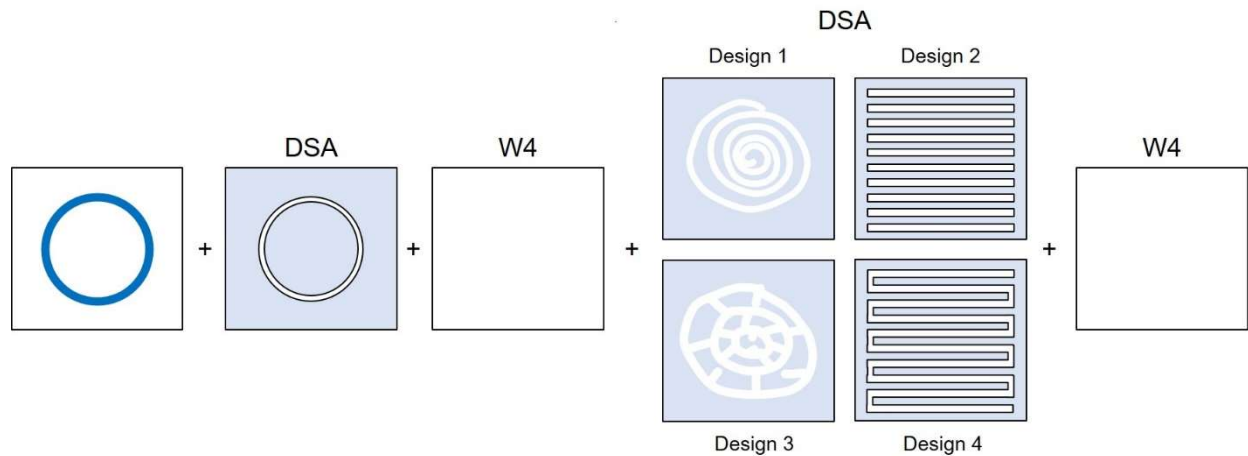
Figure A7.5 Scheme of device configuration with Whatman 4 (W4) filter paper and double-sided adhesive (DSA) layers. The entire stack of paper and tape is sealed with lamination sheet, with a sample inlet cut out of it.
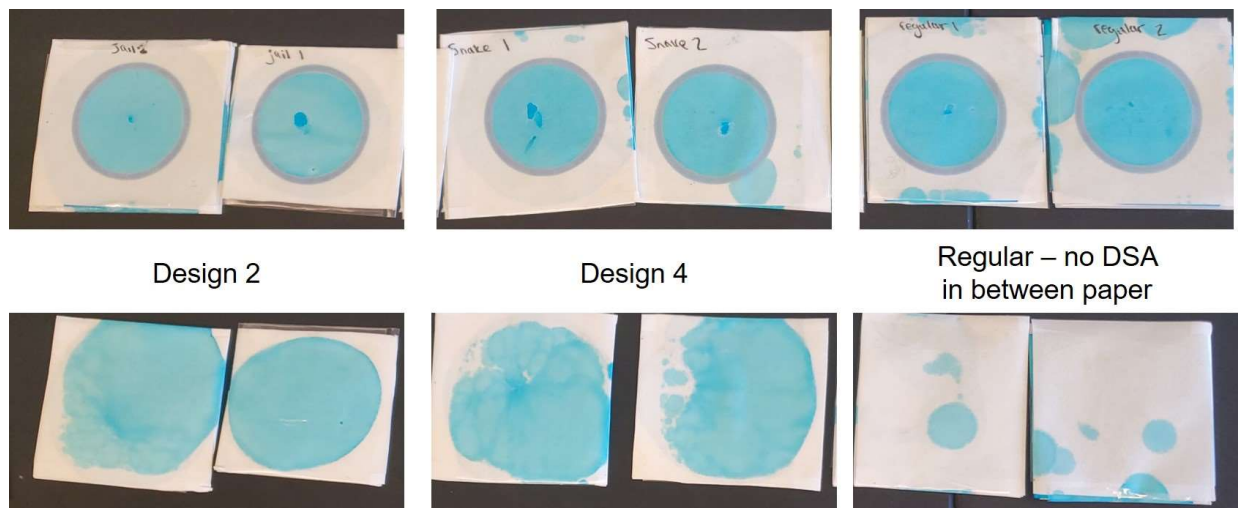
Figure A7.6 Evaluation of different shapes of double-sided adhesive (DSA) following the device scheme in Figure A7.5 with the addition of blue colored water.